PHOTOTHERMAL REFRACTION AND FOCUSING

by

Andrew Forbes

Submitted in partial fulfillment of the
requirements for the degree of
Doctor of Philosophy,
in the
Department of Physics,
University of Natal.

Durban,

December 1997

Abstract

This thesis begins with an introduction to the interaction and refraction of light in continuous media. It is shown how these properties can be exploited to achieve focusing of parallel light rays in such a medium. Past work on Gas Lenses is reviewed, highlighting the progress in design of gas lenses, leading to a justification for the research described in the rest of the chapter. Original work by the author on the subject of continuous gas lenses at low and high pressure is then presented. Experiments show that gas lenses at low pressure have stable foci, but long focal lengths, while at high pressure two foci are produced, both of unstable character. These results are explained by a simple theory, and future applications of such lensing properties are presented.

Chapter two introduces the concept of the Colliding Shock Lens (CSL), and presents shallow water wave simulations, conducted by the author, as a useful analogy to the interaction of shocks in the CSL. All the properties of the CSL lensing action are reproduced in the water simulations, yielding useful insight, by means of a simple experiment, into the physics of interacting shock waves.

Chapter three presents original work by the author on the subject of multiple pulse thermal lensing. A theory is developed which predicts the behaviour of thermal lenses seen in an industrial laser chain. Experiments on thermal lensing, as well as some solutions, are presented and discussed.

Chapter four revises the theory of Zernike Polynomials and their application to the study of aberrations. Thermal aberrations are studied, including the aberrations introduced by thermal lensing and thermal blooming. The relationship between aberrations and subsequent beam quality and beam propagation is explored.

Chapter five looks at the use of adaptive mirrors for mode matching. Although the theory of adaptive systems is well known, no-one has as yet tackled the problem of correcting for mode matching changes. A new way of thinking about mode matching is proposed, and the merits of this system, called *characterisation space*, are explained.

Chapter six comprises the theory and design of a novel vacuum chamber which has applications in gas lens designs. All the gas lenses used in pressure experiments were housed in compressional vacuum chambers. The idea of a Tensional Vacuum Vessel (TVV) is introduced, and experiments show that such chambers are very successful low vacuum chambers. The advantages and applications of TVVs are discussed, specifically those relating to gas lens applications.

At the end of this thesis it was apparent that more questions had been generated than answers. This is probably true of any study. Chapter seven therefore outlines some as yet unanswered questions, and gives some suggestions for starting points. Some of this work is presently being undertaken by the author.

The whole question of imagination in Science is often

misunderstood by people in other disciplines . . .

Our imagination is stretched to the utmost, not, as in fiction,

to imagine things which are not really there,

but just to comprehend those things which are there.

– R.P.Feynman.

Preface

The study in this thesis was started in the Department of Physics, University of Natal, Durban, during the period January 1993 to December 1994, under the supervision of Prof. M.M. Michaelis. Further work was continued as part of the research towards an MLIS (Molecular Laser Isotope Separation) plant, in the beam propagation group, under the guidance of Dr S.P. van Heerden. The author is presently employed to conduct the above mentioned research.

This study represents original work by the author. It has not been submitted in any form to another University, although parts of this work have been published as conference proceedings and as journal publications. Where use was made of the work of others it has been duly acknowledged in the text.

The commercial nature of the MLIS project requires that knowledge of integral parts of the process be kept secret. It is always unfortunate when information is controlled like this, since invariably it is in such large scale projects that Nature reveals her most interesting behaviour. It is like getting a free ticket to the theatre, but having to watch the show alone. I therefore apologise in advance for the lack of detail in some chapters. Several internal reports are referenced here which are classified and therefore not available for the reader.

Acknowledgements

The author would like to thank sincerely and acknowledge gratefully the following for their generous co–operation in contributing to the success of this thesis:

- Prof. M.M. Michaelis for his expert assistance and invaluable guidance, provided spontaneously, during the preparation and compilation of this thesis. I don't think I would ever have managed without the enthusiasm of Max.
- Dr S.P. van Heerden for knowledge and advice in abundance – producing original work is easy when you associate with such original thinkers. It has been a great honour working with you Fanie.
- Mr W. de Beer and Mr D. Davies, of the Physics workshop, for time and advice during the design and construction of the experimental apparatus.
- The many authors of books and articles, whether mentioned by name or not, whose ideas are contained in this thesis.
- The Foundation for Research Development, (FRD), for financial assistance through the award of a scholarship.
- The South African Optical Society, (SAOS), for the award of an optics study bursary.

- The University of Natal for the financial support of a Graduate Assistantship.
- The Faculty of Science Officer, for invaluable administrative assistance over the past few years.
- The Atomic Energy Corporation for the wonderful opportunities they have given me.
- My mother and family, for love and support when it was needed most.
- And finally, my loving wife, for encouraging me every step of the way.

Contents

1 Gas Lenses

1.1 Introduction

1.1.1 The Optimal Path

In this chapter we consider the refraction and focusing effects of gases. Specifically, we would like the refraction effects to be such that under certain conditions all the rays entering a medium will emerge converging to a point. We are therefore primarily interested in how the properties of the medium determine the path a ray of light will take. This leads rather naturally to an opening for this chapter which looks at an idea in physics that carries with it a tremendous influence on the development of physical thought in and beyond the study of classical and quantum optics. It is a law of nature that can be stated very simply, yet is mystifying in its implications: *the principle of least action.* Consider then the following analogy given by Gleick in his book *GENIUS* [*Gleick*,1993].

> A lifeguard, some feet up a beach, sees a drowning swimmer diagonally ahead, some distance offshore and some distance to one side. The lifeguard can run at a certain speed and swim at a certain lesser speed. How does one find the fastest path to the swimmer? A straight line, the shortest path, is not the fastest. The lifeguard will spend too much time in the water. If instead he angles far up the beach and dives in directly opposite the swimmer–the path of least water–he still wastes time. The

> best compromise is the path of least time, angling up the beach and then turning for a sharper angle through the water. Any calculus student can find the best path. A lifeguard has to trust his instincts. The mathematician Pierre de Fermat guessed in 1661 that the bending of a ray of light as it passes from air into water or glass–the refraction that makes possible lenses and mirages–occurs because light behaves like a lifeguard with perfect instincts. It follows the path of least time.

This idea was in contradiction of the existing theory by Hero of Alexandria, who believed light followed a path of *least distance*. This seems true if one only considers the reflection of light. Fermat, in considering both reflection and refraction, hit upon the idea of *least time*. It is easily shown that Fermat's principle of least time can be formulated into an equivalent statement: that light rays take the path with the *smallest optical path length*. In modern times Fermat's principle of least time has been altered slightly to read: A light ray must traverse an optical path length that is *stationary* with respect to the *variation* of that path.

This was one of the first examples of what is now known as a variational principle. Fermat's principle inspired others to ask similar questions about the motion of projectiles and the orbits of planets: could Newtonian mechanics be re-written as a variational principle? The answer was yes! Maupertius, Euler and later Lagrange, showed that the paths of moving objects are always, in a special sense, the most economical. They are the paths that minimise a quantity called *action*. Action is an abstract quantity; the difference between kinetic and potential energy $(K-U)$. For a ball or a planet moving along a certain path, it turns out that the path taken is the one for which the total action is a minimum. Of course we now have the problem that balls, planets and rays of light seem to *choose* their path. They seem to know all the possibilities in advance, but always opt for the one which minimises action. The physicist David Park phrased the question simply: how does a ray of light know which path to choose?

The answer to this question was made a little clearer by Richard Feynman. He found that, like classical mechanics, quantum mechanics could also be written as a variational principle: Feynman's *path–integral* view of nature. The formulation of this view is simple. Suppose a particle is emitted and later detected at A. The probability of arrival P, is given by $P = |\Phi|^2$ where Φ is some probability amplitude and is necessarily complex. This property gives the function an amplitude and a phase (much like a wave, hence the term 'wave function'). Now there are several different routes the particle (eg. photon) could take (eg. 1,2,3 ...) and Feynman postulated that *each path contributes to the total probability amplitude*

$$\Phi = \Phi_1 + \Phi_2 + \Phi_3 + \cdots,$$

so

$$P = |\Phi_1 + \Phi_2 + \Phi_3 + \cdots\ |^2,$$

and that the *magnitude of these individual probability amplitudes are all equal*, even if their respective phases are not. In fact, the phase depends on the path taken. To see how this is equivalent to Fermat's principle, and in fact even helps explain it, we note that there are many paths a ray of light or photon could take, but only those paths close to the actual path, the stationary path given by Fermat, will arrive nearly in phase. Hence it will be these paths which provide the predominant contribution to P. Paths far from the optical path length will arrive out of phase and interfere destructively, tending to cancel each other out. Feynman's path–integral view is therefore equivalent to the principle of least action.

The principle of least action seems to be a statement about the grand scheme of things, without any concern for the contributing mechanisms; being not so much computational as it is a concise way of thinking about the propagation of light. It seems almost as if the Universe wills simplicity. Newton's laws provide the mechanics; the principle of least action ensures grace.

1.1.2 The Ray Equation

Given that we know what path a ray of light will follow, we would now like to be able to trace such a path through a medium in which the refractive index (n) is slowly changing.

We begin with the scalar wave equation of optics [*Hecht*,1989]

$$\nabla^2\phi - \frac{n^2}{c^2}\frac{d^2\phi}{dt^2} = 0, \tag{1.1}$$

where $\phi \equiv E, B$. If the refractive index was constant, then a possible solution would be

$$\phi = \phi_o e^{i(k.r-\omega t)};$$

i.e. a plane wave, where the wave number k and frequency ω are related by $k = 2\pi/\lambda = n\omega/c$.

However, if we want to consider geometric optics where n is not constant but varies slowly, the plane wave will no longer be a solution as the wave is refracted and bent as n varies. Since we assume n varies slowly we look for a solution that looks like a plane wave but allows for the bending due to refraction

$$\phi = e^{A(r)}.e^{ik_o(\mathcal{S}(r)-ct)}, \tag{1.2}$$

$\mathcal{S}$ is the optical path length and is sometimes called the *Eikonal*. To place restrictions on $\mathcal{S}$ and A in order for ϕ to be a solution, we substitute the above equation back into the wave equation, which now becomes

$$ik_o[2\nabla A.\nabla \mathcal{S} + \nabla^2 \mathcal{S}]\phi \; + \; [\nabla^2 A + (\nabla A)^2 - k_o^2(\nabla \mathcal{S})^2 + n^2 k_o^2]\phi = 0. \qquad (1.3)$$

Since both A and $\mathcal{S}$ are real, the expressions in the square brackets must separately be zero:

$$\nabla^2 A + (\nabla A)^2 + k_o^2(n^2 - (\nabla \mathcal{S})^2) \; = \; 0, \qquad (1.4)$$

$$\nabla^2 \mathcal{S} + 2\nabla A.\nabla \mathcal{S} \; = \; 0. \qquad (1.5)$$

These properties are derived from the wave equation without any approximations having been made. To relate this to geometric optics we assume that the wavelength is small compared to the dimensions of any change in the medium due to n varying slowly, i.e. as $\lambda_o \rightarrow 0$ so $k_o \rightarrow \infty$. Hence in dividing Equation (1.4) by k_o^2 we find that

$$n^2 = (\nabla \mathcal{S})^2. \qquad (1.6)$$

This is the Eikonal equation of geometric optics.

Solutions of Equation (1.6) describe a family of surfaces of constant optical phase, which could be mapped for increasing values of the constant to give the path of the radiation field. Since all changes to the beam must occur over a scale length much larger than the wavelength, it can be argued that over a short distance successive wavefronts propagate as plane waves. This allows the definition and concept of rays of light that propagate perpendicular to the wavefront. Using this concept, a unit vector normal to the wavefront can be defined by

$$\hat{u} = \frac{d\vec{r}}{ds},$$

where ds is an element along the ray. The wavefronts $\mathcal{S}$ = *const* are surfaces of constant phase, hence $\nabla\mathcal{S}$ is a vector normal to the surface, with magnitude

$$|\nabla\mathcal{S}| = n. \tag{1.7}$$

Therefore

$$n\frac{dr}{ds} = \nabla\mathcal{S},$$

which after some manipulation yields

$$\frac{d}{ds}\left(n\frac{dr}{ds}\right) = \nabla n, \tag{1.8}$$

which is known as the *Ray Equation.* It describes what path a ray of light would follow in a medium where the refractive index changes slowly along the ray path. In order to use this equation, one needs to know how the properties of the medium determine the function n – the refractive index.

1.1.3 The Refractive Index

We have seen, from the principle of least action, that rays of light somehow 'know' what path to take through changing media. We also have a relation – the ray equation – which fully describes such paths in the limit of geometric optics. This equation involves the function n, which is defined as the ratio of the speed of light in a vacuum to that in the medium in question. We now examine how the properties of the medium affect the speed of light, and directly cause a change in n. (It is more true to say that a change in the refractive index causes a change in the speed of light, rather than vice versa).

From the Lorenz-Lorentz equation, the refractive index of a mixture of non-polar gases is given by

$$\frac{n^2-1}{n^2+2} = \sum R_i\rho_i, \tag{1.9}$$

where R_i is the specific refraction, and ρ_i the partial density of the i^{th} component of the mixture. The function R_i is dependent on wavelength and pressure, but for small changes in pressure it has been shown [*Owens*, 1967] that R_i is very nearly constant – it increases by 0.01% when p increases by 0.5 Atm – and is given by

$$R_i = \frac{4}{3}\pi\left(\frac{N_a}{M_i}\right)\alpha_i. \tag{1.10}$$

If we now define N to be the number of molecules per unit volume, and A to be the molar refractivity, then from Equations (1.9) and (1.10) we have

$$\alpha = \frac{3}{4\pi N}\frac{n^2-1}{n^2+2}, \tag{1.11}$$

$$A = \frac{4}{3}\pi N_a\alpha. \tag{1.12}$$

Since $N_a/N = RT/p$ we have that

$$A = \frac{RT}{p}\frac{n^2-1}{n^2+2}. \tag{1.13}$$

For a gas $n^2 \approx 1$, so

$$A \approx \frac{RT}{p}\frac{n^2-1}{3}.$$

and hence we have the relation, (since A is roughly constant)

$$n^2 - 1 \approx \frac{3Ap}{RT}, \tag{1.14}$$

where if we further assume $n + 1 \approx 2$ we can reduce Equation (1.14) to the usual Gladstone-Dale law:

$$n - 1 = k\rho, \tag{1.15}$$

and k is a constant (given by $3/2A$).

We see from Equations (1.14) and (1.15) that as the medium becomes more dense, so the refractive index increases. Fermat, reasoning backwards, surmised that light must travel more slowly in denser media. Later Newton thought that he had proved the opposite: that light, like sound, travels faster in denser media (for example, water). Fermat, with his faith in a principle of simplicity, was right.

Newton was however correct in realising that $n = n(f)$ i.e. n is frequency dependent. However, in this chapter we deal with the properties of gases, and to good approximation gases do not disperse light substantially (implying that n is approximately independent of frequency).

1.2 The Principle of Gas Lenses

Knowing now how the refractive index varies with the properties of the medium, and knowing what path a ray of light would take through any such medium, we now turn our attention to the principle of a gas lens.

Gas lenses refract light to a focal point by a process of continuous refraction rather than stepwise refraction (as at the surfaces of solid lenses when viewed macroscopically). This is achieved by passing light through a medium where a refractive index (RI) gradient exists. Such lenses are referred to as GRIN (Graded Refractive INdex) lenses, the success of the lens depends on how well the refractive index gradient has been created. From Equations (1.14) and (1.15) we see that such a gradient can be created by invoking a pressure, temperature or density gradient in the would-be lens. If this gradient is symmetric about the axis, then focusing could be achieved. The paths of the rays through such a lens are fully described by the ray equation.

One could divide gas lenses into two subgroups: continuous gas lenses and pulsed gas lenses. Continuous gas lenses, as the name suggests, implies that the structure of the RI gradient is independent of time – it is always the same (continuous). An example would be a spinning heated pipe. Pulsed gas lenses have time varying RI gradients, achieved, for example, by colliding shock waves. The operating principle is therefore slightly more complex in the case of the pulsed gas lenses. Mathematically we can express the differences as follows: for continuous gas lenses we require $n(r) = n(-r)\ \forall\ t$ for focusing (with r measured from lens axis). Once the conditions are achieved, they will remain as such. For pulsed gas lenses, $n = n(r,t)$, and for focusing $n(r,t) = n(-r,t)\ \forall\ t$ but $n(t_i) \neq n(t_j)$. Thus, while continuous gas lenses are varifocal in that a change in initial conditions will change the focal length, pulsed gas lenses are doubly so. Not only will the focal length change with a change in initial conditions, but also the focal length is time varying. Depending on the time the ray passes through the lens, so will it experience a different refractive index gradient. Both continuous and pulsed gas lenses have been developed at the *University of Natal, Durban (UND), Laser laboratory*, and more detailed discussions of each are given later.

As an example of how a symmetric RI profile will result in focusing of a beam of parallel rays, consider the following analysis (for a more detailed treatment, see [*Notcutt et al.*, 1988]).

Assume that the RI profile is such that n is greatest at the centre of a cylinder (axial value) and decreases radially outwards such that

$$n(r) = n_o - \frac{Cr^2}{2},$$

where C is a constant. Consider the path of a ray entering at position $r = r_o$. Its path will be governed by Equation (1.8). Since all the rays are nearly parallel, $ds = dx$, where x is normal to the radial vector, and s is the ray direction. Now ignoring the product of small terms and realising that $n \approx 1$ we have

$$\frac{d^2r}{dx^2} = \frac{dn}{dr} = -Cr,$$

which has to be solved subject to

$$\left.\frac{dr}{dx}\right|_{x=0} = 0,$$

with $r = r_o$ at $x = 0$.

A solution of this is

$$r = r_o \cos(\sqrt{C}\, x).$$

It can be seen from this solution that the ray is waveguided by being alternatively focused and defocused. Once the ray leaves the medium, its path will be given by

$$r = -r_o\sqrt{C}\sin(\sqrt{C}\, l)x + r_o\cos(\sqrt{C}\, l) + r_o l\sqrt{C}\sin(\sqrt{C}\, l),$$

where l is the length of the lens.The roots of this give the position at which the rays cross the x-axis

$$x = l + \frac{\cot(\sqrt{C}\, l)}{\sqrt{C}}.$$

Notice that all the rays entering the medium will converge to the same point on the x-axis, implying that the beam is focused. A square law RI profile is an approximation to that used in graded index optical fibres. In fact the square law RI profile is only one example of a RI profile that would achieve focusing. In general any even, symmetric function that was independent of x would cause the rays to converge (although not necessarily giving a good focus). In the experiments discussed in the next section such a profile was generated by spinning a heated pipe. Many researchers have devised methods of achieving a focus with other RI profiles, and a review of this work is given next.

1.3 Review of past work on Gas Lenses

Gas lenses were first developed at the Bell Systems Laboratories for applications as waveguides. It was hoped that the effects of mirages could be reproduced in a controlled manner to alternatively focus and defocus a beam, thus 'guiding' the beam along a channel. Berreman [*Berreman*,1964] and Marcuse [*Marcuse*,1964] started the work on tubular gas lenses – using a heated pipe to focus or guide a laser beam. Marcuse continued the work and later showed [*Marcuse*,1965] that a thermal gradient gas lens approximates a thin lens since the two principle surfaces almost coincide. He showed that the principle surface is not a plane. His thermal gradient gas lens worked on the principle of injected (cool) gas passing through a heated cylinder. The gas heats up close to the walls of the cylinder and the heat penetrates radially into the gas establishing a temperature gradient that causes a corresponding density gradient. The gas density, and consequently its refractive index, are higher at the centre of the tube and decrease radially towards the wall. The gas flowing through the tube acts as a lens and focuses light beams travelling through the tube. He found an optimum gas velocity that yields not only the minimum focal length but also minimises lens distortions.

Steier [*Steier*,1965] confirmed the theory proposed by Marcuse, with the exception of differences due to gravity effects. It was noted that convection caused distortions in such lenses, with the effects more pronounced in carbon dioxide than in air.

In 1967 Gloge [*Gloge*,1967] showed that the optical centre of the lens is displaced downwards proportionally to the fourth power of the tube diameter and with the square of the gas pressure. He showed that if the tube diameter is greater than 1cm, then for a carbon dioxide lens the optical centre would be outside the lens. Despite these distortion effects, gas lenses still had certain applications. Gas lenses were used as objective lenses in telescopes [*Aoki*,1967] but this was not wholly successful. Gas lenses were also used to guide laser beams around obstacles and as focusing elements within a laser in the bent state [*Kaiser*,1968]. Optical distortions still plagued gas lenses. This prompted Kaiser [*Kaiser*,1970] (perhaps due to his dismal telescope!) to make a slight modification to the gas lens design. He found that the optical quality of a thermal gas lens could be significantly improved if the heated gas is exhausted radially. He constructed a lens with outlets for the hot gas, with cool gas still pumped through as before. Imaging and waveguiding properties were improved with this design.

By the end of the sixties and into the early seventies a new field called *Aerothermooptics* was beginning to establish itself. It dealt with the relationship between thermohydrodynamic parameters and optics. Two papers of relevance were published from the *Heat and Mass Transfer Institute, Minsk* by Martynenko [*Martynenko et al.*,1972], [*Martynenko*,1975]. They showed how rotating the gas lens overcomes the asymmetric nature of the temperature field and consequently the refractive index field. This is an important result given that free convection causes optical aberrations.

Without knowledge of the Minsk results, the University of Natal Laser group [*Michaelis et al.*,1986] used a heated vertical pipe to create a long focal length lens for medium diameter laser beams (a few centimeters). This was used for drilling of holes in metal sheets, but again aberrations due to overheating and turbulence were observed. This lens did however differ from other designs in that the gas was not injected into the pipe – it used no gas flow. Independently in 1988, Notcutt et al. [*Notcutt et al.*.1988] managed to maintain a continuous focus in a horizontal pipe by using a combination of a gas jet and a spinning pipe. They found that if the pipe is rotated at less than 1Hz, the convection patterns are unaffected except for a slight tilt, but at more rapid rotations favourable temperature and density profiles are momentarily created. Although these become prone to Rayleigh–Taylor instabilities, the injection of gas seemed to overcome this.

This type of gas lens was further developed and shown to have some applications. Gas lenses were used in laser–produced plasma experiments [*Waltham et al.*,1990], for the final focusing element of high power laser systems and for the drilling and cutting of metals [*Michaelis et al.*,1991b]. The application of gas lenses in telescopes was illustrated beautifully with images taken of the Sun and Moon using a gas lens as an objective lens for a telescope [*Michaelis et al.*,1991c].

Properties of the spinning pipe gas lens were investigated by Lisi et al. They showed [*Lisi et al.*,1994] that a flat temperature distribution exists in the middle region of the pipe, while two regions of strong transverse thermal gradients are present near the edges of the pipe. They also concluded that the optical quality of the lens would decrease as the optical aperture approached the pipe aperture, due to weakly refracted rays at the walls of the pipe.

All the gas lenses developed were continuous gas lenses. It was realised by Michaelis [*Michaelis et al.*,1991a] that a pulsed gas lens would be a solution to the optics problem in Inertial Confinement Fusion (ICF). This idea was pursued by Buccellato [*Buccellato*,1992] who conducted experiments on a pulsed gas lens consisting of a gas at high pressure which is instantaneously released into the atmosphere. The resulting density gradients caused the laser beam to deflect. Simulations carried out on a cylindrical vessel indicated that this could be used to focus a laser beam. A more practical pulsed gas lens was designed and built by Buccellato et al. and was named the Colliding Shock Lens (CSL). They showed [*Buccellato et al.*,1993b] that colliding shocks could be used to focus a laser beam and that such a lens would have applications ranging from an industrial drill to an intracavity Q-switch element [*Lisi et al.*,1993].

Part of the work in this chapter is a follow–up of a statement made by Waltham et al. [*Waltham et al.*,1990]. They pointed out the need for an investigation into the stability of the focal point at even larger apertures, as well as the behaviour of the gas lens at low pressure. This work is discussed in the next section.

1.4 The Spinning Pipe Gas Lens

1.4.1 Introduction

As mentioned in the literature review given in § 1.3, much work has been done in the field of gas lenses, with the *UND Laser laboratory* giving special attention to the applications of spinning pipe gas lenses. The effects of pipe temperature and length on the focal length of the lens and the focal spot quality have been well understood for some time now. For most applications of gas lenses, these parameters could be varied to achieve a useful focal spot. However, the spinning pipe gas lens has the disadvantage that it only produces a good focus when the pipe diameter is small. For certain applications (eg. Astronomy), this limits the usefulness of the lens. Another point to be made is that all research on spinning pipe gas lenses was carried out under atmospheric conditions.

In this section we investigate the properties of a spinning pipe gas lens at pressures above and below atmospheric pressure. In particular we are interested in how the focal length and focal quality vary as a function of gas pressure. The research was conducted with the hope that at low pressures there would be less turbulence, perhaps allowing a route to increase the pipe diameter. This would then allow the scaling up of the lens aperture, resulting in furthering the applications and usefulness of gas lenses. The author has no knowledge of any experiments similar to the ones discussed in this chapter having been done elsewhere. A detailed explanation of the experimental arrangement is given, since this was designed, and in part built, by the author, requiring as much time and care as the experiment itself.

1.4.2 Experimental Arrangement

The gas lens comprised a 125cm long aluminium pipe, with an internal diameter of 47mm, which was mounted on two sets of brass rollers connected by a belt to an AC motor. The motor caused the rollers to rotate, which in turn resulted in the pipe rotation. (This design is sometimes referred to as a *friction driven device*). The lens was mounted on aluminium supports which were made to fit the contour of the chamber. Care was needed to ensure that all vibrations were damped; failure to do so affected the optical alignment when the pipe was rotating, and caused lens distortions.

In order for the pipe to 'lens', it must be heated and spun, while both of these parameters – temperature and rotation speed – should be controllable. To heat the pipe, a series of five ceramic heaters, each with a power rating of 375W, were arranged below the pipe and along its length. The heaters were connected to a common ground. A control board, consisting of five switches, each wired via a variac, was used to control the output power of each heater separately. The switches were wired in parallel and connected to the mains.

To connect the heaters, which were on the inside of the vacuum chamber to the switches, which were on the outside of the chamber, a set of six brass electrical pins were machined. The pins served as an electrical connection through the nylon flange, while vacuum conditions were maintained by using small O-rings with each pin. There were an additional two pins for the power input of the motor (the motor was mounted behind the lens on the inside of the vacuum chamber). A variac was used to regulate the input to the motor, thus controlling the pipe rotation speed.

Controlling the speed of rotation of the pipe was relatively easy once the pipe had been calibrated with respect to the variac settings (see Appendix B: *Calibration Techniques*). To monitor the temperature of the pipe, a series of thermocouples were designed which made use of the *Seebeck Effect*. For a full discussion of this phenomenon, see Appendix B. Five thermocouples were constructed and mounted inside a tuflon[1] rod. Holes were drilled into the rod to allow the thermocouple junctions to sit at set positions, just above the pipe surface (on the outside of the lens). The tuflon rod was mounted such that its axis was parallel to that of the gas lens. A second nylon flange was used as an insulating material to provide a connection, via inserted pins as before, between the thermocouple wires on the inside of the chamber, and the multimeter on the outside of the chamber. The multimeter was calibrated to give the temperature at the thermocouple junction above the gas lens surface.

The vacuum chamber, used to house the gas lens for the low and high pressure experiments, was roughly cylindrical in shape, with optical windows at either end for the laser input and output. Two ports were made to fit rotary vacuum pumps: these enabled the chamber to be pumped down to low pressures quickly. One

---

[1] Tuflon is an inert material similar to nylon

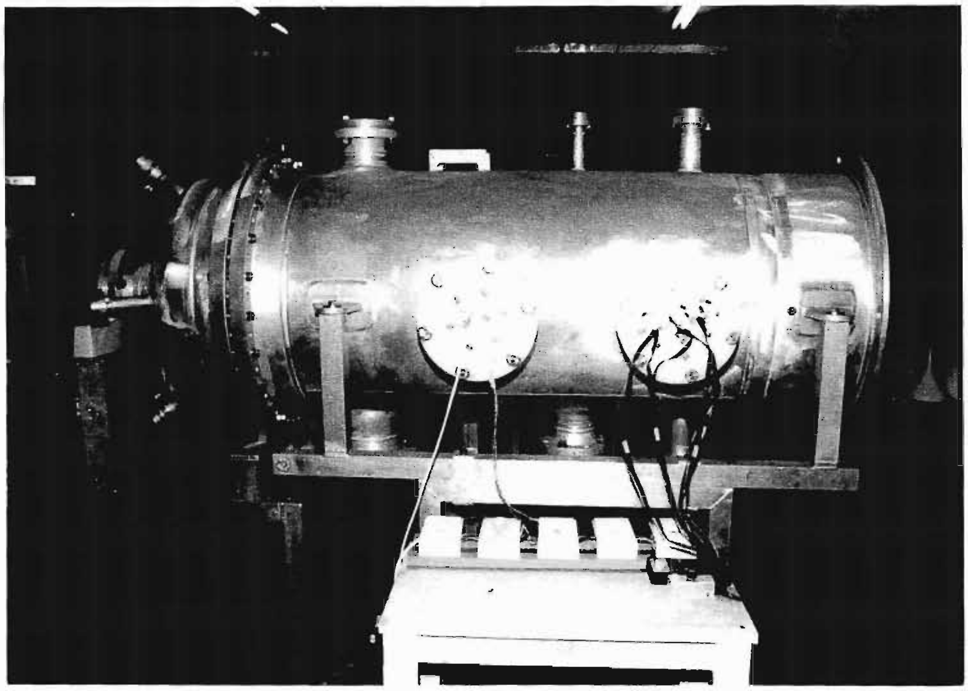

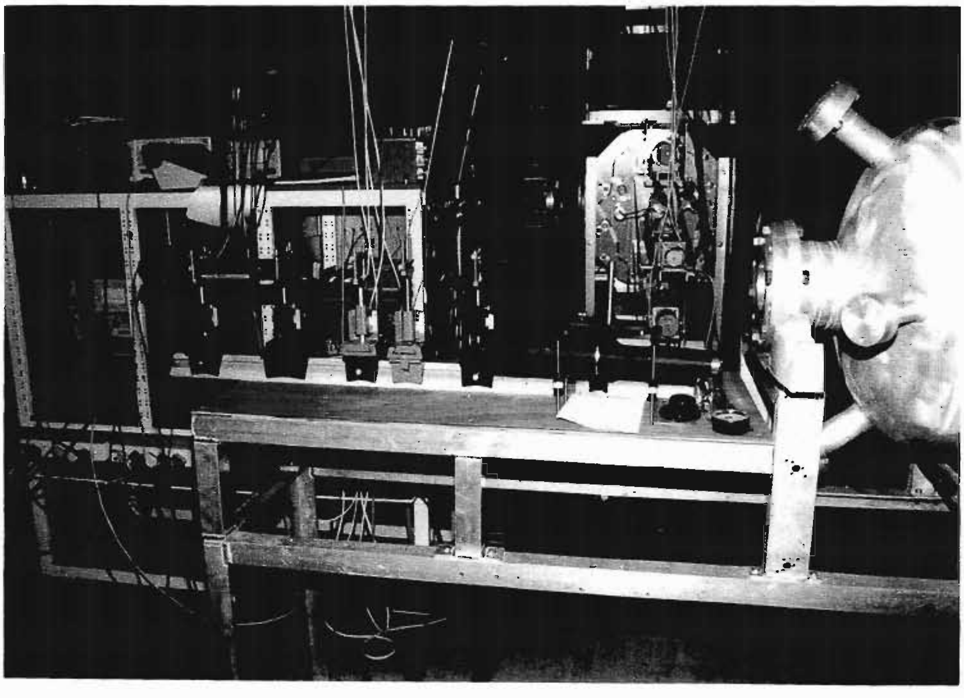

Figure 1: Photographs showing the main chamber with the optics and vacuum ports. The optics bench was supported behind the chamber, and this was where the laser and optics were mounted.

of these ports was fitted with a vacuum gauge to monitor the pressure. One of the vacuum ports was later converted to act as an inlet for pressurised gas (carbon dioxide and air). When the chamber was used for 'high' pressure experiments, the vacuum valve was closed and the vacuum gauge replaced by a pressure gauge. Absolute pressure was never increased beyond 3.5atm. Two additional ports were used for the electrical connections between the inside of the chamber and the outside. The entire chamber was raised off the ground by a trolley, which could be adjusted such that the gas lens was horizontal. (see Figure 1)

The optical system consisted of a helium-neon laser, a spatial filter, a telescope, and finally the gas lens. The He-Ne laser was the source of the light rays. In order to improve the beam quality, a spatial filter was used between the laser and the telescope. The spatial filter was a simple design which used a 10cm focal length lens, a 500μm diameter pin-hole, and a 15cm focal length lens. The spatially filtered beam was then expanded by passing it through the telescope, until the beam diameter was 45mm: just slightly less than the internal pipe diameter. Alignment was difficult, but crucial: if the beam was not parallel to the lens axis, reflections off the pipe walls caused distortions.

In order to capture images, a screen was placed at the focal length of the lens (which varied according to the initial conditions). A camcorder was used to record images, which were later digitised. For immediate digital images, a CCD camera was placed with its face plate in the focal plane of the gas lens. A schematic of the optical arrangement is shown in Figure 2.

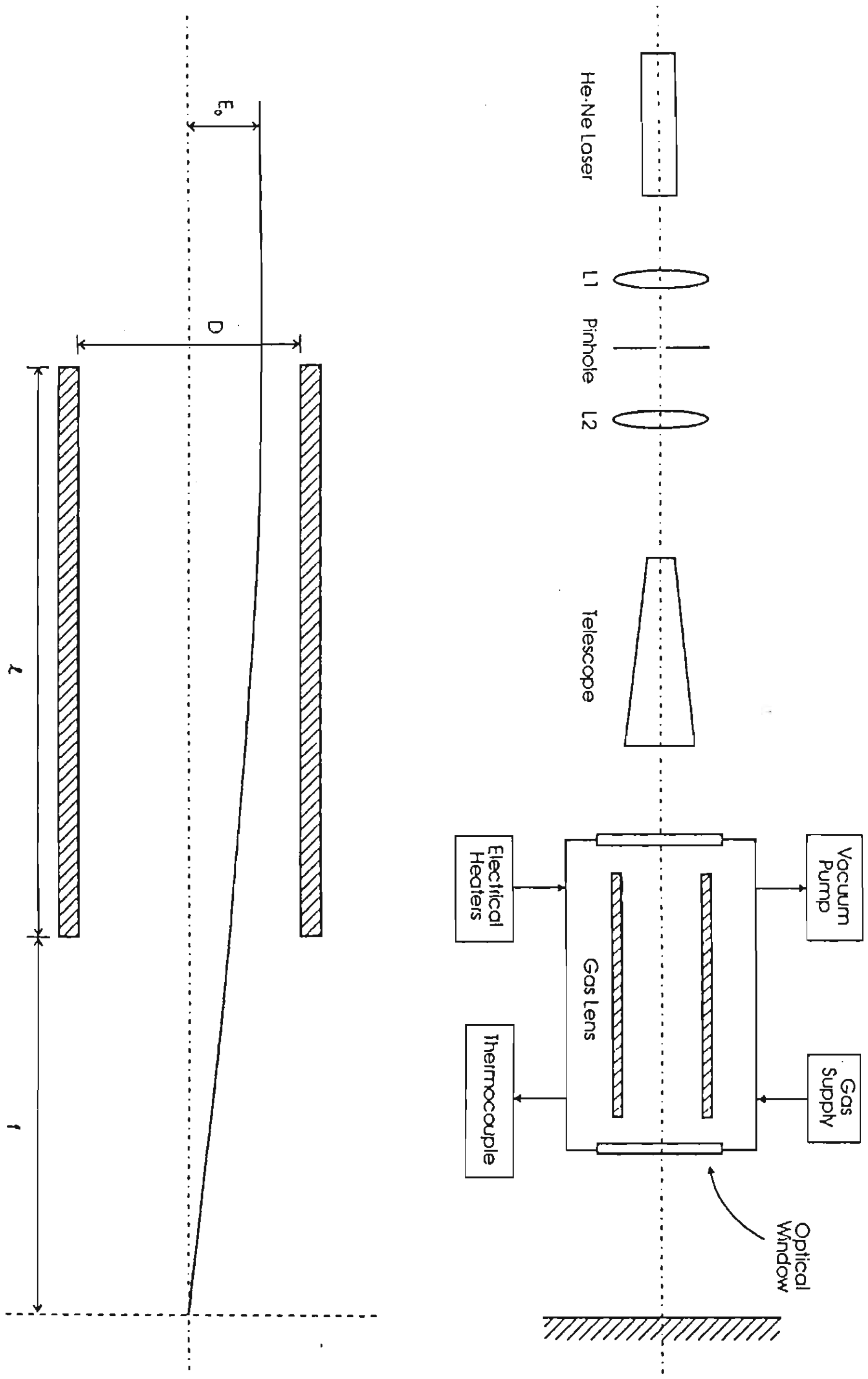

Figure 2: A schematic of the optical arrangement. The lens was housed in the main chamber with the remaining optics outside this chamber. A CCD camera was placed at the position of the screen.

1.5 Experimental Results

The first set of experiments was qualitative. The various parameters of the gas lens, namely, rotation speed (ω), temperature (T), and pressure (P), were each varied in turn, while keeping the others constant. We noted that the focal length *decreased* as the pipe temperature *increased*. This is a well known result, observed and explained by others [*Michaelis et al.*, 1991a]. However, we found that for any given value of T and P, there seemed to exist a small range of ω values for which the focal spot was stable. This could have been due to the stability (or rather the lack of it) of the pipe on the rollers, but perhaps also due to the onset of Rayleigh–Taylor instabilities (as the different density regions of the gas in the pipe mix). Despite the sometimes erratic focus, we did observe that as ω *increases*, so the focal length *decreases*.

Finally we observed how operating the gas lens at pressures above and below atmospheric (which from now will be referred to as high and low pressure respectively), affects the focal length and focal spot quality. These results were that of the first tests done on gas lenses at low/high pressures, as opposed to the above results which were verifications of known relationships. We found that the focal length *increased* with *decreasing* pressure. At low pressures the focal point was of good quality[2] (near diffraction limited), while at high pressures the focus was surrounded by a bright ring. In order to achieve a good focus the rotation speed of the pipe, ω, had to be *increased* as the pressure was *decreased*, otherwise the beam did not converge. At high pressure the focal spot quality was critically dependent on ω, becoming very unstable at large speeds, as opposed to the low pressure case where a large ω was needed to achieve focus. (An example of a large ω would be 10Hz).

---

[2] This was calculated using the geometric approximation of $1.22\lambda/D$ to determine a spot size.

1.5.1 Low Pressure Experiment

The results of the low pressure experiments were very consistent and easily reproducible. The values used in Figure 3 represents the average of several experiments. The temperature reading on the thermocouples was kept at a constant $50°C$, while rotation speeds of 15 Hz and 10 Hz were used. The largest uncertainty in the experimental results was in the measurement of the focal length; typically we found an error of 20cm, which at worst was 5% . This error originates from both the fluctuations in the focal length of the lens (due to the instability of the pipe) and from the measurement error (determining the focal plane by looking for a minimum spot size on a screen).

The results of the experiment, to determine how the focal length of the gas lens changes at low pressure, are shown in Figure 3. As the gas pressure was decreased from atmospheric to zero bar, so the focal length increased. This increase became more rapid as the pressure approached vacuum conditions, and at 0.2 atm no focus was observed. The initial beam was 45mm in diameter, at which the focal plane of the lens produced foci of between 1mm and 2mm. The diffraction limited spot for such a lens is roughly 0.3 mm to 0.5 mm. The focal spot was surrounded by a disc of low intensity light: possibly weakly refracted rays (unfocused). The focus was stable, typically for several seconds, while the unfocused light seemed very unstable. This could be due to the unstable method of rotation, as the pipe would speed up and then slow down from time to time, although always maintaining an average speed of around 15Hz.

At distances less than the focal length, a sharp ring focus appears, which converges to a point as the screen is moved towards the focal plane. The focal length was measured from the front of the pipe (the pipe end where the refracted rays exit

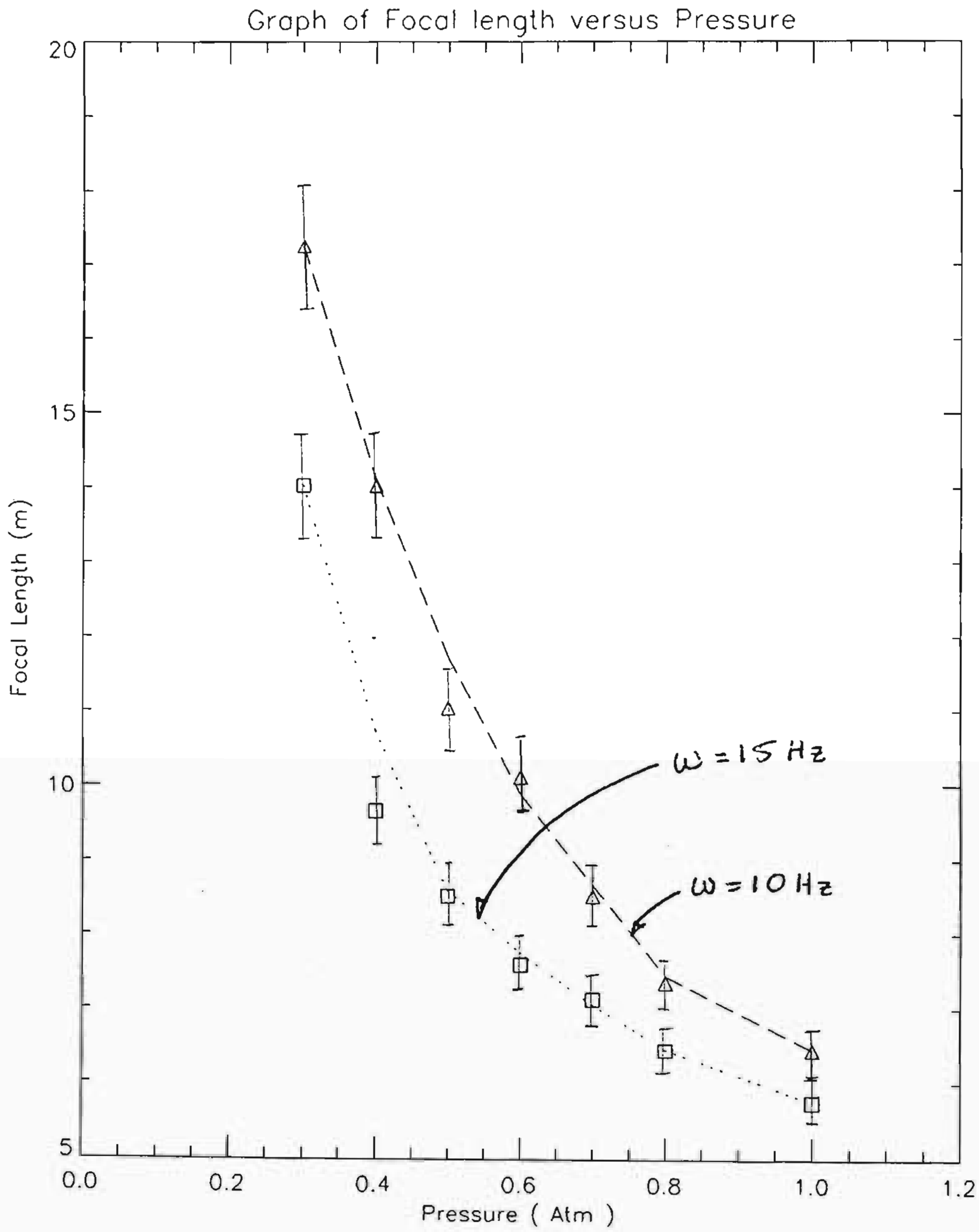

Figure 3: Graph of the focal length change for low pressures. At higher rotation speeds the focal length decreases.

the lens) to the screen, which was placed in the focal plane of the lens (where the ring converges to a point). The experiment was repeated, but with a new rotation speed of 10Hz. As can be seen by comparing the two curves in Figure 3, an *increase* in ω causes a *decrease* in the focal length at low pressures (this result was known for atmospheric conditions, and there was no reason to think that it might change).

1.5.2 High Pressure Experiment

In contrast to the low pressure experiment, where one focus was observed for any given pressure, at high pressures (above atmospheric, but below 2.5atm) *two* foci were observed for a given pressure: one near focus, at short focal lengths, and one far focus, at longer focal lengths. Both foci were examined in experiments similar to those described earlier, with $T = 50°C$ and $\omega = 10$Hz, while the pressure was increased from 1atm to 2.5atm.

The focal length of the near focus, as a function of pressure, is shown graphically in Figure 4 (a). As the pressure is *increased*, so the focal length *decreases*. The focus was characterised by a small central spot (roughly 2mm), surrounded by a disc of low intensity, unfocused light, which was bounded by a bright ring of light. We guessed that the ring was the 'far focus' rays, yet to converge to their focal plane. Moving the screen until the ring converged to a point proved this to be correct. The near focus was very unstable, and consequently of poor optical quality. The reason for this is explained by a conjecture discussed later.

The focal length of the far focus, as a function of pressure, is shown graphically in Figure 4 (b). There appeared to be no correlation between the focal length of the far focus and the gas pressure. The results were very erratic and not easily

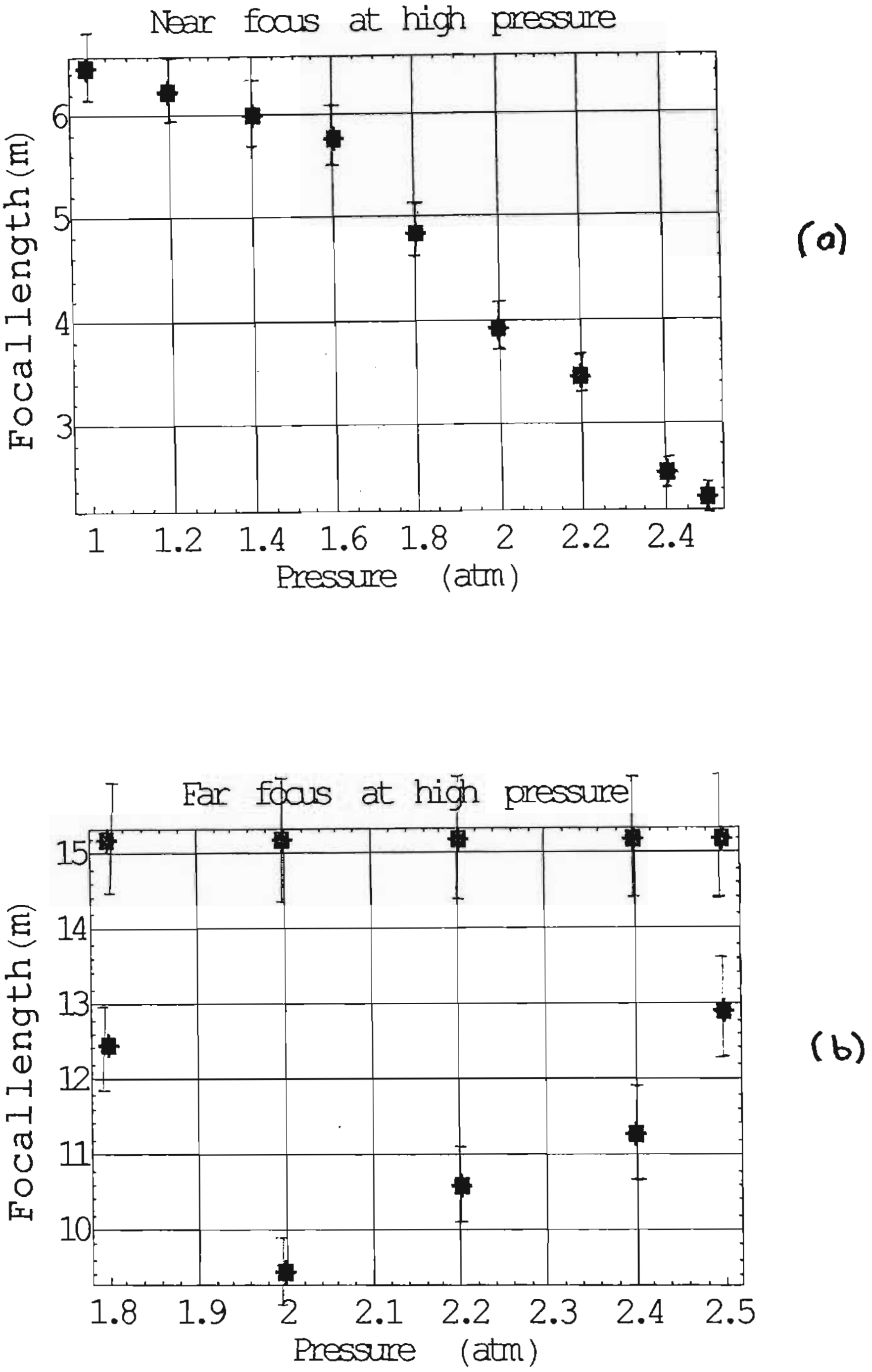

Figure 4: (a)For the *Near* focus, the focal length decreased as the pressure was increased, whereas (b) the *Far* focus shows no correlation between focal length and pressure change.

reproducible. The focus was characterised by a large focal point (3–4 mm) in the centre of a large, complex refractive fringe pattern. The focal spot quality improved with a *decrease* in gas pressure. At 2.5atm the focal spot had a diameter of 4mm, while at 1.8atm this was reduced to 2mm, which is close to the diffraction limited spot size calculated to be 0.5 mm. Four times diffraction limited is good for such an experimental lens. However the focus was unstable, seemingly oscillating inwards and outwards. Again this could have been be a problem with the pipe and not necessarily a problem with the lensing action itself. An interesting feature was observed when the pipe rotation speed was quickly increased from 0Hz to 10Hz; as the initial beam pattern changed, the gas lens produced a momentary focus, lasting only for a fraction of a second, before this disappeared to be replaced by a large (4mm) unstable focus.

In light of the experimental results, we now make the following conjecture: *At high pressure the gas lens has two distinct lensing regions: the near focus is a result of rays focused by the outer regions of the gas lens (near the heated walls), while the far focus is produced by weakly refracted rays from the central region of the gas lens (near the lens axis).* This conjecture then implies that the density gradient, and hence refractive index gradient, must be flat at the centre of the pipe while a large gradient should exist at the edges of the pipe (near the walls). Such a gradient could be modelled as a Super-Gaussian function, and this analysis is followed through in § 1.6. We would then expect, as has been observed, that the outer regions producing the near focus should be strongly refracted, and hence have a short focal length, whilst rays from the central region of the lens will be weakly refracted and hence should have a long focal length.

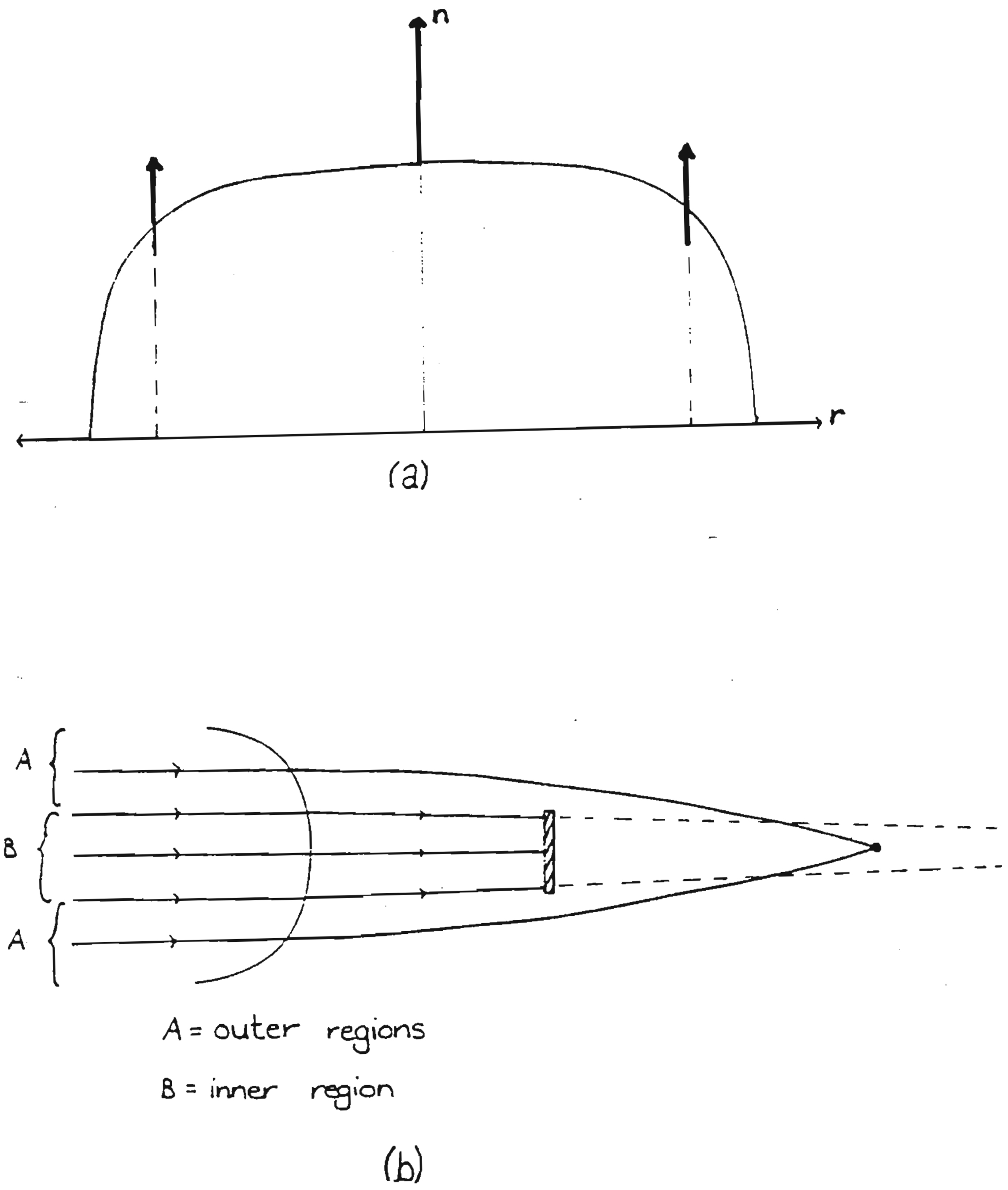

Figure 5: Diagram of: (a) Proposed refractive index gradient, and (b) Experiment to test conjecture. We propose that the central region has a flat RI profile, while the outer regions have a steep RI profile.

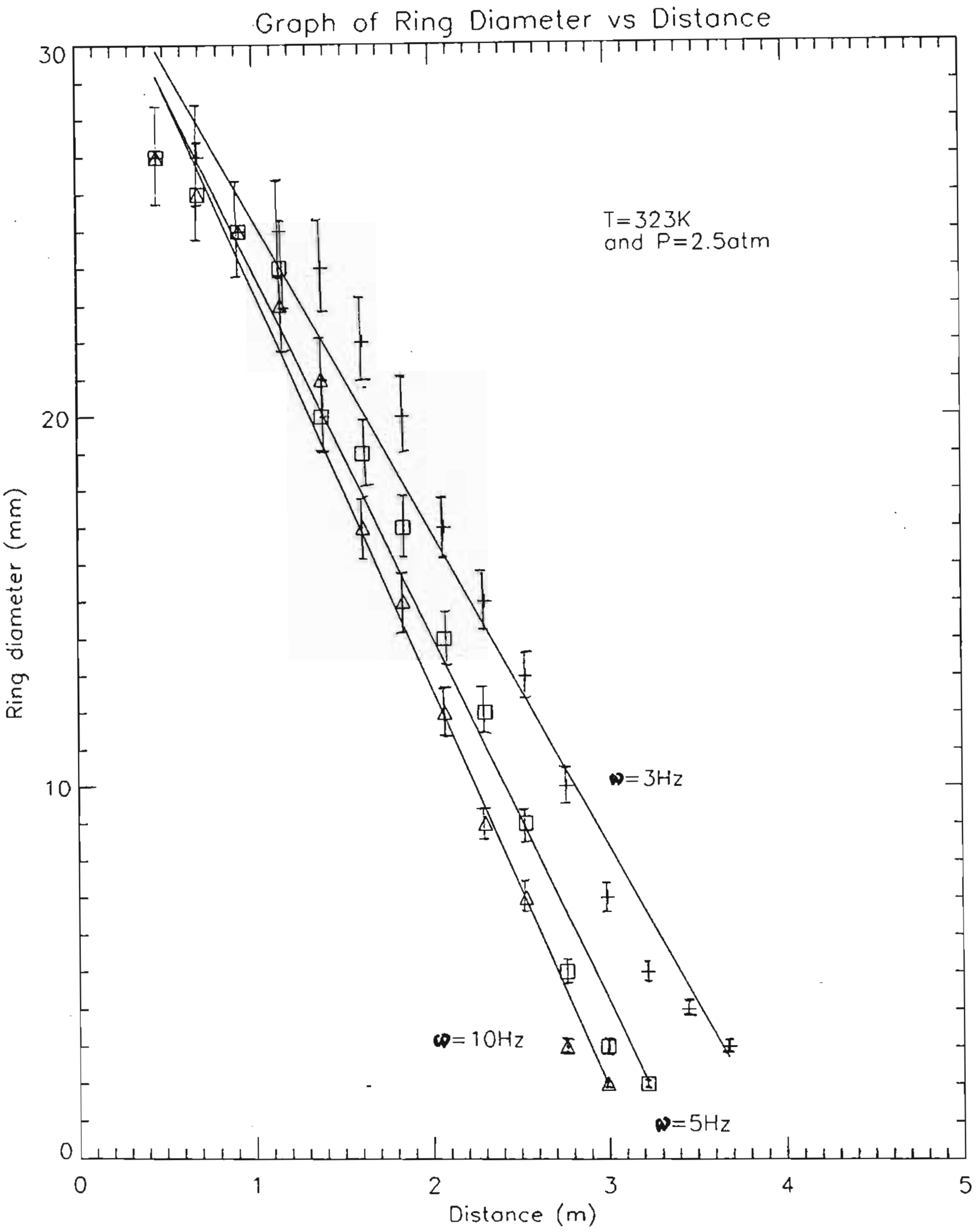

Figure 6: Convergence of outer rays (ring) to a point. As the rotation speed was increased, so the ring converged faster, but the focus became less stable.

To test the conjecture that at high pressure the gas lens has two distinct lensing regions: a strongly focusing outer region, and a weakly focusing interior, a metal disc of diameter 30mm (roughly 2/3 of the lens aperture) was centred over the lens aperture. The result was a shell of light passing out of the lens; the rays coming only from the outer regions of the lens (see Figure 5). Since the refractive index gradient is believed to be large near the pipe surface, and flat at the centre, the disc should block the far focusing rays, resulting in only a converging ring and a near focus: there should be no far focus, only the near focus.

The results were very promising. Only one focus was observed, at focal lengths that corresponded perfectly with those shown in Figure 4. This would then suggest that the conjecture was correct. The quality of the focus was critically dependent on the rotation of the pipe. At low ω the focus was stable, whereas at high ω the focus was unstable. This gives further support to the belief that the near focus discussed earlier was unstable due to the instability of the pipe itself. The fact that it is more pronounced here could be because the pipe vibrates when rotating, and in this experiment only the rays near the vibrating walls were considered.

To see the effect of rotation speed on focusing effects, the convergence of the ring to a focal point was observed for rotation speeds of 3Hz, 5Hz and 10Hz. The results are shown in Figure 6. As can be seen, the faster the pipe is rotated, the shorter the focal length becomes. However, what the graph fails to show is that, at slower speeds, the focus is more stable. Hence at both high and low pressure, the desire for stability by reducing ω must be traded off with the need for short focal lengths.

Finally, an intensity plot of the focus at low pressure is given in Figure 7 (a), and that for high pressure in Figure 7 (b). Both plots show a sharply rising

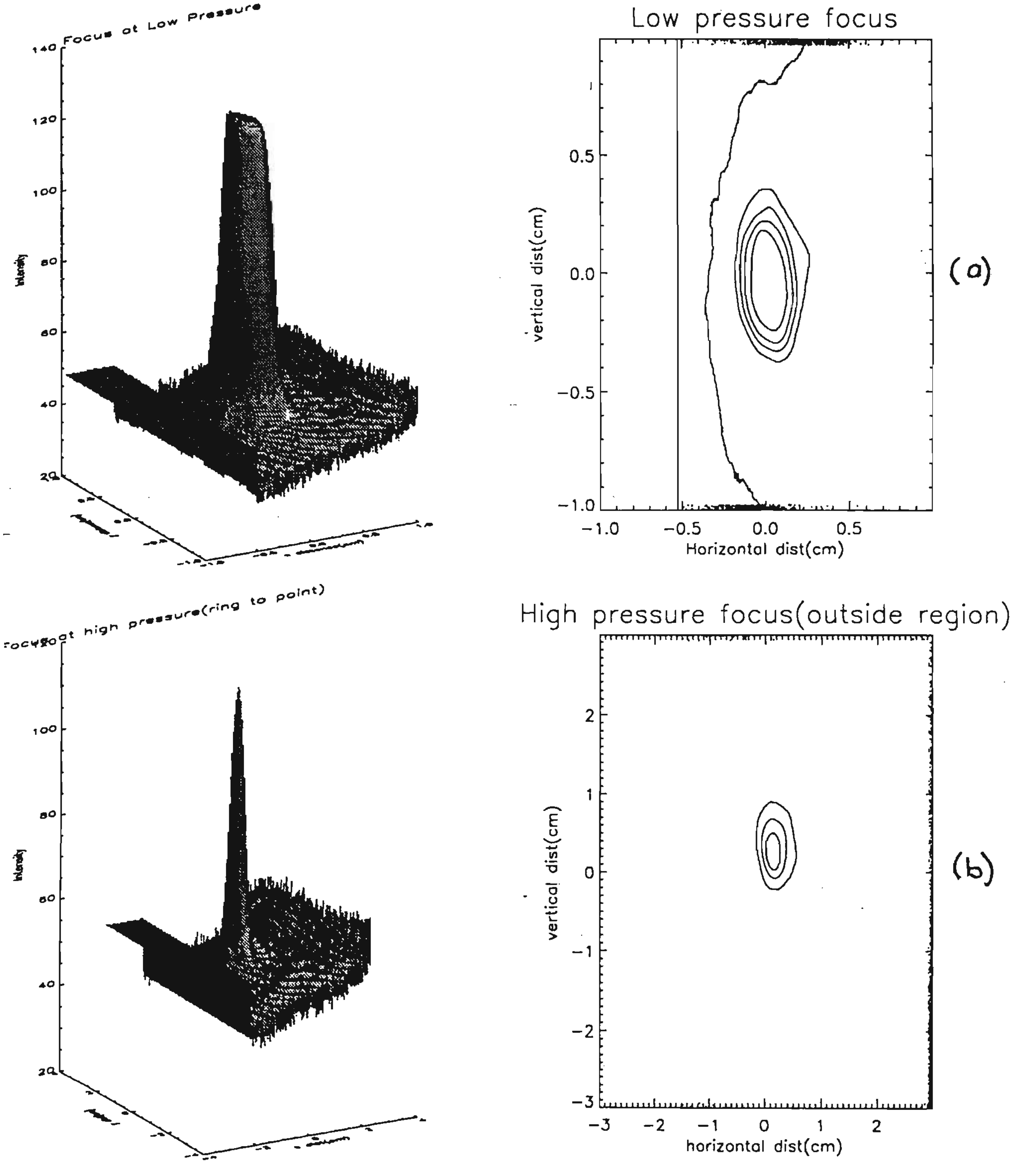

Figure 7: 3–D intensity profile and contour of, (a) low pressure focus and, (b) high pressure focus. The intensity flattening in (a) is due to the saturation of the camera.

peak, especially for the low pressure plot. The flattening of the peak in Figure 7(a) is due to the CCD camera saturation and is not a property of the focal spot.

1.6 Gas Lens Theory

Most of the work done in the field of gas lenses has been purely experimental. It is useful, however, to have at least some theory in order to make predictions regarding the results of future experiments. An attempt is therefore made here to treat the spinning pipe gas lens in an idealised model, not to predict exact numbers, but rather just to have a feel for the physics behind the processes - to give qualitative results.

We start then with three simple equations discussed earlier in § 1.1:

$$\frac{d}{ds}\left(n\frac{dr}{ds}\right) = \nabla n; \tag{1.16}$$

$$n - 1 = k\rho; \tag{1.17}$$

$$P = \rho RT. \tag{1.18}$$

If we assume a radially symmetric refractive index gradient, and assume that the optical path length $ds \approx dz$, then Equation (1.16) becomes

$$\frac{d^2r}{dz^2} = \frac{dn}{dr}.$$

Now combining Equations (1.17) and (1.18) we find that

$$\begin{aligned} P &= \frac{(n-1)RT}{k} \\ \Rightarrow\ n - 1 &= \frac{Pk}{RT}, \end{aligned}$$

which then gives

$$\frac{dn}{dr} = \frac{-Pk}{RT^2}\frac{dT}{dr}. \tag{1.19}$$

Here we have assumed that the density and temperature are functions of the radial distance, but conditions of constant pressure apply. We are assuming that the gas in the experimental vessel applies a constant pressure to the gas inside the pipe, while the heating of the pipe causes a temperature and density change to the gas inside the pipe. This is a reasonable assumption since the volume of the gas in the vessel is much larger than the volume inside the pipe. Furthermore, let us consider an approximation where the refractive index gradient is roughly linear i.e.

$$\frac{dn}{dr} \approx \frac{\Delta n}{\Delta r},$$

and

$$\frac{dT}{dr} \approx \frac{\Delta T}{\Delta r}$$

finally gives

$$\Delta n \approx \frac{-Pk\Delta T}{RT^2}. \tag{1.20}$$

Then the angle the rays leave the lens with is $\theta = l\Delta n/\Delta r$ (l is the lens length) which gives a focal length of

$$f \approx \left|\frac{r^2T^2R}{lPk\Delta T}\right|. \tag{1.21}$$

Here we have used the relation $f = r/\theta$, and taken Δr to be the difference between the position of the edge ray (at r) and the centre ray (at $r = 0$). Thus the parameter r in Equation (1.21) refers to the pipe radius.

If we consider the case where only the diameter of the pipe and the pressure are the variables of interest, then we may ask how will the focal length change under different gas pressures, and for various pipe diameters? Equation (1.21) suggests that:

(i) $f \propto D^2$. The focal length will increase as the square of the diameter of the pipe. For some applications this is an unwelcome result, since large diameter, or rather large optical aperture lenses, with short focal lengths are often more useful.

(ii) $f \propto 1/P$. The focal length increases with a decrease in pressure. Thus, at low pressures, we would expect long focal lengths; while at high pressures, short focal lengths should be observed.

Another point of interest is that Equation (1.21) suggests the obvious result that $f \propto 1/l$. Clearly this must be so, since, as the pipe length is increased, so the rays are refracted more, leaving the medium at a larger angle θ and therefore converging to a focus faster.

The result in (ii) above goes some way to explain the experimental results discussed in §2.3. As the pressure was decreased, so the focal length increased sharply; while for increasing pressures, the focal length decreased. However, this simple model does not account for the double focus observed at high pressures, nor does it fully describe the transition from high pressure with two foci, to low pressure with one distinct focus. This is not surprising given that Equation (1.21) was derived assuming a linear refractive index gradient. Nevertheless, Equation (1.21) gives some useful insight into the qualitative behaviour of the system. For a more quantitative description, we consider the effect of spinning the pipe.

It is a well known fact that rotating a glass of water results in the water surface deforming from the flat, horizontal shape, to a hollow parabaloid. As one spins the glass faster, so the parabaloid hollows further, with the result that the water edge – the circle that marks the intersection of the water surface with the glass – moves upwards until a critical rotation speed is reached where the water spills over the glass edge. What happens then, if one turns the spinning glass through 90°, so that now the glass axis is in the horizontal plane? One would expect that some sort of deformation due to gravity would occur, and intuitively one would expect that spinning the glass faster would help in reducing such a deformation, while still remembering that if it is spun too fast the water will be lost very quickly. And if one now replaces the water with gas, say air or carbon dioxide, how would that change the situation? To understand the effects this would have, it helps to expand the above analogy. The water surface takes on a parabolic shape (in 2–D) because the water acts as an almost perfect fluid, and fluids cannot sustain any forces tangential to their surface. This property results in the aforementioned surface shape. Unlike gases, water is essentially incompressible. This results then, in the spinning pipe gas example, of not one parabaloid but several, each a surface of constant phase, and each slightly deformed due to gravity. This analogy is useful in that it not only sheds a little light on the physics of the spinning pipe, but also helps explain some experimental observations: for any given set of gas lens parameters $(T, P, D$ etc$)$ there seems to exist a critical rotation speed, ω, at which the focus is best. We can interpret this by noting that, at low ω, the deformations due to gravity and natural convection dominate, hence destroying the symmetry, just as in the water case, the surface is flat when not rotating; while at high ω, just as the water spills at the critical speed, so in the gas dynamics example, Rayleigh-Taylor instabilities take over and the motion becomes turbulent.

One can derive the parabolic shape of the water surface by considering the inward forces that result in circular motion. For the gas dynamics in the spinning pipe, we are interested in the pressure and density gradients resulting from the rotation. It is expected that such gradients will be rendered symmetric by the rotation effects. To confirm this, we note that (by equating the radial pressure gradient and centrifugal forces at any radius)

$$\frac{dP}{dr} = \rho\omega^2 r,$$

which from Equation (1.18) gives

$$T = \frac{\frac{\omega^2}{2R}r^2 + T_o}{1 + \ln\left(\frac{\rho}{\rho_o}\right)}, \tag{1.22}$$

where $T = T_o$ at $r = 0$. Thus to a first approximation, spinning the pipe seems to result in a symmetric temperature gradient. If we take changes in T to be small over the radius of the pipe, then

$$\begin{aligned} \frac{d\rho}{\rho} &= \frac{\omega^2 r\, dr}{RT} \\ \ln\left(\frac{\rho}{\rho_o}\right) &= \frac{\omega^2 r^2}{2RT} \\ \Rightarrow \rho &= \rho_o e^{\frac{\omega^2 r^2}{2RT}}. \end{aligned} \tag{1.23}$$

Thus, after some manipulation, the refractive index becomes

$$n - 1 = \frac{2P}{k[\beta^2 + C]} e^{1 - \frac{C}{\beta^2}}, \tag{1.24}$$

where $\beta = \omega r$ is the velocity, and $C = 2RT_o$. This is only true for $\beta^2 \gg C$, i.e. when the pipe is spun sufficiently fast.

Using the relations $\theta = l\, dn/dr$ and $f = r/\theta$, we find the focal length is given by

$$f \approx \frac{k[\beta^2 + C]^2}{4Pl\omega^2\left(1 + \frac{C}{\beta^2}\left[1 + \frac{C}{\beta^2}\right]\right) e^{1 - \frac{C}{\beta^2}}}. \tag{1.25}$$

A simpler relation can be obtained by noting that $n \propto 1/T$, and since $n-1 = Pk/RT$ we have

$$\begin{aligned} \frac{n-1}{n_o-1} &= \frac{T_oP}{TP_o}, \\ &= \frac{T_oP}{P_o\left[\frac{\beta^2}{C}+1\right]}, \\ \Rightarrow \quad n-1 &= \frac{(n_o-1)P}{P_o\left[1+\frac{\beta^2}{C}\right]}. \end{aligned} \tag{1.26}$$

Finally giving a focal length of

$$f = \frac{P_oC\left[1+\frac{\beta^2}{C}\right]^2}{2\omega(n_o-1)lP}. \tag{1.27}$$

Equations (1.25) and (1.27) are both new results, so it is worthwhile comparing them for similarities to earlier established results.

It is interesting to note that both Equations (1.25) and (1.27) predict the same relationship between focal length and pressure, as given by the simple model described by Equation (1.21) but distinctly more complicated relations for pipe diameter and rotation speed. If one wanted to find the path any ray would take in the refracting medium, one would use Equation (1.26) with the ray equation (Equation (1.16)), to find solutions of $r(z)$. This is not shown here since we were only interested in how the lens parameters determine the focal length and other lensing characteristics.

One final point worth mentioning is that our starting point for the calculations of the focal length was Equation (1.22), which illustrates the effect of rotating the pipe on the temperature profile. It does not, however, incorporate any effect due to natural convection, and we would expect a correction term to be introduced into

Equation (1.22) such that it might read:

$$T = \frac{\omega^2}{2R}r^2 + T_o + T_c,$$

where T_c represents the correction due to convection. However, since the objective was to gain some insight into the effects of rotating the pipe, the influence of convection is delayed till later.

The above analysis does not explain the two foci observed in the high pressure experiments. Recall that the conjecture called for the existence of a refractive index distribution that was "flat"in the centre, but sharply decreasing near the pipe wall. Such a distribution would look somewhat like a high order Super-Gaussian. As a sort of theoretical vindication that such a gradient would explain the double focus, a simple analysis of the properties of a Super-Gaussian gradient is explored.

Assume that the refractive index profile is given by the following function for a high pressure gas lens:

$$n(r) = ke^{-(\frac{r^2}{a^2})^N}, \tag{1.28}$$

where N is the Super-Gaussian order, and a is the pipe radius. The constant k is arbitrary, but one would expect it to be a function of the lens parameters, but independent of r.

Following the same analysis as before, we look for the first derivative of Equation (1.28) with respect to r, and relate this directly to the induced focal length by assuming the propagation of parallel rays. We find, after some simple algebra, that

$$f(r) = \frac{-a^2}{2klN(\frac{r^2}{a^2})^{N-1}}e^{(\frac{r^2}{a^2})^N}, \tag{1.29}$$

It is very clear that for a high order Super-Guassian (a high order means a flat centre, with steep edges) two distinct focal lengths are introduced. For rays near the centre ($r = 0$), the focal length is very long, and tends to infinity for very high orders. At the edge ($r = a$), the focal length takes on a value of:

$$f(a) = \frac{-a^2 e}{2klN}. \tag{1.30}$$

The transition point from one focal region to the next is very sharp, which is what we observed experimentally. It should be possible to adjust the values of the constants to predict the precise trends, but the previous theory does not explain the generation of a Super-Gaussian profile, so one would still have to "guess" the order to choose, and justify why that order was chosen.

1.7 Conclusion

We begin with a brief summary of the important results.

- Focal length *increases* with *decreasing* pressure.
- At high pressures, two foci appear: one of short focal length and one of long focal length. This is due to the pipe having two distinct lensing regions.
- Low pressure foci were of good optical quality – near diffraction limited.
- High pressure foci (both near and far foci) were generally unstable.
- There seems to be an optimal rotation speed for which turbulence is at a minimum while still maintaining symmetry, resulting in a good focus. This varies for different gas pressures.

There were two objectives in these experiments: firstly, to understand how a spinning pipe gas lens would operate at pressures other than atmospheric, and secondly, to determine if operation at low or high pressures would allow the scaling up of gas lens apertures. The results above refer to our first objective. A brief review of the literature is required here to understand the influence this work has had on the scaling of gas lens apertures. The original thermal gas lenses developed by Berreman and Marcuse [*Marcuse*, 1982] had optical apertures of only a few millimeters (mm). These lenses were developed in the sixties to early seventies. There was not much improvement in the aperture size until a group at the Academia Sinica [*Xie et al.* 1985] managed to get a 13mm gas varifocal lens to produce the same Airy disc pattern as an equivalent glass lens. This aperture was further increased by the *UND, Laser Laboratory* [*Notcutt et al.* 1988], [*Michaelis et al.* 1991c], where the lens aperture was increased to 25mm. It then seemed that a threshold had been reached, and no further increase in the gas lens aperture could be made without introducing distortions which would destroy the focus. This experiment shows that a gas lens of aperture 47mm yields a stable, diffraction limited focus at low pressures, but has a very long focal length. At high pressures only the outside region of the heated pipe has good lensing properties (if the pipe were mechanically perfect this would be so). This is a significant increase in the lens aperture, suggesting that future lenses could be made even larger. A brief qualitative experiment was conducted on a gas lens of diameter 68mm, and the first results suggest that this lens produces a focus at low pressures.

The obvious disadvantage of such lenses is the long focal length. However, there are certain future applications where such properties are desirable. Phipps and Michaelis have suggested [*Phipps, Michaelis*, 1994] that long and variable focal length lenses could be used for satellite propulsion/launching. Gas lenses, with their long focal lengths and high power threshold would be able to direct the beam (20 Hz, 200 kJ per pulse), necessary for the ten minutes or more. For such an application, a large aperture gas lens at low pressure would be ideal (especially if the launching pad eventually becomes Mt Kilimanjaro as suggested!).

2 Shallow Water Simulations

2.1 Introduction

Waves are all around us. From the EM waves that propagate light to pressure disturbances which result in sound. Even without any physics background, everyone is familiar in some intuitive way with wave motion. There are however other 'waves' where intuition fails – where the usual laws of reflection and refraction are not always as we know them to be. Such disturbances differ the above examples in that they are governed by *nonlinear* equations. Examples range from the disturbances resulting from the detonation of explosives to the supersonic motion of projectiles, and collectively these disturbances are referred to as *Shock Waves.*

Shock wave conditions are difficult to analyse for several reasons, the main reason these being that they are non-linear, hence making analytical solutions complex, while in practice they travel very fast, making image capture a non-trivial task. Indeed, a high speed camera was purchased by the UND laser group for the purpose of analysing the shock and rarefraction conditions in the pulsed gas lens. Fortunately nature is sometimes kind to physicists. Water waves, under certain conditions, act as almost perfect analogies to other wave phenomena, hence giving us an easily observed wave motion that can be used in various ways to gain insight into general wave propagation.

In this chapter we consider the simulation of a pulsed gas lenses by shallow water waves. It will be shown that under certain conditions these waves can be said to approximate shock wave phenomena, and this property we exploit in using a ripple tank to simulate the colliding shock lens. The theory of shallow water waves is extended to fully describe the conditions that prevail in our experiments, and these results are supported by other water wave analogies. Images of the colliding water waves have the characteristics of the images taken using the colliding shock lens, hence implying the success of the simulation.

We begin then with the analogy between waves in shallow water and gas dynamics.

2.2 Shallow Water Analogy

If we consider a *simple wave*, where the term *simple wave* refers to the linear theory of a travelling plane wave extended to include disturbances of arbitrary amplitude, then

$$u = \int_{p_o}^{p} (\rho c)^{-1}\, dp, \tag{2.1}$$

where c refers to the wave speed relative to the fluid, p is the driving pressure difference, ρ is the density of the medium, and u refers to the velocity of a disturbance into (or out of) the medium (eg. the speed of a piston moving into a gas).(For a more comprehensive discussion see [*Stoker*,1957], [*Ferri*,1949] and [*Baldock, Bridgeman*,1981]). To show the similarities between gas dynamics and water waves, we use Equation (2.1) to calculate the properties of two different disturbances

(i) *Sound waves in a perfect gas:* We assume $(p/p_o) = (\rho/\rho_o)^\gamma$ and $c/c_o = (\rho/\rho_o)^{(\gamma-1)/2}$ from the properties of an ideal gas. If $\rho = \rho_o$ and $c = c_o$ at $p = p_o$ then from Equation (2.1) we have that:

$$u = \int_{p_o}^{p} (\rho c)^{-1}\, dp = \int_{\rho_o}^{\rho} \rho^{-1} c\, d\rho = \frac{2(c - c_o)}{\gamma - 1}.$$

Hence for a simple wave

$$c = c_o + \frac{(\gamma - 1)u}{2} \tag{2.2}$$

The absolute speed $u + c$ of a signal is thus increased above c_o by

$$u + c - c_o = \frac{(\gamma + 1)u}{2}. \tag{2.3}$$

And from the properties of an ideal gas we conclude that

$$\frac{\rho}{\rho_o} = \left[1 + \frac{(\gamma - 1)}{2}\left(\frac{u}{c_o}\right)\right]^{\frac{2}{(\gamma-1)}}; \tag{2.4}$$

$$\frac{p}{p_o} = \left[1 + \frac{(\gamma - 1)}{2}\left(\frac{u}{c_o}\right)\right]^{\frac{2\gamma}{(\gamma-1)}}. \tag{2.5}$$

(ii) *Shallow Water:* Consider long waves in open channels, with cross-section uniform and arbitrary, except that the breadth b remains constant i.e. height or depth can change. Then the wave speed relative to the fluid becomes

$$c = \sqrt{gA}\, b^{-1/2},$$

where g is gravitational acceleration. When the water's cross-sectional area changes from A_o to A, we have

$$u = \int_0^{p_e} (\rho_o c)^{-1}\, dp_e = g^{1/2} b^{-1/2} \int_{A_o}^{A} A^{-1/2}\, dA = 2(c - c_o).$$

Thus

$$c = c_o + \frac{1}{2}u, \tag{2.6}$$

and as before we get

$$u + c - c_o = \frac{3}{2}u \tag{2.7}$$

and

$$\frac{A}{A_o} = \left(1 + \frac{u}{2c_o}\right)^2. \tag{2.8}$$

Notice the similarities between the sets of Equations (2.2), (2.3), (2.4) and (2.5) from (i) and the Equations (2.6), (2.7) and (2.8) from (ii). It is often said that such *simple waves* (long waves or shallow water) behave exactly like those in a perfect gas with $\gamma = 2$ (not that any such gas exists!).

In fact, if we take the density of the water to be ρ and the pressure p then we can introduce new variables (using z as a depth parameter) *density* $\bar{\rho} = \rho z$ and *pressure* $\bar{p}$ with

$$\bar{p} = \frac{1}{2}g\rho z^2,$$

giving

$$\bar{p} = \frac{g}{2\rho}\bar{\rho}^2,$$

which evidently corresponds to the relationship between the real pressure and density for a polytropic gas with $\gamma = 2$. Apart from the now obvious analogy, it is also worth noting that there is a direct relationship between the depth of the water and the pressure and density of a real gas. Essentially, water depth simulates density, $\bar{\rho} \propto z$ and depth squared simulates pressure, $\bar{p} \propto z^2$.

2.3 Shock Wave Analogies

One of the properties of shock waves is that the density rise of the shock front is completed in such a short time, and over such a short distance that the shock can essentially be treated as a discontinuity. This is illustrated in Figure 8, where the real and ideal profiles are plotted.

It can be shown (see any standard text, eg [*Whitham*,1979], [*Stoker*,1957], [*Ferri*,1949]) that we can treat a *weak shock* as one where a *simple wave* distorts continuously up to the moment when the waveform slope is tending to infinity – a discontinuity again. If we take the shock strength to be given by $\beta = (P_a - P_b)/P_a$, then a weak shock is one where $\beta < 0.5$ (subscripts a, b denote conditions immediately ahead of and behind the shock wave respectively).

Consider the situation where we have two vertical planes $x = a_o(t)$ and $x = a_1(t)$ *s.t.* $a_1 > a_o$. Suppose there is a finite discontinuity in the surface elevation η at $x = \xi(t)$, $a_o < \xi < a_1$, as shown in Figure 9 (a).

Then if we define $u_o = \dot{a}_o$, $u_1 = \dot{a}_1$ and let $\dot{\xi}$ be the velocity of the discontinuity, we find that upon applying the laws of conservation of mass and momentum we get

$$\rho(\eta_1 + h)v_1 - \rho(\eta_o + h)v_o = 0; \tag{2.9}$$

$$\rho(\eta_1 + h)u_1v_1 - \rho(\eta_o + h)u_ov_o = \left(\frac{1}{2}\right)\rho g(\eta_o + h)^2 - \left(\frac{1}{2}\right)\rho g(\eta_1 + h)^2; \tag{2.10}$$

where $v_1 = u_1 - \dot{\xi}$ and $v_o = u_o - \dot{\xi}$.

Making the same transformations as before

$$\bar{\rho} = \rho(\eta + h) \text{ and } \bar{p} = \frac{g\rho}{2}(\eta + h)^2 = \frac{g}{2\rho}\bar{\rho}^2;$$

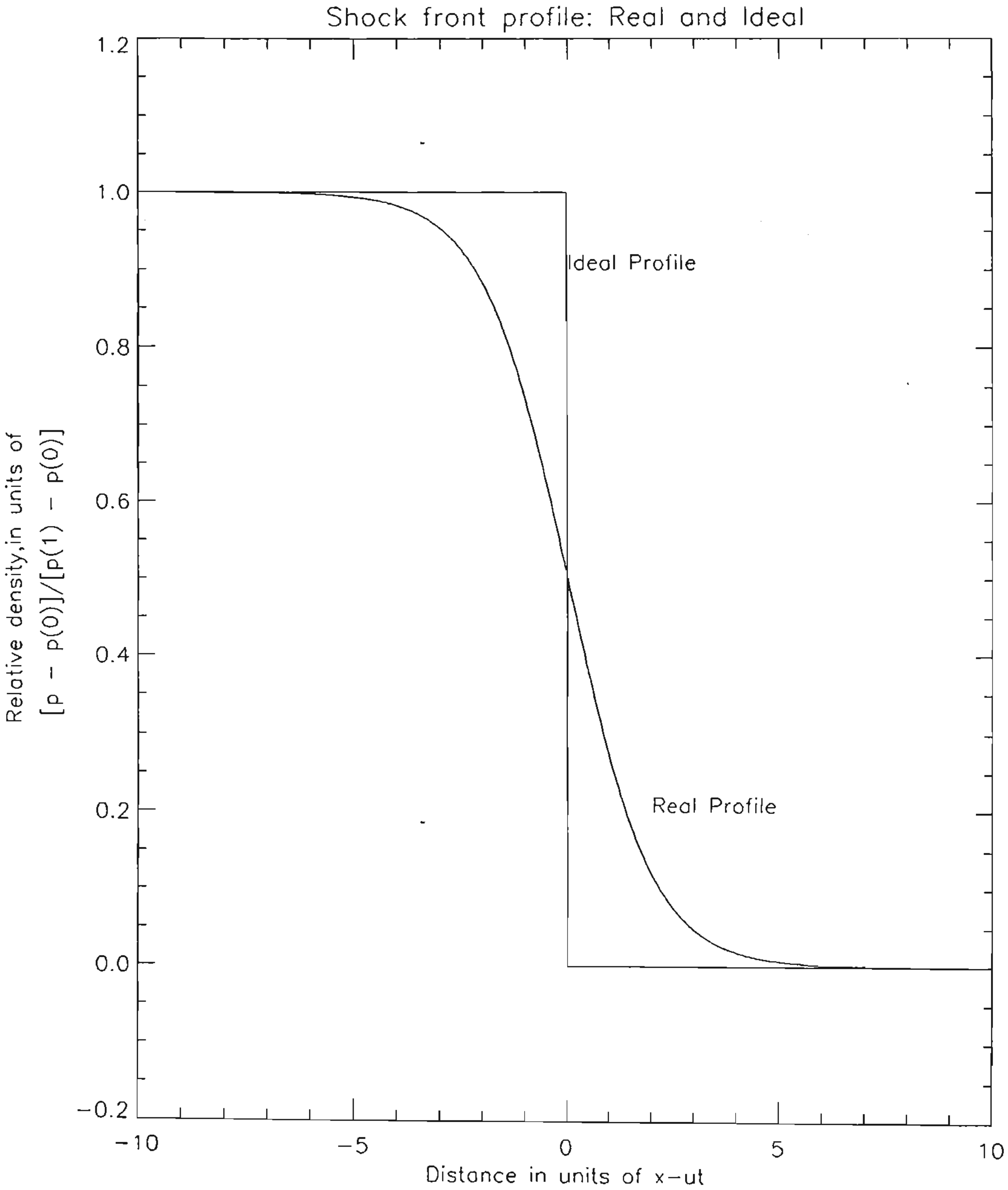

Figure 8: Comparison of a real shock profile to an idealised profile. For most cases, the shock front rises fast enough for it to be approximated by the idealised model.(see [*Ferri*,1949])

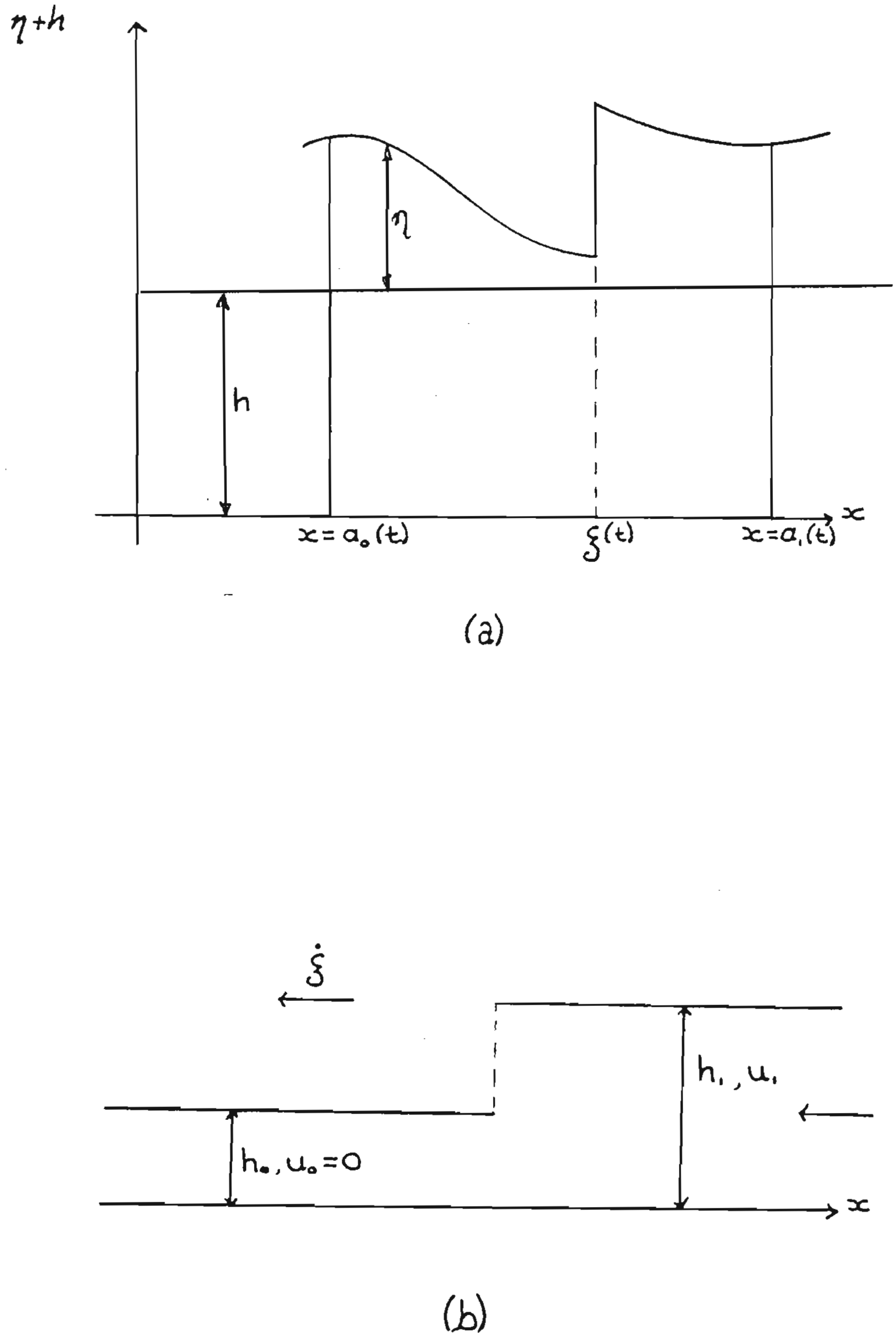

Figure 9: Diagrams of Discontinuity: (a) General case of a discontinuity on the surface, shown here as the vertical line at $\xi(t)$.(b) propagation of this discontinuity towards shallow water of constant depth.

we find from Equations (2.9) and (2.10) :

$$\bar{\rho}_1 v_1 = \bar{\rho}_o v_o, \tag{2.11}$$

$$\bar{\rho}_1 u_1 v_1 - \bar{\rho}_o u_o v_o = \bar{p}_o - \bar{p}_1. \tag{2.12}$$

Equations (2.11) and (2.12) are identical in form to the mechanical conditions for a shock wave in gas dynamics, hence we can call any discontinuity in shallow water, satisfying Equations (2.11) and (2.12), a *shock wave* or simply as a *shock* (even though in fluid mechanics, such occurrences are better known as bores). If M represents the mass flux across the shock front, then the above two equations can be rewritten as

$$\bar{\rho}_1 v_1 = \bar{\rho}_o v_o = M,$$

$$M(v_1 - v_o) = \bar{p}_o - \bar{p}_1.$$

What we want to do now is show that conservation of energy does not hold across a shock. Since we do not want to postulate an energy source at the shock front, we assume that the water particles do not gain energy upon crossing a shock front. By considering the energy balance across a shock we find that the rate at which energy is created or destroyed is given by [*Stoker*,1957] :

$$\frac{dE}{dt} = \frac{Mg}{\rho} \frac{(\bar{\rho}_o - \bar{\rho}_1)^3}{4\bar{\rho}_1\bar{\rho}_o}. \tag{2.13}$$

Hence energy is not conserved unless $\bar{\rho}_o = \bar{\rho}_1$. Of course, what we actually mean when we say energy is not conserved is that we cannot balance the energy by considering the action of the mechanical forces alone (Energy is 'lost' in the form of heat, etc). If we suppose $M > 0$ then the water particles cross the shock front in the direction $0 \rightarrow 1$, and from our energy balance $\bar{\rho}_o < \bar{\rho}_1$. i.e.

> *Particles always move across the shock from a region of lower total depth to one of higher total depth.*

Or to put this another way . . .

> *The water level is always lower on the front side of the shock than on the back side, since mass flux is from the front to the back.*

As an illustrative example, consider the case (see Figure 9 (b)) where water is at rest on the front side and so the discontinuity propagates into still water of constant depth (this is analogous to a shock wave propagating into, say, the atmosphere at constant density ρ_o).

Then

$$\bar{\rho}_1(u_1 - \dot{\xi}) = -\bar{\rho}_o\dot{\xi}, \tag{2.14}$$

and

$$\dot{\xi}^2 = \frac{g\bar{\rho}_1}{2\rho}\left(1 + \frac{\bar{\rho}_1}{\bar{\rho}_o}\right). \tag{2.15}$$

We take $u_o = 0$ and $\bar{\rho}_1 > \bar{\rho}_1$ hence the shock front must move in the direction from 1 → 0. It is useful to introduce the depths h_o and h_1 of the water on the two sides of the shock:

$$h_o = h + \eta_o,$$

$$h_1 = h + \eta_1.$$

Then since $\bar{\rho}_i = \rho h_i$, Equation (2.15) becomes

$$\dot{\xi} = -\sqrt{\frac{gh_1}{h_o}\left(\frac{h_1 + h_o}{2}\right)}.$$

Hence if $h_1 > h_o \Rightarrow |\ \dot{\xi}\ | > \sqrt{gh_o}$ and

$$u_1 = \dot{\xi}\left(1 - \frac{h_o}{h_1}\right).$$

If we look at the speed of the shock front relative to the water particles behind it

$$v_1 = u_1 - \dot{\xi} = -\frac{h_o}{h_1}\dot{\xi},$$

so

$$v_1 = \sqrt{\frac{gh_o}{h_1}\left(\frac{h_1 + h_o}{2}\right)},$$

which implies that $v_1 < \sqrt{gh_1}$: *the speed of the shock front relative to the water particles behind it is less than the wave propagation speed.* As will be shown later, we have tried to simulate these conditions by having the depth decrease resulting in a sharp amplitude travelling slower than the wave (speed) behind it.

2.4 Shallow Water Theory

Thus far we have shown that shallow water waves can, to good approximation, be used to simulate waves in gas dynamics. We have also shown that *simple waves* have direct analogies with weak shocks, and that a discontinuity in shallow water can be used to simulate weak shocks.

We develop here the theory of waves in shallow water, in particular using the equations to solve for the conditions that we use in the experimental simulation, which will be discussed in § 2.8. We start then with the basic assumptions of fluid dynamics. Assume the water to be an incompressible fluid (always true under our conditions), hence in the standard equations of fluid dynamics we take ρ = const, and we linearise the equations by assuming $\mid q.\nabla q \mid \ll \mid q_t \mid$. (See appendix C: *Mathematical Results*). The *Continuity Equation* and *Euler Equation* now become

$$\nabla . q = 0,$$

$$\frac{\partial q}{\partial t} + \nabla \left(\frac{p}{\rho} + W \right) = 0,$$

where $q(r, t)$ is the velocity field, $p(r, t)$ is the pressure and $W(r)$ the potential energy per unit mass.

If we now assume irrotational flow, then we can think of the fluid as a velocity potential ϕ such that $\vec{v} = \nabla\phi$ and $q = \vec{v}$. Then the two fluid equations above become

$$\nabla^2 \phi = 0, \tag{2.16}$$

$$\frac{\partial \phi}{\partial t} + \frac{p}{\rho} + W = 0. \tag{2.17}$$

Because the motion is not turbulent, it is assumed that the boundary surface always consists of the same particles of the fluid. If $F(r, t) = 0$ is such a surface, then

$$\frac{\partial F}{\partial t} + v . \nabla F = 0. \tag{2.18}$$

Also, at the free surface of a liquid, surface tension produces a discontinuity in the pressure across the surface, given by

$$p_1 = p_o - T \left(\frac{1}{R_1} + \frac{1}{R_2} \right), \tag{2.19}$$

where p_1, p_o are the pressures just inside and outside the surface, T is the surface tension and R_1, R_2 are the principle radii of curvature of the surface. Let the elevation

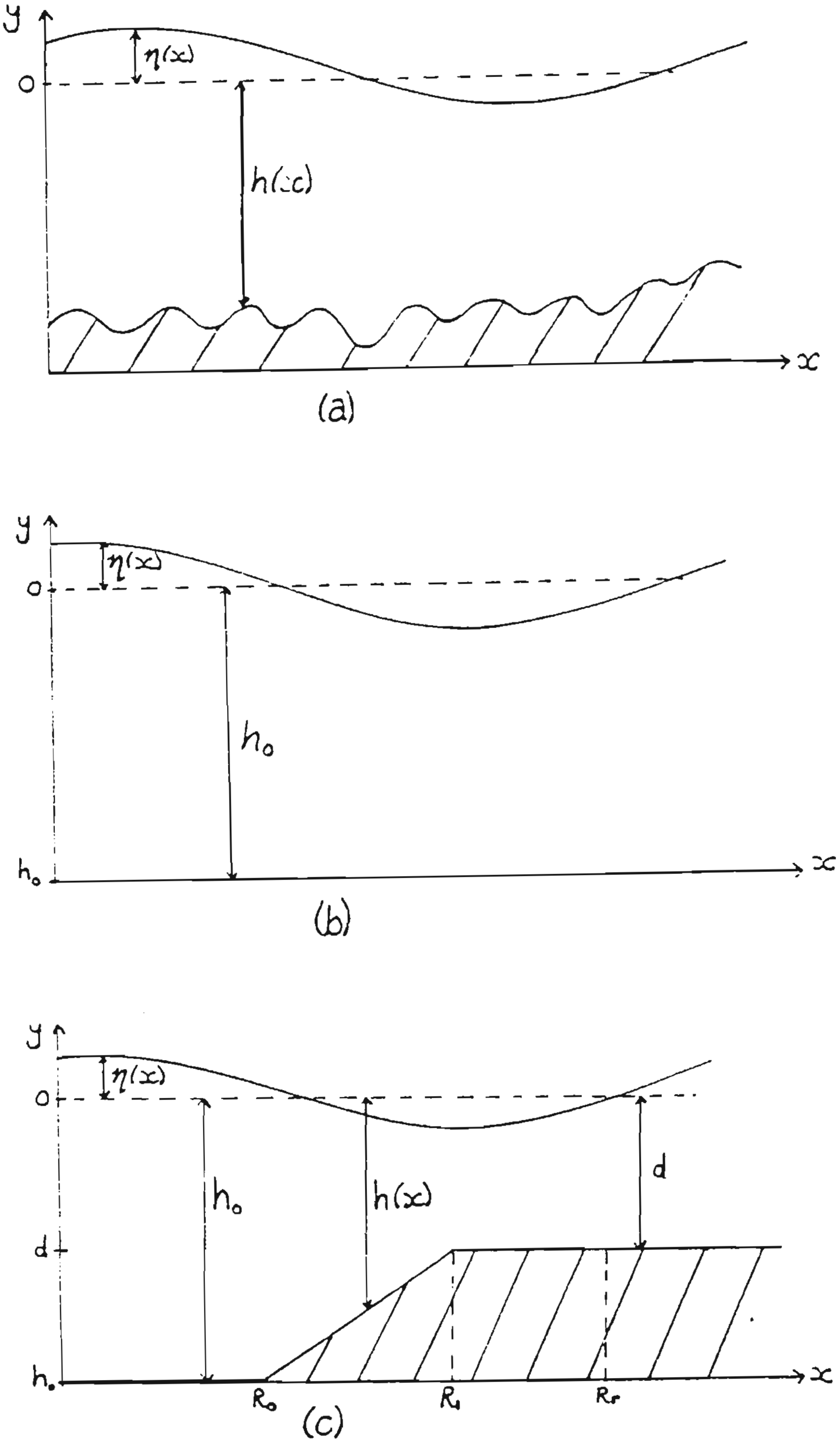

Figure 10: Schematic of co-ordinate systems: (a) General: Any wave above some arbitrary surface at depth h(x) (b) Constant depth case: Conditions for the experiment with a flat bottom, (c) Changing depth case: Conditions for the experiment with the bottom surface changing linearly.

of the water at any point be denoted by $\eta(x,t)$, as seen in Figure 10 (a), then the equation of the free surface is

$$\eta(x,t) - y = 0.$$

Similarly the equation of the lower boundary over which the water moves is given by

$$h(x) + y = 0.$$

From (2.18) we now have the relations

$$\nabla\phi.\nabla\eta - \phi_y = -\eta_t \quad y = \eta. \tag{2.20}$$

$$\nabla\phi.\nabla h + \phi_y = 0 \quad y = -h. \tag{2.21}$$

For motion under gravity, $W = gy$, so equation (2.17) becomes

$$p = -\rho g y - \rho\frac{\partial\phi}{\partial t}. \tag{2.22}$$

We now consider the following approximations:

(i) The boundaries suffer only small departures from the horizontal, implying that $\mid \nabla\eta \mid \ll 1$ and $\mid \nabla h \mid \ll 1$. We therefore neglect the products $\nabla\phi.\nabla\eta$ and $\nabla\phi.\nabla h$ and replace the factor $1/R_1 + 1/R_2$ by η_{xx}.

(ii) The elevation η is small enough to neglect changes in the vertical component of the velocity $\vec{v}$ between the free surface and the equilibrium plane. Thus the kinematic conditions (2.20) and (2.21) reduce to

$$\phi_y = \eta_t \qquad y = 0, \tag{2.23}$$

and

$$\phi_y = 0 \qquad y = -h. \tag{2.24}$$

(iii) The vertical component of the acceleration is small compared with g i.e. $\phi_{ty} \ll g$. Hence we find that on the free surface, (2.22) becomes

$$\phi_t + g\eta - \frac{T}{\rho}\nabla^2\eta = 0 \quad y = 0. \tag{2.25}$$

For verification of the above approximations see § C:*Mathematical Results.*

We now have the situation reduced to a series of differential equations involving the wave amplitude $\eta(r,t)$ and the velocity potential $\phi(r,t)$. These equations, together with their boundary conditions, give the possible solutions to the behaviour of waves in shallow water. In the next section, we attempt to solve these equations for the conditions of our experiments – that of a constant depth and a decreasing depth, as shown in Figures 10 (b) and (c).

2.5 Shallow Wave Solutions

As will be discussed later, we compare the results of two experiments conducted in a ripple tank – one where the depth is constant and the other where the depth gradually decreases. We consider first the case of constant depth. We seek the functions $\eta(x,t)$ and $\phi(x,y,t)$ such that they satisfy the equations derived earlier (Equation (2.16) and Equations (2.23) to (2.25)), namely:

$$\phi_{xx} + \phi_{yy} = 0, \tag{2.26}$$

$$\phi_y = \eta_t \quad y = 0, \tag{2.27}$$

$$\phi_y = 0 \quad y = -h_o, \tag{2.28}$$

$$\rho\phi_t + \rho g\eta - T\eta_{xx} = 0 \quad y = 0, \tag{2.29}$$

where $h = h_o$ is the constant depth of the ripple tank.

Since Equation (2.26) is separable, we have the immediate solution

$$\phi = A \cosh k(y + \varepsilon) \cos(kx - \omega t),$$

from which we get

$$\phi_y = Ak \sinh k(y + \varepsilon) \cos(kx - \omega t);$$

so from (2.28) we have that $\varepsilon = h_o$ and hence from (2.27)

$$\eta_t = Ak \sinh(h_o k) \cos(kx - \omega t),$$

$$\Longrightarrow \eta = \frac{-Ak}{\omega} \sinh(h_o k) \sin(kx - \omega t). \tag{2.30}$$

Notice that the amplitude of the wave is constant, given by:

$$\frac{-Ak}{\omega} \sinh(h_o k). \tag{2.31}$$

Substituting into (2.29) gives

$$\omega^2 = gk \left(1 + \frac{T}{\rho g} k^2\right) \tanh(h_o k), \tag{2.32}$$

which is the dispersion relation!

If we consider the individual particle motion in our case, where $kh_o \ll 1$ i.e. wavelength is large compared to depth, we find that the particle motion is almost entirely horizontal and independent of the depth (at intermediate depths the motion is elliptical with the ellipse flattening out until at the bottom it is horizontal).

From Equation (2.32) we see that surface tension has a negligible influence for wave numbers $k \ll k_m$, where $k_m^2 = \rho g / T$. For water where $T = 0.074\, Nm^{-1}$ and $\rho = 1000\,\mathrm{kgm}^{-3}$ we get $k_m = 360\, m^{-1}$ and $\lambda_m = 0.017\, m$.

Waves with $\lambda \gg \lambda_m$ are called *pure gravity waves,* and the dispersion relation reduces to

$$\omega^2 = gk \tanh(kh_o). \tag{2.33}$$

For shallow water (or long waves), when $kh_o \ll 1$ we have

$$\omega^2 = gh_ok^2,$$

$$\Longrightarrow \frac{\omega}{k} = V_p = \sqrt{gh_o}. \tag{2.34}$$

This implies that all waves travel with the same speed: group velocity equals phase velocity, and the waves are *not* dispersed.

More specifically, if we re-write the dispersion relation as

$$c^2 = \frac{1}{k}\left(g + \frac{Tk^2}{\rho}\right)\tanh(kh),$$

where c is the wave speed, and expand this in powers of k we obtain:

$$c^2 = gh + \left(-\frac{1}{3}gh^3 + \frac{Th}{\rho}\right)k^2 + \mathcal{O}(k^4). \tag{2.35}$$

We see from (2.35) that the medium is non-dispersive if

$$h = \sqrt{\frac{3T}{\rho g}},$$

which in the case of water gives $h \approx 5\,mm$. This result is depicted graphically in Figure 11 where it is clear that as h approaches 5mm, so the wave speed becomes independent of wavelength (i.e. nearly constant). The dashed line indicates the shallow water value. This result is important in that it sets limits on the depth of the water in the ripple tank experiment.

Next we consider the case when the water depth is not necessarily constant. In the experiment discussed in § 2.8, the depth is a function of position in the ripple tank: it is constant for the first region, decreases linearly in the second region and finally remains constant for the collision of the waves. If x represents the radial

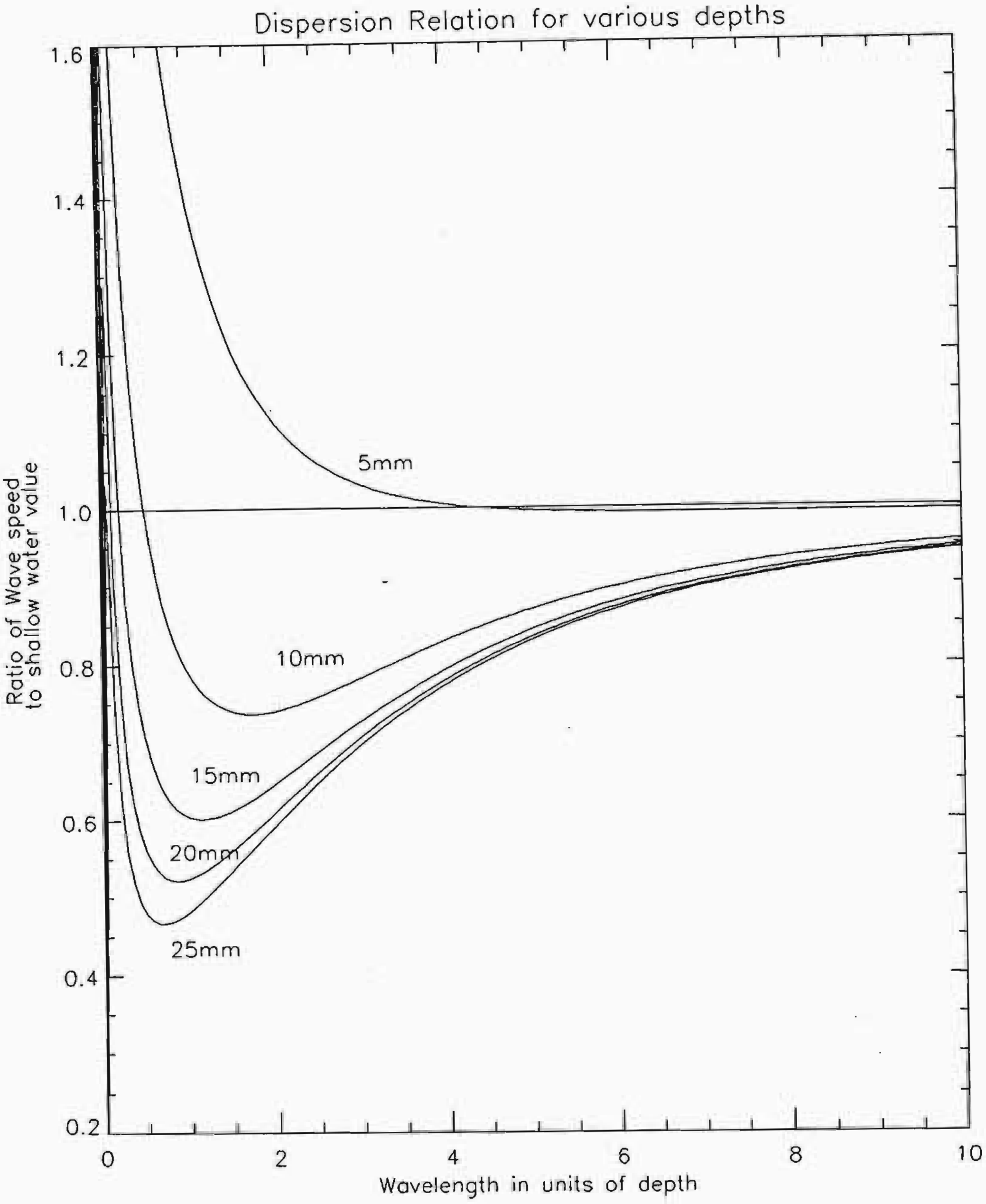

Figure 11: (a) The dispersion relation with parameter depth. As the wavelength decreases, so the surface tension dominates. Without surface tension we would get the relation shown in Figure 13.

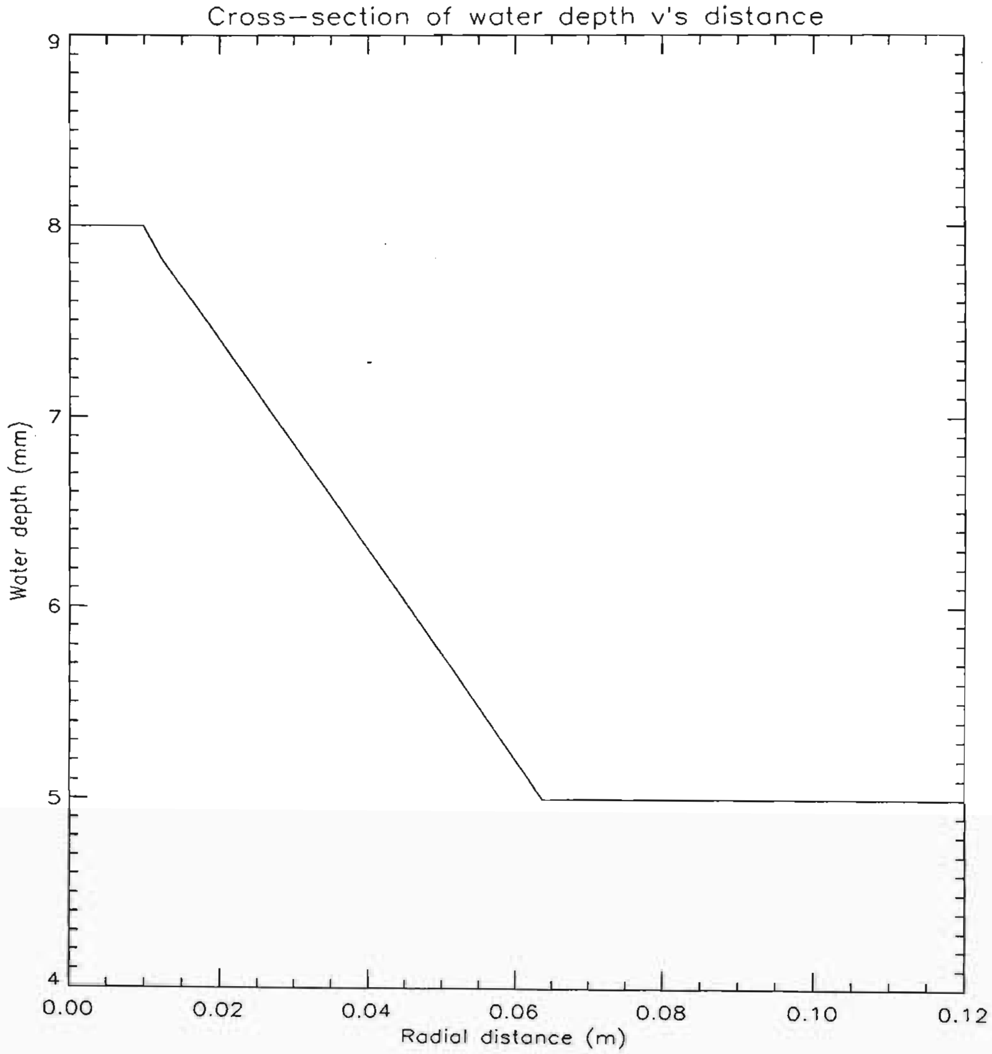

Figure 12: Water depth as a function of radial distance from source to collision point. The water level is greater at the source than at the point where the waves collide.

distance from source to collision point, then the depth function, $h(x)$, is defined as:

$$h(x) = \begin{cases} h_o & \text{for } 0 \leq x < R_o \\ mx + c' & \text{for } R_o \leq x < R_1 \\ d & \text{for } x \geq R_1 \end{cases}$$

where m and c are fixed constants (see Figure 12). Clearly in regions 1 and 3, the solutions will be identical in form to the case with constant depth, and indeed the wave is fully described by the functions η_1 and η_3, where

$$\eta_1 = \frac{-Ak}{\omega} \sinh(kh_o) \sin(kx - \omega t), \tag{2.36}$$

$$\eta_3 = \frac{-Ak}{\omega} \sinh(kd) \sin(kx - \omega t). \tag{2.37}$$

Here A is the amplitude, and k the wavenumber. We now come to region 2 where the depth, $h(x)$, is a linearly decreasing function of x. The system of differential equations used for the level surface cannot be used in the case of the sloping surface, well not all of them anyway. The problem is that an additional term arises in the horizontal momentum equation due to the force acting at the bottom surface. One could state the problem mathematically by saying that the amplitude function $\eta(x,t)$ for the flat surface case must satisfy $\eta_{tt} = gh_o\eta_{xx}$, which is just the wave equation with constant speed $c = \sqrt{gh_o}$. In the non-uniform case, we get an additional term due to the sloping bottom:

$$\eta_{tt} = gh(x)\eta_{xx} + gh(x)\eta_x.$$

To find solutions for $\eta(x,t)$ we use the Equations (2.26) – (2.29) but with (2.28) replaced with

$$\frac{\partial \phi}{\partial n} = 0 \qquad \text{at } y = -h(x), \tag{2.38}$$

which becomes

$$m\phi_x + \phi_y = 0 \ , \ \ y = -h(x).$$

The solution to the new equations yields some interesting results. Firstly, the amplitude of the wave decreases as x increases, and in fact has a $x^{-1/4}$ dependence. Using the approximation that $m \to 0$, it can be shown [*Whitham*,1979] that the amplitude satisfies

$$A^2 V_g = \text{const}, \tag{2.39}$$

where V_g is the group velocity $\partial\omega/\partial k$. This can be explained as conservation of wave energy: as the wave approaches a beach say, it slows down but the energy stays the same due to an increase in the amplitude.

For the dispersion relation one finds that

$$\omega^2 = gk\left(1 + \frac{Tk^2}{\rho g}[1 - m^2]\right)\tanh(kh(x)) + \frac{2Tk^3 m}{\rho}\cot(kx - \omega t), \tag{2.40}$$

which in the limit of shallow water theory i.e. $\lambda \ll \lambda_m$ and $m \to 0$ reduces to

$$\omega^2 = gk\tanh(kh(x)). \tag{2.41}$$

As x increases, or as we approach the collision area, the function $h(x)$ decreases from h_o to d. Since the shallow water approximation held for $kh_o \ll 1$ we can assume that it will also hold for the stronger case $kh(x) \ll 1 \ \forall\, x$, giving

$$\omega^2 = gh(x)k^2,$$

$$\Longrightarrow \frac{\omega}{k} = \sqrt{gh(x)} = V_p = V_g.$$

To see this consider the wave speed c written as

$$c = \omega/k = [gk^{-1}\tanh(kh(x))]^{1/2}.$$

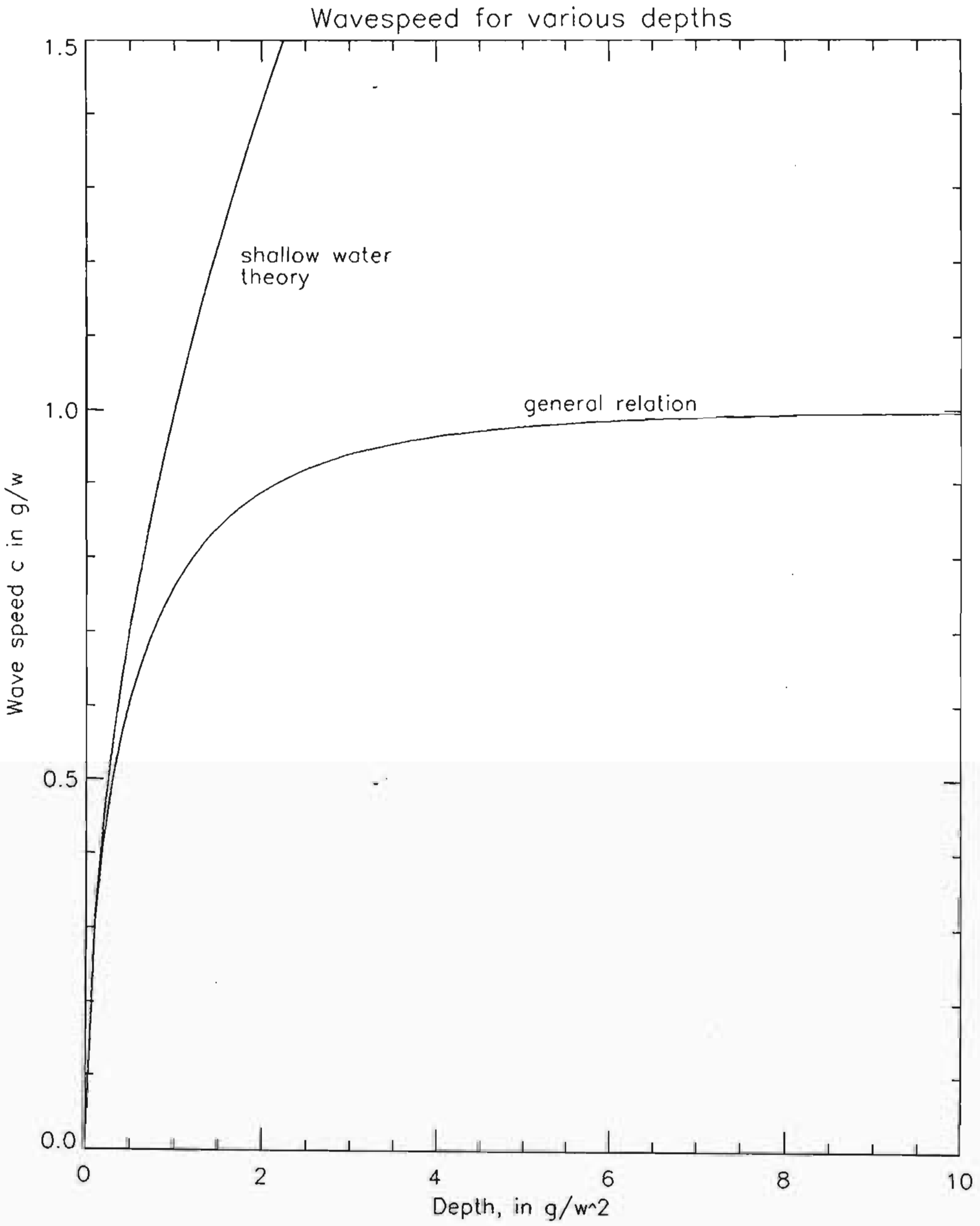

Figure 13: Wave speed vs shallow water value. This confirms that the shallow water approximation is accurate for small depth ($h < 0.07\lambda$)

If we look at the ratio $\tanh(kh)/kh$, it lies between 0.97 and 1 for $kh < 0.44$ i.e. the shallow water approximation is accurate to 3% provided that $h < 0.07\lambda$. Re-writing the wave speed in terms of ω (we do this because now k is not constant), we get

$$\frac{\omega}{g}c = \tanh(\frac{\omega h}{c}).$$

This is plotted in Figure 13 and clearly for small depths the speed c approximates the shallow water value.

Combining equations (2.39) and (2.34) we find that the amplitude over the region $R_o \leq x < R_1$ *increases* as

$$A(x) = \left(\frac{h_o}{h(x)}\right)^{1/4} A_o, \tag{2.42}$$

where A_o is the initial amplitude of the wave in region 1 (where $h(x) = h_o$), and $h(x) = d$ in the collision area.

To summarise the results for region 2: the depth of the water *decreases* as the wave progresses further inward, which results in a velocity *decrease* and a wavenumber *increase*. The most important result, however, is the *increase* in wave amplitude. Similar effects are found in long ocean waves. As the waves approach the shoreline (where the depth decreases), the amplitude of the wave increases while the speed decreases. The theory here does not predict the 'breaking' effect since this is a non-linear phenomena and, as previously mentioned, the initial equations were linearised.

To conclude this section it is worth pointing out the results obtained that will have direct bearing on the experimental section that follows. We compare the properties of the waves travelling in constant depth to those travelling in the changing depth case. The following ratios then summarise the important results:

Amplitude

$$\frac{A(x)}{A_o} = \begin{cases} 1 & \text{region 1} \\ \left(\frac{h_o}{h(x)}\right)^{1/4} & \text{region 2} \\ \left(\frac{h_o}{d}\right)^{1/4} & \text{region 3} \end{cases} \tag{2.43}$$

Velocity

$$\frac{V(x)}{V_o} = \begin{cases} 1 & \text{region 1} \\ \sqrt{\frac{h(x)}{h_o}} & \text{region 2} \\ \sqrt{\frac{d}{h_o}} & \text{region 3} \end{cases} \tag{2.44}$$

Wavenumber

$$\frac{k(x)}{k_o} = \begin{cases} 1 & \text{region 1} \\ \sqrt{\frac{h_o}{h(x)}} & \text{region 2} \\ \sqrt{\frac{h_o}{d}} & \text{region 3} \end{cases} \tag{2.45}$$

where the subscripts o above refer to the properties in the flat surface solution. These results are depicted graphically in Figures 14 and 15.

Thus it would seem that in theory we should be able to distinguish between the two cases outlined above, with the changing depth case having some properties of shocks, while the flat surface situation should not have any analogy in shock interaction. We look for these differences in the results of experiments that are discussed in § 2.8.

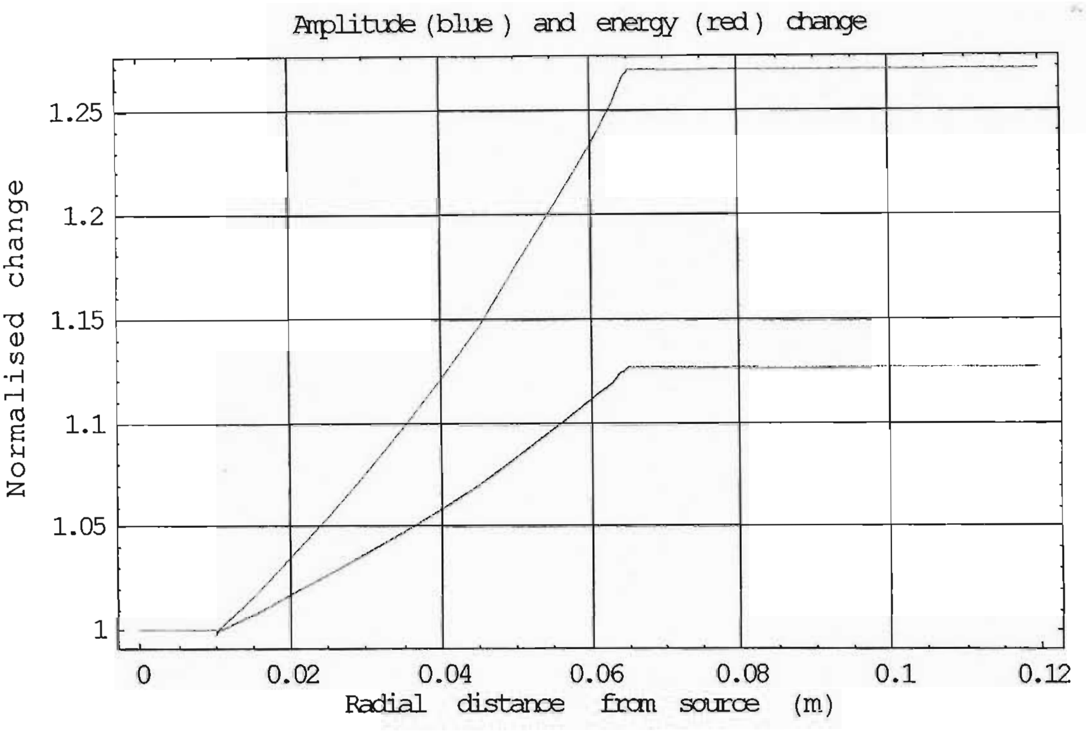

Figure 14: Amplitude and Energy ratios. With a decreasing depth the Energy and Amplitude of the waves increase. A similar observation can be made by watching waves approach the beach.

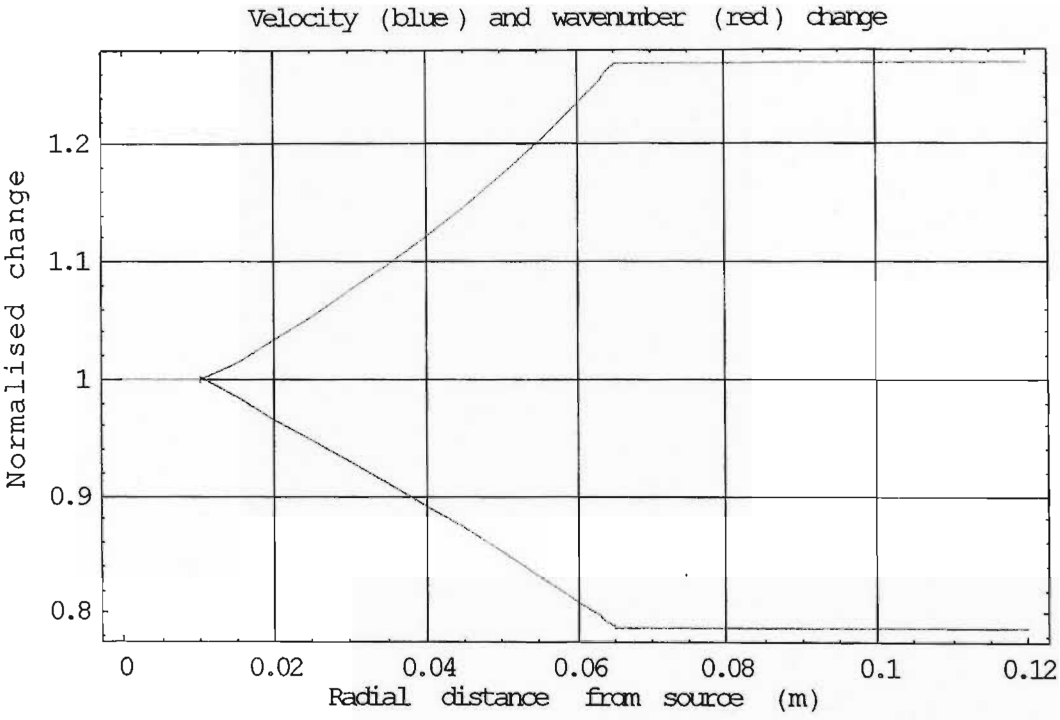

Figure 15: Velocity and Wavenumber Ratios. As the waves approach the shallower collision area so they slow down. This causes the wavelength to decrease and the amplitude to increase.

2.6 The Colliding Shock Lens

The original intention was to use shallow water waves to simulate the Colliding Shock Lens (CSL). Therefore a brief overview of the CSL principle is necessary.

The CSL is a novel type of pulsed gas lens developed by the *UND Laser group*. The CSL consists of a number of spark gaps equally spaced on the arc of a circle. When a capacitor is discharged through the spark gaps, each gap acts as the point source for an expanding spherical shock wave. These waves converge to the centre of the lens where they collide to form an axially symmetric cigar shaped density distribution. This region then expands outwards, and during this expansion the CSL acts as a time varying GRIN lens (that is, the focusing is due to the radially symmetric density gradient within the expanding region, and this changes with time as the region expands). The energy of the capacitor is such that the shock waves formed are of intermediate Mach numbers ($M \approx 1.5$), for which the interaction of the shock fronts is non-linear but orderly (i.e. not turbulent). Most of the CSLs used eight sources of shock waves, and a sequence of images taken with one of these lenses is shown in Figure 16. Initially the shocks converge to a common point (the collision point) and this can be seen in frames (a) to (g) of Figure 16. At around points (h) and (i) the shocks have collided to form a high density and pressure cigar shaped profile. After collision the interacting shocks expand again, but because of Mach addition, all "memory" of the previous state is lost, and the shocks expand as a ring like structure (see frames (j) to (p).). It is during this expansion phase that the CSL can be used as a varifocal lens. Notice the symmetry of the situation and the circular expanding ring formed by the Mach addition of the interacting shock waves. It is these properties we seek to simulate in the shallow water collision of water waves.

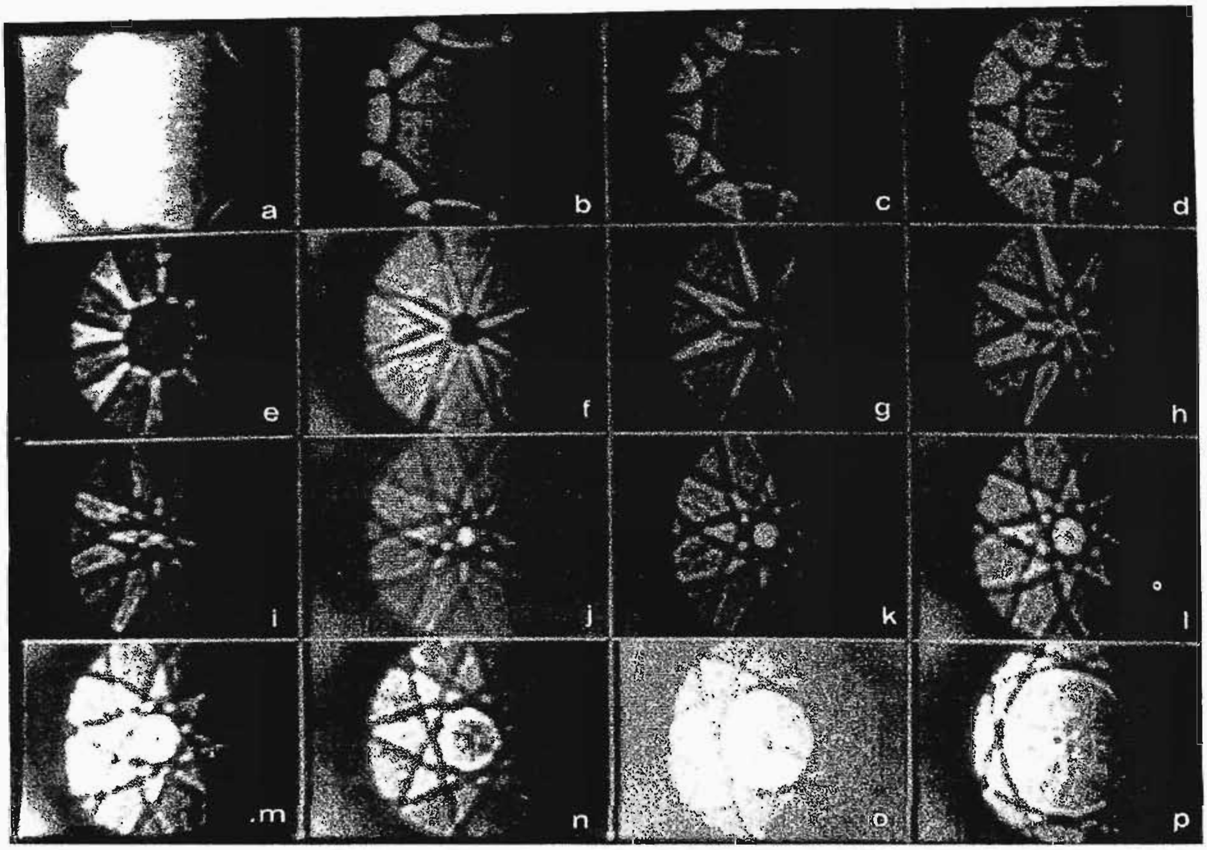

Time sequence of an eight arc CSL imaged 19 cm from the CSL at (a) 3.2 µs, (b) 5 µs, (c) 6 µs, (d) 6.9 µs, (e) 8 µs, (f) 10 µs (g) 10.4 µs, (h) 10.9 µs, (i) 11.3 µs, (j) 11.6 µs, (k) 11.8 µs, (l) 12.2 µs, (m) 12.4 µs, (n) 13.1 µs, (o) 14 µs, (p) 15.6 µs.

Figure 16: Image sequence of an 8 pin CSL. In the diagram the shock waves approach a common centre (a to h), then collide in frame (i). At this point Mach addition results in a ring like structure expanding outwards (j to p).

2.7 Experimental Arrangement

In this experiment we hoped to be able to distinguish between ordinary water waves that collide, and waves that simulate shock conditions. In all the experiments carried out there were always two different cases: one where the depth of the water was constant and the standard water wave collisions were noted, and the other where the depth gradually decreased. All experiments were performed in a ripple tank with depth 8mm. For the decreasing depth experiments, perspex plates were placed into the tank in such a manner that the waves passed through three distinct regions : the first was the standard 8mm depth of the tank, next the depth decreased linearly from 8mm to 5mm, and the final region where the waves collided was kept at constant depth of 5mm, this value was chosen from the dispersion theory derived earlier. The waves were produced by having a metal ring with attached bobs which dip in and out of the water. Care had to be taken to ensure that the ring was horizontal, otherwise the delay between the various wave initiations distorted the results. The number of bobs attached to the ring could be varied, but in most experiments eight bobs were used (all arranged symmetrically around the ring). It was also found that the best results were obtained when the ring was removed from the water rather than immersed in water, so most of the images shown will be for this case (obviously a wavelet will be formed when both the bob is removed from and inserted into the water. One is just a little easier to control than the other).

A light source was placed directly above the collision area and the resulting light patterns produced on a white sheet of paper on the floor were recorded with a Camcorder. Figure 17 shows a schematic of our arrangement. Once the images were recorded on video tape, they were transferred to a digital file and analysed

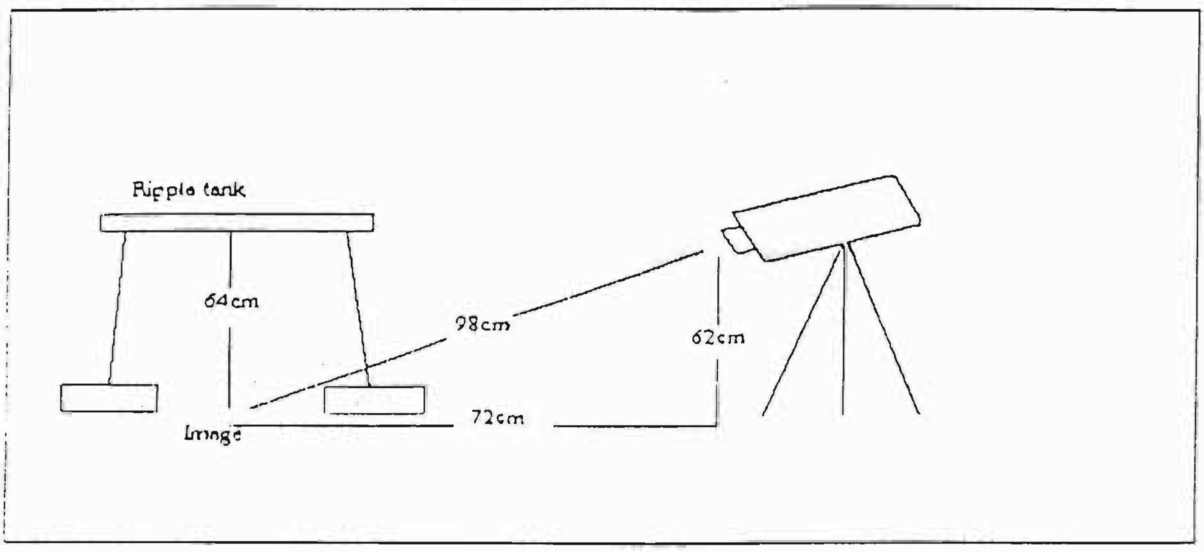

Experimental Setup

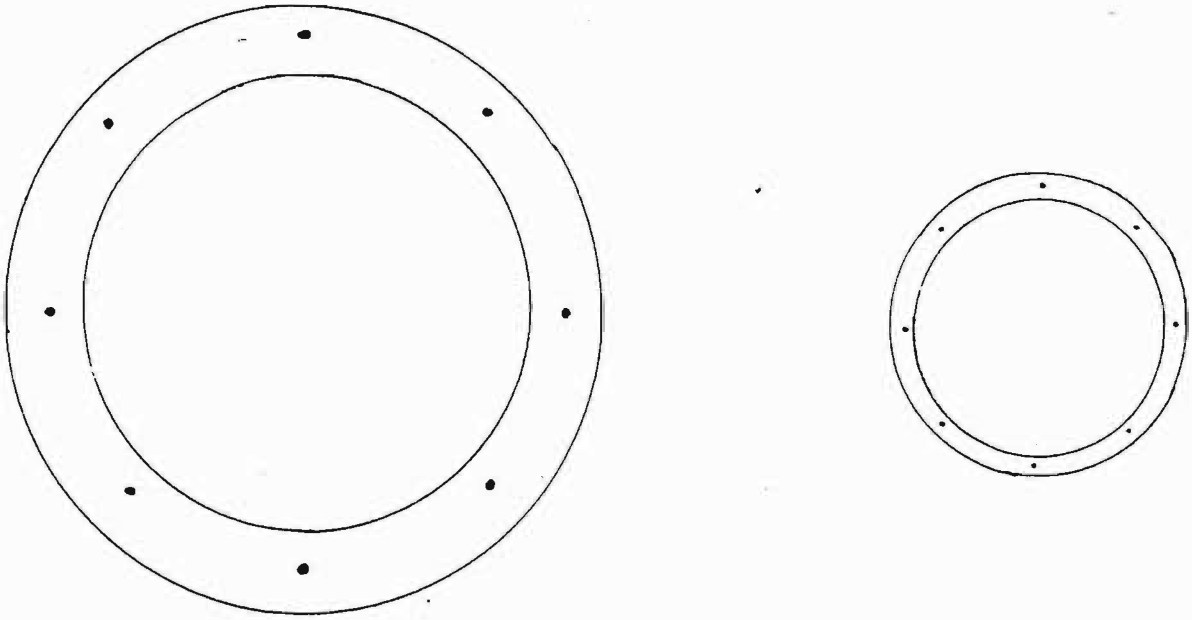

Actual ring
Inner diameter : 18 cm
Outer diameter : 20 cm

Image produced on paper
Inner diameter : 53,1 cm
Outer diameter : 58,8 cm

Figure 17: Experimental set-up for the collision of the water waves and for the capturing of the images. A camcorder was used, facing a lit ripple tank. The waves were generated with a set of 8 bobs arranged around a metal ring.

using an image processing package (IDL – Interactive Data Language). In all the images taken, one side is slightly brighter than the other. This is due to the fact that the light source was not directed vertically downwards, but rather at an angle. Only on analysing the images was this noticed. Also, the images do not appear perfectly circular. The distorted effect is due to the angle which the camera made with the paper. In an ideal situation one would have the camera directed vertically downwards, but due to the light source and reflections from the glass and water, this was not possible. The result is that the scaling of the vertical and horizontal planes are not the same.

2.8 Experimental Results

There exists a direct analogy between shallow water waves and disturbances in gas dynamics, as was noted earlier. It was shown that the pressure of the gas is analogous to the depth of the water squared ($P \propto h^2$), while the density was proportional to the depth ($\rho \propto h$). In the CSL, a radial density distribution, produced by the interacting shock waves, refracts light so as to form a varifocal lens. What, we ask, is the analogy in the shallow water simulations?

Firstly it is worth pointing out that there are two complementary effects in action as the waves interact while moving towards the collision area. The first is the usual effect of superposition of waves, and the second is the effect of a changing depth, going from deep to shallow water. Regardless of water depth, as water waves collide so the principle of superposition will result in an increased amplitude at that point. However, in the case of the waves moving from a deep to a shallow region, as

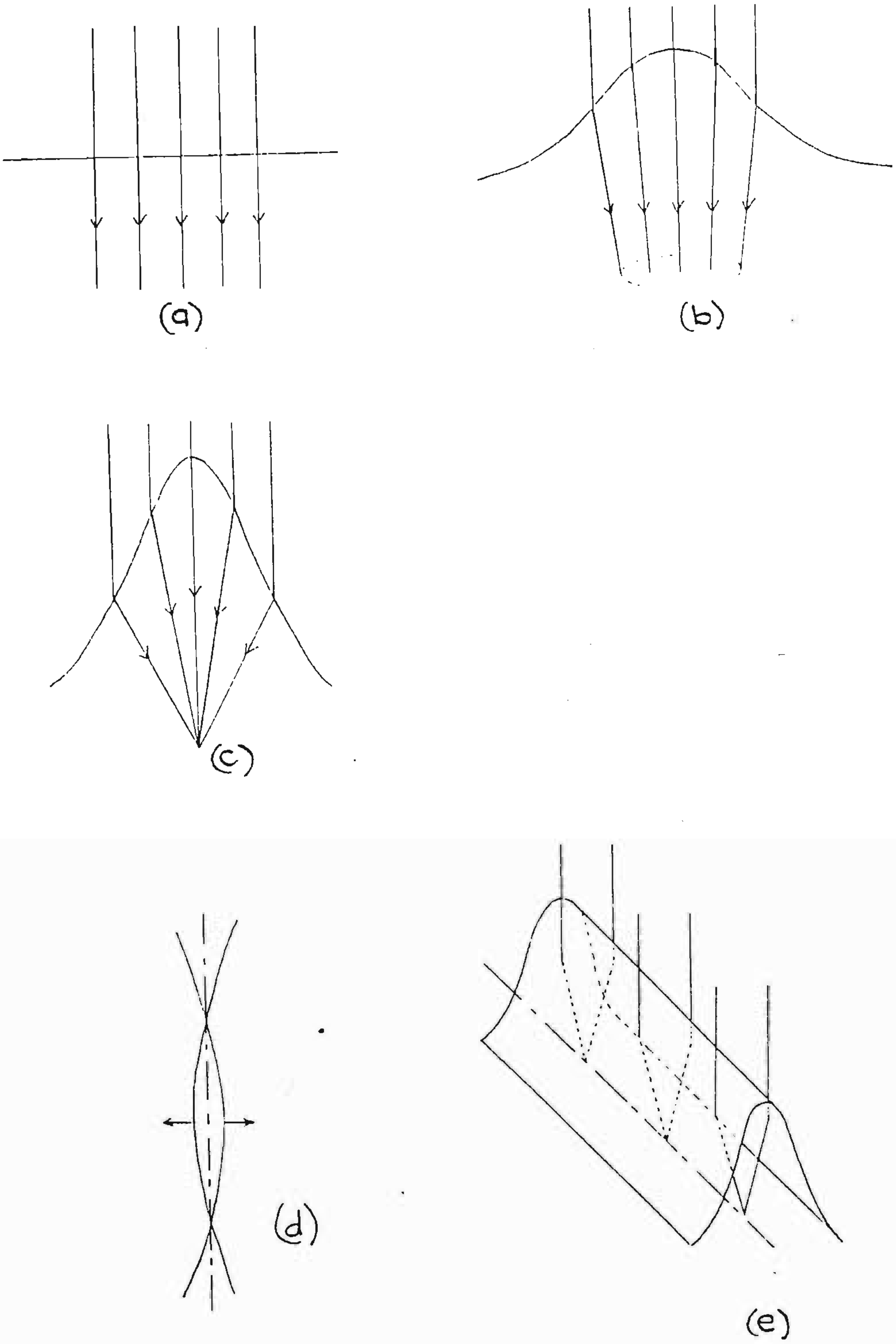

Figure 18: A schematic of the focusing principle of a sloping water surface (due to superposition of waves). Focusing only occurs when the water height is symmetric, with a steep gradient.

is the case in these experiments, there will also be an amplitude increase due to the changing depth, the theory of which was discussed in detail earlier. The consequence of this is that both the experiments with plates and without plates could be expected to show convergence of the light source, while in the case with plates (changing depth) this effect should be more pronounced, and moreover we should be able to observe shock wave analogies.

Consider what happens when the water waves emerging from the eight sources approach the centre of the ripple tank, which, in these experiments, represents the collision area. Initially the water surface is flat, and, as expected, no light rays from the light source (above the collision area) will converge – they will all pass through the water almost parallel to one another (see Figure 18 (a)). As the waves move closer to the collision area, so the water amplitude starts to increase, due to the superposition of the waves. This slight increase in amplitude at the centre, due to the converging waves, causes the light rays to be weakly refracted, as shown in Figure 18 (b). At the moment of collision, the water wave amplitude is at a maximum in the centre, falling off sharply away from the centre. This 'water amplitude gradient' results in strongly refracted edge rays which converge to a point focus (see Figure 18 (c)). As the waves start to diverge from the centre (during the expansion phase), so the amplitude decreases again, resulting in the light rays gradually being refracted less strongly, producing larger focal spots and longer focal lengths, until no focus is evident (rays are parallel again). This is directly analogous to the CSL, where, as the density gradient flattens during the expansion phase, so the focal length increases because the rays are now weakly refracted. The distance between the ripple tank and the image plane will clearly affect the image seen. If this distance is too long, or too short, then the focussing effects described above will be missed. In this experiment the distance was such that a focus was observed. This implies that a small movement of the image plane closer or further away would only change the frame in which the focus was seen (i.e., if it was closer, then a stronger gradient would be necessary to see a focus; since the gradient changes with time, so would the frame in which the focus was seen).

The effect of having the depth change is that now the water waves will increase in amplitude as they move towards the centre, shallower region and this amplitude increase will depend on the position of the wave. The front of the wave should experience a larger amplitude increase than the back of the wave, thus the superposition of the waves will amplify this non-linear difference.

In the CSL, the radial symmetric density gradient is produced because the shock waves interact in a manner described as *Mach addition*. Essentially, the shock waves do not pass unaffected through one another, but rather 'join' or 'add', to form a converging ring like structure. This is illustrated very nicely in the sequence of images in Figure 16. (shown earlier).

Whether the shock waves pass through each other or experience Mach addition depends largely on the shock strength, and the angle between the shock propagation directions when they interact (see Figure 19). A water wave analogy would be waves on the beach. When there is a sidewash or backwash, small amplitude waves travel at an angle back towards the ocean. Depending on the angle these waves make with the incoming waves, and the amplitude of the returning waves, either joining occurs and *Mach Addition* is observed, or the two sets of waves pass unaffected through one another. In the CSL and in the water wave simulation, the magnitude of the shocks (or shock simulations) is such that at large angles (angle θ in Figure 19) between the waves, when the wave directions are at right angles, no Mach addition occurs. This explains why the initial shocks(waves)from the point sources

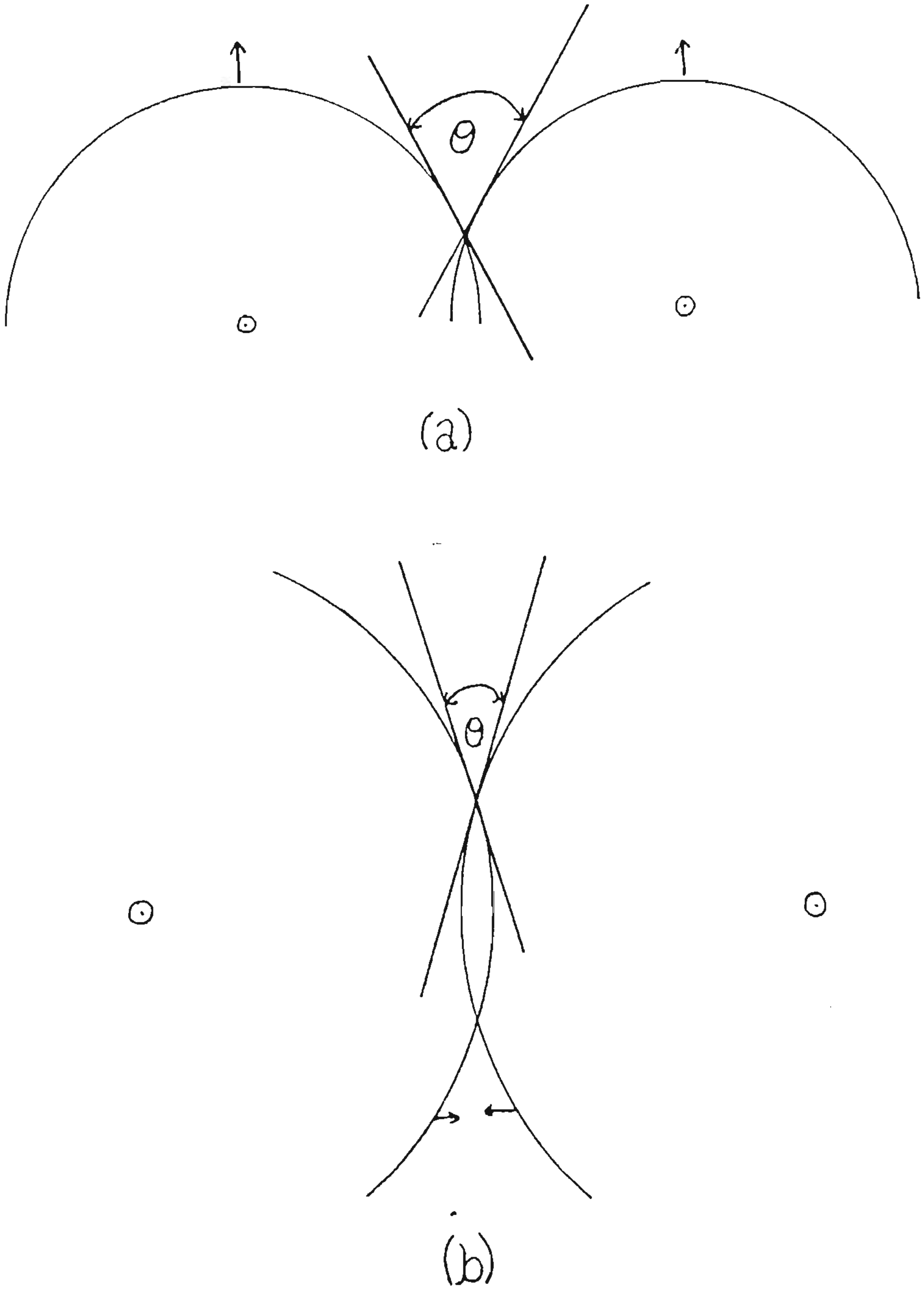

Figure 19: The conditions for *Mach Addition* depend on both the shock strength and the angle between the interacting waves.(a)No Mach addition because the propagation directions are at right angles, (b)for intermediate shocks, when the wave directions are parallel or opposite, Mach addition

do not show Mach addition (i.e. waves from adjacent sources do not 'join'), whereas after collision, when θ is smaller, or the wave directions are almost opposite, Mach addition is observed. Examples of Mach addition in the water wave simulations are discussed next.

From the experiments *without* a sloping bottom, the ripple tank simulates the weakly interacting CSL which does not focus. That is why, from the images taken (see Figure 20, for example), it is apparent that no Mach addition occurs, and the expansion phase consists of eight weakly interacting waves. A careful examination of all the images taken from the experiments without a sloping bottom, reveal what is called the cusping effect: the expansion phase still retains information of the original number of sources, as the expansion surface consists of eight arc segments, moving outwards independently.

From the experiments *with* a sloping bottom, Mach addition is observed on the water wave convergence. More important still, on the water wave divergence, the 'memory loss' phenomena of the CSL expansion phase is replicated. The central non-linear collision and wave superposition erases all information about the original number of shocks. This effect is evident in images taken of the colliding water waves on a sloping bottom (see Figures 21, 22 and 23), where the expansion phase appears to be originating from a point source positioned at the collision point, and not from the eight original sources. Where one could see the cusps of the eight waves in the flat bottom experiments (Figure 20), in this case all evidence of this is 'lost'.

The sequence of images shown in Figures 21 , 22 and 23 were taken with different time delays between frames, and at different initial starting times. Thus they illustrate the various phases of convergence and divergence the waves pass through.

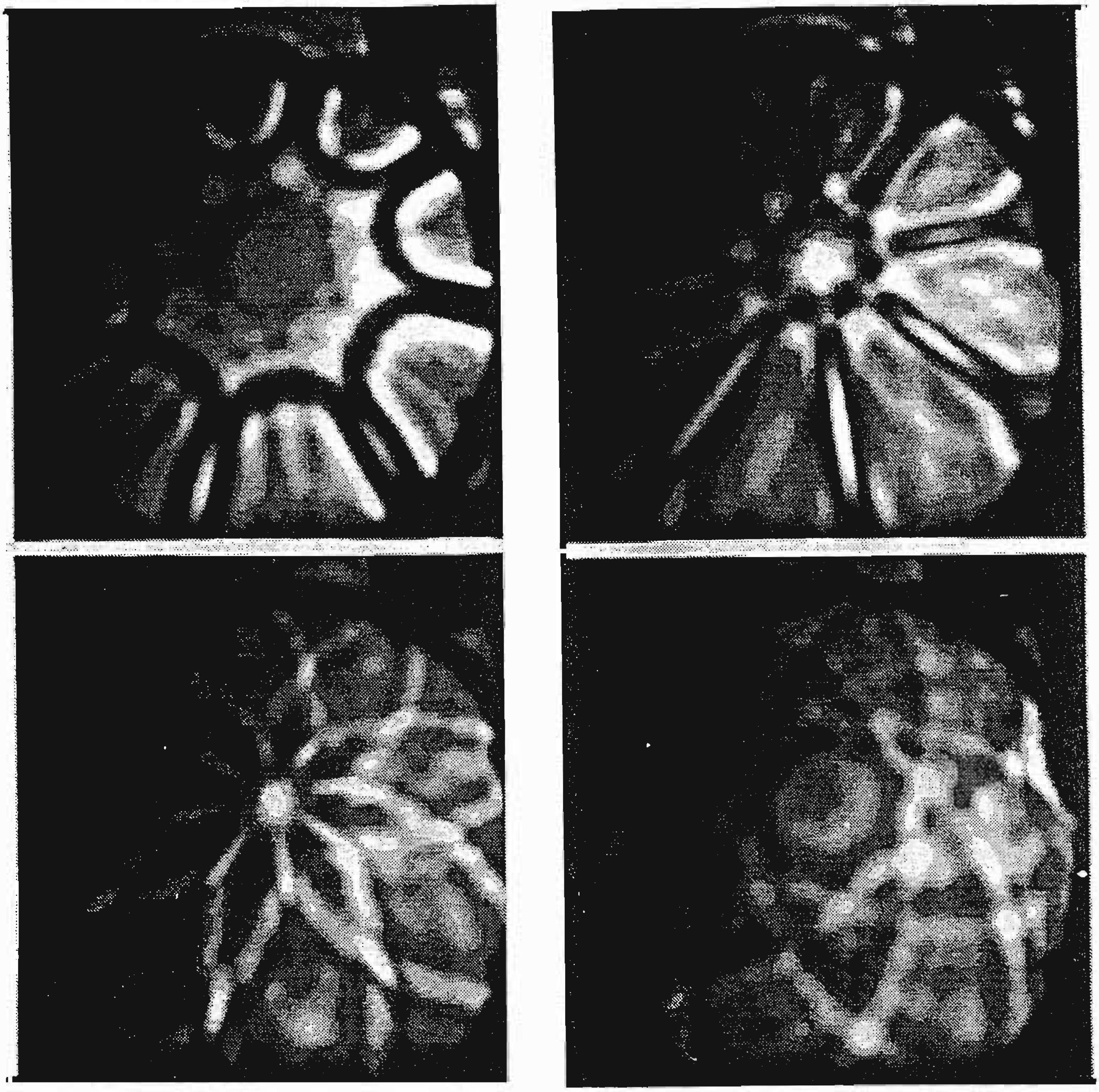

Figure 20: Time sequence of 8 waves on a horizontal surface. There is no Mach addition and the cusping effect is evident. Time delay between images is 100ms.

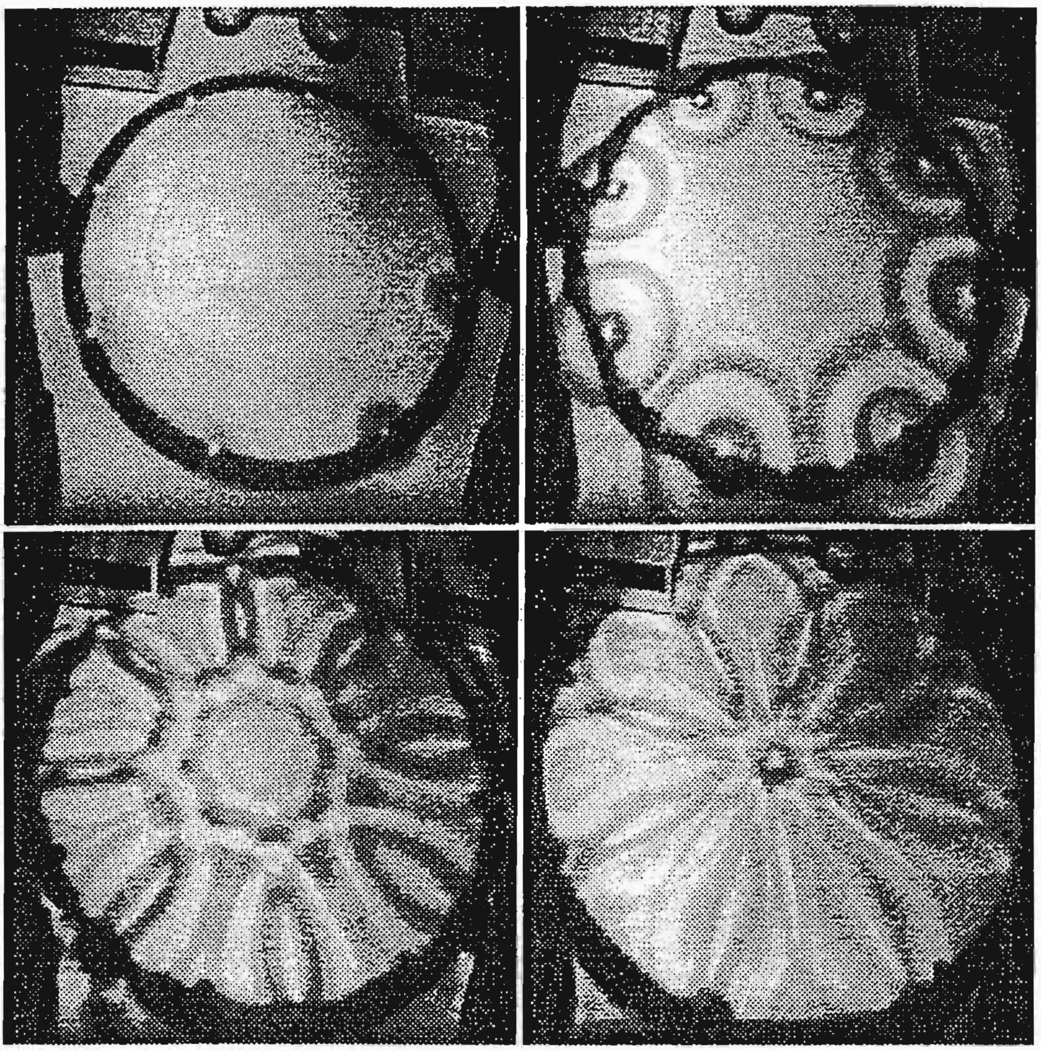

Figure 21: Time sequence of 8 waves on a sloping surface, from initial points to collision point. Time delay between images is 100ms.

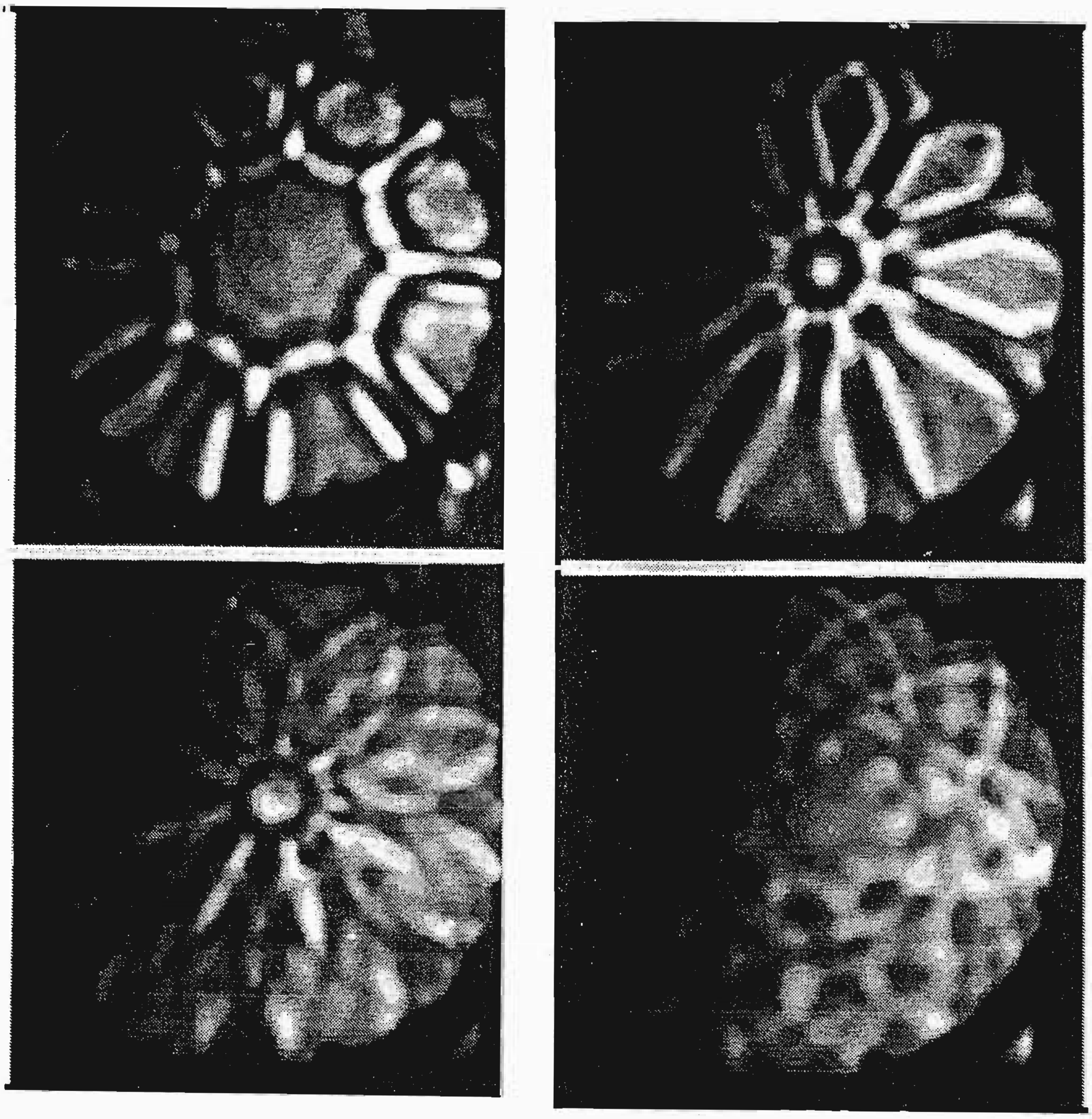

Figure 22: Time sequence of 8 waves on a sloping surface. The top righthand frame illustrates the convergence of the waves, while the bottom lefthand frame shows the ring structure due to Mach addition. Time delay between images is 100ms.

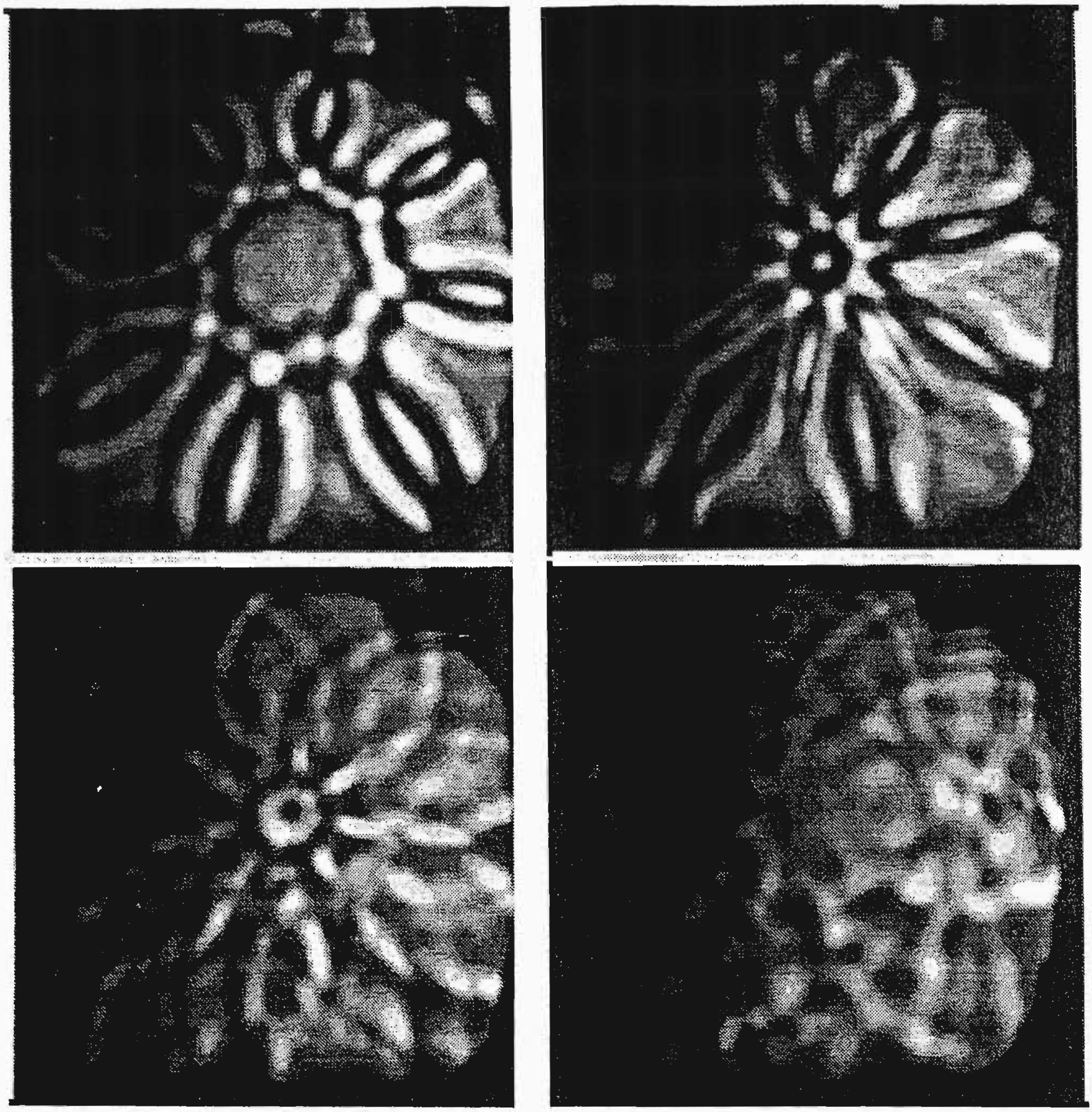

Figure 23: Time sequence of 8 waves on a sloping surface. These images show a focus (top right) expanding outwards as a ring (bottom left). Time delay between images is 50ms.

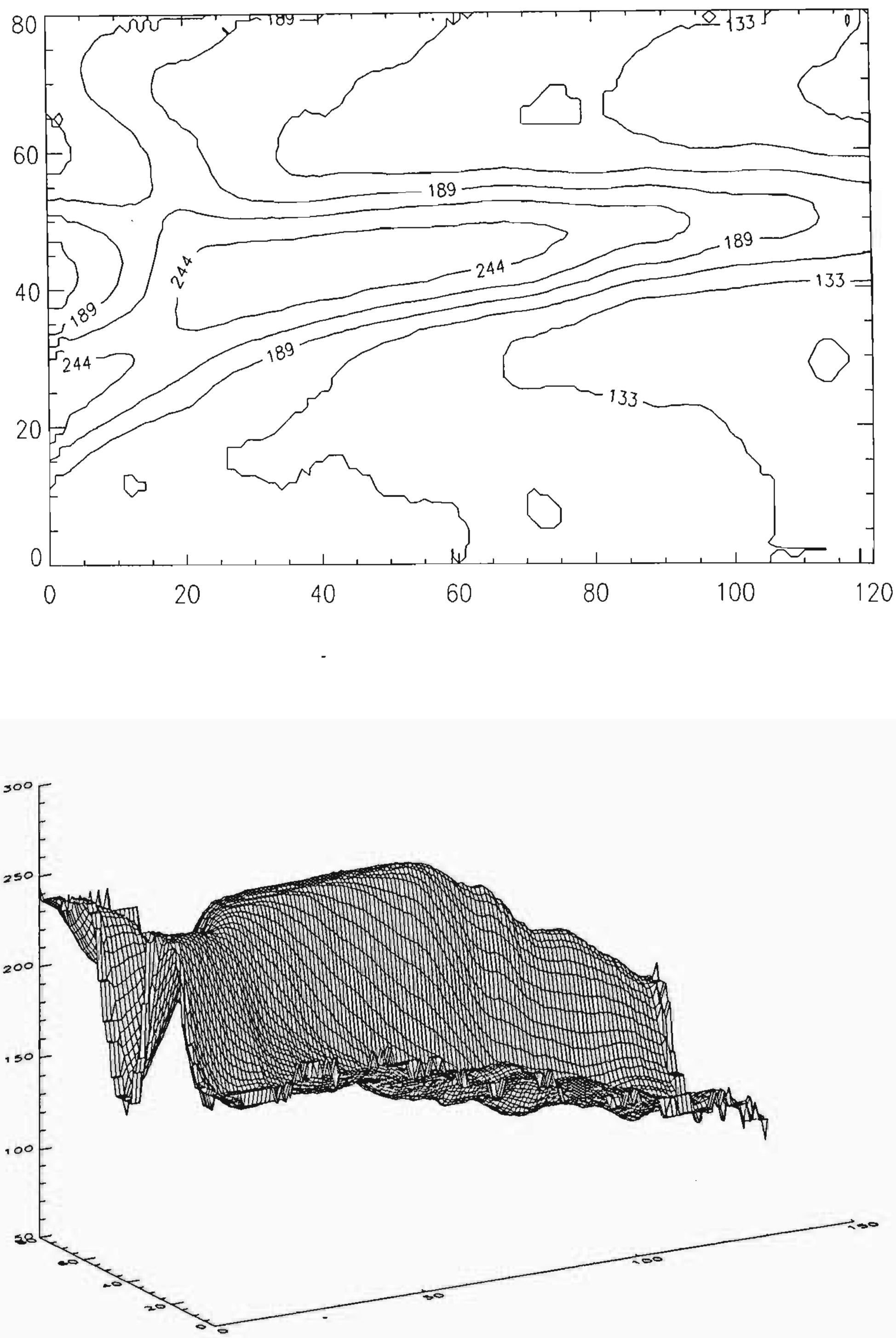

Figure 24: Intensity profile of a line focus. The sloping effect could be due to the light source not being uniform or perhaps even evidence of the non-linear amplitude across the waves. This type of focus is useful for exciting x-ray lasers.

Two features of interest require an explanation. Firstly, there are very clear examples of line foci in some frames. This feature is also apparent in the CSL. It arises because, as the waves collide, so the water amplitude increases not only at the centre, but also, to a lesser extent, along the length of any two interacting arcs (see Figure 18 (d) and (e)). This results in a water depth gradient across the line of intersection, which is symmetric along this intersecting section. The result, illustrated in Figure 18 (e), is a line focus. A 3–D intensity plot of one such line focus is shown in Figure 24. The line focus was produced using only two interacting water waves on a sloping bottom. It is interesting to note that a line focus was the first type of focus noticed by the CSL researchers, and is presently being re-examined for possible applications in the excitation of X-ray lasers. The second feature that requires an explanation is the turbulence seen in the final frame of Figure 21. This is *not* a property of the simulation, but arises simply because the water waves, after collision, are eventually reflected by the ripple tank walls, causing interference and turbulence.

The CSL is a varifocal gas lens: its focal length changes with time, going from a short focal length at the collision moment, to longer focal lengths as the gas expands outwards. Imaging on a plane would result in the focal spot size increasing with time until there was no focus.

The water wave simulations beautifully reconstruct this property of the CSL. As the waves converge to the collision point, so the wave amplitude increases, resulting in the light being more strongly refracted (as described earlier). At the moment of collision a focus is produced which increases in size as the waves expand outwards (resulting in a decreasing amplitude). Figures 25 (a) and (b) show the intensity profiles of the focal spot. Figure 25 (a) is the intensity at some time before the waves have fully collided, hence the weak focus due to weakly refracted rays.

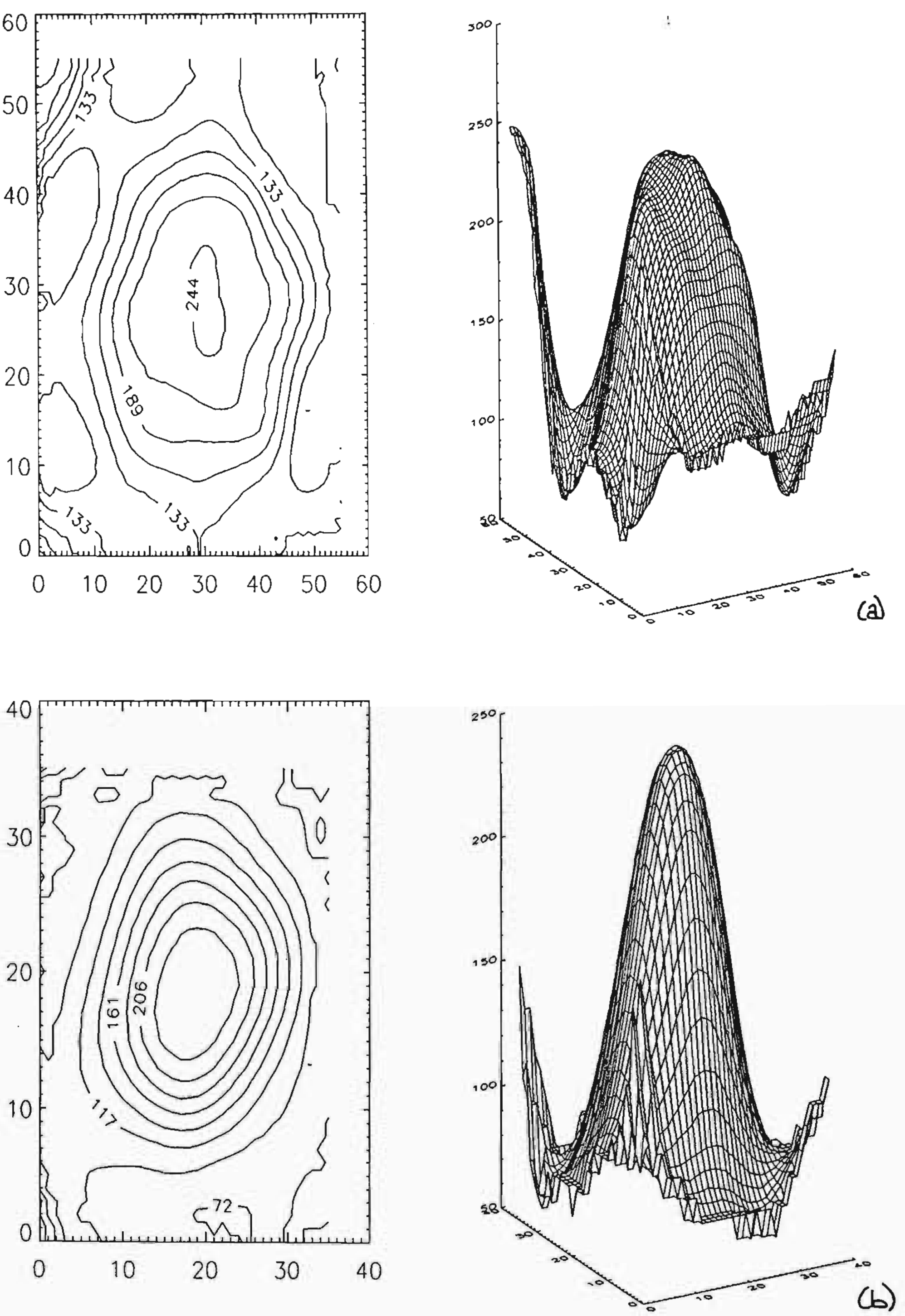

Figure 25: Intensity profile of the central bright region (a) Slightly before focus and (b) At the time of focus (or very near). Notice the symmetry of the focus – nearly Gaussian.

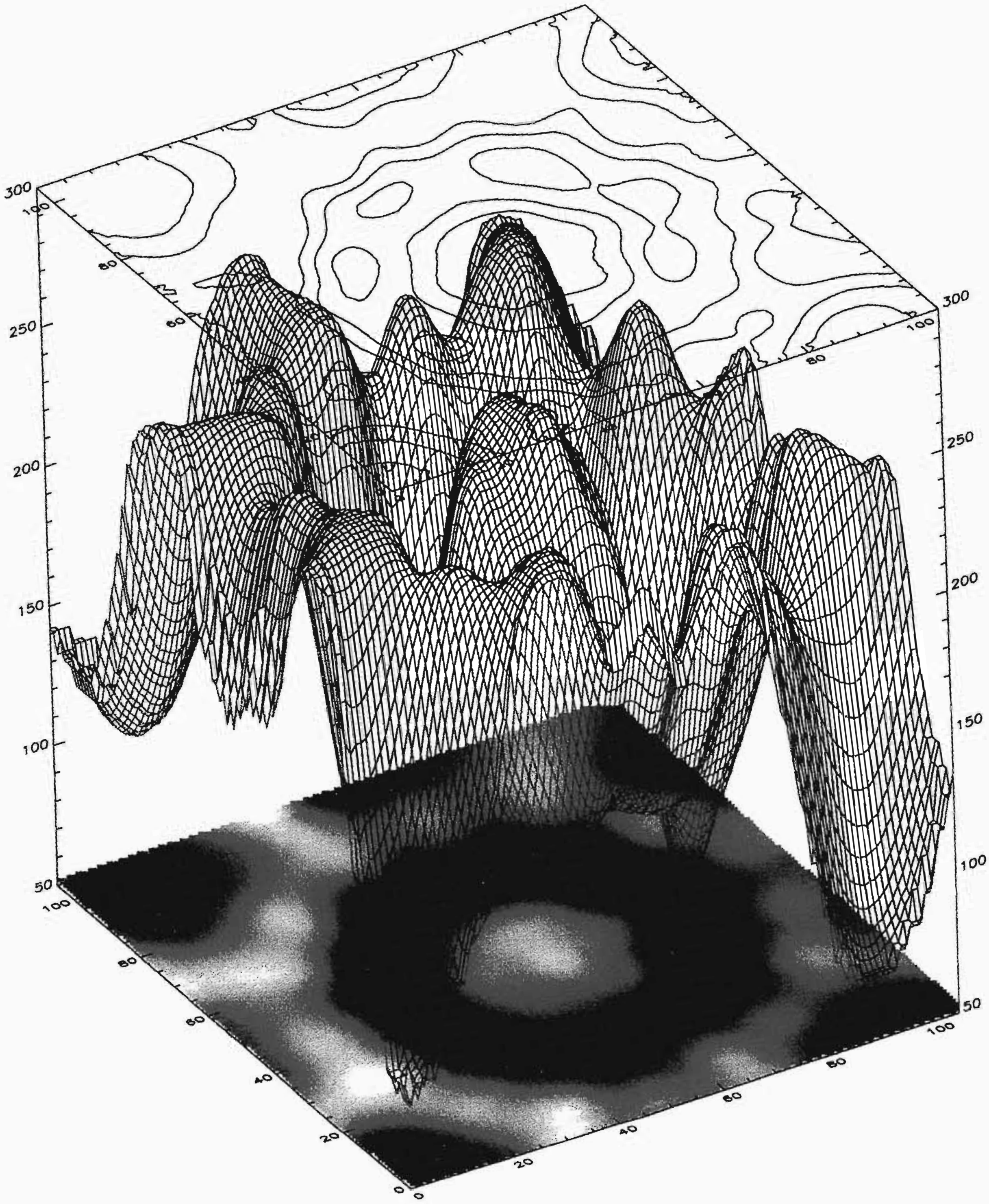

Figure 26: Intensity profile of the expanding ring structure. After collision the waves experience Mach addition. This results in a ring like structure expanding outwards.

Figure 25 (b) is very close to the moment of collision, and hence a steep water depth gradient produces a very good focus, as can be seen from the large, narrow, symmetric peak in the intensity profile. Thus the colliding shallow water waves have simulated the lensing principle of the CSL, most importantly that of a variable focal length. Because the image plane to ripple tank distance was determined arbitrarily (but such that a focus was seen), and because the recording conditions of the CSL were not known (i.e., how was the image plane determined for the CSL experiments), the focal qualities cannot be directly compared, only the fact that the focus is clearly time dependent in both.

Finally, Figure 26 shows the ring like structure due the Mach addition, formed here during the expansion phase of the water waves.

2.9 Conclusion

The objective of this work was to try and simulate the CSL using shallow water waves. We showed how shallow water waves could be used as an analogy to other waves in gas dynamics, and in particular to certain shock conditions. Using the equations of fluid dynamics and shallow water theory, a complete analytical solution was found for the properties of waves travelling under the conditions of our experiment.

Experiments show that there are very strong similarities between the properties of the CSL and the colliding water waves on a sloping bottom. Without a sloping bottom, the simulation is equivalent to that of a weakly interacting CSL which does not focus. With a sloping bottom, Mach addition is observed, and the 'memory loss' of the CSL expansion phase is replicated. Finally, the colliding water waves behave as a varifocal lens, due to a changing water wave amplitude with time, just as the CSL is varifocal, due to a changing density gradient with time.

A note to the reader is required at this point: The work done in this chapter, and the previous chapter, deals with gas lenses, and attempts to experiment with and model them. In this chapter the modelling process led to a water wave experiment to simulate the CSL. The following chapters deal with the lenses created in solid state optical materials; a problem for large laser chains. The link between the chapters is that we move from a gas lensing action, to a solid state lensing action, and all the while we attempt to understand the processes under investigation by utilising existing tools, whether that be water wave theory or beam propagation theory.

3 Thermal Lensing

3.1 Introduction

For the MLIS (Molecular Laser Isotope Separation) process to be successful, high energy, high repetition rate laser beams must be available. For the generation of high repetition rate CO_2 laser pulses, a line tuneable TEA-CO_2 oscillator and several TEA-CO_2 amplifiers are used. An intra-cavity aperture is utilised as a spatial filter for generating a TEM_{oo} spatial mode with an $M^2 \approx 1.3$ (see § 4.5.1 for a discussion of this parameter). At high repetition rates the average power delivered by this chain ranges from $300W$ to more than $1kW$. The master-oscillator-power-amplifier (MOPA) chain consists of a $CW - CO_2$ injection seeded oscillator and several TEA-CO_2 amplifiers. Typically, the output of the chain is more than $1J$ at repetition rates higher than $500Hz$. The beam has to propagate over extensive distances (longer than $50m$) through the amplifiers and a multiple pass Raman cell. For this reason, it is important to know the beam parameters of the CO_2 beam throughout the chain.

A number of possible problem areas were isolated that could have an influence on the beam propagation:

- absorption through the transmission optics
- radius of curvature changes of reflective metal mirrors due to absorption/expansion
- blooming effects due to absorption in air or stationary volumes within the lasers

- effects due to the discharge volumes in the amplifiers

In this chapter, only the effects of the high average power propagation through transmission optics will be dealt with. These effects were observed at average powers higher than 100W. The heating of transmission optics leads to a refractive index gradient – generating a *thermal lens*.

The thermal lens effect is a time dependent phenomena where the spatial profile of a Gaussian laser beam is transformed into a spatial temperature profile within the substrate. This local heating is a result of absorption of the laser radiation; for a Gaussian beam the heating is therefore more pronounced in the centre than on the edges. A radial temperature distribution is created which in turn produces a refractive index change by a factor dn/dT. It is this refractive index change which results in the absorbing medium acting as a lens.

3.2 Review of Theory

The thermal lens effect was discovered by Gordon, Leite, Moore, Porto, and Whinnery [*Gordon et al*, 1965]. The analysis of this effect revealed that it might provide a sensitive means of measuring very small absorptions in liquids.

The thermal lens effect has been theoretically treated under a variety of conditions. These models cover the thermal lens effects which are generated under different excitation conditions, different pump/probe geometries, and different sample conditions (most thermal lensing papers deal with its application to calorimetry). Several review articles have been published on this field [*Franko, Tran*, 1996] [*Harris* , 1986].

A review of the existing single pulse theories shows up some discrepencies. Twarowski [*Twarowski, Kliger*, 1977] developed a model using the parabolic approximation, but found a result that differed from earlier results by Hu and Whinnery [*Hu, Whinnery*, 1973]. Later Dovichi and Harris[*Dovichi, Harris*, 1981] referenced the original Twarowski model, but somehow managed to insert a normalisation constant of 2.303. Following back in other references shows that the source term for use in the heat transfer equation had a normalisation constant of $2\ln(10)$. In reworking the theory, I have not been able to justify or find the origin of this term. What everyone seems to agree on, is that for a single pulse, the focal length takes on an initial value, $f(0)$ and then decays to infinity according to:

$$\frac{1}{f(t)} = \frac{1}{f(0)} \frac{1}{(1 + 2t/t_c)^2}, \tag{3.1}$$

where t is the elapsed time, and t_c is called the relaxation time of the lens. The value of $f(0)$ is calculated to be:

$$f(0) = \frac{\pi \kappa a^2 t_c}{\alpha l E_o \frac{\partial n}{\partial T}}, \tag{3.2}$$

where all the terms are explained and derived in the next section. Figure 27 shows the behaviour of the thermal lens after a single pulse. This decays back to infinity, if the optic is left to cool, which is perfectly reasonable. The question is, what happens if there is not enough cooling time before the next pulse arrives?

3.3 Multiple Pulse Theory

The multiple pulse model [*Forbes et al*, 1996][*van Heerden et al*, 1996] is an extension of the single pulse theories, in that it takes into account the residual heat due to

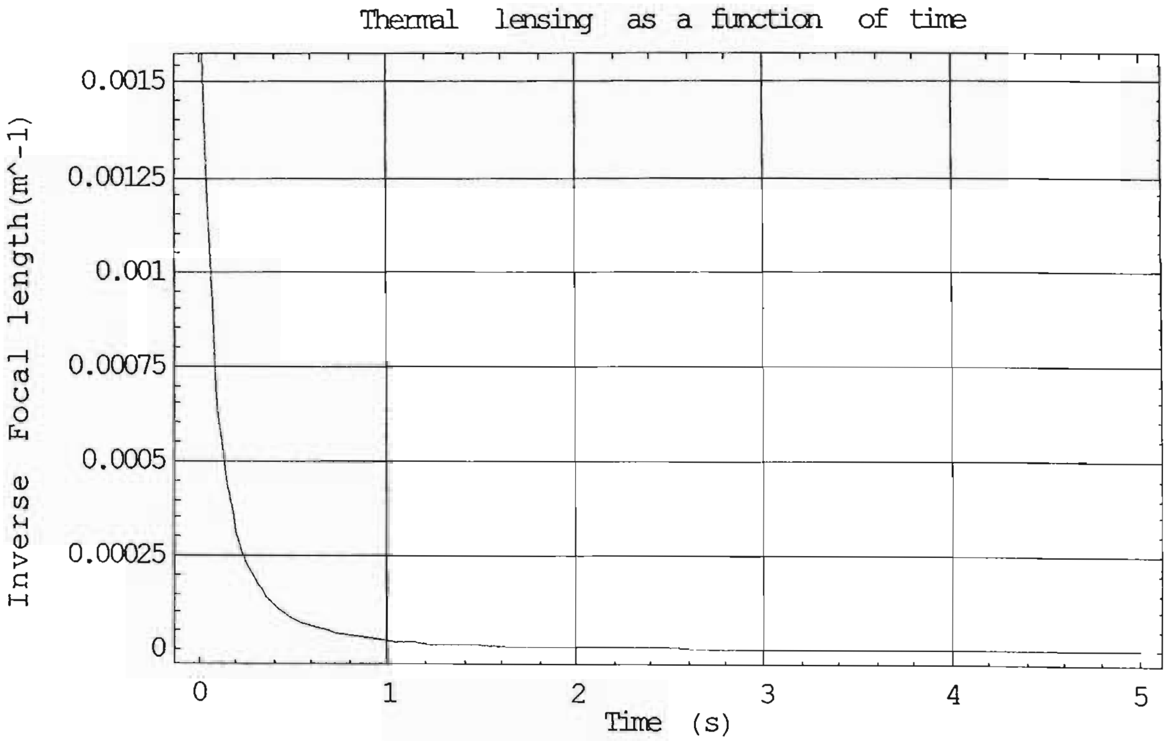

Figure 27: After only one pulse, the optic takes on an initial focal length, and then gradually cools until the inverse focal length is zero.

previous pulses. As far as we know, this is the first analytical expression for this particular problem; many numerical models exist for similar problems.

To find an analytical solution, one first solves the standard heat transfer equation for this problem [*Carslaw, Jaeger*, 1947]:

$$\rho C_p \frac{\partial T}{\partial t} - \nabla\kappa . \nabla T = Q. \tag{3.3}$$

Here T is temperature, κ is thermal conductivity and ρ and C_p are density and specific heat capacity of the material respectively.

Since the source term (Q) is a Gaussian beam, we assume it to be given by:

$$Q = \frac{\alpha E_o e^{\frac{-2r^2}{a^2}}}{\pi a^2 t_o}, \tag{3.4}$$

where α is the material bulk absorption coefficient at the given wavelength, E_o is the pulse energy, t_o is the FWHM pulse width and a is the $1/e^2$ beam radius on the optic. Dividing Equation (3.3) by ρC_p yields

$$\frac{\partial T}{\partial t} = D\nabla^2 T + \frac{Q}{\rho C_p}, \tag{3.5}$$

where D is the diffusivity, given by $\kappa/\rho C_p$, and it has been assumed that the conductivity is constant.

We now make the following assumptions:

- Heat loss to the surroundings, through the optic surface, can be ignored.
- The window acts as a semi-infinite plate, with a constant boundary temperature.
- Both κ and C_p are temperature independent.

- The laser beam pulse is switched on at $t = 0$, and switched off at $t = t_o$, both instantaneously.
- Beam power and radius are constant within the sample.

As a justification for the above, note that the pulse width of the beam is typically 80 ns (FWHM value) and therefore no ablation is observed. Because the conduction through the edges is very good, most of the heat is transfered by this mechanism, and therefore the surface heat loss is ignored. Also, we note that since the optical holders act as very good heat sinks, the boundaries are indeed at constant temperature. Furthermore, the spot size on the optic is always much less than the optic diameter, hence the semi-infinite plate (the thickness of the optic is also much less than the diameter). The absorption is significant, but nevertheless small compared to the transmitted energy, thus the beam parameters remain constant within the sample. Finally, the temperature rise is small, thus κ and C_p can be considered constant (it will be shown that the temperature *gradient* and not a temperature increase induces a lens).

These assumptions result in a Green's Function solution to Equation (3.5) [*Prinsloo*, 1995]

$$G(r,t;r',t'=0) = \frac{1}{4\pi\kappa l} e^{\frac{-(r^2+r'^2)}{4Dt}} I_o(\frac{rr'}{2Dt}), \tag{3.6}$$

where I_o is a modified Bessel function. Through integration of

$$\Delta T = 2\pi l \int_0^\infty Q(r')G(r,t;r')r'dr', \tag{3.7}$$

one finds that the temperature variation caused by the multiple pulses can be determined as:

$$\Delta T = \sum_{q=0}^{m} \frac{\alpha E_o}{\pi \rho C_p a^2 (1 + \frac{2n\tau}{t_c})} e^{(\frac{-2r^2}{a^2} \cdot \frac{1}{1+\frac{2q\tau}{t_c}})} . \tag{3.8}$$

We note from *Born and Wolf* [*Born*, *Wolf*, 1975] that

$$\frac{1}{f} = -l \left(\frac{\partial^2 n}{\partial r^2} \right)_{r=0} , \tag{3.9}$$

where in our case l is the thickness of the optic, and f is the focal length.

In the single pulse theory, many authors approximate the lens with a parabolic profile. One can now justify this by expanding the refractive index in a McLaurin series about $r = 0$:

$$n = n_o + r(\frac{\partial n}{\partial r})_{r=0} + \frac{1}{2} r^2 (\frac{\partial^2 n}{\partial r^2})_{r=0} + \cdots$$

Since $(\frac{\partial n}{\partial r})_{r=0} = 0$, a parabolic approximation will be accurate near the centre of the optic (by the symmetry of the arrangement). However, we note that

$$\frac{\partial n}{\partial r} = \frac{\partial n}{\partial T} . \frac{\partial T}{\partial r} ,$$

and hence

$$\frac{\partial^2 n}{\partial r^2} = \frac{\partial^2 n}{\partial r \partial T} . \frac{\partial T}{\partial r} + \frac{\partial n}{\partial T} . \frac{\partial^2 T}{\partial r^2} . \tag{3.10}$$

But we know also that $(\frac{\partial T}{\partial r})_{r=0} = 0$, therefore the first term of Equation (3.10) is eliminated, and substituting the result into Equation (3.9) gives

$$\frac{1}{f} = -l \frac{\partial n}{\partial T} (\frac{\partial^2 T}{\partial r^2})_{r=0} . \tag{3.11}$$

The factor $\frac{\partial n}{\partial T}$ is determined from published tables, and is roughly constant for solid state IR materials over a large temperature range.

We are at last able to determine the focal length induced into the optic by the effect of heat transfer from m pulses of the laser. Evaluating Equation (3.11) using Equation (3.8) gives, after a little algebra:

$$\frac{1}{f(t)} = \sum_{q=0}^{m} \frac{\alpha l E_o}{\pi \kappa a^2 t_c} \left(\frac{\partial n}{\partial T}\right) \left(\frac{1}{1+\frac{2q\tau}{t_c}}\right)^2 . \tag{3.12}$$

This result is identical to that from the single pulse theory, but with the factor

$$\left(1+\frac{2t}{t_c}\right)^{-2},$$

replaced with

$$\sum_{q=0}^{m} \left(1+\frac{2q\tau}{t_c}\right)^{-2}.$$

Note that $q\tau$ is a measure of the elapsed time, since q is the number of pulses and τ is the inverse of the repetition rate (or time between pulses). This is remarkable, since it was never the intention to get the multiple pulse theory into the same format as the existing single pulse theory – the algebra merely reduced it to this convenient form. The similarity between the two is very encouraging.

The variables in Equation (3.12) can be grouped as follows: those that are properties of the beam, and those which are properties of the substrate. Properties of the substrate which influence the lensing are:

- The absorption coefficient, α.
- The thickness of the element, l.
- The conductivity of the material, κ.
- The constant factor $(\partial n/\partial T)$.

Properties of the beam which have an effect on the lensing are:

- The beam energy, E_o.
- The repetition rate $1/\tau$.
- The number of pulses q.
- The beam radius at the position of the optic, a.

A term which falls under both categories and which was introduced earlier and again here after the algebra, is the factor t_c, called the *relaxation time* of the system, and is defined as

$$t_c = \frac{a^2}{4D}.$$

The meaning of this term and its influence on the lensing will be discussed later (in § 3.3.1). Recall that a refers to the beam radius (a beam parameter), and D is the Diffusivity, a material parameter.

The beauty of having an analytical expression for the time dependence of the induced focal length is now very apparent. One is able to look at the equation and see if it is going to follow the trends that one's intuition suspects to be true. By considering the parameters in Equation (3.12), we are able to make the following predictions on behaviour trends which intuitively seem reasonable:

- Both the laser parameters and material parameters will influence the lensing.
- The thermal lensing will be stronger for higher pulse energies and higher repetition rates.
- Damaged optics, with higher absorption coefficients, and thick elements, such as Fresnel prisms, will experience stronger thermal lensing.

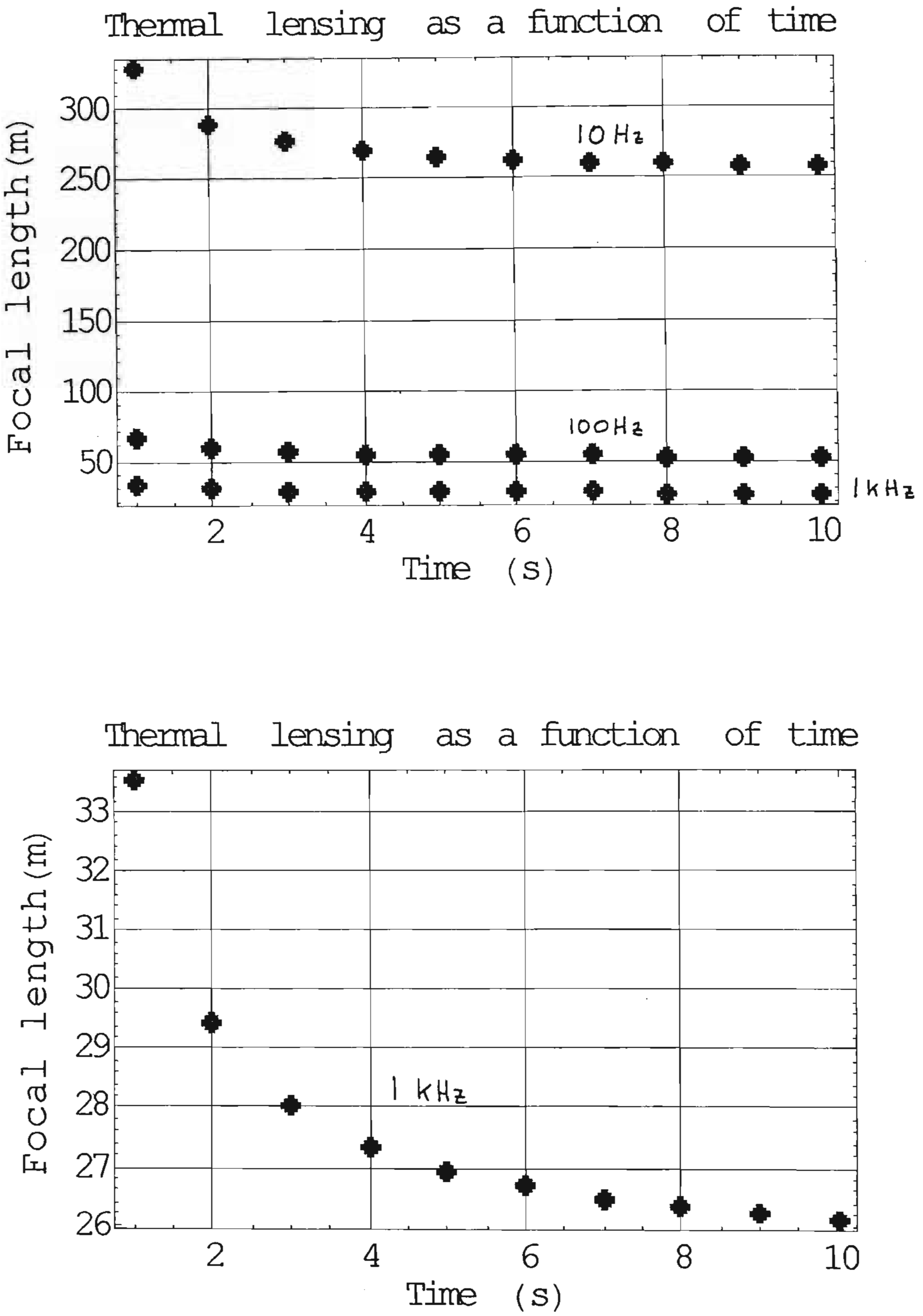

Figure 28: Predicted focal length changes as a function of time, for three different repetition rates (10 Hz, 100 Hz and 1 kHz). The 1 kHz plot is shown separately.

- Smaller spot sizes on the element, which results in higher fluences, will also result in stronger thermal lensing.

Finally, in order to simplify discussions later, we make the following substitutions:

$$f(t) = \frac{f(0)}{\sum_{q=0}^{m}(1+\frac{2qT}{t_c})^{-2}}, \tag{3.13}$$

with

$$f(0) = \frac{\pi\kappa a^2 t_c}{\alpha l E_o \frac{\partial n}{\partial T}}; \tag{3.14}$$

this is the initial focal length induced into the optic. If there was only a single pulse, this would then decay back to infinity as is the case with the single pulse theory. Notice that the initial focal length predicted by this theory is exactly the same as that of the single pulse theory, with the exception of the normalisation constant $2\ln(10)$ in the latter. Figure 27 shows how the focal length takes on an initial value, and then decays back to infinity if only one pulse is considered. Note that inverse focal length is plotted, so the function tends to zero with increasing time. In Figure 28, it is clear that the induced focal length decreases rapidly during the first few seconds, until an equilibrium value is reached. This value is repetition rate dependent. At $10Hz$ there is almost no change, while at $300Hz$ the change is almost a factor of 80 larger (i.e. if the window initially acts as a lens of focal length $80m$, then after a few seconds it acts as a lens of focal length $1m$!). Such a change can introduce severe beam propagation problems.

3.3.1 Relaxation time

The relaxation time depends on both the diffusivity, a material consideration, and the beam radius at the position of the substrate– a beam propagation parameter.

Because the focal length is described by a converging series, it makes sense to speak of rates of convergence. Hence forth we shall speak of these rates of convergence in terms of units of t_c, the relaxation time of the system. We choose this as a reference because of the structure of Equation (3.12). Notice that the time elapsed is given by

$$t = q\tau,$$

which is then divided by the relaxation time t_c. It is logical therefore to count time in units of t_c, with the number of pulses after x units of t_c given by

$$q = \frac{xt_c}{\tau}.$$

It is important to realise that although one can "look" at the convergence of the series in terms of the relaxation time, one cannot "count" or "add" the series in terms of units of t_c, unless it is related back to the corresponding number of pulses i.e. the sum must be over q and not t/t_c.

The first interesting property of the relaxation time is that it is independent of the repetition rate of the laser. Thus after $10t_c$ for example, you are always a given percentage towards the stable focal length. At higher repetition rates it requires more pulses, but this is balanced by the fact that the pulses are arriving that much faster.

To test for the convergence of the series, we compare how close the value of $f(xt_c)$ is to $f(\infty)$. Because it is not practical to allow a series to sum for an infinite number of terms, a value of $10t_c$ is chosen for the convergence time. Some simple input of numbers will show that the difference $f(100t_c) - f(10t_c) < 0.001$, with this difference decreasing as more terms are summed. Thus stopping after $10t_c$ is acceptable[3]. Figure 29 (a) shows how quickly the series converges to the stable focal length. After only $3t_c$ the resulting focal length is 90% of the final value. To use KCl

---

[3] Only under stable conditions. If damage occurs, so does thermal runaway, and then the lensing deteriorates until finally the optic cracks or explodes.

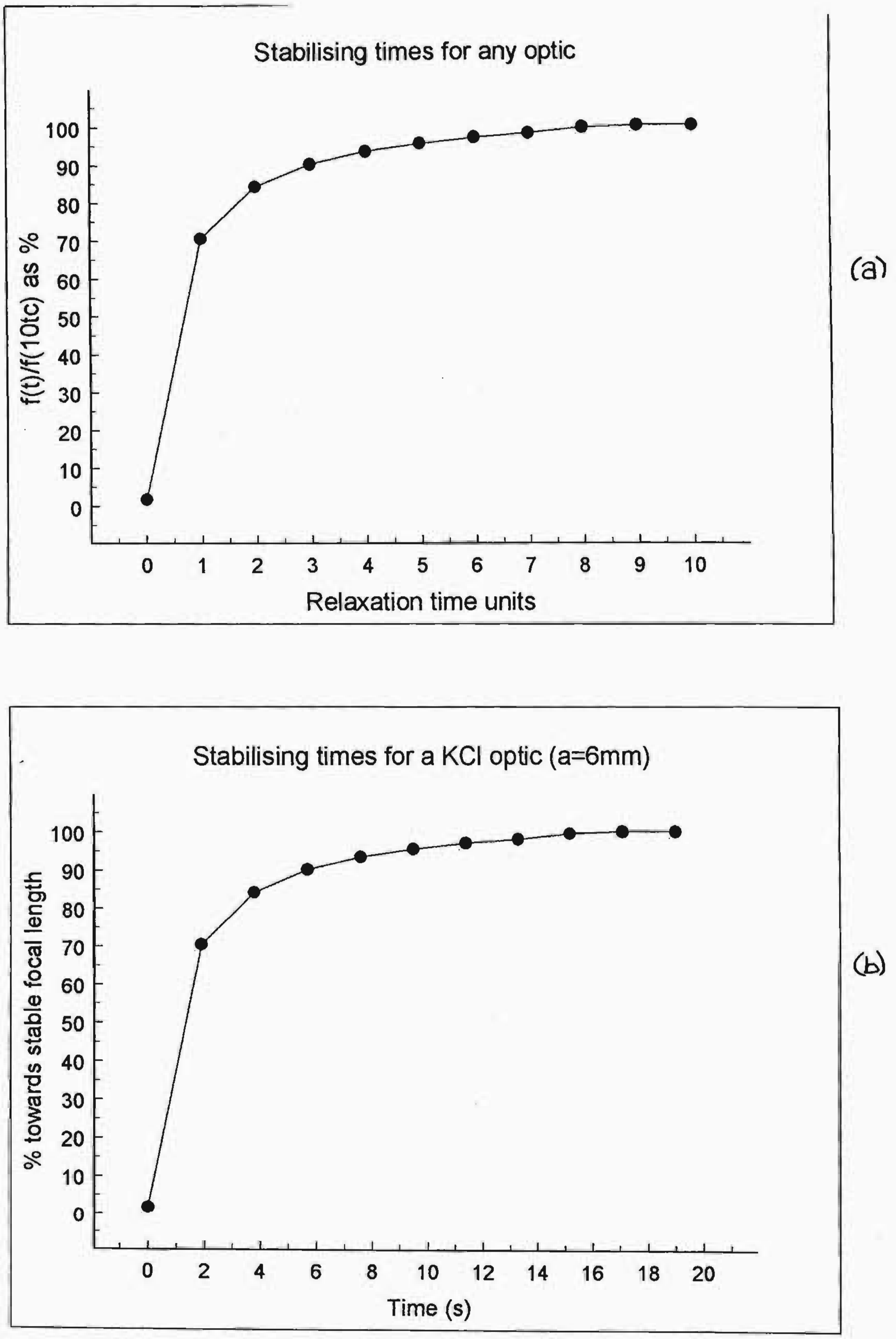

Figure 29: (a)The value of $f(xt_c)$ as a % of $f(\infty)$ shows that after a time interval of $3t_c$ the focal length is 90% towards the covergence value. After $10t_c$ the series has, for all practical purposes, converged.(b) Predicted times for a KCl window.

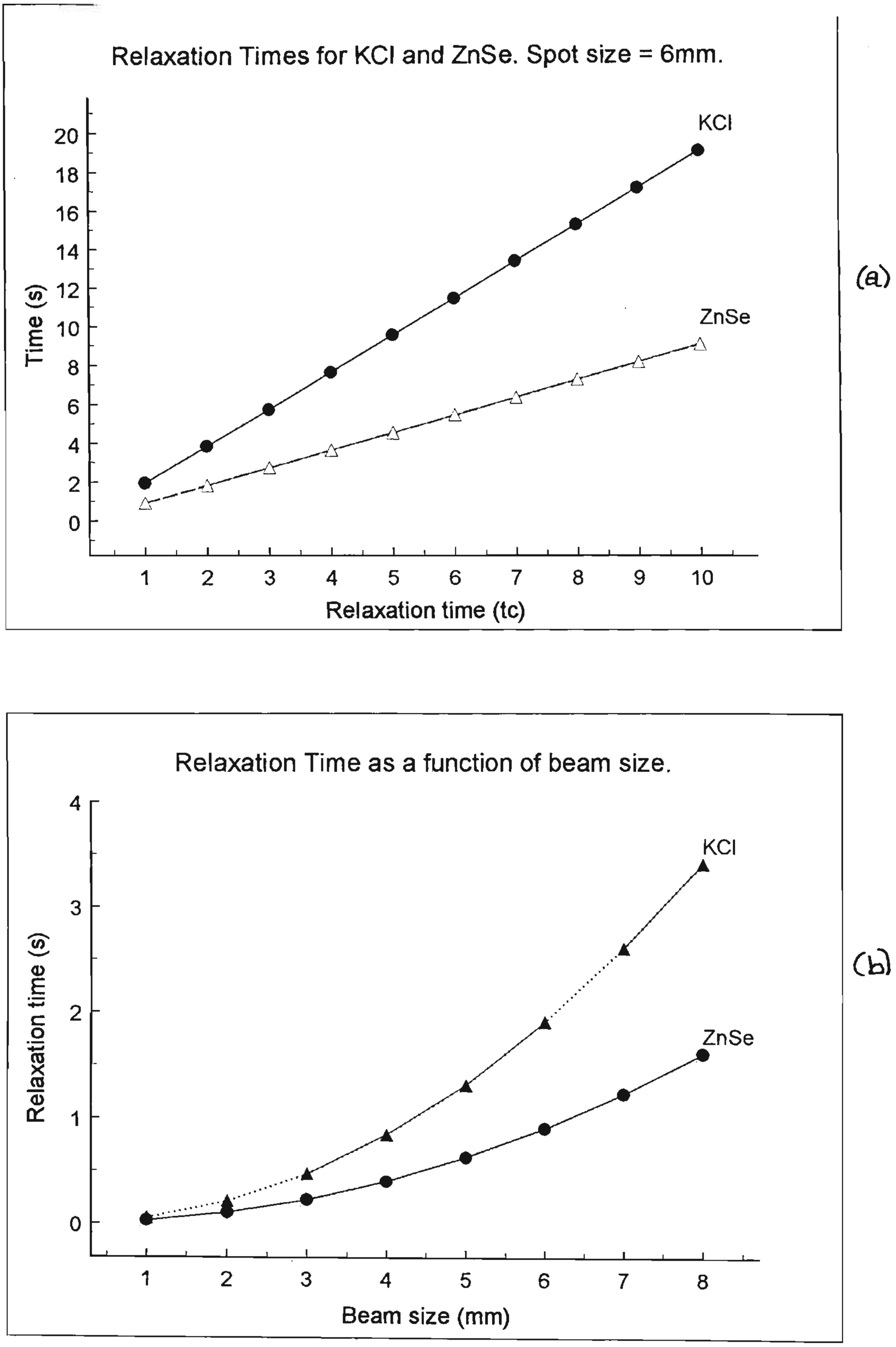

Figure 30: (a) Comparison of the relaxation times and convergence for KCl and ZnSe.(b) Relaxation time as a function of beam size.

as an example, this implies that for a 6mm beam radius on the window ($a = 6$mm), the relaxation time is 1.9s, and after only 5.7s the focal length is 90% of the stable value. It is interesting to note that the material does have measurable effects. By keeping the same conditions, we find that the relaxation time for a ZnSe window is 0.9s – less than half that of the KCl value. Thus ZnSe will stabilise faster compared to KCl, but note that this does not indicate what that stable value will be. In order to decide how long we should allow for the optic to stabilise, note that after $t = 3t_c$, the focal length is 90% of its stable value. Since 10% is a reasonable difference (it only has an appreciable effect for large focal lengths, but in that case the focal length can be ignored anyway), we will take the $3t_c$ time as an effective stabilisation time. Some relaxation times are shown for KCl and ZnSe optics in Figure 30 (a)

In Figure 30(b), the change in t_c is shown for different spot sizes. This derives from the fact that $t_c \propto a^2$. Thus for larger spot sizes it takes longer to stabilise the lensing. To see how two different relaxation times are related, we note that

$$t_c' = \left(\frac{a'}{a}\right)^2 t_c, \tag{3.15}$$

which implies that a change of only $\sqrt{2}$ in the beam size will double the time to stabilise (e.g. a beam radius change from 5mm to 7mm would double the value of t_c). Although this is not altogether beneficial, there are other factors to consider. Changing the spot size, and consequently the relaxation time, also changes the resultant focal length. This will be discussed next.

3.3.2 Spot size and focal length

If we consider Equation (3.13), the focal length of the lens is the division of two terms. The numerator, $f(0)$, is described by Equation (3.14). This shows us that there is a $f \propto a^4$ dependence, since the numerator of Equation (3.14) involves the product of a^2 and t_c, but $t_c \propto a^2$. Thus, as the spot size of the beam increases, say by changing a mirror or altering the M^2 of the beam, so the value of $f(0)$ also increases. The denominator of Equation 3.13 shows that the series will converge to a value that depends on the relaxation time, and consequently on a^2. The model predicts that as the spot sizes increases, so the convergent value of the series also increases, thus reducing the focal length of the optic. To summarise, both the numerator and denominator increase as the spot size changes, but since the numerator increases as a^4 , it increases faster than the denominator, giving the net effect that as the spot size increases, so the focal length also increases. Mathematically we say that we would like to choose a material such that

$$f(0) \gg \sum_{n=0}^{\infty} \frac{1}{(1 + 2n\tau/t_c)^2}, \qquad (3.16)$$

noting that the term $f(0)$ is largely dependent on the properties of the optic, this translates into saying that an optic must be found with properties such that the above equation holds. When Equation (3.16) fails entirely, then the material is not suitably chosen for the application (the specific repetition rate of the laser), and the resultant focal length is less than 1m, which is catastrophic for mode matching.

Figure 31 shows how the focal length of KCl and ZnSe windows changes with increasing spot size, for different repetition rates. Notice that only at high repetition rates and small spot sizes does the focal length fall below 1m.

3.3.3 Thermal lensing and Beam propagation

In the previous section, § 3.3.2, we looked at the effect that the beam size on the optic has on the induced focal length. In this section we consider the effect the thermal

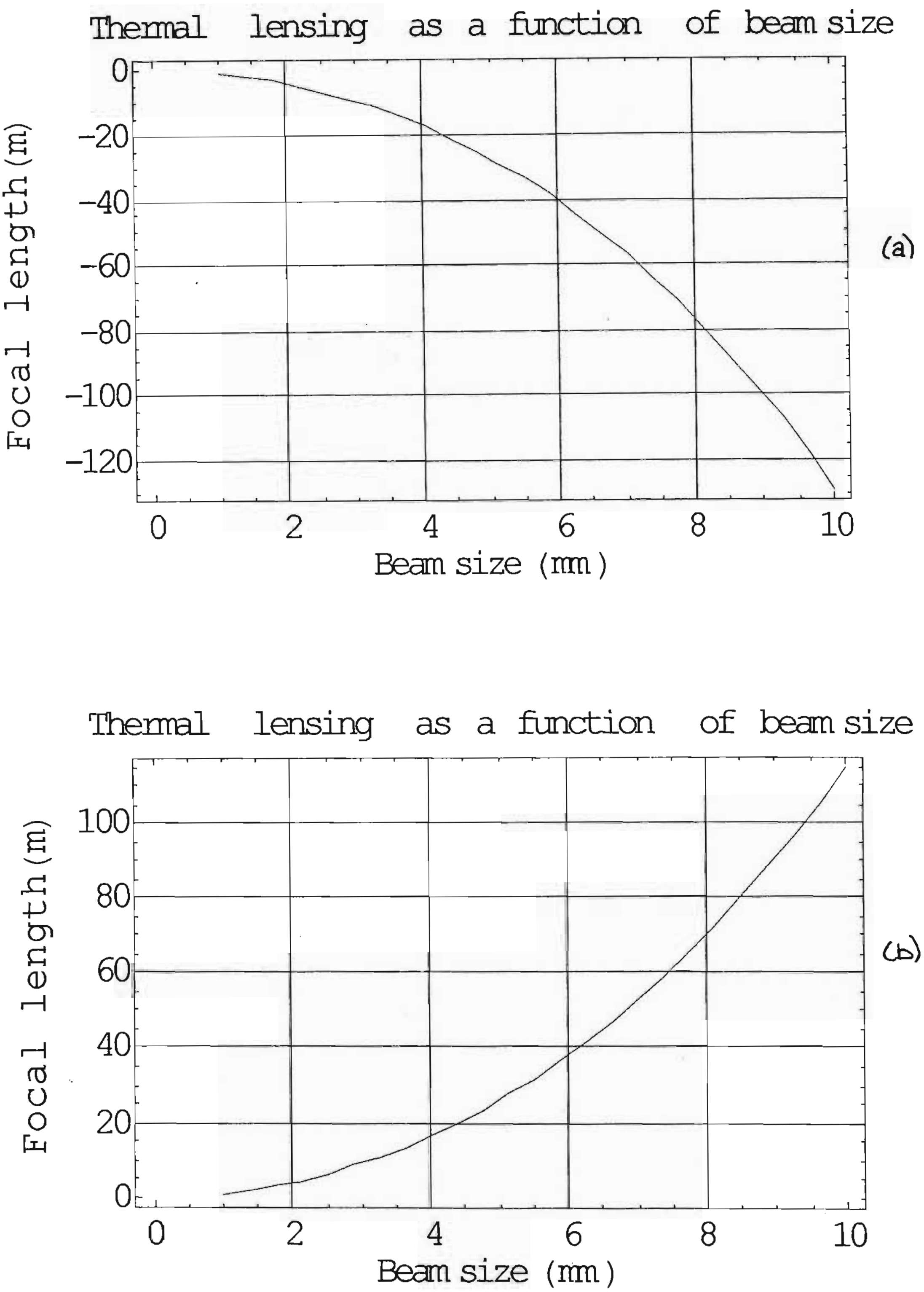

Figure 31: Focal length dependence on beam radius for (a) KCL window, and (b) a ZnSe window.

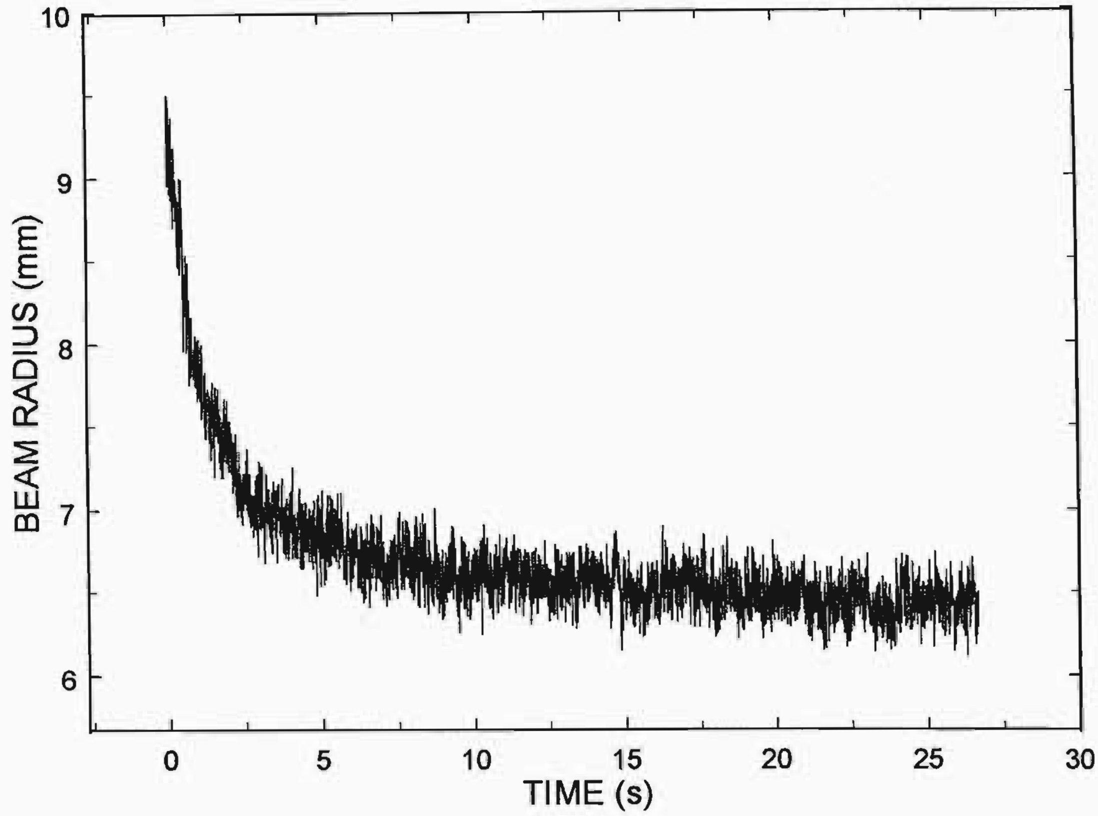

Figure 32: An example of the beam size change, as a function of time, as measured in the MLIS laser chain. This time dependence is a result of thermal lensing.

lens has on the propagation of the beam. A detailed analysis of propagation effects will be left until § 5, but some analysis is necessary now in order to make sense of some of the experimental data to follow. An example of the effect that a thermal lens has on the spot size can be seen in Figure 32.

For the purpose of this analysis, the thermal lens is treated as a thin lens, and the Gaussian propagation laws are used. This enables one to write the optical chain as an ABCD matrix (see Figure 33 for some typical ABCD matrices), and using the formalism of *Reng and Eppich*[*Reng, Eppich*,1992]:

$$\omega_2^2 = A^2\omega_{0,1}^2 + B^2\theta_1^2, \tag{3.17}$$

$$\theta_2^2 = C^2\omega_{0,1}^2 + D^2\theta_1^2. \tag{3.18}$$

Here the subscripts 1 and 2 refer to the beam before and after the thermal lens respectively; θ is the far field divergence of the beam, and ω is the $1/e^2$ beam radius defined by the second moments calculation (a subscript 0 refers to a waist, or minimum radius). In order to simplify the calculation, and without any loss of generality, we take the input beam to have a waist on the window, as shown in Figure 34, and determine the ABCD matric coefficients from:

$$\begin{pmatrix} A & B \\ C & D \end{pmatrix} = \begin{pmatrix} 1 & z \\ 0 & 1 \end{pmatrix} \begin{pmatrix} 1 & 0 \\ \frac{-1}{f(t)} & 1 \end{pmatrix}.$$

This then gives the following values for the ABCD coefficients:

$$A = 1 - \frac{z}{f(t)}, \tag{3.19}$$

$$B = z, \tag{3.20}$$

$$C = -\frac{1}{f(t)}, \tag{3.21}$$

(1) Homogeneous Medium: Length d	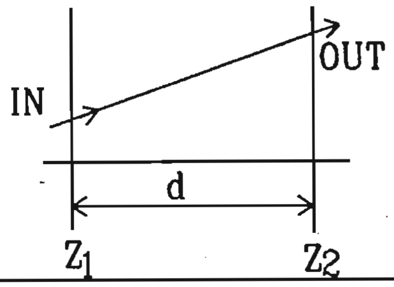	$\begin{bmatrix} 1 & d \\ 0 & 1 \end{bmatrix}$
(2) Thin Lens: Focal length f (f>0,converging; f<0,diverging)	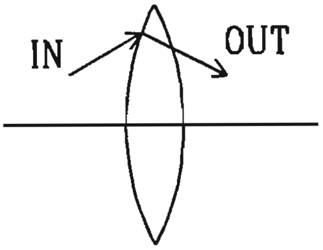	$\begin{bmatrix} 1 & 0 \\ \frac{-1}{f} & 1 \end{bmatrix}$
(3) Dielectric Interface: Refractive indices n_1, n_2	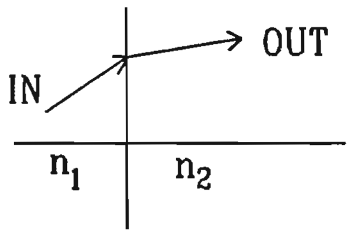	$\begin{bmatrix} 1 & 0 \\ 0 & \frac{n_1}{n_2} \end{bmatrix}$
(4) Spherical Dielectric Interface: Radius R	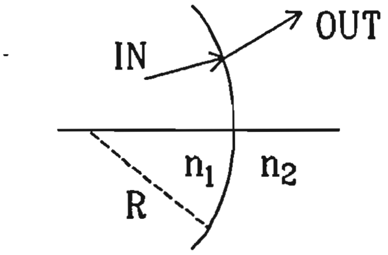	$\begin{bmatrix} 1 & 0 \\ \frac{n_2 - n_1}{n_2} \frac{1}{R} & \frac{n_1}{n_2} \end{bmatrix}$
(5) Spherical Mirror: Radius of curvature R	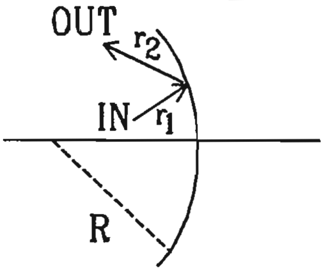	$\begin{bmatrix} 1 & 0 \\ \frac{-2}{R} & 1 \end{bmatrix}$

Figure 33: A table of some standard ABCD matrix representations.

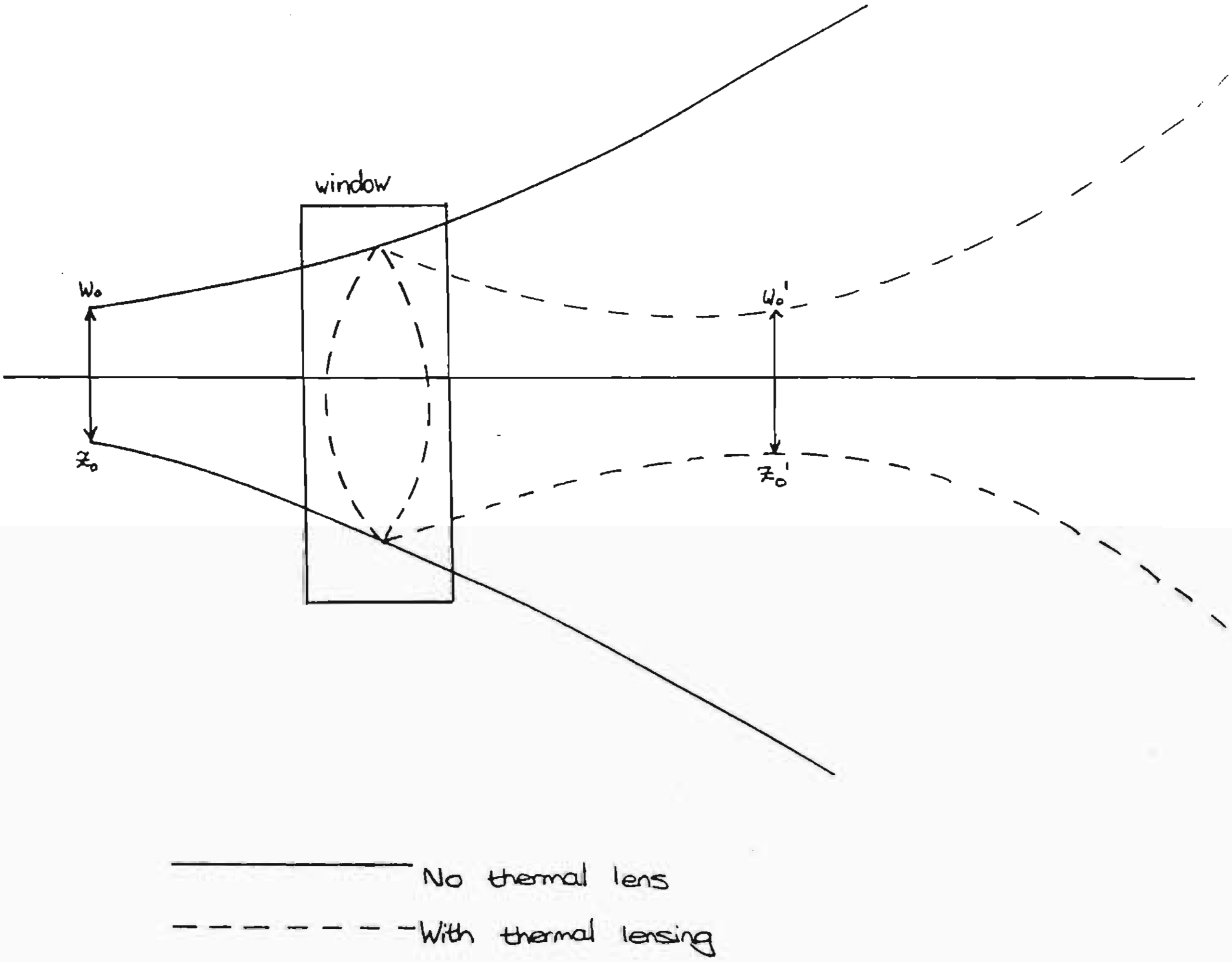

Figure 34: A schematic of the thermal lensing problem. After the window has stabilised, the new "lens" changes the propagation of the beam.

$$D = 1. \tag{3.22}$$

Clearly, since the coefficients A and C are functions of time, we see from Equations (3.17) and (3.18) that the propagation of the beam after the window will now also be a function of time.

Some simulations of what a detector would see if placed at various distances from a thermal lens are shown in Figures 35 – 37. For the simulations,an input beam radius of $3mm$ was used. The imaginary detector is place at three different distances (as measured from the window): $1m$ being a near field view; $5m$ showing an intermediate field view, and $10m$ being classed as far from the window. To generate a weak, intermediate and strong lens, the repetition rate and pulse energy was varied. The weak, intermediate and strong lenses had focal lengths of around 9m, 5m and 2m respectively (actually all three of these values would be considered problematic in the MLIS laser chain).

The reason for including this is to illustrate just how non-linear the resultant beam propagation is. To predict the behaviour of the beam using only one measurement point will only be of use if the beam parameters before the lens are known exactly. The problem with the MLIS chain is that there are several windows, which all have an effect. The problem is compounded by the fact that, as is shown by Equations (3.17) and (3.18), not only does the time dependent focal length influence the resultant beam, but also the input beam parameters, which are in turn influenced by the previous lens. Thus making predictions for the entire chain is a complex process.

To explain the counter-intuitive graphs of beam size as a function of time, consider the situation in Figure 38. If the detector is placed at a distance closer to the window than the stabilised focal length of the lens, then effectively one can

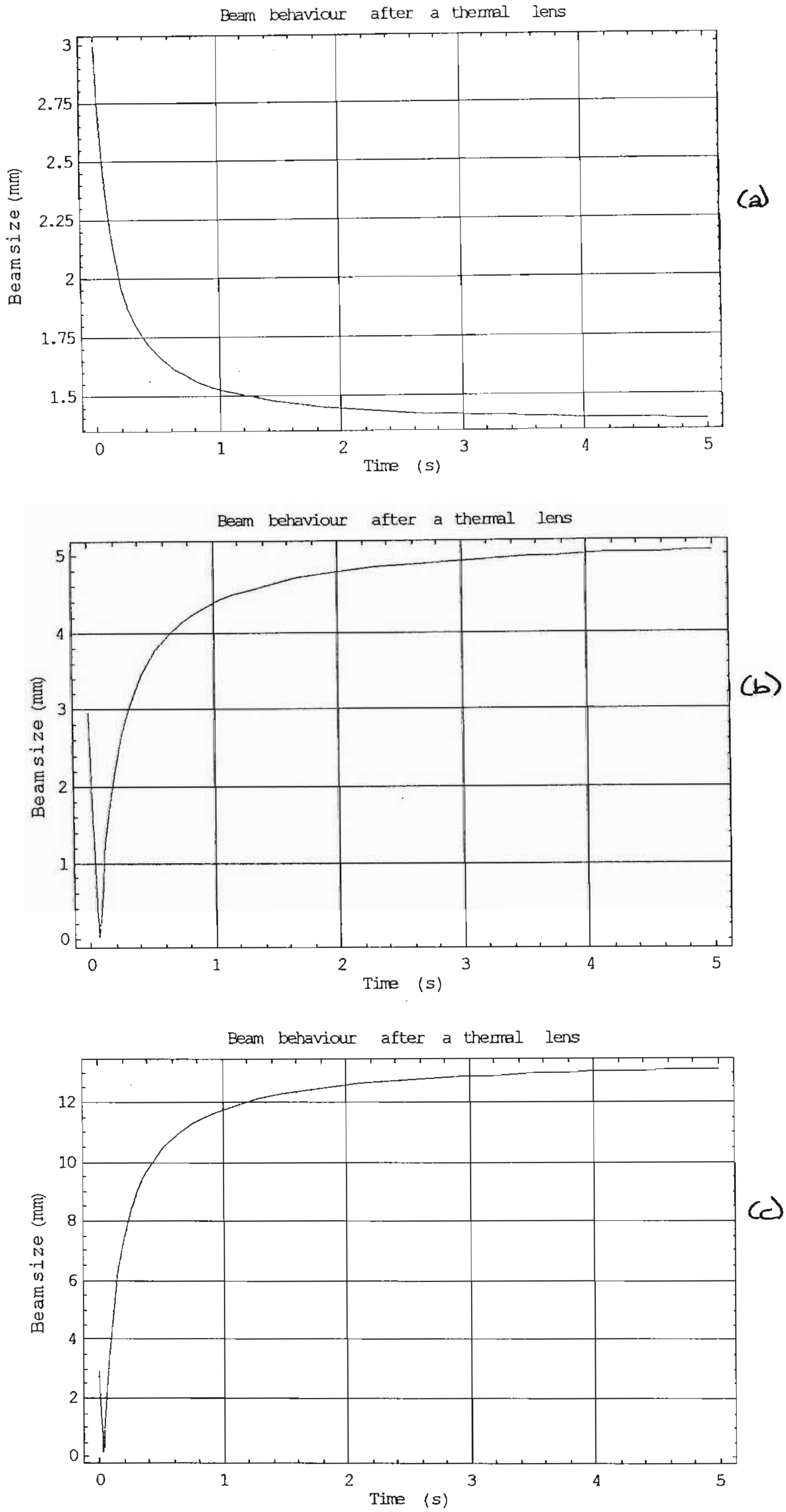

Figure 35: The beam size as a function of time for a strong lens: (a) shows the simulation near the window, (b) shows the behaviour at some intermediate distance, and (c) is the behaviour far from the window.

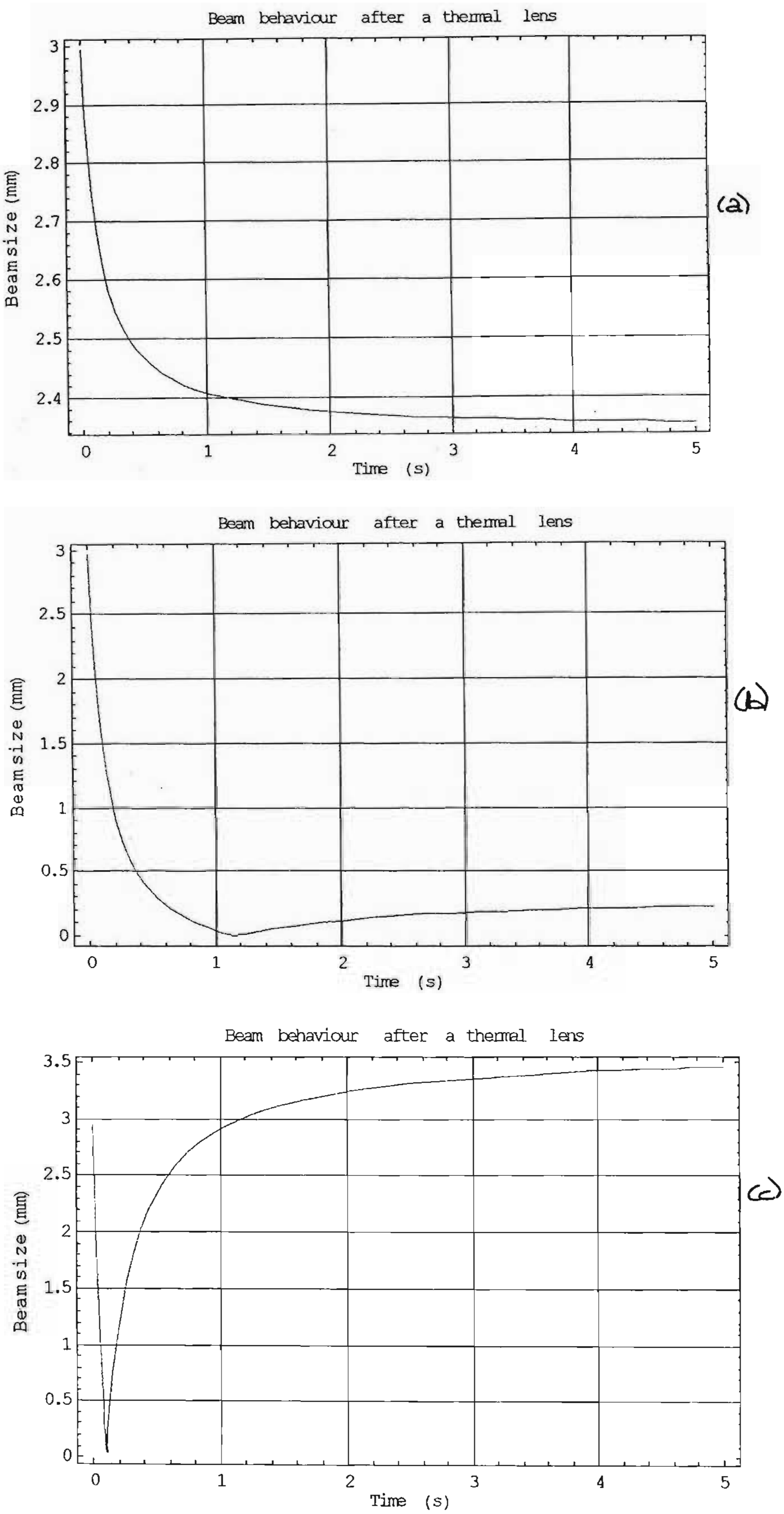

Figure 36: The beam size as a function of time for a intermediate lens: (a) shows the simulation near the window, (b) shows the behaviour at some intermediate distance, and (c) is the behaviour far from the window.

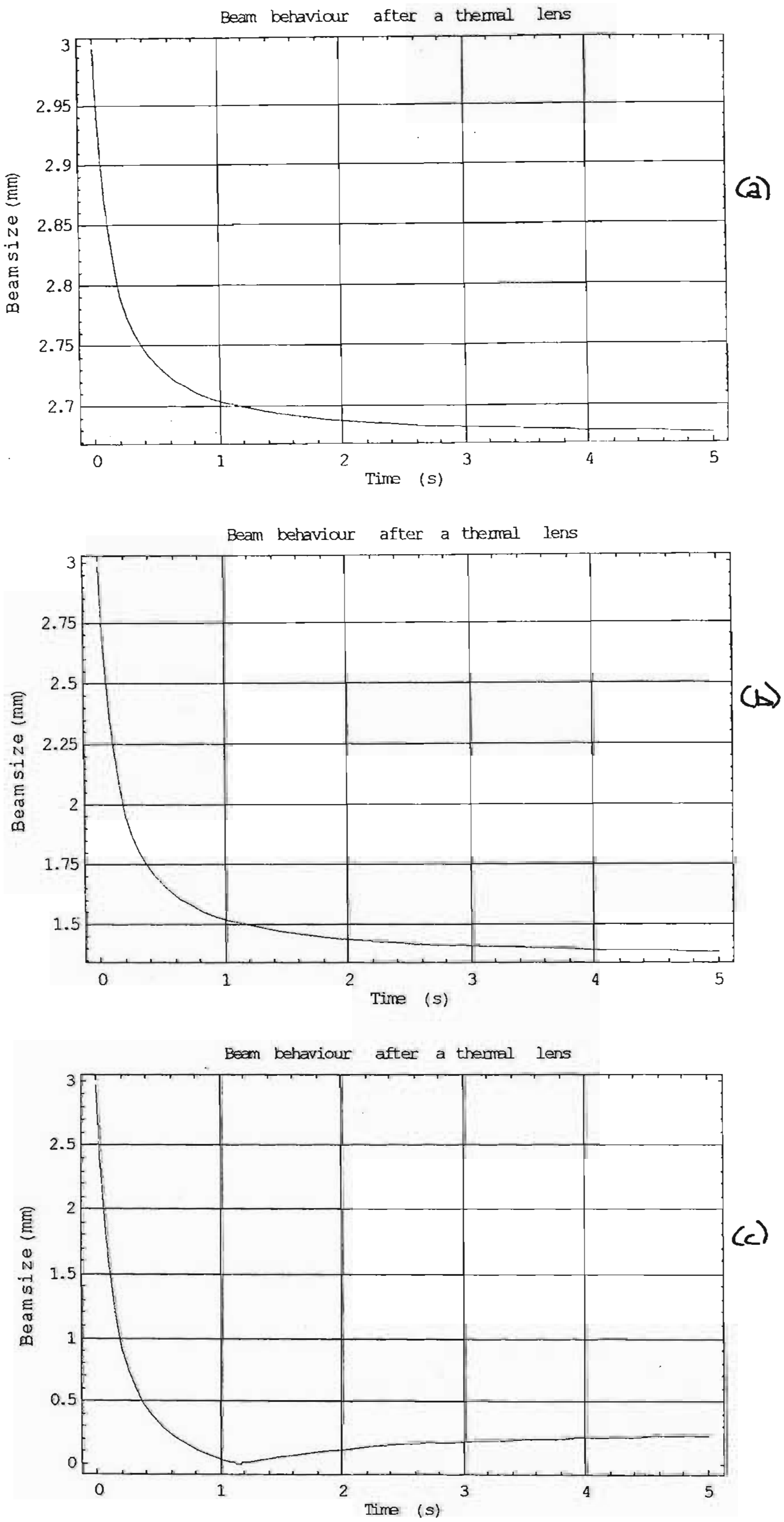

Figure 37: The beam size as a function of time for a weak lens: (a) shows the simulation near the window, (b) shows the behaviour at some intermediate distance, and (c) is the behaviour far from the window.

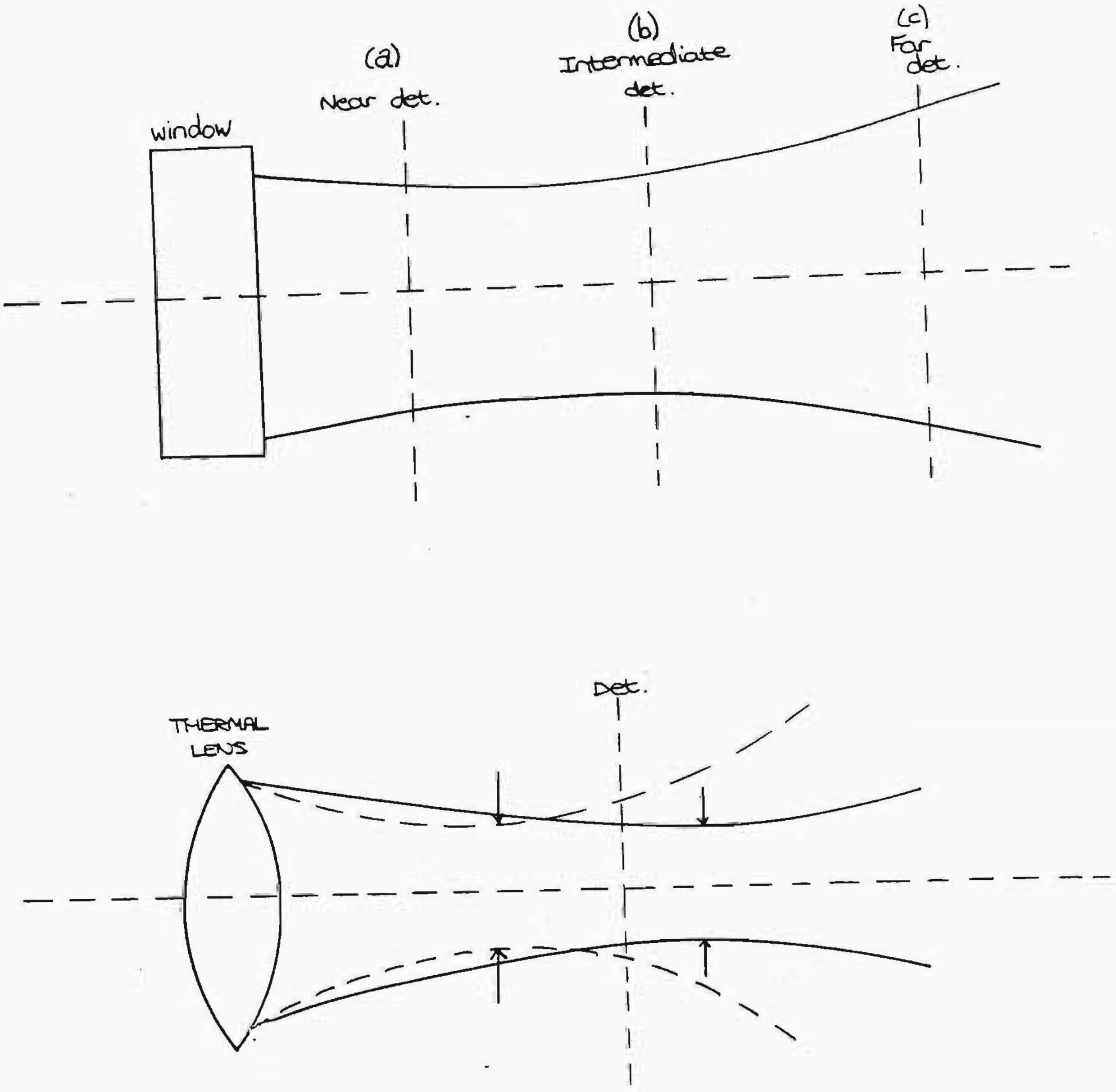

Figure 38: This schematic illustrates how some of the non-linear behaviours in Figures 35 - 37 can be explained. As the focus moves towards or away from the detector, so the measured spot size will change as a function of time.

picture the beam waist moving from right to left, from a long focal length to a short focal length, which would result in the graph of Figure 35 (a). If, for example, the detector is placed very close to the window, closer than the new waist position, then the detector will see a decreasing spot size until it stabilises after a few seconds. Similarly, if the detector is far from the window, beyond the initial focal length, then an increasing spot size with time will be seen (until stabilisation occurs) . All the other graphs can be explained by similar scenarios.

Finally, before the experimental results are discussed, the reader is refered to Figure 39. This was a test done to establish the correlation between the analytical model for the thermal lens, and a numerical model. The numerical model starts with a finite element analysis of the problem, which results in a temperature profile over the window. This is then used with the Fresnel diffraction integral to establish the resultant beam propagation after the window. By looking at the change in focal position after a known lens, the focal length of the thermal lens can be deduced. This procedure takes several hours to run, and needs to be repeated each time a variable is changed. For the correlation test, the focal length as a function of the pulse energy was investigated. The finite element analysis was done by W. Groenewald[4] and the propagation analysis by S.P. van Heerden[5]. The result of this test is shown graphically in Figure 39. Clearly there is very good agreement between the analytical model and the numerical calculations. At very strong thermal lensing, the deviation is in the order of 7%. For weak thermal lensing, the deviation is around 1%. The value of the analytical model is that it took only a few seconds to generate the focal length dependence on pulse energy (as a continuous function), while the numerical data only samples selected input parameters, and takes several hours to generate

---

[4] private communication

[5] see § 4.5.2

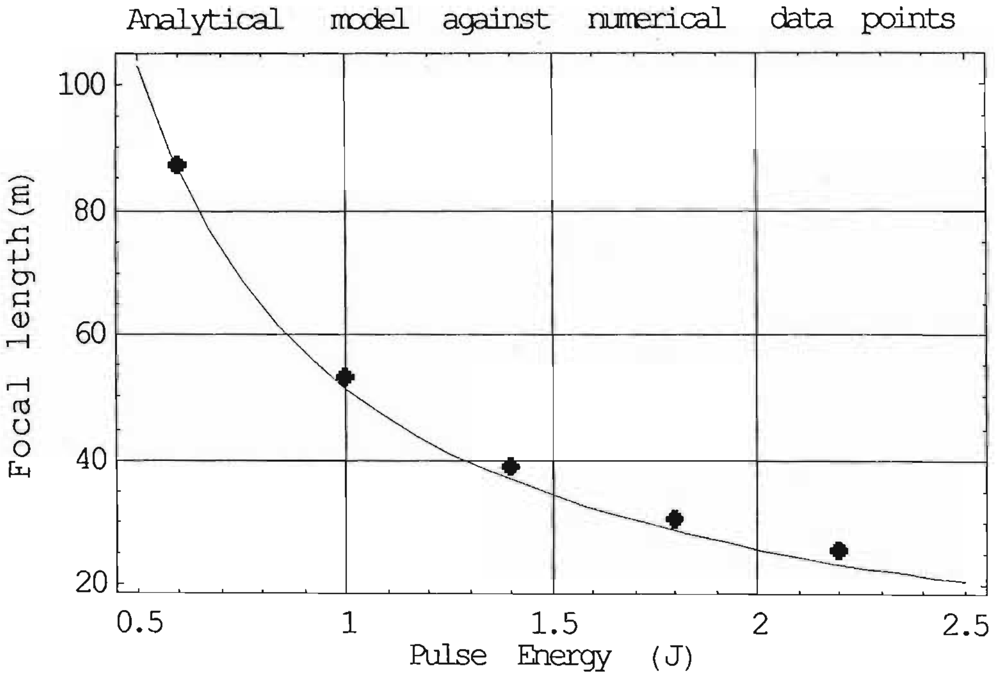

Figure 39: There is a very good correlation between the analytical model and a numerical model for predicting the focal length change in a thermal lens as a function of pulse energy.

only one point on the graph. This test goes some way in validating the analytical result.

3.4 Experimental Results

In this section, experimental results from the MLIS laser chain are presented. All the measurements were made with the *3-element detector*, a shot for shot beam size measuring device, developed by W Klopper[*Klopper*, 1995] for high repetition rate measurements.

One of the problems with experiments such as these, is the possibility that in sampling the beam, say with Holographic Beam Samplers, one destroys that which one seeks i.e. the sampler also introduces thermal lensing, which is an unknown quantity. The beauty of the 3-element detector is that it can accommodate very high fluences, thus allowing one a shot-to-shot monitoring device for the severe conditions under which pronounced thermal lensing is expected.

3.4.1 Laser damage effects

An important feature of Equation (3.12) is the dependence of the focal length on the absorption. As the absorption by the sample increases, so the focal length decreases, i.e. the window substrate acts as a stronger lens. This can have serious side effects for the mode matching in the laser chain. Figure 40 shows the lensing through the chain with three amplifiers in operation. The “no window” case refers to the lensing due to the previous optics in the chain, and is therefore taken as the reference. With this recorded, experiments were done with both a new window and damaged window in

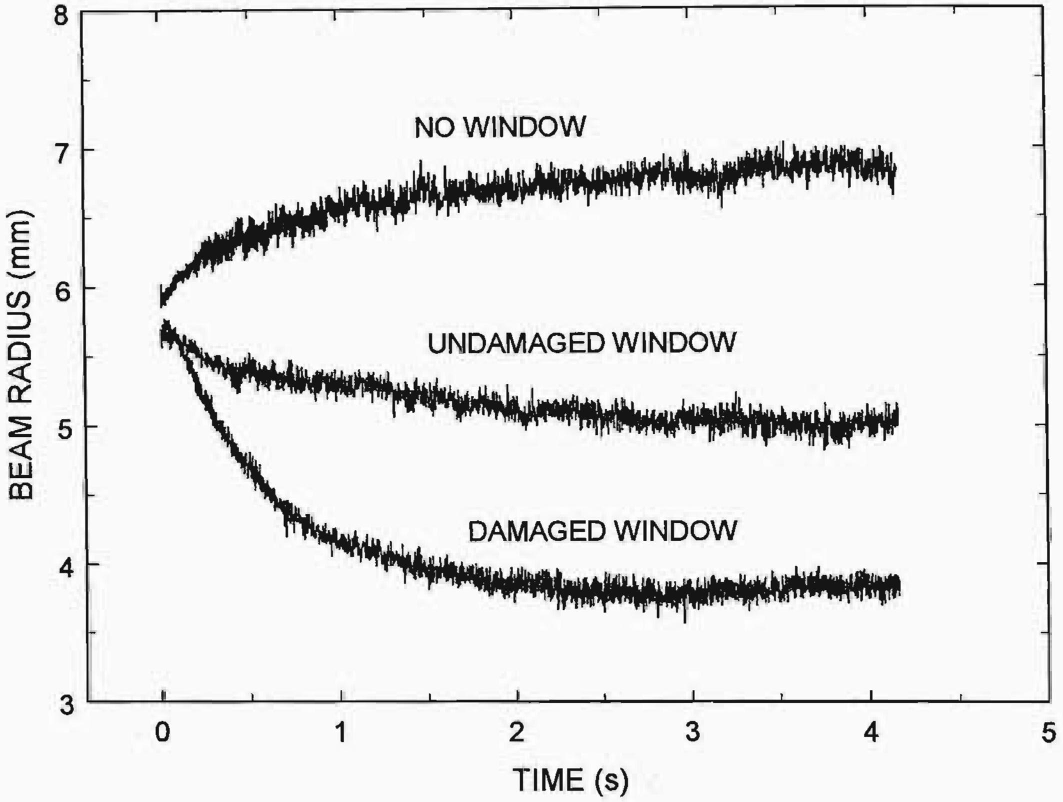

Figure 40: Compared to the reference measurement of no windows, we see that undamaged optics have a minor influence on the lensing when compared to the damaged optics.

place. It is clear that with the ideal ZnSe window in the final amplifier, some lensing is observed. However, with damaged ZnSe windows and the beam radius measured in the same position, the lensing is far stronger (when looking at the graphs, one should consider the absolute beam size change – the undamaged and "no window" changes are similar, whereas the damaged window change is larger) . This is not surprising given that the focal length is inversely proportional to the absorbance. The coefficient of absorption, α, is related to the optical quality of the window. Damaged optics have higher absorbance[*Scatena, Herrit*, 1990] which results in the thermal lensing being more pronounced for damaged or inferior quality optics.

3.4.2 Rotating window

As a means of reducing the induced temperature gradient (or average power density) the amplifier window was rotated with the beam passing off-axis through the window. This idea stems from a paper which suggests a relative movement between the beam and the optic in order to reduce thermal distortions [*Sparks*, 1971]. When an undamaged ZnSe window is rotated, the result is a decrease in the thermal lensing (see Figure 41 (a)). However, with the same technique applied to a damaged ZnSe window, we see very little improvement in the lensing, while the beam size and position became erratic (see Figure 41 (b)). These changes in the size are probably due to an asymmetric thermal gradient induced by the localised window damage. The wedge on the optic also had an influence on the pointing stability of the beam.

When a KCl window is rotated, a similar result to the damaged ZnSe window (periodic beam radius structure) was observed. Clearly an optic with a wedge will introduce a periodic structure on the position of the beam when rotated, and will have a serious effect on the pointing stability of the beam. It is apparent

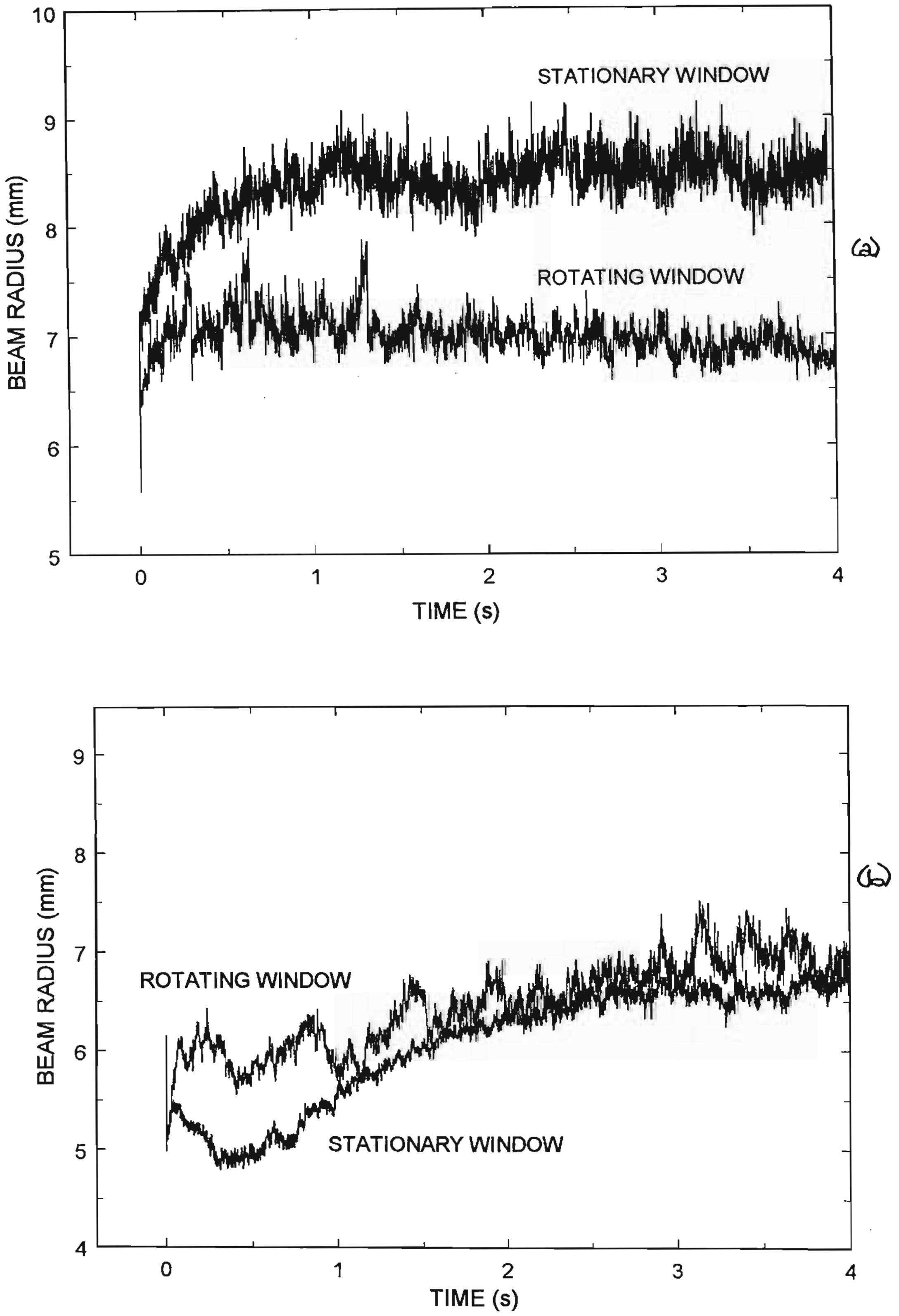

Figure 41: (a) Improvement in lensing due to the rotation of the final exit window of the laser chain, (b) No apparent improvement in the lensing behaviour for a damaged rotating window.

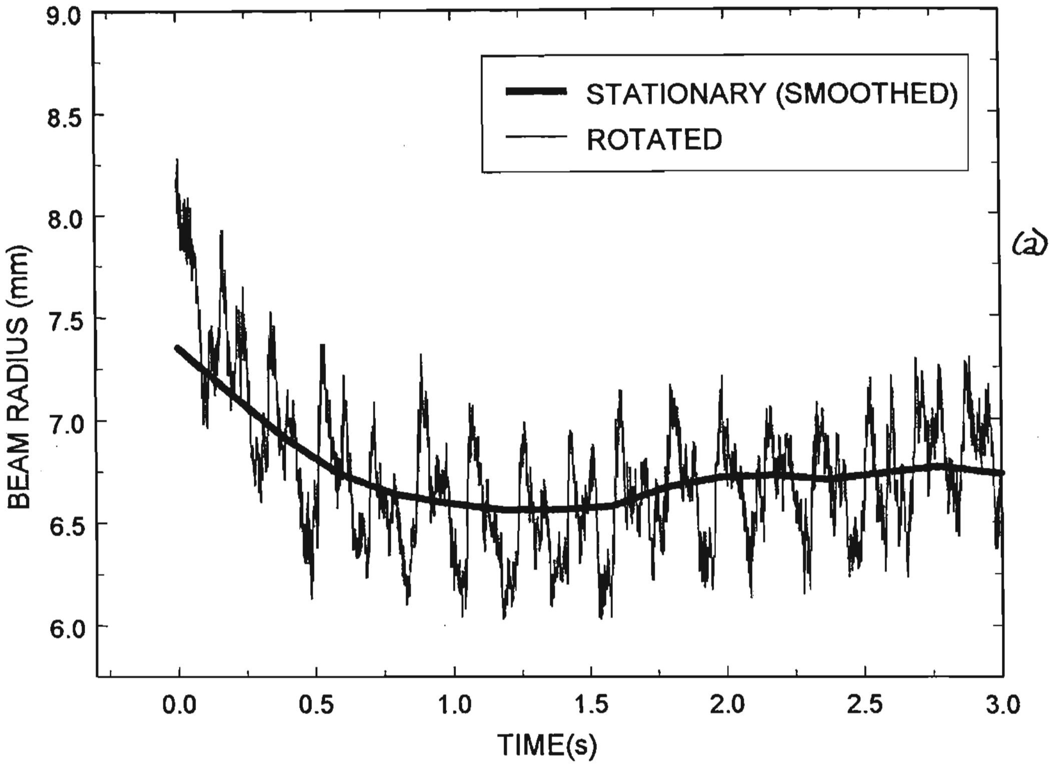

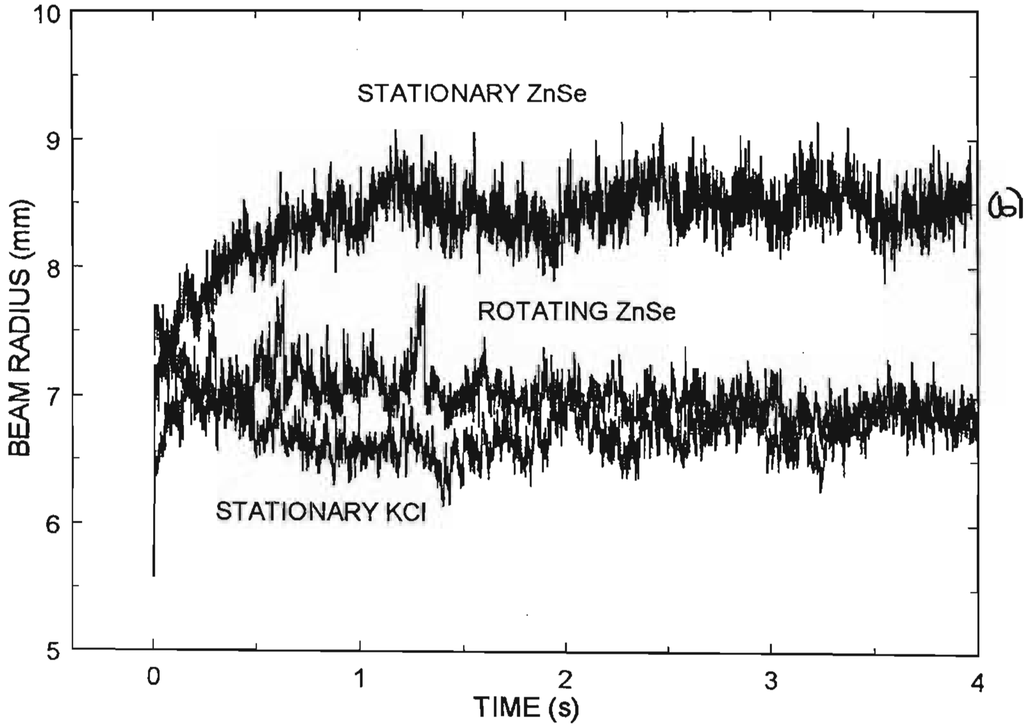

Figure 42: (a) Periodic beam radius structure due to the rotation of a KCl window, (b) Comparison of the lensing for ZnSe and KCl, with the ZnSe rotated and stationary.

Entity	**KCl**	**ZnSe**
α	0.002 cm^{-1}	0.003 cm^{-1}
G	-2.04 10^{-5} K^{-1}	7.1 10^{-5} K^{-1}
d (optic thickness)	5 mm	3 mm
κ	6.7 W/ m K	18 W/ m K
C_p	679 J / Kg K	356 J / Kg K
ρ	1.98 g / cm^3	5.27 g / cm^3
D	5 10^{-6} m^2 / s	9.6 10^{-6} m^2 / s
$\partial n / \partial T$	-3.5 10^{-5} K^{-1}	6.2 10^{-5} K^{-1}

Table 1: Some typical bulk material parameters for KCl and ZnSe optics.

that there is no advantage to be gained by rotating a KCl window for the beam conditions used here(see Figure 42). This could be due to a combination of low conductivity and a very long relaxation time (see Table 1 for some typical KCl and ZnSe parameters). The temperature rise in a KCl optic is higher than that of a ZnSe optic, and there is a larger temperature difference between the centre and the edge of the KCl optic, both due to the smaller thermal conductivity of KCl. Because of this, rotating the KCl window has little effect on the thermal lensing, but because of large wedge angles on KCl windows, the pointing stability of the beam is degraded.

3.4.3 Comparison of KCl and ZnSe optics

As mentioned above, the induced temperature gradient for KCl is much larger than that for ZnSe. This is a result of the thermal conductivity; ZnSe has a thermal conductivity that is three times higher than that of KCl. A low thermal conductivity results in an accelerated temperature rise on the surface of the optic. However, the lensing effect generated by the KCl optic is significantly less than that generated by the ZnSe optic (see Figure 42 (b)). These two statements seem to contradict one another.

The answer to this paradox lies in the mechanism for lensing. We note that KCl is an alkali halide, forming an ionic crystal structure, while ZnSe is a covalent, polycrystaline material. As a result of these structural differences, KCl has a **negative** $\partial n/\partial T$, which generates a *divergent* lens, while ZnSe has a positive $\partial n/\partial T$, which generates a *convergent* lens. Next, we note that the thermal expansion of KCl is 5 times higher than that of ZnSe. A thermal expansion will generate a convergent lens in these two materials. Thus if one only considered thermal expansion, KCl would also be the stronger lens, but this time convergent. The answer is now apparent: in the case of ZnSe, the thermal expansion effect simply enhances the effect of the refractive index variation. As a result of this, ZnSe shows strong thermal lensing. For KCl, however, the strong negative refractive index variation is balanced by the strong thermal expansion effect, resulting in a weak net thermal lens. Thus the degree of lensing in ZnSe optics is more pronounced than that generated in KCl optics.

Despite the thermal lensing advantages to be gained by using KCl, we nevertheless make extensive use of ZnSe. The reason is that KCl, being a salt, is very hygroscopic, and therefore very easily damaged. The results of damaged optics have already been shown.

3.4.4 Removal of windows

An obvious solution to thermal lensing through transmission optics is to simply not have any. Unfortunately, the transmission optics in question are amplifier windows, and therefore were important to the operation of the amplifiers. However, some solutions were investigated where the windows were removed. These solutions included:

- Placing the amplifiers in a tandem arrangement, as shown in Figure 43.
- Using aerodynamic windows at the end of the chain, where thermal lensing is at its worst.

Some experimental results have been compiled on the thermal lensing effect with aerodynamic window solutions applied. Without an aerodynamic window as the last amplifer window, we see a much stronger lensing effect, with the beam focusing down after a few metres. In fact, when operating the chain with all the amplifiers on at high repetition rate, we observe gas break–down in the air due to the focusing

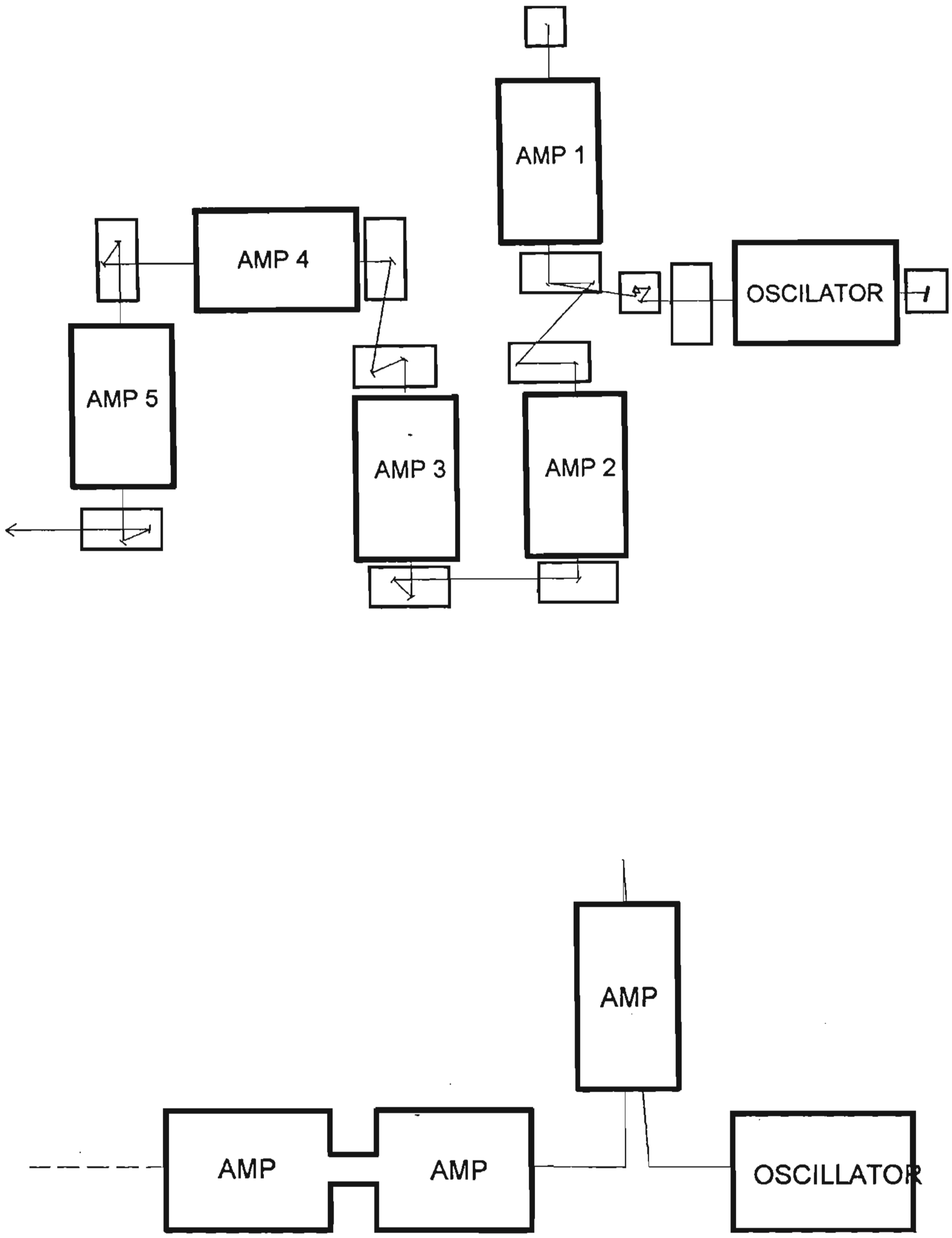

Figure 43: An illustration of the original chain layout, and the new tandem layout. The two amplifiers are joined by a pipe, thus allowing a reduction in the number of transmission optics.

effect from the last window. The rotating window and aerodynamic window both have a negative effect on the pointing stability; this is a serious disadvantage, since the beam propagates over very long distances, thus even a small centroid movement is amplified to extreme proportions.

3.5 Conclusion

The multiple pulse model is a very good analytical tool for making predictions about the beam propagation in the MLIS laser chain. It predicts all the trends observed experimentally. This theory does have its shortcomings: it only considers bulk absorption, whereas we know that the coatings on the windows must also play a role. It has also not been tested quantitatively because of the difficulty in accurately determining the absorption coefficient of the windows. This problem is compounded by the fact that this coefficient changes as the optic nears the end of its lifetime, which at $1kHz$ and a few Joules is rather short. Thus strictly speaking, the absorption coefficient is a function of time.

Analysis of the thermal lensing problem has allowed the implementation of some solutions not discussed here. Those which have been addressed seem to reduce the lensing effect, but perhaps at the expense of wavefront distortions. This will be considered in the next section.

4 Thermal Aberrations

4.1 Introduction

The previous chapter dealt with thermal lensing, considering only the change in focal length induced in the optic. This caused a curvature change in the wavefront of the beam after the element, either diverging or converging the beam. In this chapter we consider other effects on the wavefront. This is useful in determining whether a thermal lensing solution improves the lensing at the expense of other wavefront distortions.

The propagation parameter, or beam quality parameter (M^2) (see § 4.5.1) gives an indication of the quality of the beam. It is useful to think in terms of a higher M^2 indicating a poor or degraded beam. It does not, however, tell one what has degraded or what aberrations have been introduced. Thus in comparing two optical paths, say for example a rotating window as opposed to a stationary window, we do not have a quantitative way to describe the relative aberrations introduced by each.

The Zernike polynomials allow one to monitor the contributions of each aberration to the total wavefront. It is for this reason that an outline is given here of how to use these polynomials. The understanding of Zernike polynomials is also crucial for adaptive systems, since most commercial systems calculate the polynomial coefficients to determine the amount of adapting each actuator performs[*Alda,* *Boreman*, 1993],[*Neal et al*, 1996].

In the next section, some theory of Zernike polynomials is given, and three worked examples are used to illustrate their usefulness.

4.2 Zernike Polynomials and wavefront aberrations

4.2.1 Theory

The Zernike circle polynomials are a complete orthogonal set over the interior of the unit circle. Hence, an expansion of an arbitrary function $\Phi(r,\theta)$ where $r \in [0,1]$ and $\theta \in [0,2\pi]$, in an infinite series of these polynomials will be complete.

The circle polynomials of Zernike have the form of a complex angular function modulated by a real radial polynomial:

$$Z_n^m(r,\theta) = R_n^m(r)e^{im\theta}, \tag{4.1}$$

where $n \geq m$, $n \geq 0$ and $n - m =$ even.

It can be shown that the radial function also obeys an orthogonality relation, and is given by[*Murison*, 1995][*Born, Wolf*, 1975]:

$$R_n^m(r) = \sum_{k=0}^{\frac{n-m}{2}} \frac{(-1)^k (n-k)! r^{n-2k}}{k!(\frac{n+m}{2}-k)!(\frac{n-m}{2}-k)!}. \tag{4.2}$$

The radial function is normalised such that

$$R_n^m(1) = 1. \tag{4.3}$$

A list of the radial polynomials up to order 10 is given in Appendix C. The function R_n^m is set to zero when $n - m \neq$ even (by definition).

From Equation (4.1), we can write Z_n^m as

$$Z_n^m(r,\theta) = R_n^m(r)\cos(m\theta) + iR_n^m(r)\sin(m\theta), \tag{4.4}$$

thus we construct two real functions U_n^m, V_n^m such that

$$Z_n^m(r,\theta) = U_n^m(r,\theta) + iV_n^m(r,\theta). \tag{4.5}$$

It has been shown[*Murison*, 1995] that any function $\Phi(r,\theta)$ can be written in terms of U_n^m and V_n^m such that

$$\Phi(r,\theta) = \sum_{n=0}^{\infty}\sum_{m=0}^{n}[A_n^m U_n^m(r,\theta) + B_n^m V_n^m(r,\theta)], \tag{4.6}$$

where the coefficients A_n^m and B_n^m are given by:

$$A_n^m = K(m)\frac{n+1}{\pi}\int_0^{2\pi}\int_0^1 \Phi(r,\theta)U_n^m(r,\theta)r\,dr\,d\theta, \tag{4.7}$$

$$B_n^m = K(m)\frac{n+1}{\pi}\int_0^{2\pi}\int_0^1 \Phi(r,\theta)V_n^m(r,\theta)r\,dr\,d\theta, \tag{4.8}$$

and

$$K(m) = \begin{cases} 2, & m \neq 0 \\ 1, & m = 0. \end{cases} \tag{4.9}$$

A list of useful integrals is given in Appendix C. The properties of these integrals will help enormously in finding analytical solutions to the problem of expanding a known phase in terms of the above Zernike coefficients. A few words as to the terminology used in the rest of this chapter are in order. In this chapter, thermal aberrations are analysed by considering the change in phase of the beam, or relative phase, which is denoted by the symbols Φ or ϕ. This change in phase is then expanded as a series of Zernike polynomials. The terms of the expansion are the Zernike polynomials, Z_n^m, or U_n^m, *multiplied by* the coefficients (e.g. A_n^m) of the expansion, i.e., a full term would for example be $A_4^0 U_4^0$ and the coefficient would be A_4^0. The Zernike polynomial U_4^0 describes the kind of aberration, in this case spherical, and the coefficient by which it is multiplied, A_4^0, quantifies its contribution to the *whole* aberration. Thus a large value for the above coefficient would suggest that the primary aberration on the wavefront is spherical.

4.2.2 Aberrations

Before illustrating how to apply the above theory, it is important to understand why one would want to go to all that trouble i.e. what do you gain by expanding a function in terms of Zernike polynomials?

The earliest (1856 A.D.) full study of aberrations was completed by *Seidel*, and these are known as *primary*, or *Seidel aberrations*. His work accounts for aberrations such as spherical aberration, coma, astigmatism, defocus and tilt. A detailed study of this approach is given by *Born and Wolf*[*Born, Wolf*, 1975]. He showed that there are altogether five types of aberrations of the lowest order characterised by five coefficients B, C, D, E and F, corresponding to the aberrations of *Spherical, Astigmatism, Defocus, Tilt* and *Coma*. With a suitable choice of optical axis and co-ordinate system, these aberrations combine to describe the total aberration as:

$$\begin{aligned} \phi^{(4)} &= -\frac{1}{4}Br^4 - Cy_o^2 r^2 \cos^2\theta - \frac{1}{2}Dy_o^2 r^2 \\ &\quad + Ey_o^3 r \cos\theta + Fy_o r^3 \cos\theta\,, \end{aligned} \tag{4.10}$$

where the beam is assumed to be centred at the origin of the co-ordinate system, y_o is a constant and illustrated graphically in Figure 44. Here a cylindrical co-ordinate system is used, with r in Equation (4.10) being equivalent to the ρ in Figure 44, and representing radial distance from the z-axis.

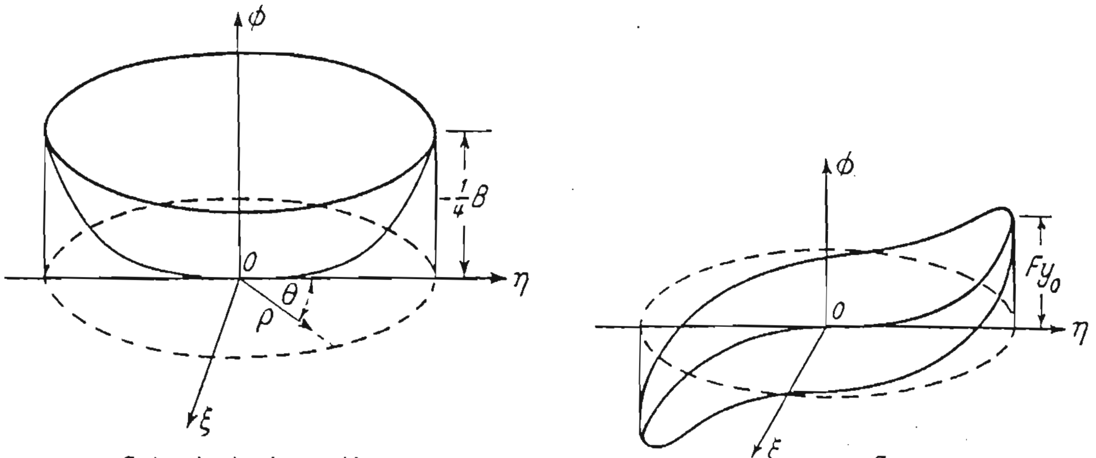

Spherical aberration

$\phi = -\frac{1}{4}B\rho^4$

(a)

Coma

$\phi = Fy_0\rho^3\cos\theta$

(b)

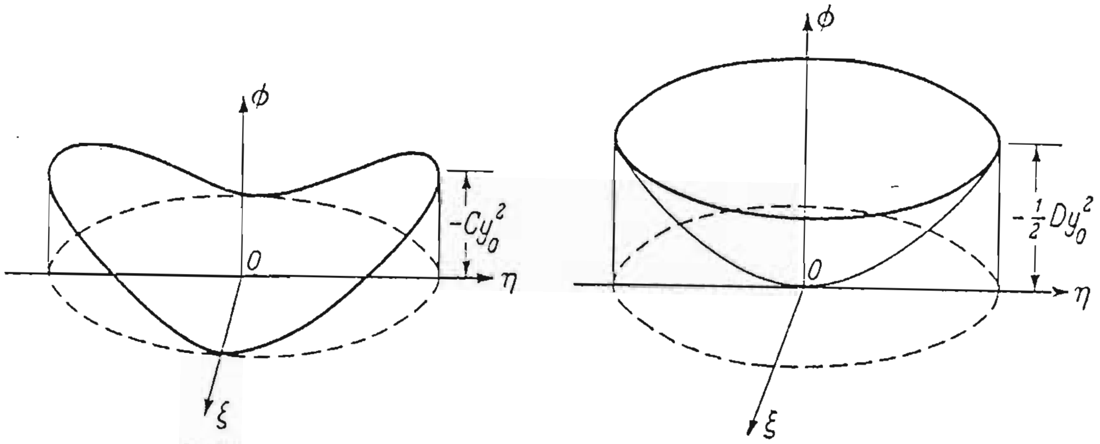

Astigmatism

$\phi = -Cy_0^2\rho^2\cos^2\theta$

(c)

Curvature of field

$\phi = -\frac{1}{2}Dy_0^2\rho^2$

(d)

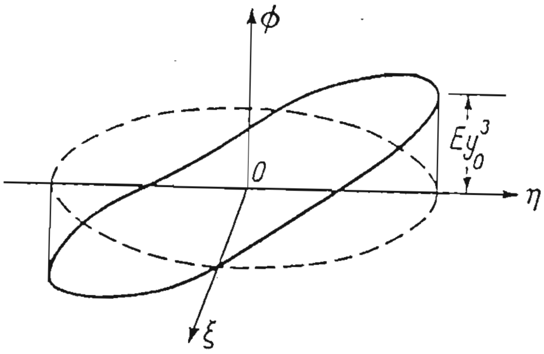

Distortion

$\phi = Ey_0^3\rho\cos\theta$

(e)

Figure 44: The primary wave aberrations(taken from *Born and Wolf*,page 212).

R^m_n	m = 0	m = 1	m =2	m=3	m=4	m=5
n=0	1 (disk-average)					
n=1		r (tilt)				
n=2	$2r^2 - 1$ (defocus)		r^2 (astigmatism)			
n=3		$3r^3 - 2r$ (coma)		r^3		
n=4	$6r^4 - 6r^2 + 1$ (spherical)		$4r^4 - 3r^2$ (astigmatism)		r^4	
n=5		$10r^5 - 12r^3 + 3r$ (coma)				r^5

Table 2: The low order Radial polynomials, $R_n^m(r)$, and their corresponding aberrations:

A schematic is given of each of the 5 primary aberrations (see Figure 44). There are many names for these aberrations; in this chapter the aberrations of "curvature of field" and "distortion" will be referred to as *defocus* and *tilt* respectively, in keeping with modern treatments. The limitation of the *Seidel* theory is that it is based on ray approximations, i.e., it calculates the aberrations by tracing rays onto some reference plane and mapping overlapping rays. Later, other theories [*Born, Wolf*,1975] reworked the understanding of aberrations by approaching the problem from the theory of diffraction. The Zernike polynomials proved an ideal tools in this approach.

The Zernike polynomials have been found to completely describe aberrations, but are not identical to the *Seidel* description. A glance at Table 2 confirms this. In fact, we note that each Zernike aberration is made up of one or more classical (or primary) aberrations. The link between the *Seidel* aberrations and the Zernike aberrations is described by *Mahajan*[*Mahajan*,1994a],[*Mahajan*,1995b]:

> A Zernike polynomial represents an optimally balanced aberration in which the terms of the highest degree (or order) in pupil coordinates is balanced with aberrations of lower degree to minimise its variance across the pupil. Accordingly, a Zernike polynomial aberration may also be referred to as a balanced aberration.

For example, the Zernike primary coma consists of the *Seidel* primary coma balanced with *Seidel* tilt, and may therefore be called balanced coma.

This balancing of the *Seidel* aberrations requires that there must exist a link between the Zernike aberration coefficients and the *Seidel* aberration coefficients. To illustrate this point, we consider the *Seidel* aberration of coma:

$$\phi(r,\theta) = F y_o r^3 \cos\theta. \tag{4.11}$$

If we write the radial polynomials as:

$$R_n^m(r) = a_n^m r^n + b_n^m r^{n-2} + \ldots, \tag{4.12}$$

then the *Seidel* coma can be expanded in terms of the Zernike polynomials according to [*Mahajan*,1995]:

$$\phi(r,\theta) = \sqrt{8} A_3^1 R_3^1 \cos\theta + 2A_1^1 R_1^1 \cos\theta, \tag{4.13}$$

where

$$A_3^1 = \frac{F y_o}{\sqrt{8} a_3^1}, \tag{4.14}$$

and

$$A_1^1 = -\frac{\sqrt{2} A_3^1 b_3^1}{a_1^1}. \tag{4.15}$$

From Table 2 we find the coefficients of the radial polynomials to be: $a_3^1 = 3$, $b_3^1 = -2$ and $a_1^1 = 1$. To check that this expansion of the Zernike aberrations coma and tilt does indeed produce the primary (*Seidel*) aberration of coma, we first substitute the above coefficients into Equations (4.14) and (4.15), to find the following link between the Zernike polynomial coefficients, and the *Seidel* coma aberration coefficient:

$$A_3^1 = \frac{F y_o}{3\sqrt{8}}; \tag{4.16}$$

and

$$A_1^1 = \frac{F y_o}{3}. \tag{4.17}$$

To complete the check on this expansion, we substitute the above results into Equation (4.13):

$$\begin{aligned}\phi(r,\theta) &= \sqrt{8}A_3^1R_3^1\cos\theta + 2A_1^1R_1^1\cos\theta \\ &= Fy_o\frac{R_3^1}{3}\cos\theta + \frac{2}{3}Fy_oR_1^1\cos\theta \\ &= Fy_o(r^3 - \frac{2}{3}r)\cos\theta + Fy_o\frac{2}{3}r\cos\theta \\ &= Fy_or^3\cos\theta,\end{aligned}$$

which is again the *Seidel* description of primary coma.

A series of notes by *Mahajan* (see References) exist which outline the various properties and advantages to using the Zernike polynomials. The reader is referred to these for a more detailed discussion of Zernike polynomials.

The Zernike coefficients, allow a quantitative measure of the contribution of a given aberration. A higher value of A_3^1 implies that *coma* is the main aberration in the wavefront. Thus the Zernike method results in an aberration barometer of sorts, allowing the user to keep tabs of the various contributions.

As an example, Figure 45 shows the Zernike description of coma and tilt. In this figure, the relative phase is plotted in Cartesian co-ordinates, with the usual transformation rules applying when converting from polar co-ordinates.

4.2.3 Worked examples

- **Constant Phase**

This could be the phase at the waist plane of a focussed Gaussian beam, or the phase of a plane wave passing through a window without any distortions.

The phase after passing through an aberration free window of length l,

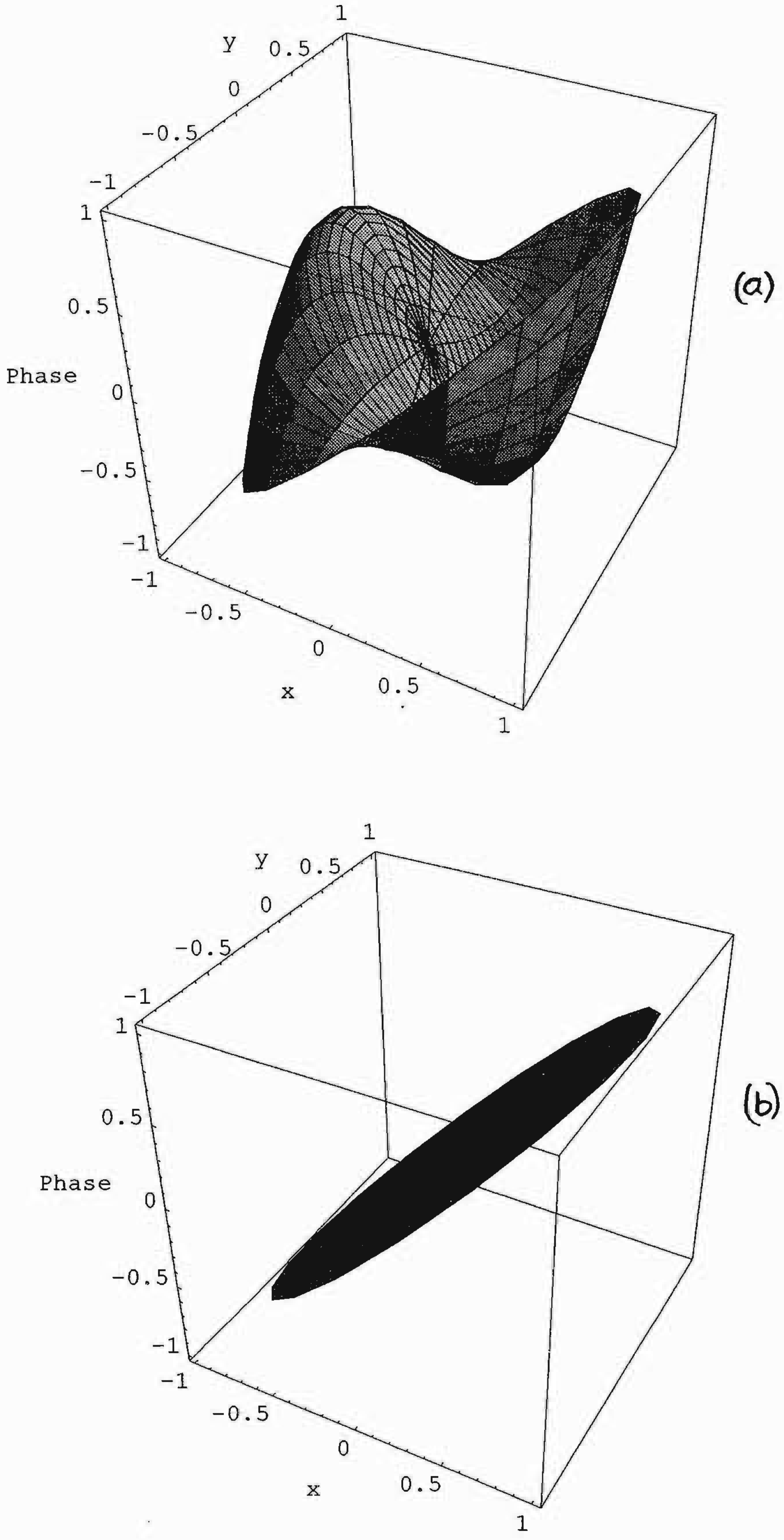

Figure 45: (a) Coma, as described by the U_3^1 term.(b) Tilt, as given by the U_1^1 term.

refractive index n_o and wavenumber k is given by:

$$\Phi(r,\theta) = kn_o l = \Phi_o, \tag{4.18}$$

where Φ_o is a constant. We now expand this phase function in terms of Zernike polynomials to identify sources of aberration. To calculate the Zernike coefficients, we have to solve the following two integrals for all values of n and m:

$$\begin{aligned} A_n^m &= K(m)\frac{n+1}{\pi}\int_0^{2\pi}\int_0^1 \Phi_o R_n^m \cos(m\theta) r\,dr\,d\theta & (4.19) \\ B_n^m &= K(m)\frac{n+1}{\pi}\int_0^{2\pi}\int_0^1 \Phi_o R_n^m \sin(m\theta) r\,dr\,d\theta. & (4.20) \end{aligned}$$

From the properties of the integrals in Appendix C, we note that $B_n^m = 0 \;\forall\; n, m$ and $A_n^m = 0 \;\forall\; m \neq 0$. To find the A_0^0 coefficient we have (using Equation (4.2))

$$\begin{aligned} A_0^0 &= K(0)\frac{1}{\pi}\int_0^{2\pi}\int_0^1 \Phi_o R_0^0 r\,dr\,d\theta \\ &= 1.\,\frac{1}{\pi}.\,\Phi_o.\,2\pi.\frac{r^2}{2}\bigg|_0^1 \\ &= \Phi_o. & (4.21) \end{aligned}$$

It turns out that all other terms (A_n^0, $n > 0$) are zero. For example, the calculation of the A_2^0 coefficient goes as follows:

$$\begin{aligned} A_2^0 &= K(0)\frac{1}{\pi}\int_0^{2\pi}\int_0^1 \Phi_o R_2^0 r\,dr\,d\theta \\ &= 1.\,\frac{1}{\pi}.\,\Phi_o.2\pi.(\frac{r^4}{2}-\frac{r^2}{2})\bigg|_0^1 \\ &= 0. \end{aligned}$$

Continuing like this, one can show that all other higher order terms are zero. Thus our wavefront, or phase, is completely described by only one Zernike coefficient, the A_0^0 term.

To test that this expansion really does completely decribe the wavefront, we return to Equation (4.6), which, with the above substitutions, and the definition of U_n^m given by Equation (4.5), gives:

$$\begin{aligned}\Phi(r,\theta) &= A_0^0 U_0^0 \\ &= A_0^0 R_0^0 \cos(0\theta) \\ &= A_0^0 \\ &= \Phi_o,\end{aligned}$$

which is what we started with! Thus the Zernike polynomial expansion is complete. The wavefront is made up only of the term related to *disk average/piston.*

- **Symmetric phase**

In this example we consider a phase profile of

$$\Phi(r,\theta) = kln_o(1-r^2)\ , \tag{4.22}$$

which could result, for example, from a plane wave passing through a graded index medium (see Figure 46). We again employ the expansion of Equation (4.6)for the phase given by Equation (4.22), and solve for the expansion coefficients A_n^m and B_n^m using Equations (4.7) and (4.8). Because there is no dependence on θ, we note that $B_n^m = 0\ \forall\ n,m$ and $A_n^m = 0\ \forall\ m \neq 0$. We evaluate the remaining terms:

$$\begin{aligned}A_0^0 &= 1.\frac{1}{\pi}.\, kln_o.\, 2\pi.\ \int_0^1 (1-r^2)r\, dr \\ &= \frac{1}{2}kln_o\,;\end{aligned}$$

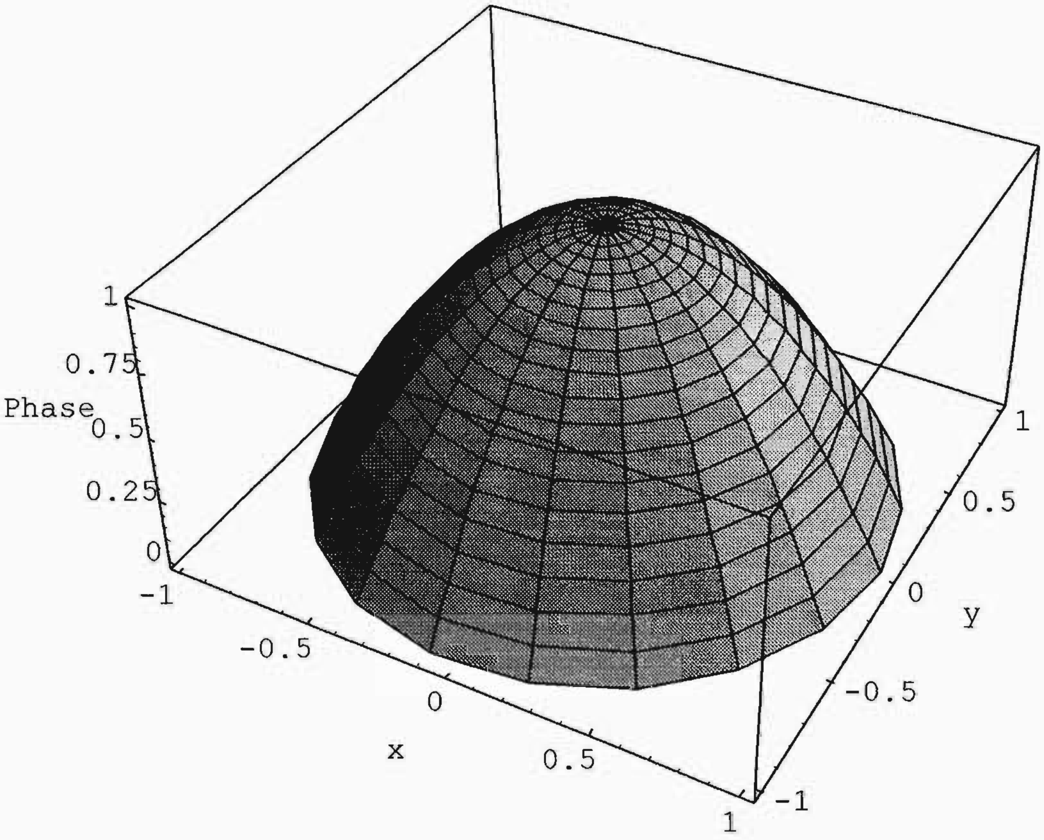

Figure 46: The symmetric phase profile, $\Phi(r, \theta)$, given by Equation (4.22).

$$\begin{aligned} A_2^0 &= 1.\frac{3}{\pi}.\, kln_o.\, 2\pi.\, \int_0^1 (1-r^2)(2r^2-1)r\,dr \\ &= -\frac{1}{2}kln_o\,. \end{aligned}$$

One can go on to show that $A_4^0 = A_6^0 = 0$. It fact it seems to be a rule of thumb that once a lower order term falls to zero, all similar (odd/even values of n) higher terms also fall to zero.

To check the completeness of the expansion, we have

$$\begin{aligned} \Phi(r,\theta) &= A_0^0U_0^0 + A_2^0U_2^0 \\ &= \frac{1}{2}kln_oR_0^0 + (-\frac{1}{2}kln_o)R_2^0 \\ &= \frac{1}{2}kln_o + (-\frac{1}{2}kln_o)(2r^2-1) \\ &= \frac{1}{2}kln_o + \frac{1}{2}kln_o - kln_or^2 \\ &= kln_o(1-r^2)\,, \end{aligned}$$

and our expansion is complete. The two coefficients this time are related to *disk average* and *defocus*(see Figure 47).

- **Asymmetric phase**

As an example of an asymmetric phase profile, we consider the following:

$$\Phi(r,\theta) = kln_o(1-r^3\cos\theta)\,, \tag{4.23}$$

which has been chosen rather arbitrarily. It was derived by taking a symmetric function and weighting it in one dimension (see Figure 48):

$$1-(x^2+y^2)x$$

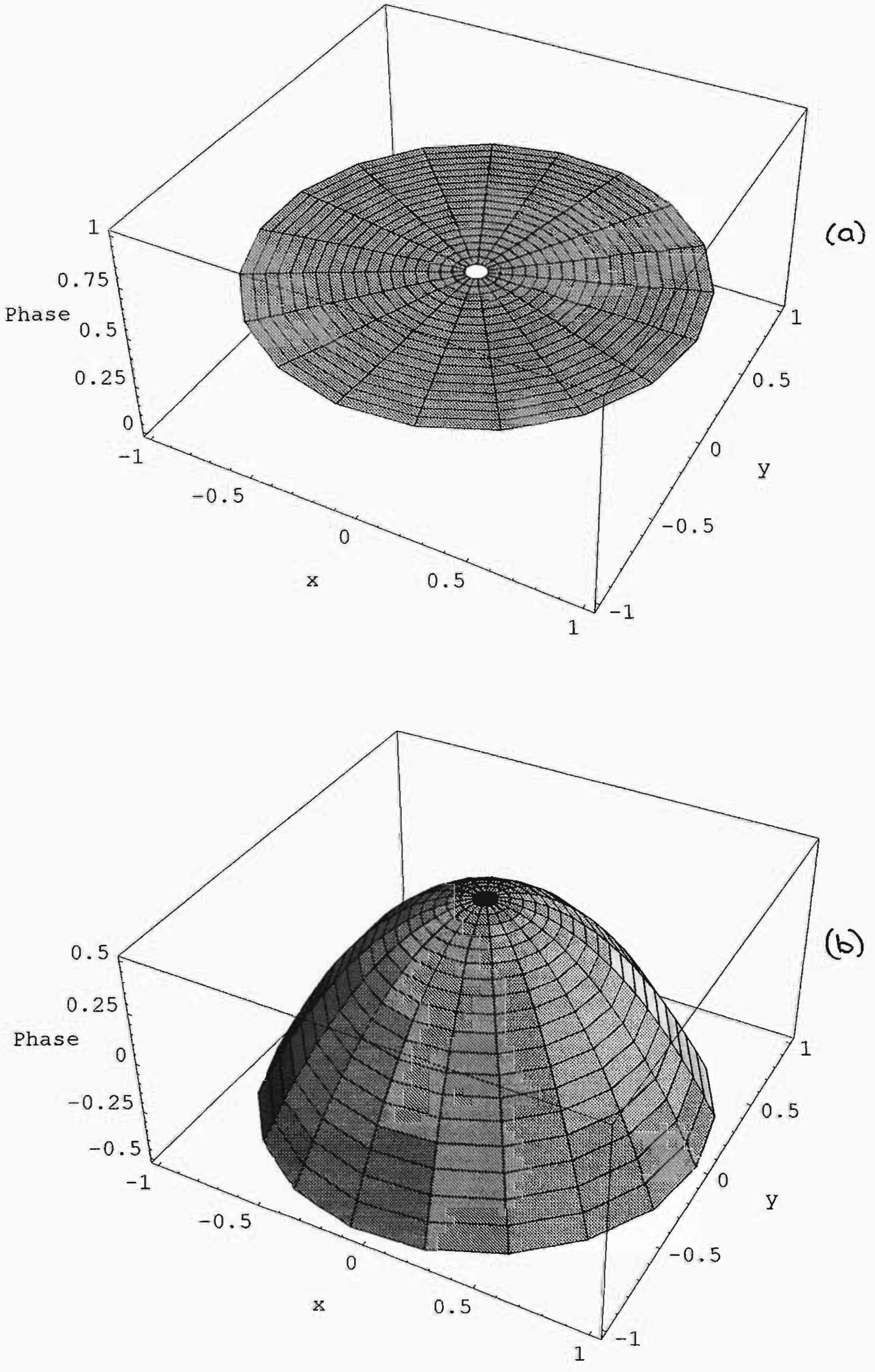

Figure 47: The original wavefront is decomposed into (a) disk-average and the aberration of (b) defocus.

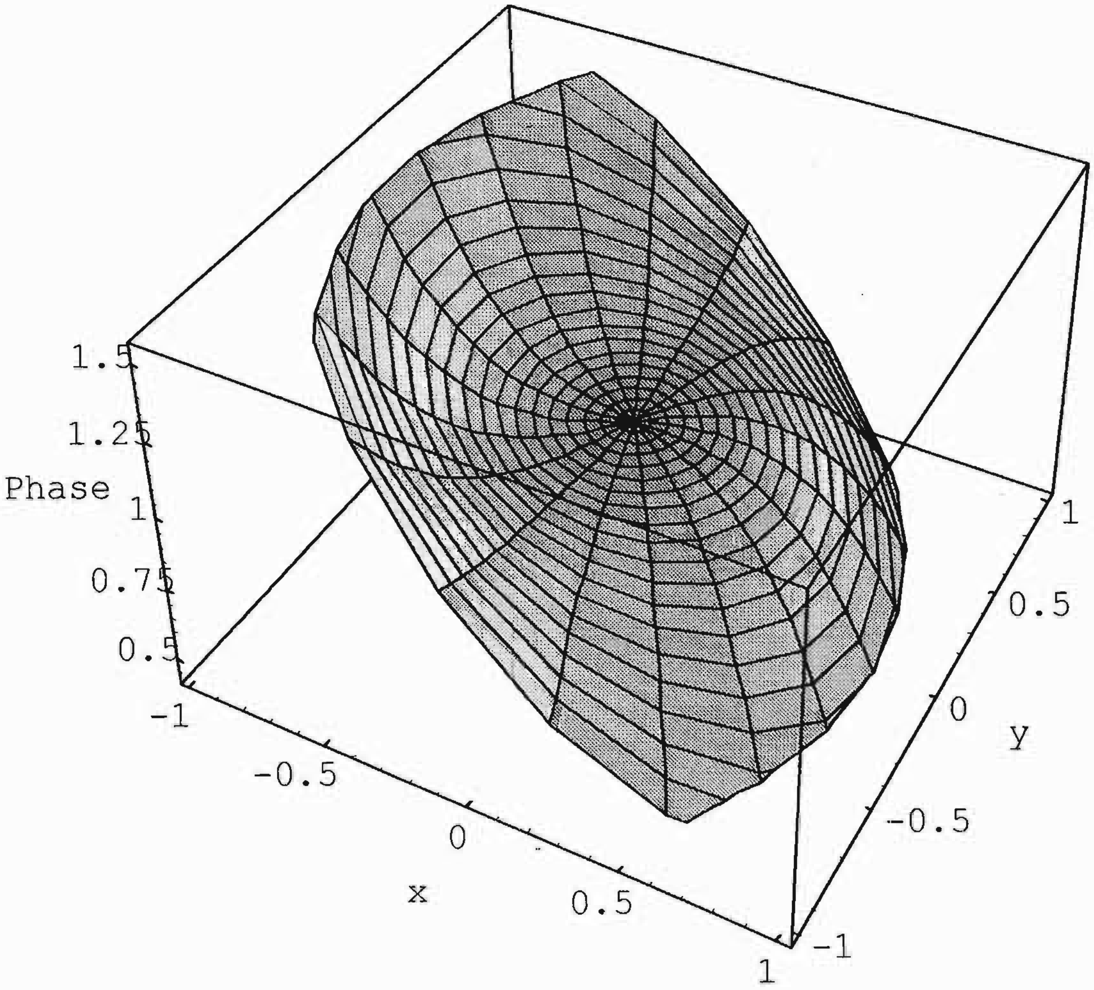

Figure 48: The asymmetric phase profile, as given by Equation (4.23).

$$\begin{aligned} &= 1 - r^2 . r \cos\theta \\ &= 1 - r^3 \cos\theta\ . \end{aligned}$$

Again we find that $B_n^m = 0$, $\forall n, m$, and so go about calculating the A_n^m coefficients:

$$\begin{aligned} A_0^0 &= \frac{1}{\pi} \int_0^{2\pi} \int_0^1 (1 - r^3 \cos\theta) r\, dr\, d\theta \\ &= 2\pi . \frac{1}{\pi} . \, kln_o . \left. \frac{r^2}{2} \right|_0^1 \\ &= kln_o; \end{aligned}$$

and $A_2^0 = A_4^0 = A_6^0 = 0$.

We also have the coefficients:

$$\begin{aligned} A_1^1 &= 2 . \frac{2}{\pi} \int_0^{2\pi} \int_0^1 (1 - r^3 \cos\theta) r^2 \cos\theta\, dr\, d\theta \\ &= 2 . \frac{2}{\pi} . \, kln_o \left. (-\frac{r^6}{6}) \right|_0^1 \\ &= -\frac{2}{3} kln_o\,; \end{aligned}$$

$$\begin{aligned} A_3^1 &= 2 . \frac{4}{\pi} \int_0^{2\pi} \int_0^1 (1 - r^3 \cos\theta)(3r^3 - 2r) r \cos\theta\, dr\, d\theta \\ &= \frac{8}{\pi} kln_o \int_0^{2\pi} \int_0^1 3r^4 \cos\theta - 2r^2 \cos\theta - 3r^7 \cos^2\theta + 2r^5 \cos^2\theta\, dr\, d\theta \\ &= \frac{8}{\pi} kln_o \pi \int_0^1 2r^5 - 3r^7\, dr \\ &= 8kln_o \left. (\frac{r^6}{3} - \frac{3r^8}{8}) \right|_0^1 \\ &= -\frac{1}{3} kln_o\,. \end{aligned}$$

All other terms are again zero. To test the completeness, we carry out the summation of Equation (4.6):

$$\begin{aligned}
\Phi(r,\theta) &= A_0^0U_0^0 + A_1^1U_1^1 + A_3^1U_3^1 \\
&= A_0^0R_0^0 + A_1^1R_1^1\cos\theta + A_3^1R_3^1\cos\theta \\
&= kln_o - \frac{2}{3}kln_or\cos\theta - \frac{1}{3}kln_o(3r^3 - 2r)\cos\theta \\
&= kln_o - \frac{2}{3}kln_or\cos\theta + \frac{2}{3}kln_or\cos\theta - kln_or^3\cos\theta \\
&= kln_o(1 - r^3\cos\theta)\,.
\end{aligned}$$

Thus the wavefront can be expressed as the sum of three Zernike terms, with the coefficients A_0^0, A_1^1 and A_3^1 representing the relative importance of *disk average*, *tilt* and *coma* respectively. The magnitude of the coefficients tells one how much each aberration contributes to the total aberration.

To see the contribution of each aberration, we plot the phase minus other aberrations. Figure 49 (a) shows the wavefront without the contribution from coma ($\Phi - A_3^1U_3^1$), and so the remaining aberration is tilt, with disk-average. The tilt is clearly visible now. Similarly, Figure 49 (b) is the wavefront minus tilt ($\Phi - A_1^1U_1^1$), and so only coma and disk-average remain.

4.2.4 Discussion

Three examples have been used to illustrate the usefulness of this approach.

A few suggestions follow which might help in applying this technique to a given problem:

- Remember that the Zernike polynomials hold over the unit circle. Thus if you want to describe some arbitrary size circle, use dimensionless variables eg.

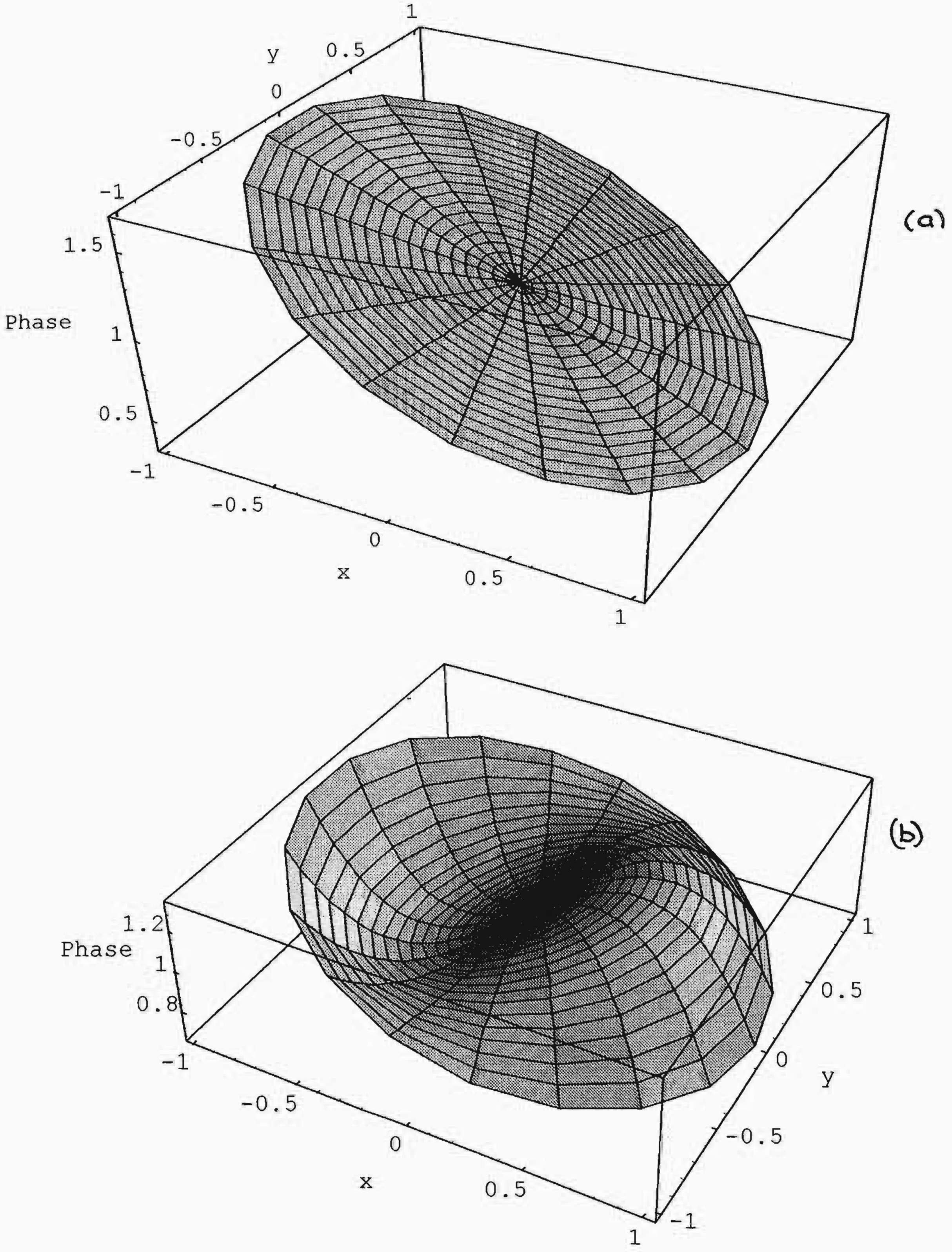

Figure 49: (a) The contribution without coma,i.e. mostly tilt, and (b) the contribution without tilt, i.e. mostly coma. Both (a) and (b) still have disk average/piston.

$x = x'/D$ and $y = y'/D$ where D is the actual radius of the circular aperture under analysis, and x' and y' are unnormalised laboratory spatial coordinates.

- If the shape of the system is not circularly symmetric, you should adapt your system to the unit circle. There are many techniques to do this, but I prefer the method of *conformal mapping.*
- If you are solving for the coefficients numerically, the methods of *least-squares* and the so-called *Gram-Schmidt* method have been found to be numerically stable and give almost identical results[*Wang, Silva*, 1980]. I point this out because it has been previously thought that the method of least-squares is not stable when used with a finite number of sample points.

4.3 Thermal lensing aberrations

4.3.1 Introduction

Much work has been done to analyse the thermal lensing problem, and this has resulted in both numerical and analytical expressions for the induced focal length in a transmission optic [*van Heerden et al*, 1996], [*Forbes*, 1996],[*Groenewald*, 1996]. The previous chapter dealt with thermal lensing in great depth.

Some of the solutions adopted to resolve this problem include the tandem amplifier arrangement and the rotating window. These solutions are based on the belief that such solutions reduce the optical distortion, as caused by thermal effects [*Sparks*,1971]. **There is no support for this view.** It is clear from beam spot size measurements that a tandem arrangement or rotating window will reduce the lensing effect, but such measurements do not indicate the effect the solution has on the quality of the beam. The beam propagation will depend on the aberrations introduced to the wavefront, and the effect of a lens, which amounts to a **defocusing** effect, is merely one such aberration.

This section considers thermally induced optical aberrations, and makes a comparison between the magnitude of the aberration or distortion from a thermal lens, and the wavefront distortions induced by thermal lensing solutions. This should enable one to quantitatively and objectively compare the effect the solutions have on the wavefront of the beam. It will be shown later how the wavefront distortions determine the beam quality and hence the beam propagation.

To determine any distortion introduced, one only has to consider the change in all the aberration coefficients. No new aberrations will be introduced by the free space propagation since it is assumed that we are in the far field (i.e., dealing with a plane wave), and free space propagation only increases the *disk average* coefficient. Thus, in this study, an initial uniform phase distribution is considered, which is then propagated through the medium under study. The resulting phase change, or wavefront change, is then analysed.

4.3.2 Aberrations

When a pulsed beam passes through a transmission optic (for example a window), some of the pulse energy is reflected, most transmitted, and a little is absorbed. This small, but significant absorption results in the window acting as a thermal lens. The temperature distribution as a result of m pulses is given by (see § 3.3):

$$\Delta T(r,\theta) = \sum_{q=0}^{m} \frac{\alpha E_o}{\pi \rho C_p a^2} \frac{e^{\frac{-2r^2}{a^2 \varepsilon(t)}}}{\varepsilon(t)}, \tag{4.24}$$

where

$$\varepsilon(t) = 1 + \frac{2q\tau}{t_c},$$

is a new parameter used to simpify the calculations. Recall from the previous chapter that τ refers to the time between pulses, and q is the number of pulses, thus the product of the two in the above equation represents the elapsed time (eg., 100 pulses for a 10 Hz represents an elapsed time of 10 s). Hence the new parameter ε is a function of time.

To calculate the phase change through a medium described by Equation (4.24), we note that:

$$\phi(r,\theta) = k\, n(r,\theta)\, l,$$

and

$$n(r,\theta) = n_o + \frac{\partial n}{\partial T} \Delta T.$$

This then implies that the phase change when passing through the thermal lens is given by:

$$\phi(r,\theta,t) = \phi_o + \phi_c \sum_{q=0}^{m} \frac{e^{\frac{-2\beta^2 r^2}{\varepsilon(t)}}}{\varepsilon(t)}, \tag{4.25}$$

with

$$\phi_o = k l n_o,$$

and

$$\phi_c = kl\frac{\partial n}{\partial T}\frac{\alpha E_o}{\pi\rho C_p a^2}.$$

Note that in order to satisfy the orthogonality relation, which only holds inside the unit circle $[0,1]$, the dimensions of the beam have been scaled with a scaling factor β, such that $[0,\beta a] \longmapsto [0,1]$; a radius encompassing βa with $\beta \in [1,2]$ can be thought of as the whole beam, since more than 90 % of the energy is enclosed in this area.

By substituting Equation (4.25)into Equations (4.7) and (4.8), one can determine the Zernike expansion coefficients which describe the phase change in the beam after passing through the thermal lens. Note that because the phase change is time dependent, we expect the aberrations to act accordingly. Furthermore, since it is known that the thermal lens does eventually stabilise, one also expects the aberrations to reach some stable value.

In solving the two integrals given in equations (4.7) and (4.8), it is useful to use the relations given in Appendix C. From these integral relations, we see that since the phase function is symmetric, all the terms given by B_n^m are identically zero. Similarly, all terms A_n^m will be zero $\forall m \neq 0$. With these observations, and after much manipulation, the following low order terms become:

$$A_0^0(t) = \phi_o + \frac{\phi_c}{2\beta^2}\sum_{q=0}^{m}\left[1 - e^{\frac{-2\beta^2}{\epsilon(t)}}\right]; \tag{4.26}$$

$$A_2^0(t) = 3\phi_o - 3A_0^0(t) - \frac{6\phi_c}{2\beta^2}\sum_{q=0}^{m}\left[e^{\frac{-2\beta^2}{\epsilon(t)}} + \frac{\varepsilon(t)}{(2\beta^2)}e^{\frac{-2\beta^2}{\epsilon(t)}} - \frac{\varepsilon(t)}{(2\beta^2)}\right]; \tag{4.27}$$

$$\begin{aligned} A_4^0(t) &= -10A_0^0 - 5A_2^0 + 10\phi_o + \\ & \frac{-60\phi_c}{2\beta^2} \sum_{q=0}^{m} \left[e^{\frac{-2\beta^2}{\varepsilon(t)}} \left(\frac{1}{2} + \frac{\varepsilon(t)}{2\beta^2} + \left(\frac{\varepsilon(t)}{2\beta^2} \right)^2 \right) - \left(\frac{\varepsilon(t)}{2\beta^2} \right)^2 \right] . \end{aligned} \tag{4.28}$$

The phase change is therefore comprised of a *Piston* or *Disk Average* term, a *Defocus* term and *Spherical* aberration. The defocus, A_2^0, is the change in curvature due to the lensing effect, while the disk average, A_0^0, is merely the effect of the window thickness. Thus a thermal lens will not only change the curvature of the wavefront, but also introduces spherical aberration (A_4^0). The integration is only carried out to the fourth order in n, but higher order terms exist. They are ignored on the basis that only the primary aberrations are of interest in this study (since these aberrations can be corrected for with adaptive mirror systems).

The dependence of the defocus (A_2^0) and spherical aberration (A_4^0) coefficients on the laser parameters is shown graphically in Figures (50) and (51), for the example of a $3mm$ thick ZnSe window. The following observations can be made:

- The defocus, or curvature, follows the same trend as the theoretical change in focal length of a thermal lens. We expect these two to be directly related.
- Spherical aberration deteriorates at higher repetition rates and at smaller spot sizes on the window.
- The aberrations are time dependent, and appear to tend towards a stable value; this value depends on the input beam and material conditions.

As an example, a comparison of the defocus coefficient and the spherical coefficient, after $t = 20s$, for a $2J$ pulse ($\lambda = 10.6\mu m$, passing through a ZnSe window, shows the following($\beta = 1.5$):

at $1kHz$ we have:

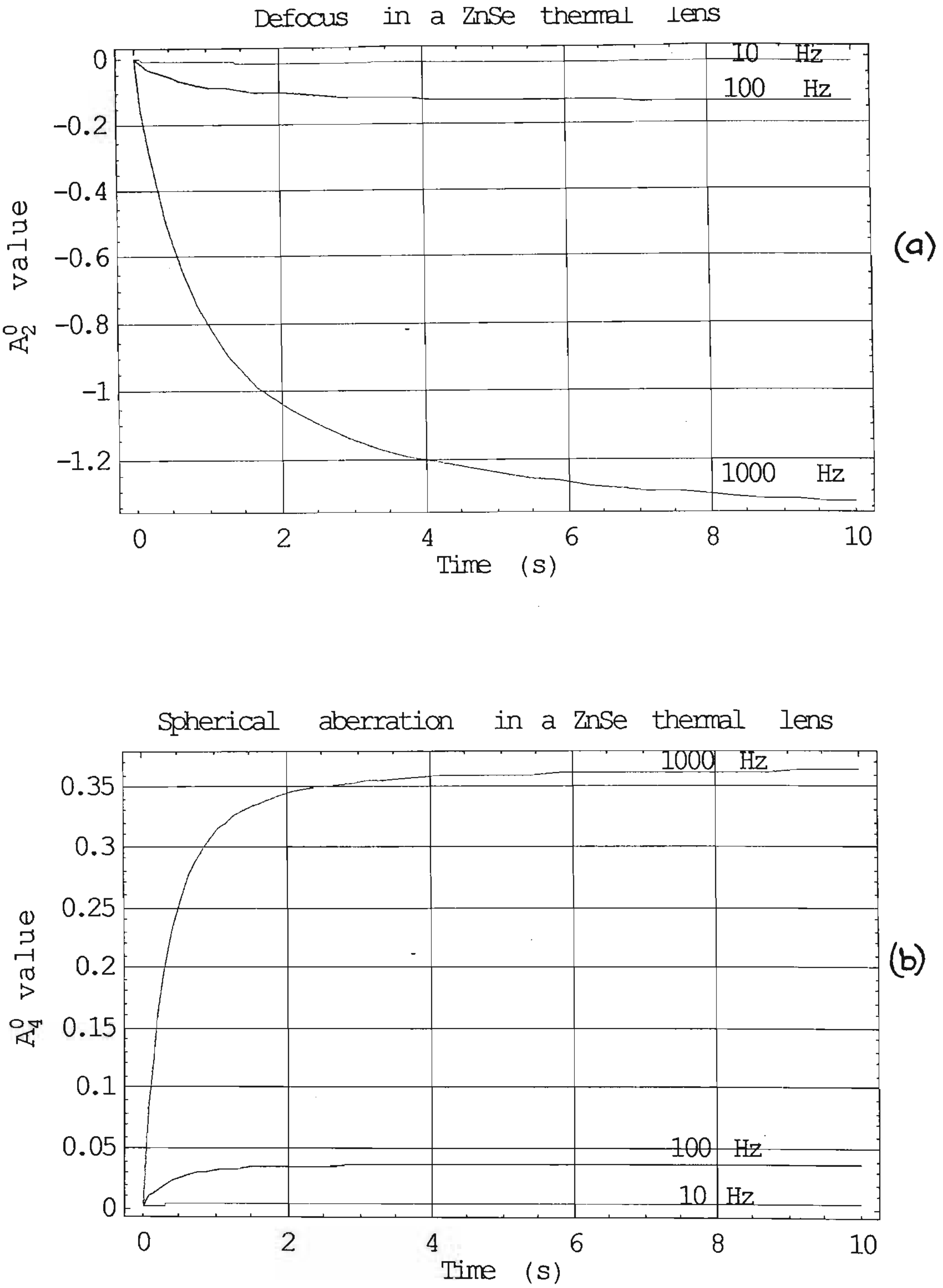

Figure 50: (a) Defocus and (b) Spherical aberration expansion coefficients in a ZnSe window, for $E = 2J$ and $w = 5mm$.

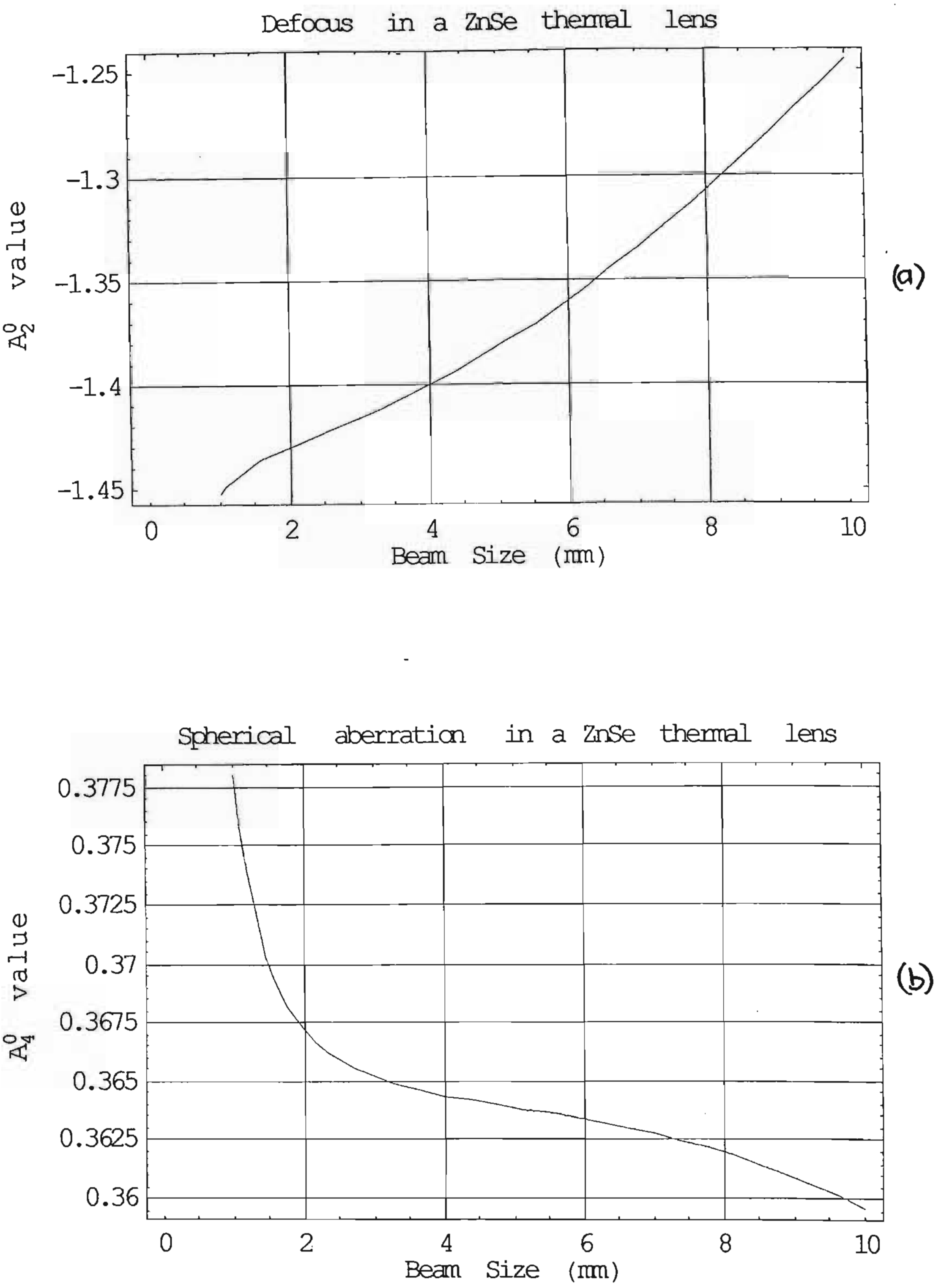

Figure 51: (a) Defocus and (b) Spherical aberration expansion coefficients in a ZnSe window, after 20*s*. As the spot size on the window gets smaller, so the aberration increases.

- For a $3mm$ spot:
  1. $A_2^0 = -1.416$
  2. $A_4^0 = 0.365$
- For a $6mm$ spot:
  1. $A_2^0 = -1.360$
  2. $A_4^0 = 0.363$

while for a constant spot size of $5mm$ we have:

- For a repetition rate of $1kHz$:
  1. $A_2^0 = -1.38$
  2. $A_4^0 = 0.364$
- For a repetition rate of $100Hz$:
  1. $A_2^0 = -0.139$
  2. $A_4^0 = 0.0369$

From the above data we see that there is a very small change in the spherical aberration coefficient when decreasing the spot size on the window (a change of only 0.5%), while the defocus, or curvature coefficient changes by 10 times this amount, but still a small 4%. The repetition rate certainly has a very large effect, with both spherical aberration and defocus increasing by an order of magnitude when the repetition rate is increased from 100 Hz to 1 kHz (i.e., one order of magnitude).

4.4 Thermal Blooming Aberrations

4.4.1 Introduction

Thermal blooming, recognised as a major source of optical degradation in high energy systems, is caused by the finite absorption of laser beam energy in the gas medium. At the heart of thermal blooming is the fact that light rays in an inhomogeneous medium are bent into the regions of higher refractive index. The refractive indices of gases decrease with increasing temperature. Thus the heating produced by the absorbed radiation leads to defocusing of the beam - referred to as *thermal blooming*.

Gas flow, either along or across the laser beam path, is generally used to reduce thermal blooming effects. In the tandem amplifier arrangement, discussed earlier in § 3.4.4, a pipe joins two amplifiers, with "axial" flow from each amplifier to the centre of the pipe (where the gas is extracted and recirculated). The idea is that this arrangement reduces thermal lensing, since two would–be windows have now been removed, while any blooming effects are negated by the axial flow.

4.4.2 The model

For the purposes of this study, the aberrations through any thermal blooming system will do. The reason is the lack of a suitable model to describe the effects in our MLIS laser system. It is therefore useful in the meantime to get an idea of what parameters are of importance for the aberrations, as well as the thermal blooming itself. Thus examples are drawn from three papers, [*Martynenko*, 1975],[*Soloukhin et al*, 1980] and [*Shen et al*, 1980]. The data used here is extracted from the latter study, and modified to be used for aberration calculations.

The experimental data of *Shen et al.* was measured by observing the optical path difference (OPD), as a function of the radial position in a $5cm$ diameter pipe, of length $6m$. A $250W$ CW CO_2 beam (TEM_{oo}), with $1/e^2$ radius of $1cm$ was propagated down the pipe. The experiment looked at how the OPD changes with axial gas flow speed and gas–wall temperature mismatch (achieved by heating the pipe walls). The gas mixture was $9\%CO_2$ and $91\%N_2$.

Shen et al conclude that increasing the flow velocity and gas–wall temperature mismatch reduces the thermal blooming, due to the flattening of the radial temperature profile in the region where the beam is located.

Before we start the analysis of the aberrations, it is worth making a few comments on these conclusions. Firstly, the authors consider a diameter of only 2ω (recall that ω refers to the $1/e^2$ beam radius) for the 'region where the beam is located'; diffraction calculations show that a beam diameter of at least 3ω, but better still 4ω is necessary to include the important effects of the wings (for example, to avoid any 'clipping' of a beam through a hard aperture, the aperture diameter should be at least 3ω). Thus the entire beam was not considered when looking at the problem. We will see that the scaling plays a very important role in such problems.

Secondly, one intuitively feels that a flattening of the radial temperature profile will reduce the thermal blooming, as the authors claim. In fact one can liken the situation to the high pressure experiments in § 1.5.2, where at the centre of the lens, where the refractive index profile is flat, we see a long focal length – reduced lensing. But, there will also be some stabilisation time involved. Figure 52 illustrates the idea: initially the area between the beam, which acts as a heat source, and the pipe walls (another heat source), will be cold, slowly heating up due to the influx of heat from both sources. Thus the optical path difference should go through a maximum at this point, somewhere between the beam centre and the pipe wall. This can clearly be seen in Figures 54 (a) and 54 (b). With time one expects this

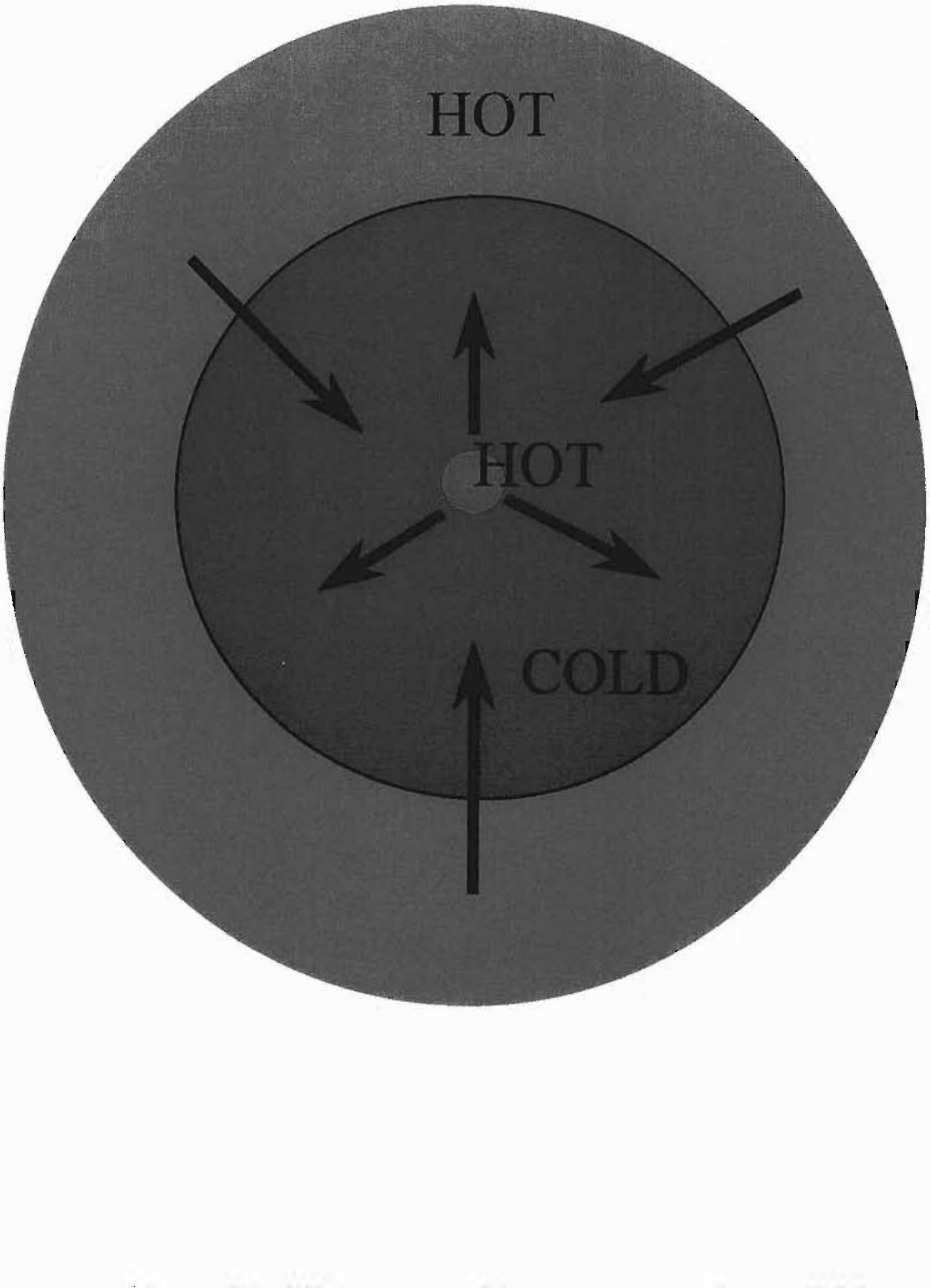

Figure 52: With a central heat source, and a radial heat source, we expect the centre to be initially at a minimum (cold), until it warms up due to the influx of heat. Eventually the temperature will stabilise and the system will radiate outwards.

profile to flatten out still further, until the entire system is in equilibrium and the heat flow is outwards, away from the pipe. The authors do not mention any of this, and therefore do not say how long the pipe had been heated for. With time their results could well have changed.

When the pipe walls are not heated, this effect should disappear since the exterior source no longer exists (the temperature will decrease radially from the source); as is seen in Figure 53 (a) and (b).

Figures 53 and 54 are a reworking of the data given by *Shen et al*; it has been put into a more "friendly" form for the purpose of this analysis. A 6th order polynomial in r' has been fitted to the data. The data plotted is the *Optical Path Difference (OPD)* in units of the wavelength used (i.e., opd/λ), against the radial distance from the centre of the pipe, in units of the pipe radius (i.e., $r' = x/R_o$, where x is the radial distance across the pipe, and R_o the pipe radius). Thus both the horizontal and vertical axes in Figures 53 and 54 are dimensionless.

A least squares fitting routine was used for the fit. The poor fit for some of the data points is due partly to the choice of the polynomial order (a higher order polynomial would produce a better fit), and partly due to the errors incured in the transfer of data from that plotted by *Shen et al* (i.e., it was difficult to get precise data values, since they did not tabulate thier data). Due to the latter consideration, the author felt that a 6th order polynomial produced a good enough fit for this analysis. However, it should be said that the choice of the function used to describe the data will ultimately determine the type and magnitude of the aberrations found. For example, one could even fit a suitable *Lorentzian* to the data, and this could well alter the final aberrations found. Finally, one of the requirements for the function was that it be symmetric about the propagation or pipe axis. This is due to the fact that a Gaussian beam will not produce asymmetric heating,and therefore the phase

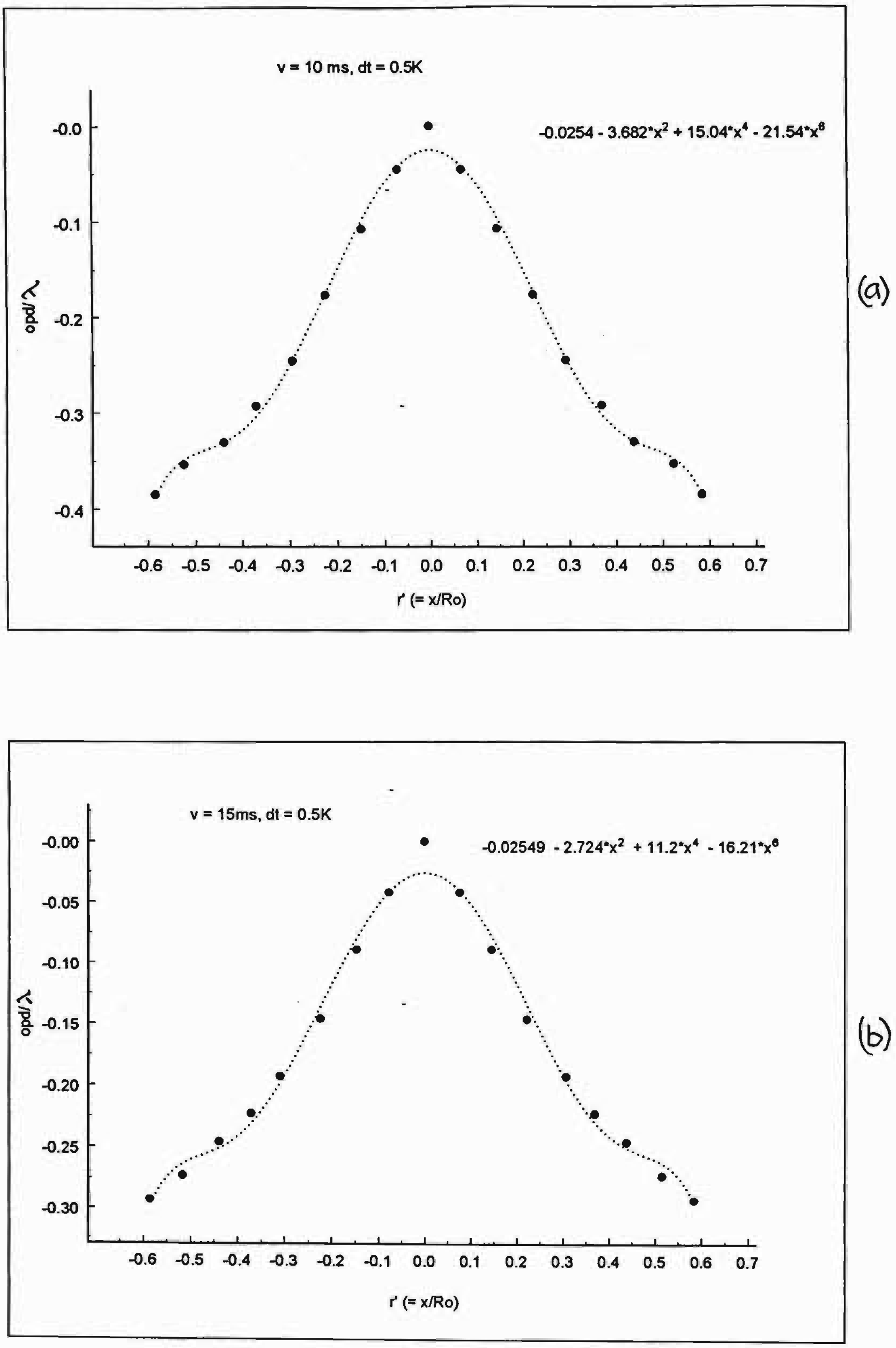

Figure 53: The OPD under the conditions of a gas–wall mismatch of $0.5K$ and, (a) an axial flow rate of $10ms^{-1}$, and (b), an axial flow rate of $15ms^{-1}$.

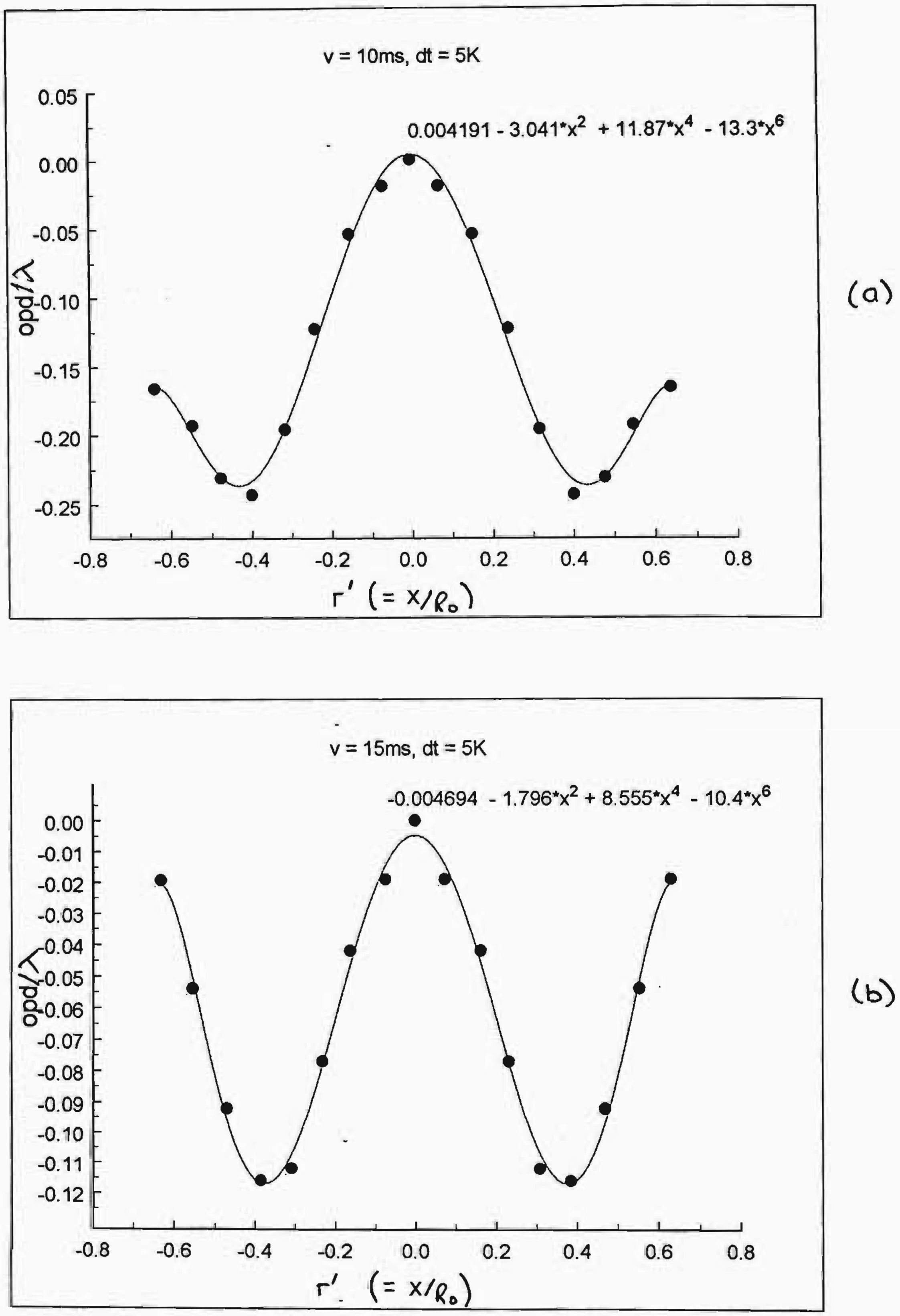

Figure 54: The OPD under the conditions of a gas–wall mismatch of $5K$ and, (a) axial flow rate of $10ms^{-1}$, and (b) an axial flow rate of $15ms^{-1}$.

change must be θ independent, and only be a function of radial position. This fact also simplifies the Zernike calculations to follow.

4.4.3 Results

The following function is fitted to the data points:

$$f(r') = a'r'^6 + b'r'^4 + c'r'^2 + d',$$

where the coefficients of each power of r' are determined from the best fit (a least squares fit), and are tabulated on the graphs.

We scale the pipe–beam system such that $r \in [0,1] \longrightarrow r' \in [0, \epsilon\omega/R_o]$, where R_o is the radius of the pipe, and ω is the $1/e^2$ beam radius. To put this into English, and attach some physical meaning to it, recall the following: the Zernike polynomials only hold over the unit circle, so r cannot be greater than 1. This then gives the first restriction. We could accomplish this by noting the suggestions made in § 4.2.4. At the same time we want to analyse a real radius that includes some multiple of the beam radius (ω), thus the $\epsilon\omega$ term. The parameter ϵ is given the value of 1 or 1.5 (to allow the diameter of the beam under consideration to be either 2ω or 3ω). This then results in a phase change through the system (of length l) of:

$$\Phi(r') = kn(r')l = kn_o l - \lambda f(r'), \tag{4.29}$$

or

$$\Phi(r) = kn_o l - (ar^6 + br^4 + cr^2 + d). \tag{4.30}$$

Here we have converted our co-ordinate system to the unit circle, evident through the presence of r, and have modified the polynomial coefficients accordingly:

$$a = \lambda a' \left(\frac{\epsilon\omega}{R_o}\right)^6 \tag{4.31}$$

$$b = \lambda b' \left(\frac{\epsilon\omega}{R_o}\right)^4 \tag{4.32}$$

$$c = \lambda c' \left(\frac{\epsilon\omega}{R_o}\right)^2 \tag{4.33}$$

$$d = \lambda d' \tag{4.34}$$

To determine the aberrations, we expand in Zernike polynomials with the expansion coefficients given by Equations (4.7) and (4.8).

Because the function is even, all odd or asymmetric Zernike coefficients vanish ($B_n^m = 0 \quad \forall n,\ m$), and we are left with the following terms (taken only to the fourth order in n):

$$A_0^0 = kn_o l - \left[\frac{1}{4}a + \frac{1}{3}b + \frac{1}{2}c + d\right], \tag{4.35}$$

$$A_2^0 = -\frac{1}{2}\left[\frac{9}{10}a + b + c\right], \tag{4.36}$$

and,

$$A_4^0 = -\frac{1}{2}\left[\frac{1}{2}a + \frac{1}{3}b\right]. \tag{4.37}$$

Again, since this study is only concerned with the primary aberrations, only a fourth order in n is considered. The results make sense. The *disk average*, A_0^0, coefficient tells us that if there was no temperature gradient, then all the r-polynomial coefficients would be zero and one would be left with the constant change,$kn_o l$, due to free propagation. In fact, even though there does appear to be some dependence on the other terms, note that each coefficient is a multiple of the wavelength; a very small number compared with $kn_o l$, which is a multiple of the inverse of the wavelength – a very large number. In this analysis for example, the wavelength is several orders of magnitude smaller then the values of the coeffcients a' through d'. Thus kn_ol clearly dominates the phase given by Equation (4.30). As expected, the *defocus* (A_2^0) coefficient does not depend on the constant phase change, i.e. kn_ol or d. It does, of course, depend on the quadratic (r^2) term coefficient, c, as well as the higher order terms (ar^6 and br^4). The spherical aberration is independent of all the constant terms as well as the quadratic coefficient c. We would be surprised if it were any other way, since spherical aberration cannot be introduced by perfect lenses (r^2 dependence), nor by free propagation (constant phase changes).

Using Equations (4.35), (4.36) and (4.37), one can calculate the Zernike coeffcient values. For the calculations, one requires the values of the primed coefficients used in Equation (4.29), the pipe radius (R_o), the beam radius (ω), the scaling parameter (ϵ) and the wavelength. The values of the primed coefficients as tabulated on the graphs (Figures 53 and 54) were used. A pipe radius of 2.5 cm and a beam radius of 1 cm was used, with the wavelength being left as a parameter (i.e., all the aberrations are left as a product of a value with the wavelength). Finally, Table 3 considers two scaling conditions: three times the beam radius and two times the beam radius. This then sets the scaling parameter to be 1.5 and 1 respectively.

The data tabulated in Table 3 shows some interesting trends. As the authors have stated, increasing the axial gas flow speed, v, and/or increasing the gas–wall temperature mismatch, T, certainly does reduce the defocus parameter, and hence the thermal blooming.

The data in Table 3 also shows that spherical aberration is introduced into the system, a fact overlooked by *Shen at al.* Considering the 3ω data, one sees that for a gas speed of $10ms^{-1}$, an increase in the temperature by an order of magnitude, from $0.5K$ to $5K$, shows a 35 % increase in spherical aberration, while the

Conditions	Defocus coefficient (3ω)	Spherical coefficient (3ω)
$v = 10\ ms^{-1}, T = 0.5\ K$	$14 \times 10^{-2}\ \lambda$	$-7.4 \times 10^{-2}\ \lambda$
$v = 15\ ms^{-1}, T = 0.5\ K$	$10.5 \times 10^{-2}\ \lambda$	$-5.3 \times 10^{-2}\ \lambda$
$v = 10\ ms^{-1}, T = 5\ K$	$5.7 \times 10^{-2}\ \lambda$	$-10 \times 10^{-2}\ \lambda$
$v = 15\ ms^{-1}, T = 5\ K$	$-1.3 \times 10^{-2}\ \lambda$	$-6.3 \times 10^{-2}\ \lambda$

Conditions	Defocus coefficient (2ω)	Spherical coefficient (2ω)
$v = 10\ ms^{-1}, T = 0.5\ K$	$14.2 \times 10^{-2}\ \lambda$	$-4.2 \times 10^{-2}\ \lambda$
$v = 15\ ms^{-1}, T = 0.5\ K$	$10.4 \times 10^{-2}\ \lambda$	$-3.1 \times 10^{-2}\ \lambda$
$v = 10\ ms^{-1}, T = 5\ K$	$12 \times 10^{-2}\ \lambda$	$3.7 \times 10^{-2}\ \lambda$
$v = 15\ ms^{-1}, T = 5\ K$	$5.3 \times 10^{-2}\ \lambda$	$2.6 \times 10^{-2}\ \lambda$

Table 3: This table shows the values of the defocus and spherical aberration terms for the two speed and temperature conditions. The chosen scaling dimensions also play an important role.

same temperature change at $15ms^{-1}$ shows a 19 % increase in spherical aberration. Similarly, keeping the temperature constant and decreasing the gas speed results in an increase in the magnitude of the Zernike coefficient for spherical aberration. Thus, although a larger gas-wall temperature mis-match reduces thermal blooming, it increases the aberrations on the wavefront (in this case spherical aberration). Increasing the gas flow speed is therefore a better solution. The scaling parameter is very important to the analysis. If the analysis is done on only a diameter of 2ω, then the spherical aberration magnitude can be a factor 2 or higher out, as compared to the 3ω calculation.

The scale of the change in the Defocus parameter illustrates the differences between the two extreme conditions used in the paper by *Shen et al* and as analysed here. However, a comparison of the numbers in Table 3 and those presented in § 4.3.2 show that the thermal lensing aberrations (discussed in the latter section) are of a much higher magnitude than the thermal blooming aberrations presented here. To see this, note that all the values of the thermal blooming aberrations are a product of the wavelength, which is in the order of 10^{-5} for infrared beams.

In the MLIS system, the tandem arrangement[6] of the amplifiers uses an axial pipe to link the amplifier mediums, and so is an exact analogy of the experimental arrangement described by *Shen et al.* With a much higher peak and average power beam in the MLIS system than that used by *Shen et al*, it can be expected that the aberrations from thermal blooming in the tandem arrangement will be larger than the aberration values presented here.

---

[6] This was discussed in the previous chapter.

4.5 Aberrated Beam Propagation

4.5.1 Beam Quality

For many years people have referred to the term *beam quality*, but with only a vague idea of what they were talking about. Terms like *times diffraction limit, Strehl ratio, 'power in the bucket'* and *coherence length* refer to methods which have been used as a measure of laser beam quality. All these methods have their limitations.

In recent years a new definition of beam quality has emerged [*Siegman*, 1990][*Johnston*, 1990]. It is beyond the scope of this thesis to review this work. For a good review of this field, see the special edition of the journal *Optical and Quantum Electronics* (in the references under *Special Edition*), and papers by Weber[*Weber*,1992] and Siegman[*Siegman*, 1990].

For the purpose of this study, a very brief, and by no way complete, explanation of the relevant terms in beam propagation is given. In the remainder of this chapter, a cartesian coordinate system (x, y, z) is used, where z is the propagation direction, and the field components of the beam can be separated into the two transverse coordinates x and y. As an introduction to the basic beam propagation equations, only one transverse co-ordinate is considered.

The work started with Siegman when he showed that any real, multimode laser beam follows the same laws as those describing Gaussian beams. That is to say, the spatial variance (σ_x) has a minimum at some plane (z_{xo}), denoted by σ_{xo}, and varies quadratically with propagation distance z:

$$\sigma_x^2(z) = \sigma_{xo}^2 + \lambda^2\sigma_{sx}^2(z - z_{xo})^2. \tag{4.38}$$

In this definition, the real beam radius $(W(z))$, waist(W_o) and far field divergence(Θ_o) are defined as second moment variances, given by:

$$\sigma_x(z) = \frac{W(z)}{2} \tag{4.39}$$

$$\sigma_{xo} = \frac{W_o}{2} \tag{4.40}$$

$$\begin{aligned} \sigma_{sx} &= \frac{1}{2\pi W_o} \\ &= \frac{\Theta_o}{2\lambda}, \end{aligned} \tag{4.41}$$

where σ_{sx} refers to the variance in the spatial–freqency domain, and λ is the wavelength of the laser beam in question. In fact, he showed that through any ABCD matrix system, if the second moments are introduced to define the beam variances, then the product of the minimum spatial variance and the spatial–frequency variance (related directly to the far field divergence through the wavelength) is invariant through transformation, and takes on a minimum value for a Gaussian beam, given by:

$$\sigma_{xo}\sigma_{sx} = \frac{1}{4\pi}. \tag{4.42}$$

For a *real* laser beam, such as any arbitrary, non-Gaussian, non-diffraction-limited and potentially multimode beam, this product is still invariant, but takes on a larger value, given by:

$$\sigma_{xo}\sigma_{sx} = \frac{M_x^2}{4\pi}. \tag{4.43}$$

What all this says, is that while the field structure of an arbitrary beam may change in a very complex way, the propagation parameters, such as the waist, waist position and far field divergence are transformed exactly as a pure Gaussian beam's parameters would, but with a measure of quality introduced, the M_x^2 parameter (and similarly a M_y^2 parameter). This quality parameter is equal to 1 for a Gaussian beam, and becomes larger the more 'non-Gaussian' the beam is. It is thus a very easy tool to use as a measure of the beam quality.

A measurement of a real beam, as opposed to a Gaussian beam, will show that the spot size and far field will both be larger by a factor M_x, and the product of the minimum spot size (waist) and far field divergence (given as θ or sometimes as θ_o) will be larger by a factor M_x^2. For Gaussian beams (ideal beams),

$$\theta w_o = \frac{\lambda}{\pi},$$

while for non-Gaussian beams (**real** laser beams):

$$\begin{aligned} \Theta W_o &= (M\theta)(Mw_o) && (4.44)\\ &= M^2(\theta w_o) && (4.45)\\ &= M^2\frac{\lambda}{\pi}, && (4.46) \end{aligned}$$

where for this example, upper-case refers to real beam parameters, and lower-case to ideal Gaussian parameters. Because the beams used in the MLIS laser chain are very nearly Gaussian, the quality parameter and beam parameters in the two transverse directions are very nearly identical, and thus the subscripts x and y are omitted in beam parameter discussions. Only if a *measurable* beam quality difference in the two directions exists will the M^2 parameter be specified separately in the x and y direction. To summarise then, if one knows the beam quality, M^2, as well as the beam waist w_o and the waist position z_o, (the far field divergence is directly related to the waist by $\theta = M^2\lambda/\pi w_o$) then the beam can be transformed by ABCD matrix systems.

There are two limitations to the above. Firstly, one usually does not measure a second moment radius, but rather a $1/e^2$ radius, otherwise known as a 86.5 %

power content value. The problem is that with this value for the beam parameters, it has been shown that the ABCD holds only approximately. Of course with the second moment definition, one does not know what amount of power is inside a beam of radius defined in this way – it evidently will depend on the field structure, which is not so easy to measure.

The second problem, is that the ABCD law does not describe aberrated systems. Thus one cannot use any of these simple relationships to predict a change in beam quality through aberrated systems. In the MLIS chain we measure a degradation in beam quality – the M^2 at the oscillator can be around 1.1, while at the output of the last amplifier it has changed to $1.5 - 1.7$. A change in M^2 will alter the propagation of the beam, so it is important to understand and predict any changes to its value.

It seems likely that aberrations will increase the value of the M^2 parameter, since the nature of aberrations is to reduce beam quality. In this next section we look at the influence aberrations have on the propagation of the beam. Because the standard propagation tools assume *a priori* that the system is aberration free, we instead are forced to consider a more rigorous approach – the Kirchoff–Fresnel diffraction integral [*Born, Wolf*, 1975].

4.5.2 Results

In this section, a phase profile is provided as the Kernel for the diffraction integral. Essentially, an input field is modified by this phase structure, which results in a different output field. By taking successive iterations of the new field through free space, the propagation of this new field can be analysed. If the field is then brought to focus by placing a perfect lens in its path, then the necessary beam parameters can be deduced i.e. the beam waist, the waist position and the far field divergence. If the Gaussian theory is compared to this freely propagating beam (after the lens), then a quality parameter, (M^2), should exist which maps the aberrated beam onto the Gaussian beam. If the M^2 has increased, it must be due to the initial phase structure – hence it must have included some aberrating effects. Because we already know how to relate phase changes to aberrations, we can deliberately introduce a known amount of aberration and see the effects. This is then a quantitative means of investigating (numerically) aberrated beam propagation, and relating aberrations to the beam quality parameter.

The diffraction program was written in C programming language by Dr S.P. van Heerden. Originally it was written for another application, but Dr S.P. van Heerden has kindly made some alterations to accommodate this study. Some results have already been presented at a local conference[*van Heerden, Forbes*, 1997][*Forbes, van Heerden*, 1997].

Figure 55 compares the Gaussian theory predictions for propagation with the calculated values from the diffraction program. The program used only a Gaussian beam and a lens, and calculated the second moment beam dimensions. The M^2 has remained equal to 1, which is what we expect. This was done in order to test the program for accuracy, since the results could be calculated analytically, so as to validate the results to follow.

Figure 56 shows the beam after passing through an asymmetric profile similar to that given in § 4.2.3. The coma introduces a wavefront distortion which changes the M^2 value – the beam is of poorer quality. Because of the assymetric nature of coma, we see that the beam quality is no longer the same in the two transverse directions. The effect of this asymmetry is that the beam propagates

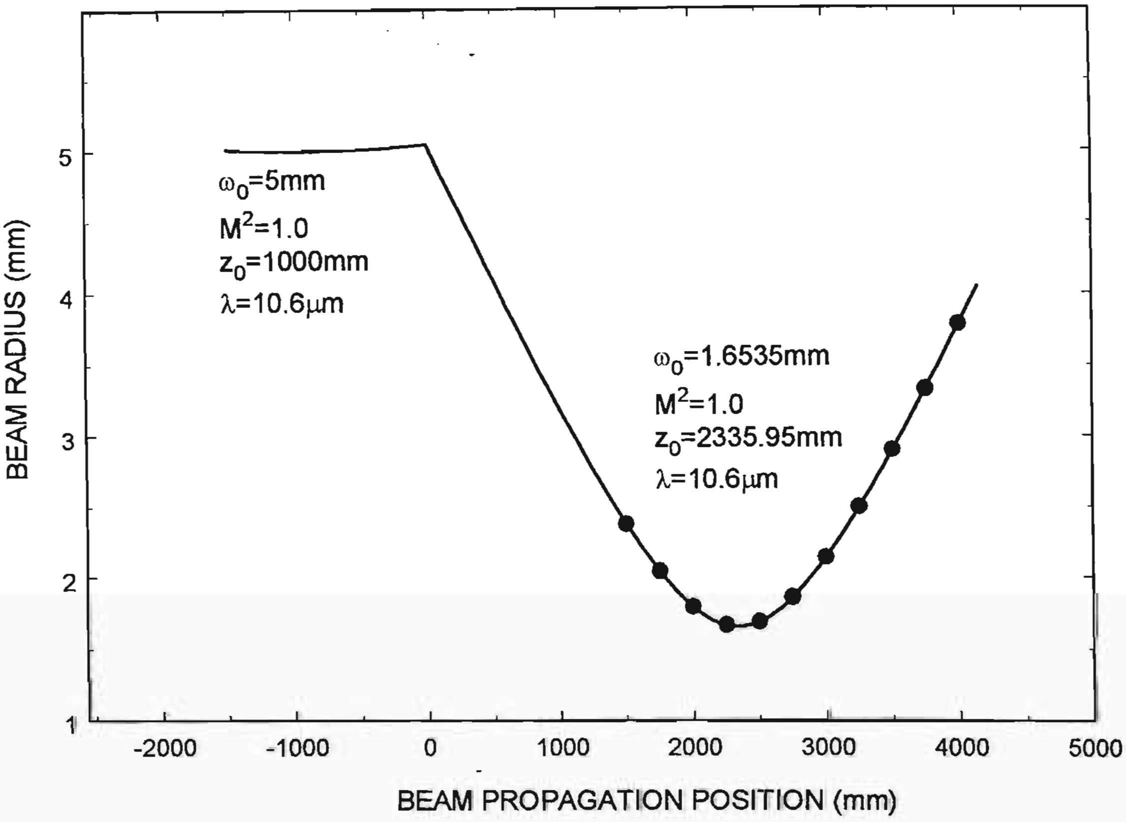

Figure 55: The propagation of a perfect Gaussian beam as predicted by the Gaussian theory (line), and by the diffraction program (points). This test shows that the program is accurate in its predictions.

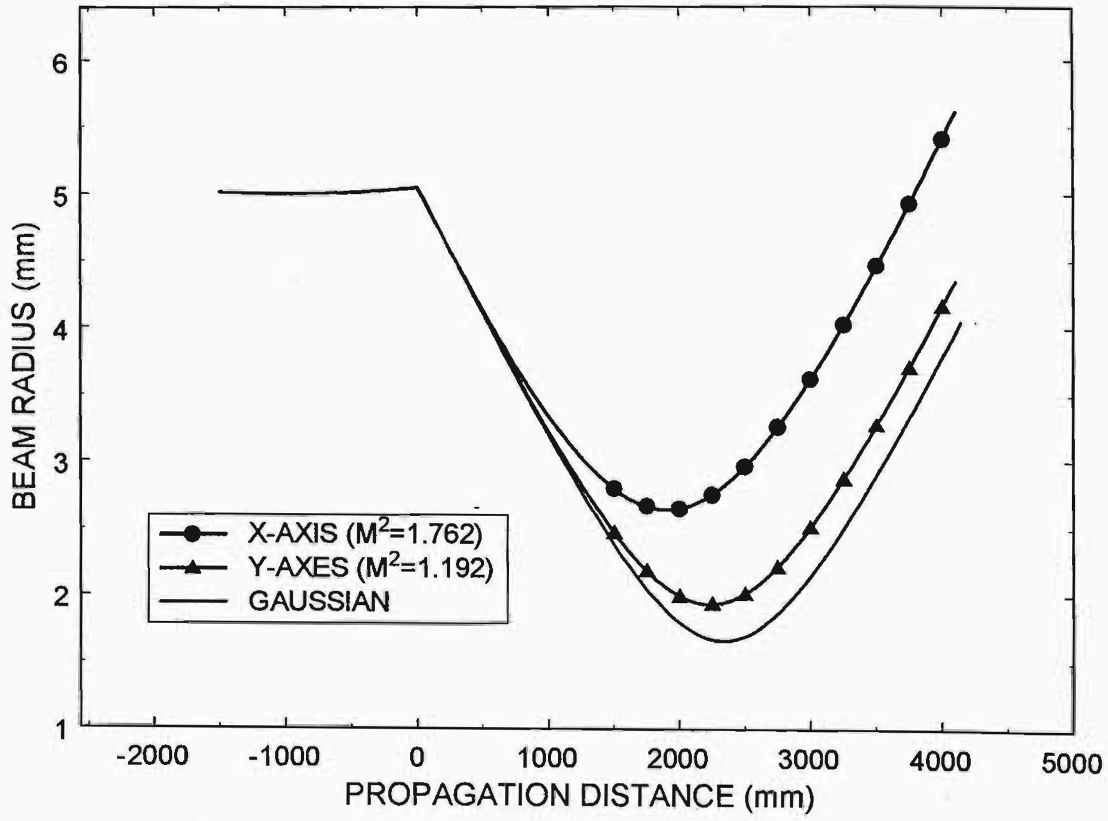

Figure 56: The resultant propagation after passing through the asymmetric field given in § 4.2. The M^2 of the beam has increased.

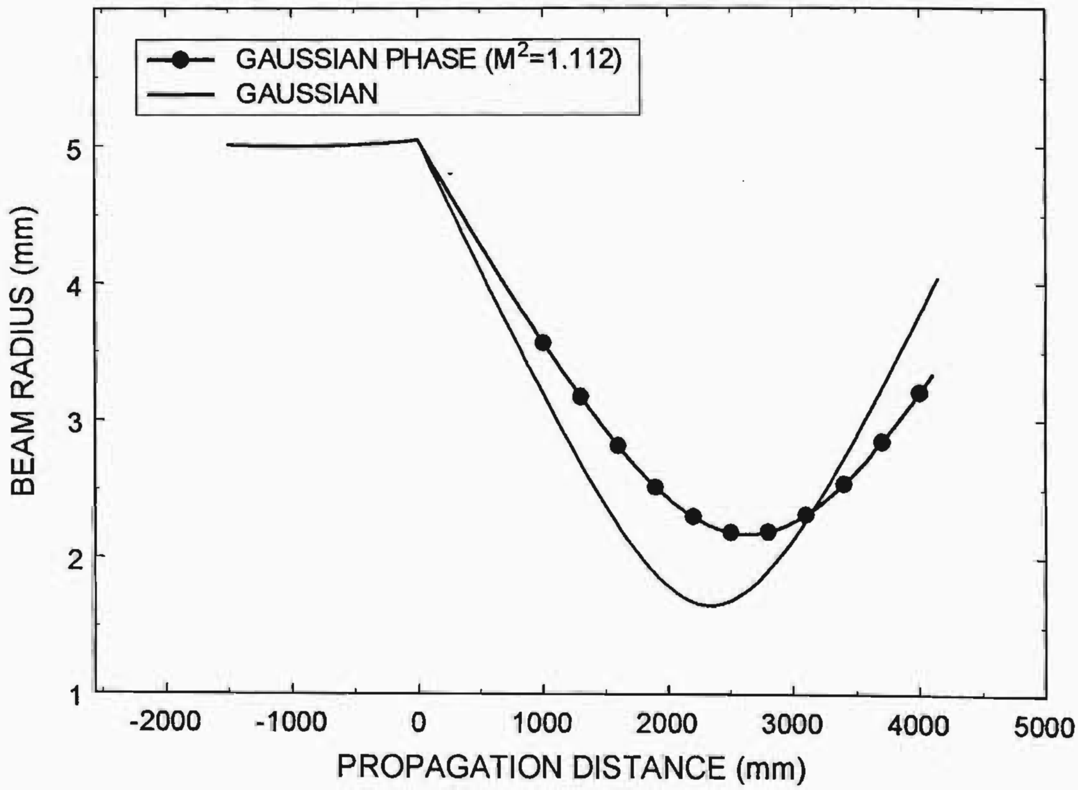

Figure 57: A Gaussian phase profile to simulate the thermal lens. Clearly this profile also introduces aberrations (spherical), resulting in poor beam quality.

differently in each transverse direction. As can be seen from the graph, the field in the y plane has a smaller waist value than that found in the x plane, and the waist position in each plane is different. If one thinks about rays for a moment, with the waist position being equivalent to the focal plane, and the waist size equivalent to the focal spot, then it is clear that coma will distort the image formed from these rays, because the focus in the x direction is larger and closer to the "system" (our imaginary phase profile) than the focus in the y direction. That is why coma is referred to as an aberration. One can think of the M^2 parameter as a quantitative measure of how bad the distortion is going to be – in this case the " sharpness" of the focus is not as good in the x plane as in the y plane, as indicated by the larger M^2 in the x plane as compared to the y plane.

The tilt contribution does not introduce any beam quality change. This profile is similar in many respects to that given by the rotating window (discussed in the previous chapter) – the temperature distribution is asymmetric and shows coma. Thus we expect the rotating window to degrade the beam quality in a similar fashion (this analysis is in progress, and is therefore not included here).

Finally, a Gaussian phase profile was used to simulate the aberrations due to thermal lenses. As has been shown earlier in this chapter, spherical aberration is introduced by such a lens. Thus we expect that the beam quality should by reduced, resulting in a larger M^2 value. Indeed, Figure 57 shows that the M^2 has now become 1.112, as compared to a Gaussian beam of $M^2 = 1$. There are two interesting conclusions to be made from this figure: firstly, by comparing the resulting beam propagation to the ideal Gaussian beam, it is clear that even a small increase in the beam quality can cause significant changes to the beam parameters over a distance of several meters; and secondly, because the thermal lens aberration is symmetric, even though the quality is poorer, the two transverse fields are affected in the same way – there is only a single quality factor, and the beam propagates the same in the x plane as in the y plane.

4.6 Conclusion

In the previous chapter, thermal lensing was looked at in detail, and some solutions were discussed. In this chapter, the aberrations resulting from thermal lenses, tandem arrangements and rotating windows were analysed.

Thermal aberrations seen in an MLIS laser chain have been calculated analytically using the Zernike Polynomial expansions. The thermal lensing aberrations are a function of the beam and material parameters, and follow similar trends to those given in the previous chapter. Connecting the amplifiers with a pipe (with axial flow), shows that while this does reduce the lensing, it introduces thermal blooming which causes spherical aberration. However, the magnitude of the aberrations in this arrangement seems to be much smaller than those found in the thermal lensing case, although a direct comparison was not possible. The rotating window was analysed by comparing it to a similar phase profile, and this suggested that coma might be the aberration to consider in such a system.

Finally, the effect that aberrations have on the beam propagation has been considered numerically by using the diffraction integrals to propagate an aberrated beam through a lens. The beam parameters were calculated for the cases of a beam with coma, and a beam with spherical aberration. It was shown that in both cases, aberrations result in a poorer beam quality, or higher M^2 parameter. In the case of the coma aberration, the beam was no longer symmetric and a different M^2 could be assigned to each transverse plane, while in the spherical aberration case, the beam remained symmetric about the propagation axis, but had a higher M^2 than a perfect Gaussian beam.

This analysis shows that while it is possible to reduce thermal lensing with novel solutions, these solutions often introduce new aberrations, which results in beam propagation problems.

5 Adaptive Systems

5.1 Introduction

In this chapter, we look at thermal lensing compensation with adaptive optics. Surprisingly, this application has not been tackled before (or perhaps it has not been addressed in the open literature). There are several reasons for this. Firstly, only in recent years have adaptive elements been commercially available, previously the applications were all military. It could be said that these days, the applications of adaptive mirrors are well known in the astronomy community[*WEB1*]. The only other group that might use adaptive mirrors is the LLNL *BeamLet* group. In the case of astronomical applications, the wavefront is accurately described as a plane wave, since the source is at infinity. In the LLNL case, the wavelength is so short, and the beam size so large, that one is essentially dealing with ray equations, and geometric optics.

In the MLIS application, a thermal lens modifies the beam propagation by changing the waist size, the waist position, and the far field divergence. Since the far field divergence is directly related to the beam waist, we will hitherto speak only of a change in waist and waist position. What complicates the use of adaptive mirrors in MLIS, is the fact that the incoming wavefront is not necessarily planar, and the output must correct for two parameter changes. Thus the application of using adaptive mirrors for mode matching correction has not been investigated.

5.2 Thermal Lens Compensation

Consider the system in Figure 58. Without any compensation for the thermal lens, the resultant beam propagation differs from the original. We ask the questions: at what distance should an adaptive mirror be placed, and what focal length should it assume, in order to return the beam to its original propagation? We imagine placing an adaptive mirror at some distance x from the window (thermal lens) and we change only the curvature on the adaptive mirror, so only its focal length changes. Then the transformation in beam parameters is given by

$$\mathcal{T} = \begin{bmatrix} A & B \\ C & D \end{bmatrix}, \tag{5.1}$$

where the terms A, B, C, D have the property $AD - BC = 1$, and are determined by taking the product of each matrix that represents the beam path (in reverse).

What we would like to do now is the following: we first define the propagation of the original beam, without any thermal lensing. Rememeber that defining the beam means knowing what the waist size, and waist position are (ω_o and z_o respectively). Once we have theses values, we insert a thermal lens, by allowing the window to have an effective focal length of f_{th}. Introducing this lens obviously changes the beam propagation, which means that the beam now has a new waist (could be larger or smaller) and a new waist position. Ideally we want to be able to compensate for this, so we introduce an adaptive mirror. To do this in the equations, we insert a lens of focal length f_a – our adaptive mirror– at a distance x from the window. Now we ask: if f_a can take on any value, and if we can place this lens anywhere after the thermal lens (f_{th}), where should we place the adaptive mirror (i.e. what should the x value be), so that the beam propagation after this whole system looks identical to the original case, which had no thermal lens, and no adaptive system. That way to

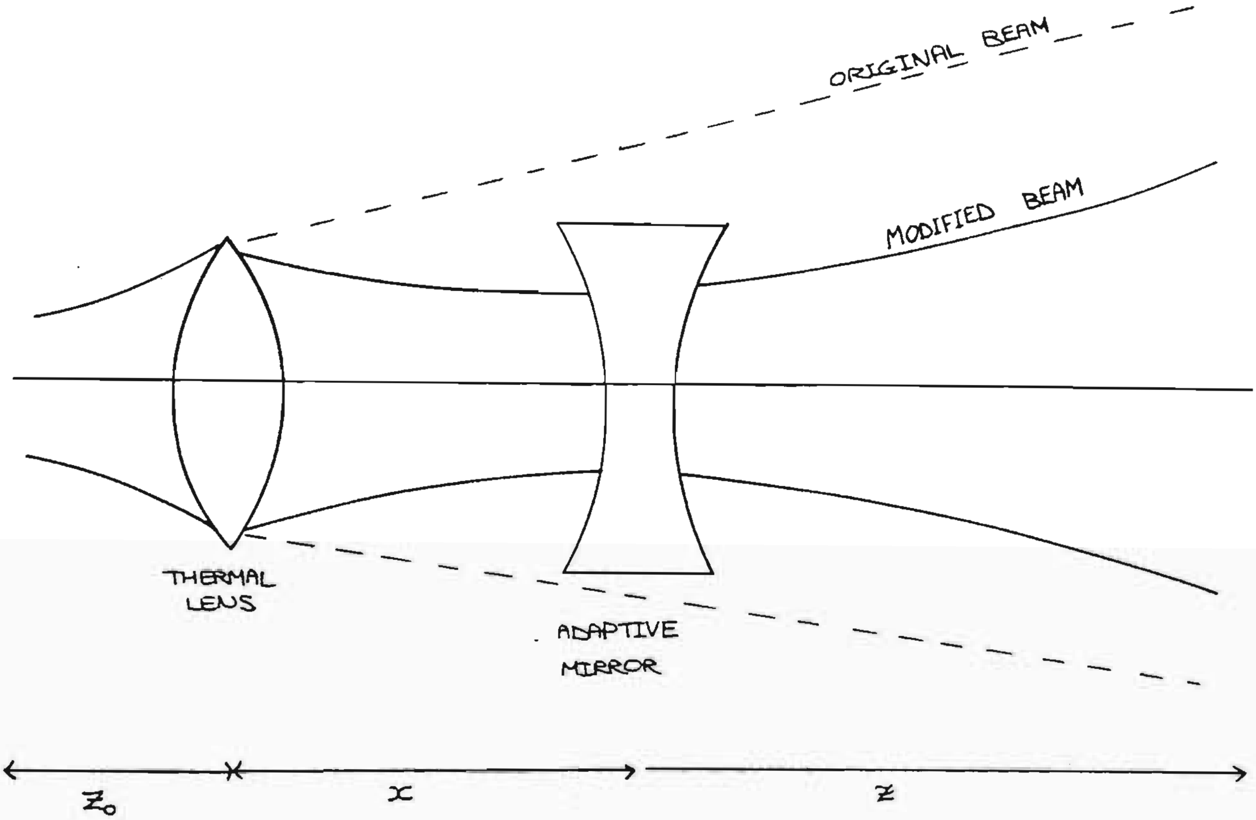

Figure 58: A schematic showing the system to be analysed. With a thermal lens in place, one would like to know where to place an adaptive mirror, in order to return the beam to its original propagation.

solve this problem is to again consider the shift in beam waist and waist position, introduced by the entire system, and then "fiddle" with the equations by changing f_a and x, until this shift is zero, i.e., the final beam waist and waist position look identical to what we started with.

Consider the case of the original beam: we define the original beam as if it does not see the thermal lens (since this is what we want). Then its propagation is given by:

$$\begin{aligned} \omega_1^2(z) &= \omega_{o,1}^2 + (z + z_o + x)^2\theta_{o,1}^2 & (5.2) \\ &= \omega_{o,1}^2 + z^2\theta_{o,1}^2 + 2z(z_o + x)\theta_{o,1}^2 + (z_o + x)^2\theta_{o,1}^2. & (5.3) \end{aligned}$$

Now the new beam, the beam after the thermal lens and the adaptive mirror, has some new waist ($\omega_{o,2}$) at a new position ($z_{o,2}$):

$$\begin{aligned} \omega_2^2(z) &= \omega_{o,2}^2 + (z + z_{o,2})^2\theta_{o,2}^2 & (5.4) \\ &= \omega_{o,2}^2 + z^2\theta_{o,2}^2 + zz_{o,2}\theta_{o,2}^2 + z_{o,2}\theta_{o,2}^2. & (5.5) \end{aligned}$$

Here we are using the same notation as previously (§ 3.3.3). The $z_{o,2}$ term represents the new waist position in region two. To match the two propagation paths exactly (i.e. to ensure that both the new and the original beam have the same beam size at any given z position), all the coefficients of z in the two equations must be the same:

$$\begin{aligned} \omega_{o,1}^2 + (z_o + x)^2\theta_1^2 &= \omega_{o,2}^2 + z_{o,2}\theta_2^2 & (5.6) \\ \theta_1^2 &= \theta_2^2 & (5.7) \\ 2(z_o + x)\theta_1^2 &= 2z_{o,2}\theta_2^2, & (5.8) \end{aligned}$$

which then implies that:

$$\theta_1 = \theta_2 \tag{5.9}$$

$$z_{o,2} = z_o + x \tag{5.10}$$

$$\omega_{o,2} = \omega_{0,1}. \tag{5.11}$$

This implies that to have the two beams propagating in exactly the same way, the waist, waist position and divergence of the two must be identical. Remembering that in region two, the beam is described by:

$$\omega_2^2 = A^2\omega_{o,1}^2 + B^2\theta_1^2 \tag{5.12}$$

$$\theta_2^2 = C^2\omega_{o,1}^2 + D^2\theta_1^2; \tag{5.13}$$

we see that together with Equation (5.2), we have the following conditions on our transfer matrix $\mathcal{T}$:

$$A^2 = 1 \tag{5.14}$$

$$B^2 = (z + z_o + x)^2 \tag{5.15}$$

$$C^2 = \frac{\theta_1^2}{\omega_{o,1}^2}\left(1 - D^2\right). \tag{5.16}$$

If we calculate the transfer matrix elements from the system described by Figure 58, that is, the entire system with thermal lens and adaptive mirror, we find that they are given by:

$$A = (f_a f_{th})^{-1}(f_a f_{th} - f_a x - f_a z - f_{th} z + xz) \tag{5.17}$$

$$\begin{aligned} B &= (f_a f_{th})^{-1}(f_a f_{th} x + f_a f_{th} z - \\ &\quad f_{th} x z + f_a f_{th} z_o - f_a x z_o - f_a z z_o - f_{th} z z_o + x z z_o) \qquad (5.18) \\ C &= (f_a f_{th})^{-1}(-f_a - f_{th} + x) \qquad (5.19) \\ D &= (f_a f_{th})^{-1}(f_a f_{th} - f_{th} x - f_a z_o - f_{th} z_o + x z_o). \qquad (5.20) \end{aligned}$$

Here f_{th} and f_a are the focal lengths of the thermal lens and the adaptive mirror respectively, and z is measured from the adaptive mirror. Because we require that $f_a \neq 0$ and $x \geq 0 \ \forall \ z > 0$, we find that, from Equation (5.14)

$$f_a f_{th} = f_a f_{th} - f_a x - f_a z - f_{th} z + x z$$

which after a little reduction becomes:

$$z(x - (f_a + f_{th})) - f_a x = 0$$

Since this is true for all $z > 0$, we have that both terms in the above equation must separately be zero:

$$f_a x = 0 \quad \Leftrightarrow x = 0, \qquad (5.21)$$

and

$$x = f_a + f_{th} \quad \Rightarrow f_a = -f_{th}. \qquad (5.22)$$

Thus, to match the beams by trying to reproduce the new waist in the original position (as an imaginary waist) with the original size, requires that the separation distance between the thermal lens and the adaptive optic be zero, and moreover, the respective focal lengths must be equal but opposite. We can make sense of this result, if we consider the following approximation from geometric optics:

$$\frac{1}{f_{tot}} = \frac{1}{f_1} + \frac{1}{f_2} + \cdots$$

Here we have produced the same result. If the separation between the two lenses is zero, then the above approximation holds exactly, and the net focal length will indeed be infinity if the two focal lengths are equal in magnitude but opposite in sign. That this is the only solution is a surprise. One would have thought that perhaps some combination of focal lengths and distances would also give a solution, but alas this seems to be a unique solution. The problem with this solution, that of $x = 0$ and $f_a = -f_{th}$, is that it is physically impossible to place an adaptive mirror at zero separation from the thermal lens (an amplifier window for example), which is what is required if $x = 0$. Even a small separation will introduce some errors, and these errors are considered next.

5.3 Errors in Mode Matching

We often talk about the mode matching of the chain. This refers to the mapping of one waist, and waist position, to another waist and waist position, by means of a lens system. A glance at Equations (5.12) and (5.13) show that these equations are useful for looking at the resultant propagation, but do not actually tell one where and what the new waist position is. Some standard equations do exist for transforming from one waist to another, but these equations only hold for real images. Another method which the author has found is to treat the propagation as a function of position z, which it is, and then ask: for what value of z is the function $\omega_2^2(z)$ a minimum? By taking the derivative of ω_2^2 (given by Equation (5.12)) with respect to z, and solving for z, one has found the waist position $z_{o,2}$. Substitution back into the original function gives the waist size, $\omega_{o,2}$:

$$\begin{aligned} \frac{\partial \omega_2^2(z)}{\partial z} &= 0 \\ \Rightarrow 2\omega_2(z)\frac{\partial \omega_2(z)}{\partial z} &= 0; \end{aligned}$$

for the non-trivial case, we have that the waist position z_o is the solution to:

$$\Rightarrow z_{o,2} = z \quad \text{such that} \quad \frac{\partial \omega_2(z)}{\partial z} = 0. \tag{5.23}$$

In general, we note that the transfer matrix elements will also be functions of z, and so their derivatives will also have to be taken into account. This does not complicate the situation excessively, and instead we find that the waist position is now given by the solution to:

$$A(z)\omega_{o,1}^2\frac{\partial A(z)}{\partial z} + B(z)\theta_1^2\frac{\partial B(z)}{\partial z} = 0, \tag{5.24}$$

with the new waist given by:

$$\omega_{o,2} = \sqrt{\omega_2^2(z_{o,2})}. \tag{5.25}$$

Most publications illustrate the change in beam propagation by plotting the beam radius versus the propagation distance. This is the logical thing to do. To illustrate the effect thermal lensing has on the overall mode matching, and to see how well the adaptive optic is eliminating the problem, the author has developed a useful abstraction, which is discussed next.

5.3.1 Characterisation Space

Think about mode matching as starting with a given waist, and waist position, and mapping this information to a new waist and waist position. If the beam quality does not change during this mapping, that is, the transformation can be described by an

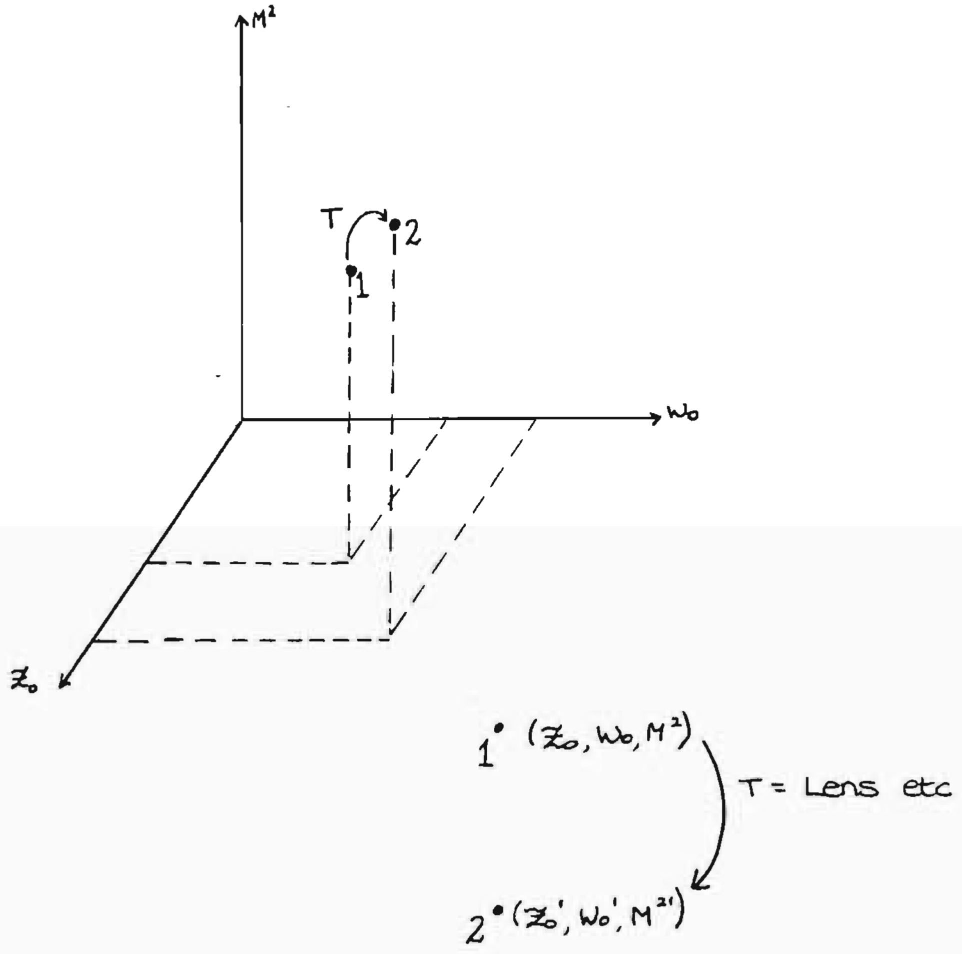

Figure 59: The characterisation space of the beam. It is a 3-D plot of the waist, waist position and M^2 parameter. Any point in this space completely describes the beam.

ABCD matrix (aberration free), then a plot of waist size versus waist position will tell one all that is needed to predict any beam parameter. Under ideal conditions, the mapping will be a single point in this space, called the *characterisation space*, because a point in the plane completely describes the beam propagation. For a change in beam quality, a third dimension can be added, the M^2 axis. Figure 59 shows the concept. In this 3-D space, if the mode matching is perfect, then only one point exists. For the following analysis, it is assumed that the M^2 stays constant, and therefore we look only at a 2-D picture.

Consider the case of thermal lensing correction. At first, when there is no induced lens, we have a single point in this plane. This is the initial mode matching. If the repetition rate of the laser is then increased, a thermal lens is introduced. The point will start to move around in this space as we change any of the parameters that have an effect on the strength of the thermal lens (see Figure 60). This is because by changing the lensing parameters, we are effectively changing the value of f_{th}, which has an effect on the beam parameters. By looking at the length of the vector joining the new position in this space to the starting point, one can tell how the beam propagation has been affected. The same transformation, but with a UV scale wavelength is shown in Figure 61. One can immediately see the effect the wavelength has on the propagation: The waist position maps the focal length directly, thus giving a very large spead in the Z_o axis, while giving a very small spead in the W_o axis. In fact, it is saying that the beam will have almost a point focus, in the focal plane of the lens.

Next we introduce an adaptive mirror. The idea is to try and alter the focal length of this element (f_a), and its distance relative to the thermal lens (x), in order to reduce the movement in the characterisation space. We want to choose parameters that will return the system to the original point, and continuously adapt for the

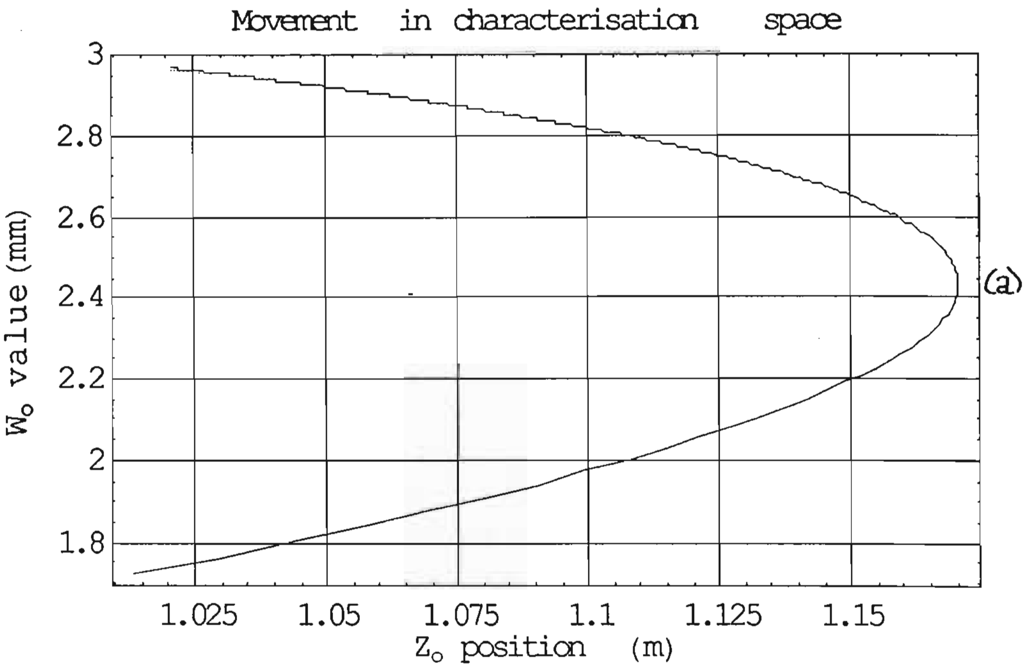

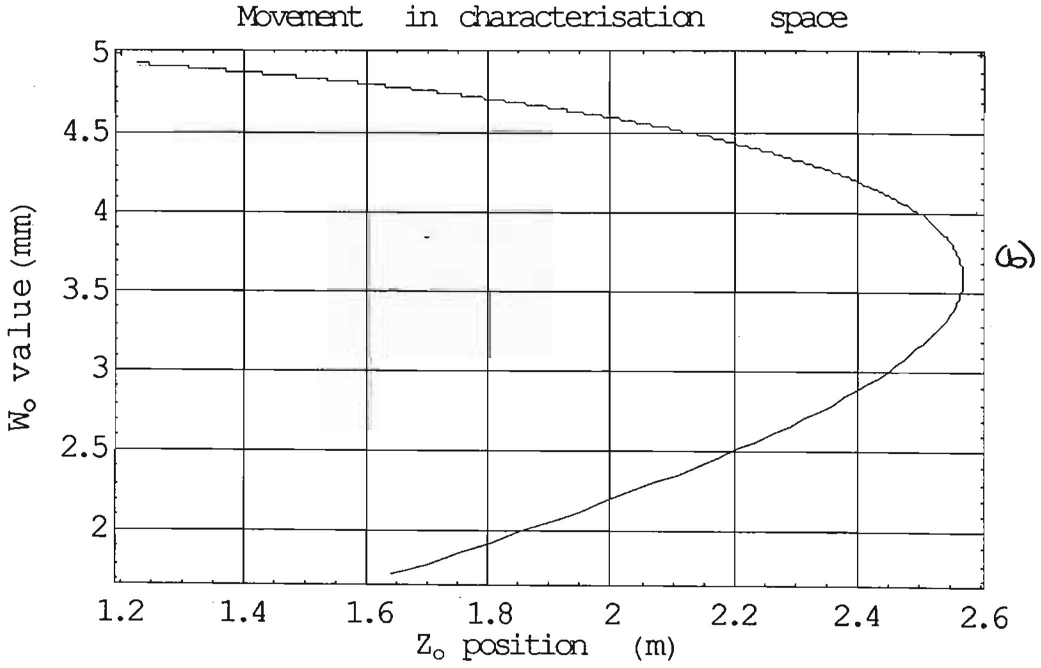

Figure 60: The above graphs show the movement in characterisation space due to transformation through a lens (of variable focal length). The input beam has dimensions of (a) 3mm and (b) 5mm.

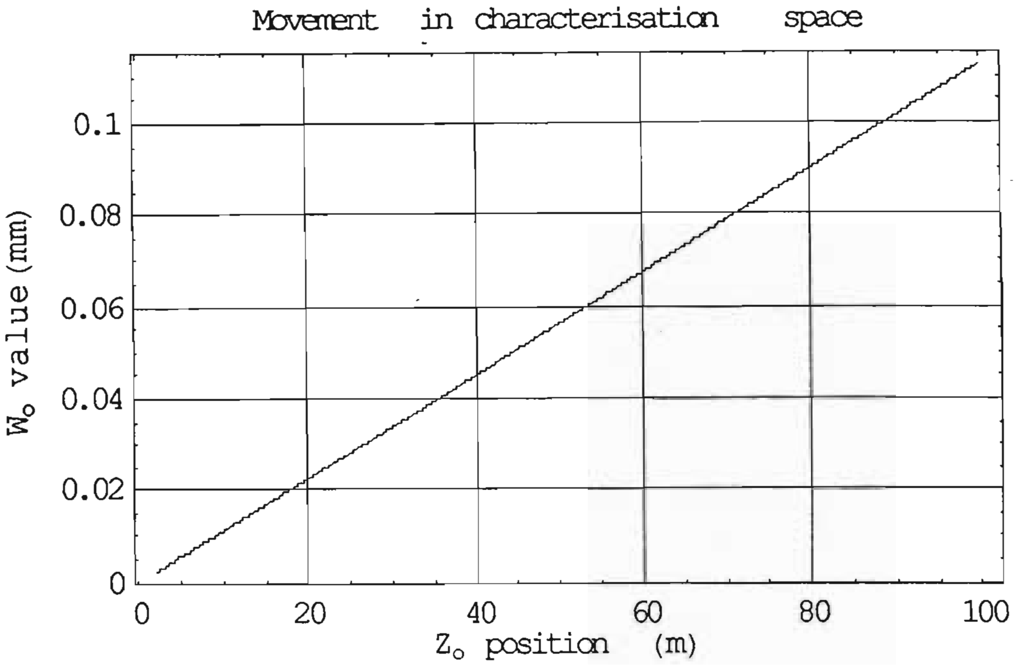

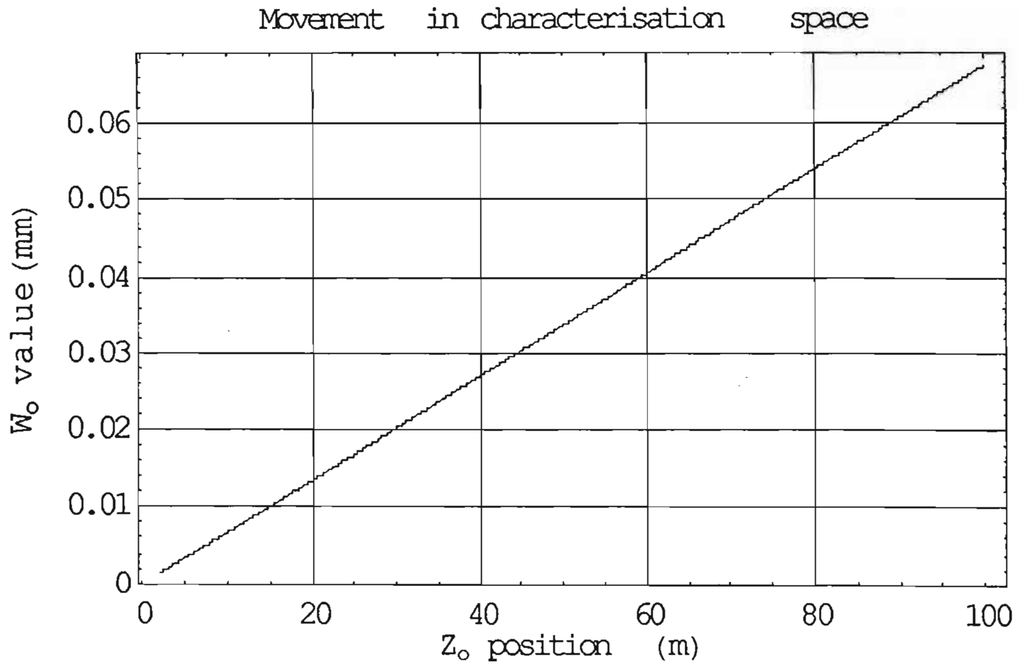

Figure 61: This is a similar plot to Figure 60, except the wavelength has been shorten from the IR to the UV. Clearly geometrical relationships are now evident.

thermal lens in order to stay at this position. We want to minimise the magnitude of the vector that relates our current position in this space to the position that we want to be in. The vector direction is an indication of whether the error is in the position of the waist, or the waist size.

As an example of how this works in practise, consider Figures 62 and 63. The strong non-linear nature of the system is now apparent. In all these figures, the thermal lens was assumed to be a divergent lens (eg. a KCl window) and the adaptive mirror was given a focal length of exactly the same magnitude as the thermal lens, but opposite in sign. The position in this space was then calculated for progressively stronger lensing, starting with a focal length of 50m and ending with a focal length of 1m. As has already been shown, this system will always introduce an error, unless the separation distance is zero ($x = 0$). The errors introduced obviously depend on the separation distance, and the strength of the lensing system. For very long focal lengths, the system should reduce back to the single point mapping; one could in fact call this initial point the attracter for long focal length systems. But in the range of short focal lengths, the separation distance amplifies the errors introduced. The initial waist size and waist position also play a role in determining the behaviour of the system.

At long focal lengths, the error in both the waist (ω_o) and the waist position (z_o) are small. The separation distance does not have a big influence. As the separation distance is increased, so the errors increase. The movement in *characterisation space* follows similar trends for a range of separation distances. However, the interesting phenomena is the effect the initial waist has on the resulting movement: the trends change dramatically. For small input waist values, the beam waist seems to move further away from the window, and then returns to the initial value, passing

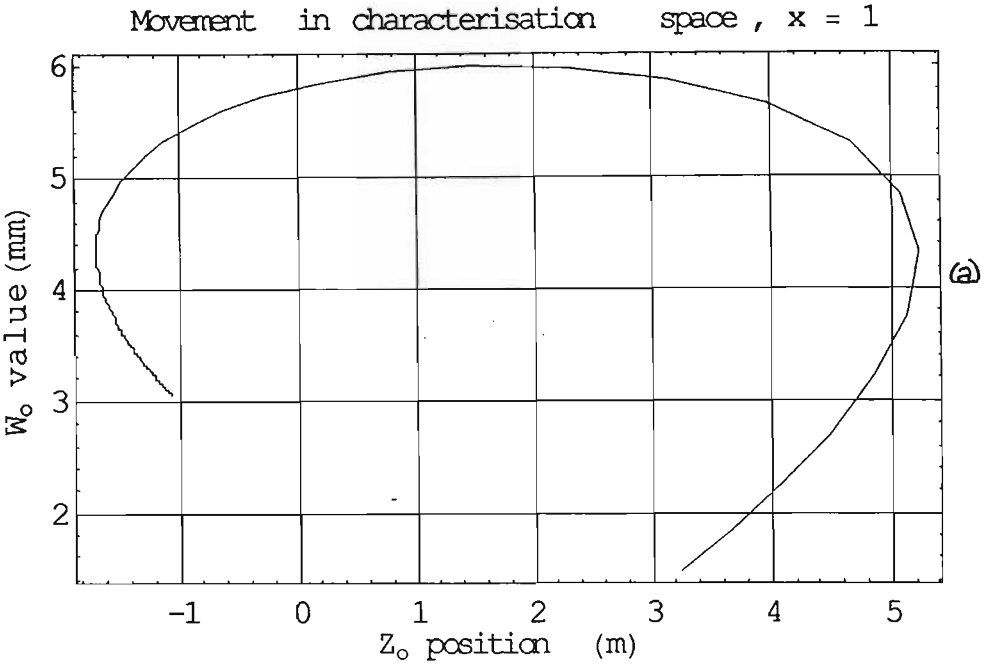

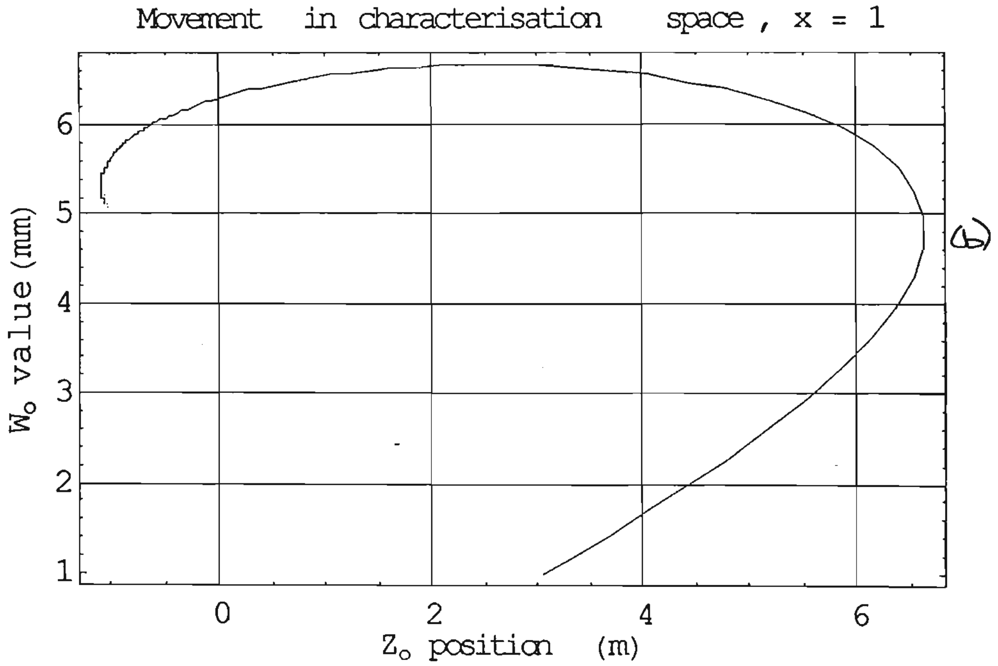

Figure 62: The thermal lens and adaptive mirror take on the same focal length, but separated by 1m. (a) has an input beam of 3mm, and (b) an input of 5mm.

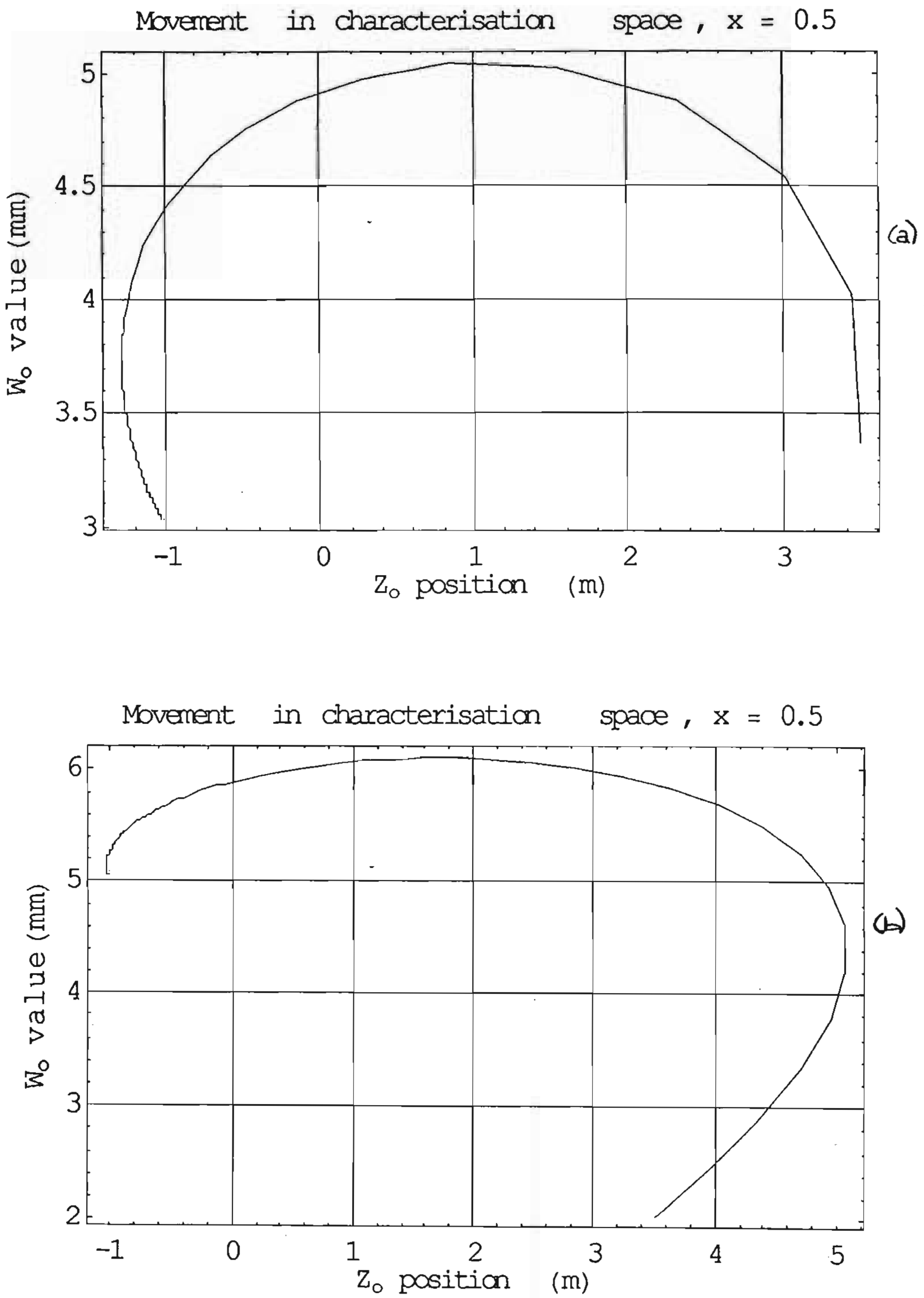

Figure 63: The thermal lens and adaptive mirror take on the same focal length, but separated by 0.5 m. (a) has an input beam of 3mm, and (b) an input of 5mm.

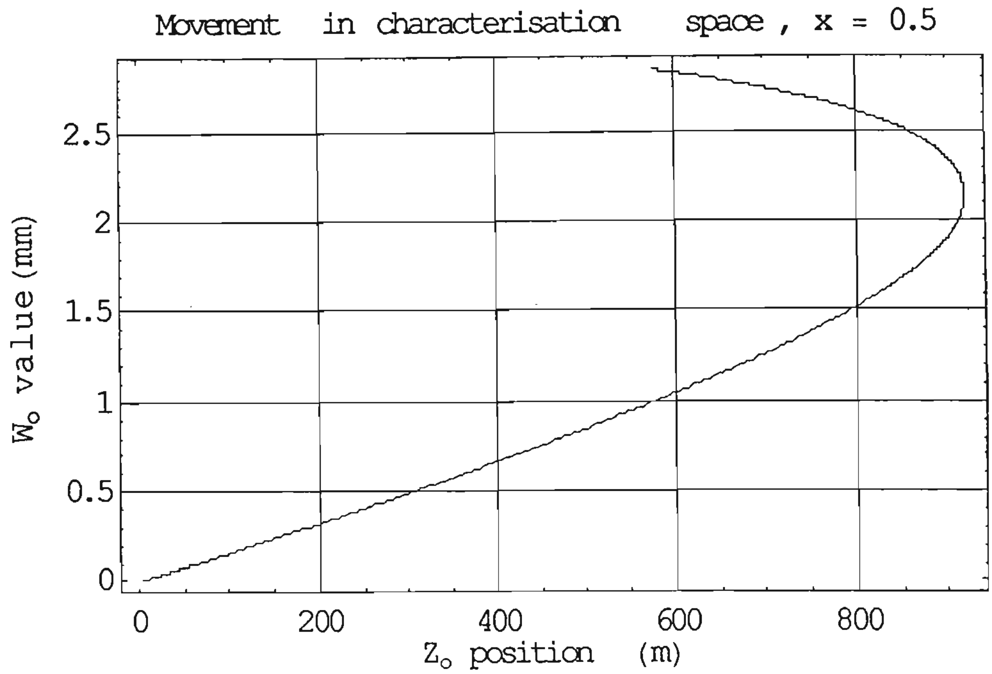

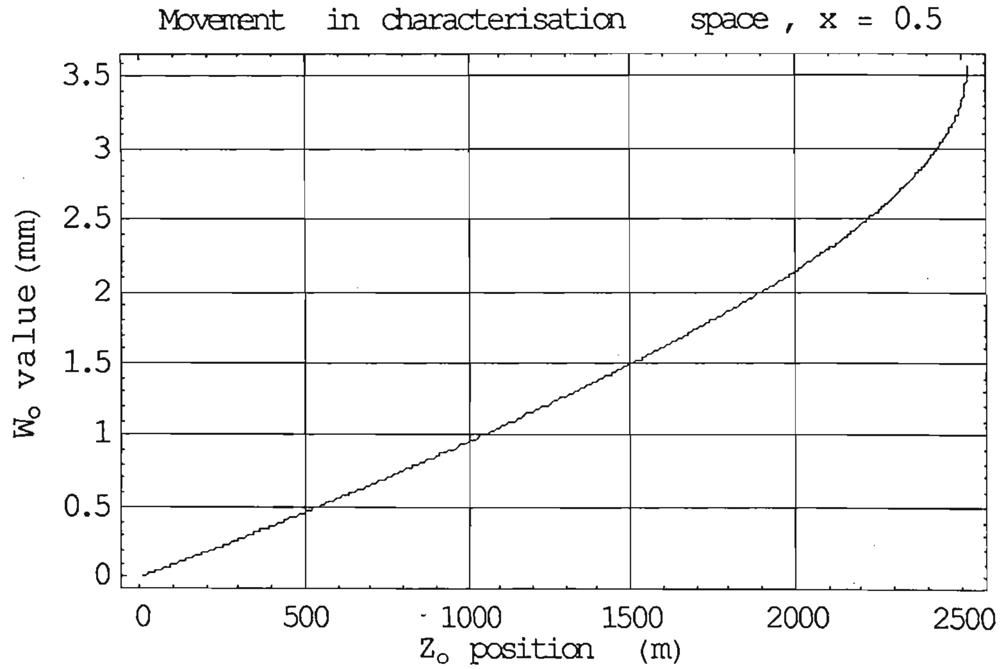

Figure 64: With the same conditions as Figure 63, but with a UV wavelength. The movement in the Z_o axis shows that the system has a very long focal length, and is very nearly compensated for (unlike the IR wavelength cases).

through it at stronger lens values. This shows that the errors can be minimised individually, but not simultaneously. At least not with this system.

Another application of this framework, is to show the behaviour under geometric optics approximations, as opposed to beam propagation laws. For very short wavelengths, we should see a significantly larger spread in the z_o value than in the ω_o value. Thus in the limit of $\lambda \longrightarrow 0$, the characterisation plot should show a horizontal line. Figure 64 is exactly this. Although the graphs look like they behave in a non-linear fashion, a glance at the scale shows that one would have to measure accurately, and extremely far from the lens system (a few hundred meters) in order to detect this behaviour. The result is one only sees linear behaviour at short wavelengths, and hence adaptive compensation is trivial. In fact, because of the negligible spread in the beam size, one is also reduced to a single changing parameter – the focal distance.

For a change in beam quality, but with the same parameters in all other respects, one would expect the movement to vary proportionally in the vertical direction. The horizontal movement should remain unchanged. The reason is that if one considers the propagation of real beams, it can be very easily shown that the beam quality does not change the position of the waist, only the size of the waist.

5.4 Conclusion

This section introduced the concept of an adaptive mirror for mode matching compensation. Only one solution was analysed here, although others do exist and give better results (such as multiple mirrors, or optimisation of the single mirror system). The idea of using a so called *characterisation space* was explored, and shown to be useful when describing systems with dynamic changes in the mode matching. It also serves to illustrate the differences between geometric optics and beam propagation.

Future work will see the use of adaptive systems, not only to compensate for mode matching changes, but also to improve for beam quality by reducing aberrations. The Zernike theory lends itself very well to this application, and indeed many commercially available products use the Zernike description to determine the potential applied to the actuators of the mirror. To produce a system for IR applications, that works at high repetition rates and very high fluences is an ongoing research project.

6 Tensional Vacuum Vessels

6.1 Introduction

All the gas chambers discussed in § 1.4 have one thing in common. It is so obvious that it is perhaps even subconscious: they are all gas chambers constructed with walls in compression. The vessel used in § 1.4 is in fact typical of this design. It is big and bulky, and because it is constructed with walls in compression, the aluminium used is necessarily thick, thus making the chamber expensive. In this chapter, the principle of a tensional vacuum vessel (TVV), developed by Prof. M.M. Michaelis and the present author, is presented. Conceptual extensions of the idea: the inflatable vacuum chamber and the lightweight or even weightless chamber are proposed. An alternative design, the symmetry vessel (SVV), is also proposed. Proof of principle experiments for both the TVV and SVV are discussed, and present, future and far future applications are briefly surveyed.

6.2 TVV principle

Most vacuum vessels (VVs) seem to be constructed with walls in compression rather than in tension. This method of design fails to employ one of the best properties of metals: high tensile strength, while inviting one of the worst structural properties: the metal's propensity to buckle in compression. Nor does the compressional method allow for the use of novel high tensile materials. Instead, we propose a new concept, that of the tensional vacuum vessel[*Michaelis, Forbes*, 1994]. The principle is simple: two linked shells in tension rather than one in compression. The tension is provided by pressurising the intermediate space. Figures 65 (a) and (b) illustrate the conceptual differences between a standard compressional VV and a TVV.

The force on each wall is given by the pressure difference across its surface times the area of the surface (see Figure 65 (b)). If the smaller pressure difference times the larger area of the outer wall equals or exceeds the larger pressure difference times the smaller area of the inner surface, the system is stable. Essentially, by pressurising the intermediate volume, the outer surface is forced outwards while the inner surface is forced inwards. If the pressure and radii are chosen carefully, these forces balance and we say both surfaces are *held in tension* (rather than compression).

Conceptually, the simplest TVV would consist of two linked concentric spheres (see Figure 65 (c)). For equilibrium, one writes

$$\sum F_{out} = \sum F_{in},$$

or

$$4\pi(p - p_o)R_o^2 = 4\pi p R_i^2, \tag{6.1}$$

where R_o and R_i are the outer and inner radii respectively, p_o is the atmospheric pressure and F_{out} and F_{in} refer to the outward and inward forces respectively.. So,

$$R_o = R_i\sqrt{\frac{p}{p - p_o}}. \tag{6.2}$$

If we write $\Delta R = R_o - R_i$ for the thickness of the intermediate space and

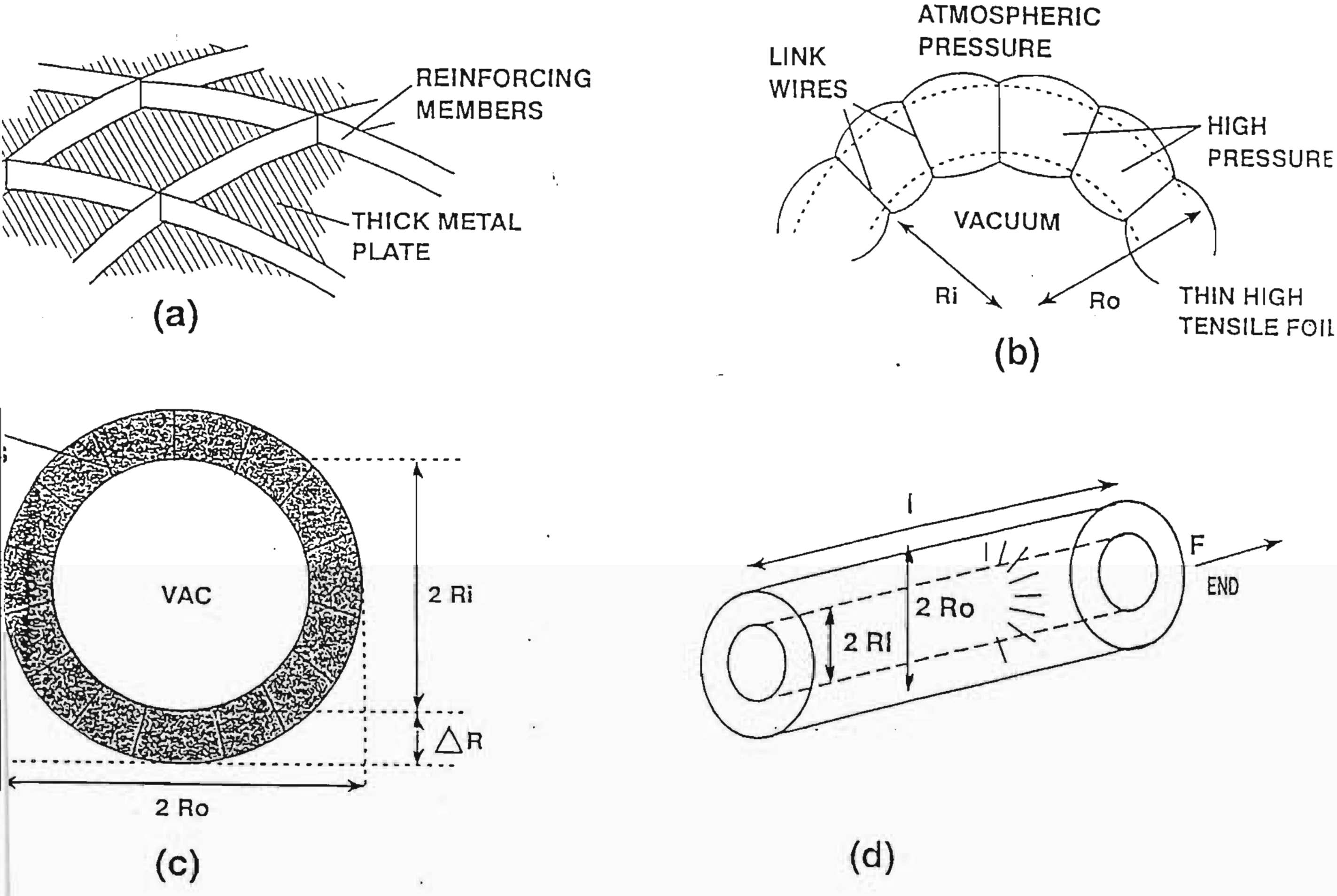

Figure 65: Vacuum vessel geometries: (a) Compressional, (b) Tensional, (c) Spherical, (d) Cylindrical

if $p \gg p_o$, then

$$R_o = R_i \left(1 + \frac{p_o}{2p}\right), \tag{6.3}$$

and

$$\Delta R = R_i \frac{p_o}{2p}. \tag{6.4}$$

Equation (6.4) shows that, as the intermediate pressure is increased, the two shells become closer together. Later, we will consider the material science limitations in having thin shells with larger differential pressures. Although conceptually the simplest, the spherical model is not necessarily the most useful. Indeed, all the gas lens designs employ cylindrical chambers; hence, we consider a double shell cylindrical TVV (see Figure 65 (d)) with two coaxial shells of length l in equilibrium:

$$(p - p_o) 2\pi R_o l = 2\pi p R_i l, \tag{6.5}$$

where

$$R_o = R_i \left(\frac{p}{p - p_o}\right). \tag{6.6}$$

If $p \gg p_o$, then $R_o = R_i(1 + p_o/p)$ and

$$\Delta R = R_i \frac{p_o}{p}. \tag{6.7}$$

At one extreme one sees that, if the pressure is high, the double shell structure can be made quite thin (typically, if $p \approx 10p_o$, then $\Delta R \approx R/10$). The other extreme, that of relatively small pressures, indicates a simple route to the experimental proof of principle which is discussed in § 6.4. A comparison of spherical and cylindrical TVVs is shown graphically in Figure 66. Notice that, in both cases, the intermediate space falls off to zero as pressure increases, but that the cylindrical TVV converges to this limit faster.

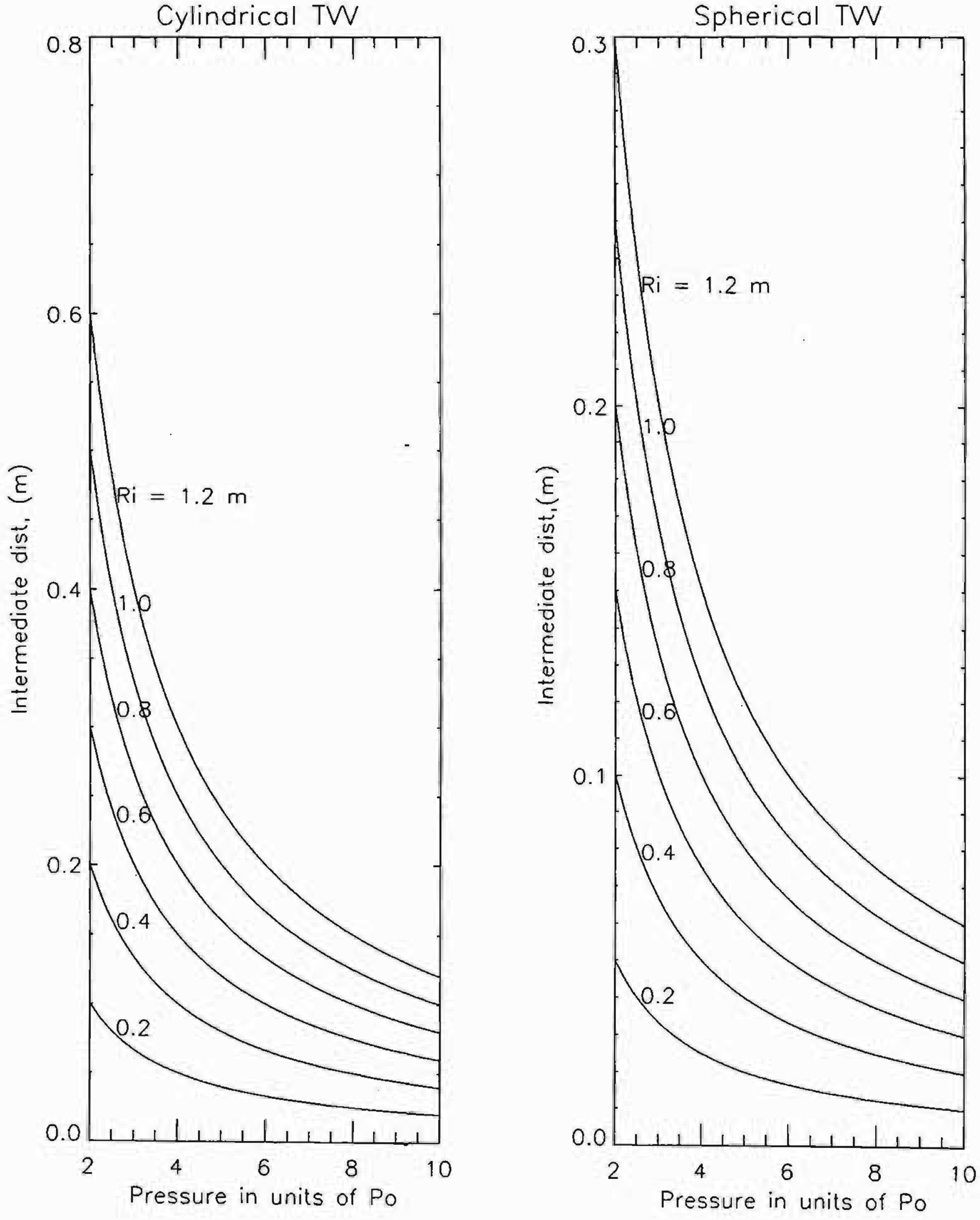

Figure 66: Comparison of Spherical and Cylindrical TVVs

Note that, because the intermediate volume is pressurised, there is more gas in the shell than there was in the now evacuated volume. If the cylindrical shells are terminated with two flat end plates, there will be a net outward force of approximately

$$F_{end} = \pi R_o^2 p_o \left(1 - \frac{p_o}{p}\right). \tag{6.8}$$

This is an important result with regards to safety, as it indicates that TVVs are more likely to *explode* than *implode*. Equation (6.8) does not make it clear that the net force is outward : as $p \gg p_o$, we find that $R_o \rightarrow R_i$ and so coincidentally $F_{end} \rightarrow \pi R_i^2 p_o$, which happens to be the net inward force due to the evacuated volume! One might conclude therefore that the endplates experience a net *outward* force initially, but as p increases so the intermediate space decreases resulting in the *inward* force dominating. That is to say, the outward force, $F_{out} \rightarrow 0$ as $p \rightarrow \infty$, which would give the result that $F_{end} \rightarrow F_{in}$ where $F_{in} = \pi R_o^2 p_o$. However, as Figure 67 shows, $F_{out} \rightarrow 2F_{in}$ and hence, contrary to what one might expect, F_{end} is always *outward* and tends towards $\pi R_o^2 p_o$.

6.3 Novel Concepts

Vacuum chambers can be bulky, expensive and space-consuming devices. One of the reasons that experiments involving vacuum are seldom demonstrated in the lecture theatre is that they require a lot of devoted manhandling. We suggest that it might be possible to build a large, cheap 'pop up' inflatable vacuum chamber: for low-vacuum demonstrations this could be of the thin transparent plastic double-wall type. For the more serious industrial applications, it might consist of three shells –

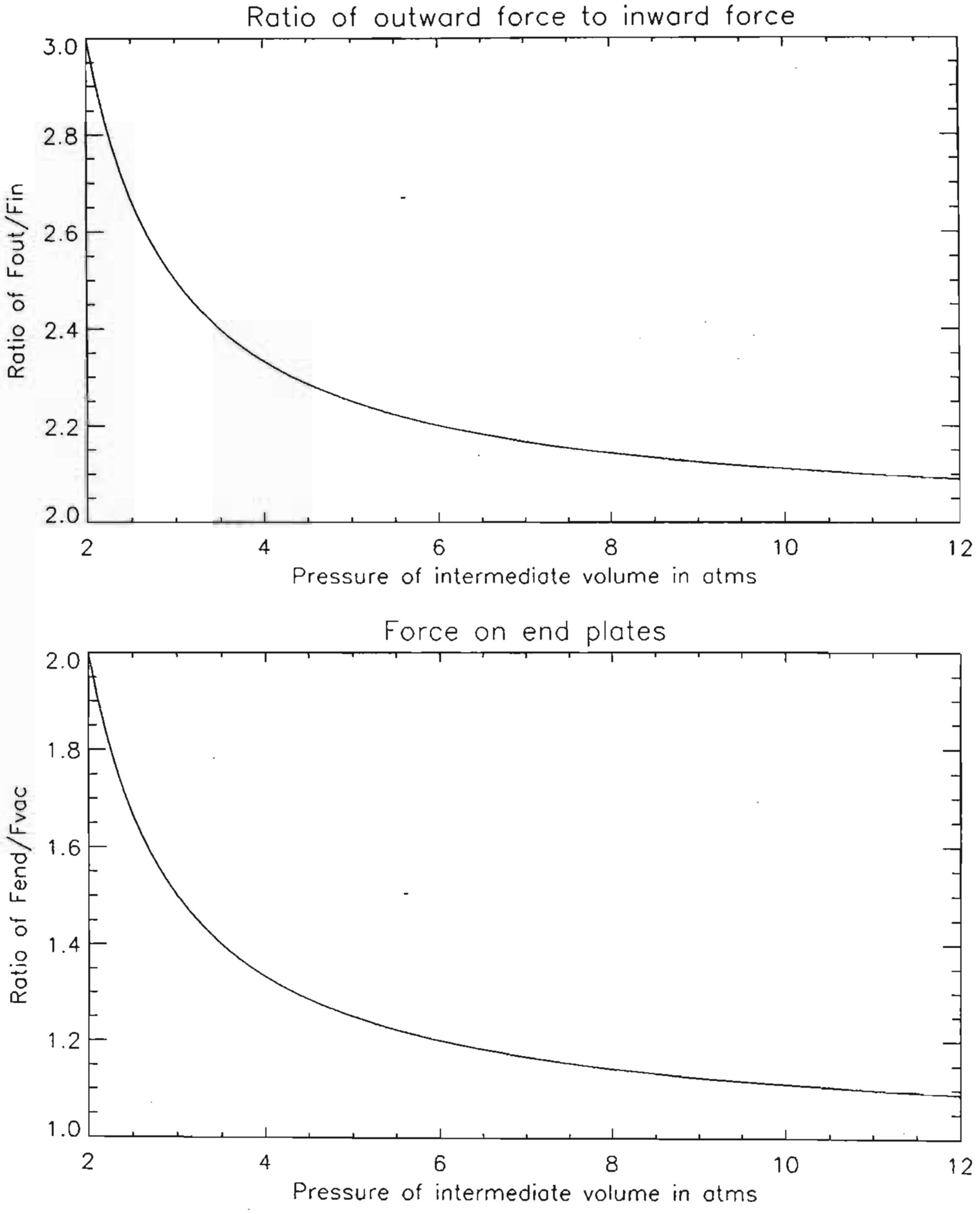

Figure 67: Endplate forces as a function of pressure

the standard two tensional shells and a loosely attached flexible inner guard shell. Both the low and the high vacuum versions could be folded into small containers when not in use.

Another concept that could become of interest, if the double wall technology develops, is that of the lightweight vacuum chamber. In principle, an evacuated chamber would be an ideal 'lifting body'. In practice, however, the weight of the chamber is much greater than the buoyancy force: vacuum chambers require sturdy supports. We pose the question, could a TVV become lighter than air? A short and very rough calculation shows that a TVV fails to become lighter than air when evacuated, even if one neglects the weight of its components.

Consider a spherical, double-walled chamber with radii determined by Equation (6.4). The intermediate volume of the gas is

$$V = \frac{4}{3}\pi(R_o^3 - R_i^3), \tag{6.9}$$

thus

$$pV \approx 4\left[\left(\frac{p}{p-p_o}\right)^{3/2} - 1\right] R_i^3 p \tag{6.10}$$

gives a rough approximation of the mass of the air in kilograms if p is now expressed in bars. The weight is approximately pVg and the effective weight of the gas in the system is

$$W_g = g(pV - V_o), \tag{6.11}$$

where $V_o g = 4/3\pi R_o^3 g$ is the weight of the gas in both chambers prior to pumping. A little algebra gives

$$W_g \approx 4R_i^3 g\left[\frac{p^{3/2}}{(p-p_o)^{1/2}} - p\right] > 0. \tag{6.12}$$

For a thin-walled spherical double shell with $p \gg p_o$, we get $W_{eff} = V_i g/2$, where V_i is the evacuated volume. That is to say, there is 1.5 times more gas in the evacuated and pressurised system than there was in the now evacuated space. A similar calculation for a cylindrical system gives $W_{eff} = V_i g$: there is twice as much gas.

At first glance, therefore, nothing seems to be gained from a weight point of view by using a TVV. However, high tensile materials can be much lighter than the thick metal sheets used in standard compressional designs. In fact, a 1m long, 1m diameter cylindrical chamber could weight as little as 5kg! Also, the picture changes if the gas used to pressurise the intermediate space is 'lighter than air'. (Remember that the important point is that the intermediate volume is pressurised: what is used to achieve this is a secondary issue. For example, water would work just as well.)

Another very rough calculation for spherical shells shows that a double-walled TVV with $R \approx$ 12mm and pressurised with Helium gas could become weightless after evacuation. For two walls, each 0.5mm thick, the volume of the material is $V_m = 4\pi R^2/1000m^3$ and the weight $W_m = \rho V_m g$ (we show later that such a thickness is not unreasonable). The buoyancy force is approximately

$$\left(V_i - \frac{\rho_{He}}{\rho_{N_2}} pV\right) g \approx 10(4R^3 - R^3) \approx 30R^3, \tag{6.13}$$

where the radius of the intermediate chamber, pressurised at 10 bar, is $\Delta R = R/20 =$ 5cm and the intermediate volume amounts to $V = 4\pi R^2 \Delta R = (\pi/5)R^3$. Equlibrium occurs for $\rho V_m g \approx 30R^3$, if $\rho \approx 3000 Kgm^{-3}$ and $R \approx$ 12m. Thus, although this simple 'ball park' calculation shows that it is possible to design a chamber that is itself 'lighter than air', such a chamber would be very large.

An extension of the TVV is obtained by the replacement of the pressurised intermediate volume of the double-shell TVV with several closed-volume unit cylinders, all arranged in symmetry about the centre of the vessel. Each unit cylinder is pressurised and made of some thin material. In principle, the collapse of each individual unit cylinder is avoided by having the internal volume pressurised, while the collapse of the vessel as a whole is avoided by the symmetry of the arrangement. The stacked layers of unit cylinders now form a *Symmetry Vacuum Vessel* (SVV), which is closed at both ends by thick metal plates.

We consider now a cylindrical SVV, which we construct by stacking the unit cylinders in a circular shape. In this model, there is a net *inward* force on each end plate given by

$$F_{end} = p_o \pi R_i^2, \tag{6.14}$$

where R_i is the effective radius of the vessel. This must now be balanced by the reaction forces applied by the unit cylinders. Thus, each cylinder experiences a compressional force of

$$F_c = \frac{p_o \pi R_i^2}{n}, \tag{6.15}$$

where n is the number of unit cylinders in each layer.

There is also a net force, acting inwards, on the outside surface of each cylinder due to the pressure difference created by the evacuation of the vessel. This is approximately given by

$$F_a = 2R_c l p_o, \tag{6.16}$$

where l is the length of each unit cylinder and R_c is the radius. For an arrangement of m layers with n cylinders per layer, the volume of the SVV is roughly

$$V \approx \frac{ml}{\pi}[R_c(n-\pi)]^2. \tag{6.17}$$

Now, Equation (6.17) is slightly misleading. It suggests that the volume of the vessel can be increased by increasing n arbitrarily. However, for a given value of R_c, there is a limit placed on n by the conditions required for the SVV to be stable. Consider any three adjacent unit cylinders in the same level, and label them i, $i-1$, $i+1$. Cylinder i experiences two equal forces, one due to cylinder $i+1$ and the other due to cylinder $i-1$. These two forces must balance F_a, the inward force on the cylinder. If ϕ is the angle subtended by each can at the SVV axis, then the contact forces acting on cylinder i are such that

$$F_c = \frac{F_a}{\sin\phi}, \tag{6.18}$$

with $\phi = 2\pi/n$ and F_c the resultant contact force (see Figure 68 (c)).

For large values of n, $\sin\phi \approx \phi$, and Equation (6.18) becomes

$$F_c \approx \frac{nF_a}{2\pi}. \tag{6.19}$$

The limit on n is that derived earlier in Equation (6.7) and the rupture pressure for the cans. But what value should be chosen for ΔR? A sensible guess would seem to be the width d of the contact area ld between the cans (see Figure 68 (e)). If p is the pressure acting at this contact area, then

$$F_c = pld = \frac{nF_a}{2\pi} = \frac{n}{2\pi}p_o 2lR_c,$$

Therefore,

$$d = \frac{n}{\pi}\frac{p_o}{p}R_c.$$

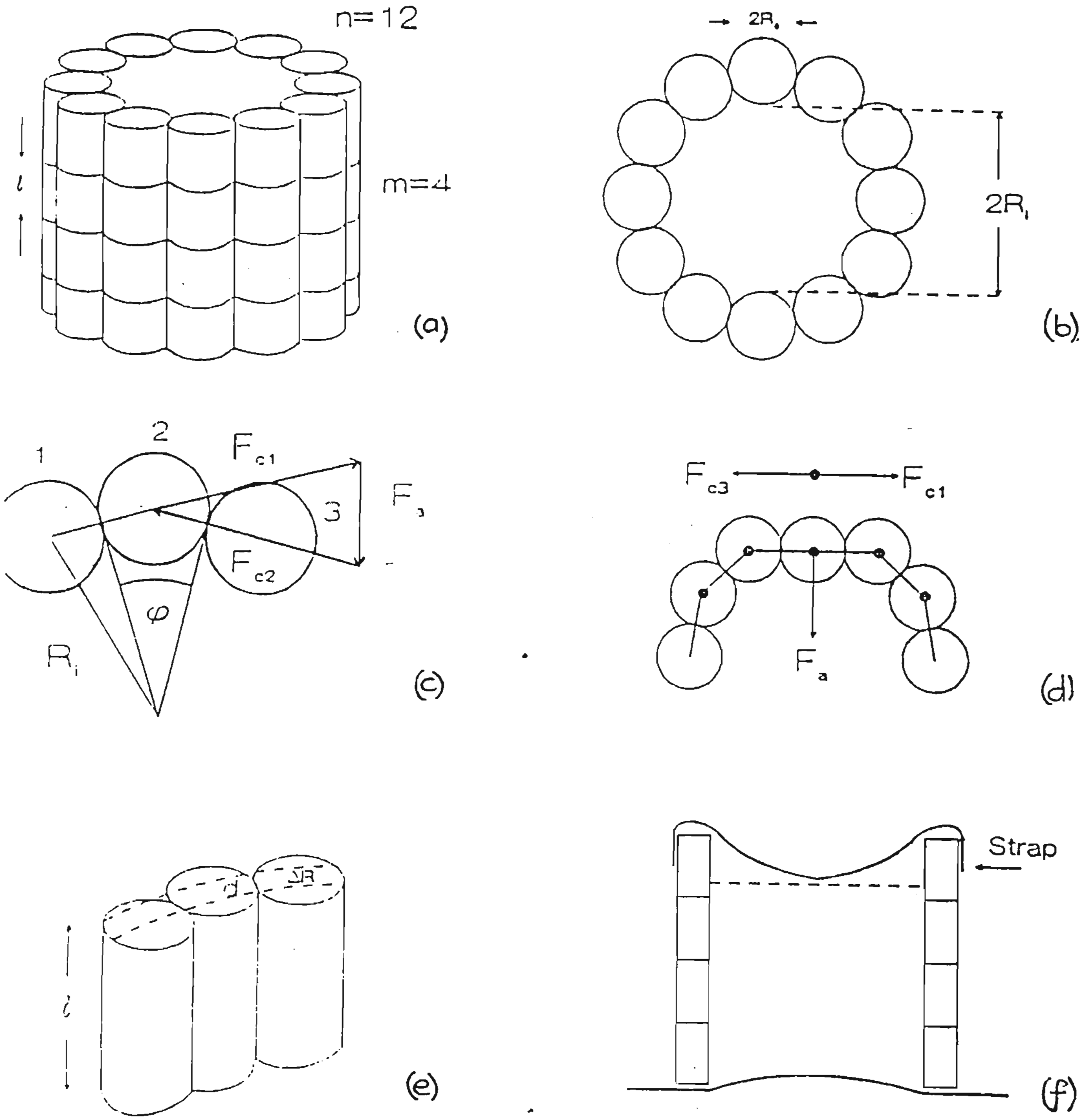

Figure 68: Diagrams (a) to (f) show various interactions of the SVV cans. The cans are arranged as shown in (a). (c) illustrates the contact forces on any given can, and (e) shows the contact area between two adjacent cans.

Noting that $2nR_c = 2\pi R_i$, we find that

$$d = R_i \frac{p_o}{p}. \tag{6.20}$$

Comparing Equation (6.7) and Equation (6.20), we see that $d = \Delta R$ for SVV's. This could also be arrived at by noting that the inner and outer can arcs could be replaced by strong flat plates joining the contact lines, with no change in the dynamics of the system. So the limit on n if p_{max} is a safe threshold pressure for the cans is

$$n_{max} = \frac{\pi d p_{max}}{R_c p_o}. \tag{6.21}$$

Geometric considerations indicate that a sensible ratio for d/R_c could be 1/3. Then $n_{max} \approx P_{max}/p_o$, which would seem to limit the number of unit cylinders rather drastically for pressures under ten atmospheres.

The next restriction on n results in a minimum number of cans appearing to be necessary. This comes from considering what happens if one of the cans happens to become misaligned so that three can centres are in line (see Figure 68 (d)). The only thing that can prevent implosion due to the atmospheric force F_a is friction. Can i experiences two normal forces due to the $i+1$ and $i-1$ cans, which results in a net load of $p_o R_i l$ on can i. This results in a frictional force to balance F_a given by

$$F_i = 2\mu_c p_o R_i l,$$

therefore

$$2\mu_c p_o R_i l \geq 2 p_o R_c l,$$

or

$$\frac{R_i}{R_c} = \frac{n}{\pi} \geq \frac{1}{\mu_c};$$

which results in a minimum value of n given by

$$n_{min} \geq \frac{\pi}{\mu_c}. \tag{6.22}$$

We now seem to have placed limits on the number of unit cylinders (cans)in each layer in order to ensure stability. For typical metal to metal values of $\mu_c = 0.2$, we find that $n_{min} \approx 16$ while from Equation (6.21) we have that $n_{max} \approx 10$. With a minimum of 16 and a maximum of 10, it begins to look as if the SVV structural stability is problematic. However, the effects of the end plates have not yet been considered. The two end plates will introduce additional frictional forces on each can. The net frictional force on the i^{th} can now becomes

$$F_i = 2\mu_c p_o R_i l + \frac{2\mu_e p_o \pi R_i^2}{n}.$$

Thus for equilibrium(and stability) we require that $F_a \leq F_i$, giving

$$2p_o R_c l \leq 2\mu_c R_i l p_o + \frac{2\mu_e p_o \pi R_i^2}{n}.$$

This results in a new value of n_{min} given by

$$n_{\text{min}} = \frac{\pi l}{\mu_c l + \mu_e R_c}. \tag{6.23}$$

where μ_c is the coefficient of friction between two adjacent cans and μ_e is the can–end plate coefficient of friction. For typical values of μ_c and μ_e we find $n_{min} \approx 14$ for the coke cans used in our SVV.

It has been shown however that under certain circumstances the effective coefficient of friction, μ_e, can be very large, reducing the minimum number of cans to a reasonable number [*Michaelis, Mckenzie, Forbes*][7]. In fact, in all the experiments conducted, the large R_c/R_i ratio for the small chambers ensured stability, while for the larger chambers, the friction due to the interlocking of the cans increased the friction between the end plates to the extent that vessels with $n \leq 15$ and $m \leq 4$ where stable. We may interpret these results as saying that since $R_i/R_c \propto n$, we

---

[7] *to be published*

cannot increase the vessel size (R_i) by increasing n arbitrarily. Because of limits placed on n to ensure stability, an increase in R_i must be accompanied by an increase in R_c. This prediction will be referred to in the next section to explain the implosions observed in the experimental SVV chambers.

6.4 Experimental Chambers

To put the idea of a tensional vacuum vessel to the test, two types of experiments were conducted. The purpose of the first was to demonstrate the TVV principle (the didactic experiments) and that of the second was to gain practical experience with 'useful' TVVs.

The didactic experiments were carried out with flexible transparent plastic bottles linked with nylon wire. Photographs of the plastic double–walled vessel are shown in Figure 69. Two domestic vacuum cleaners were attached, one in the blowing mode the other in the sucking mode. The virtue of this type of experiment is that one can see and even feel the forces at work: switch off the 'blower' briefly and the chambers immediately start to implode. Switch it back on and one observes the tensional dimples forming in the outer shell as it takes the strain. Gentle finger pressure exerted on the outer shell causes the inner shell to buckle. This 'proof of principle' experiment also serves as a test for the 'pop up' inflatable chamber discussed in § 6.3. The use of flexible plastic bottles (the standard 250ml orange juice bottle and a 2l cola bottle) had the desired effect of producing a cheap but robust vacuum vessel.

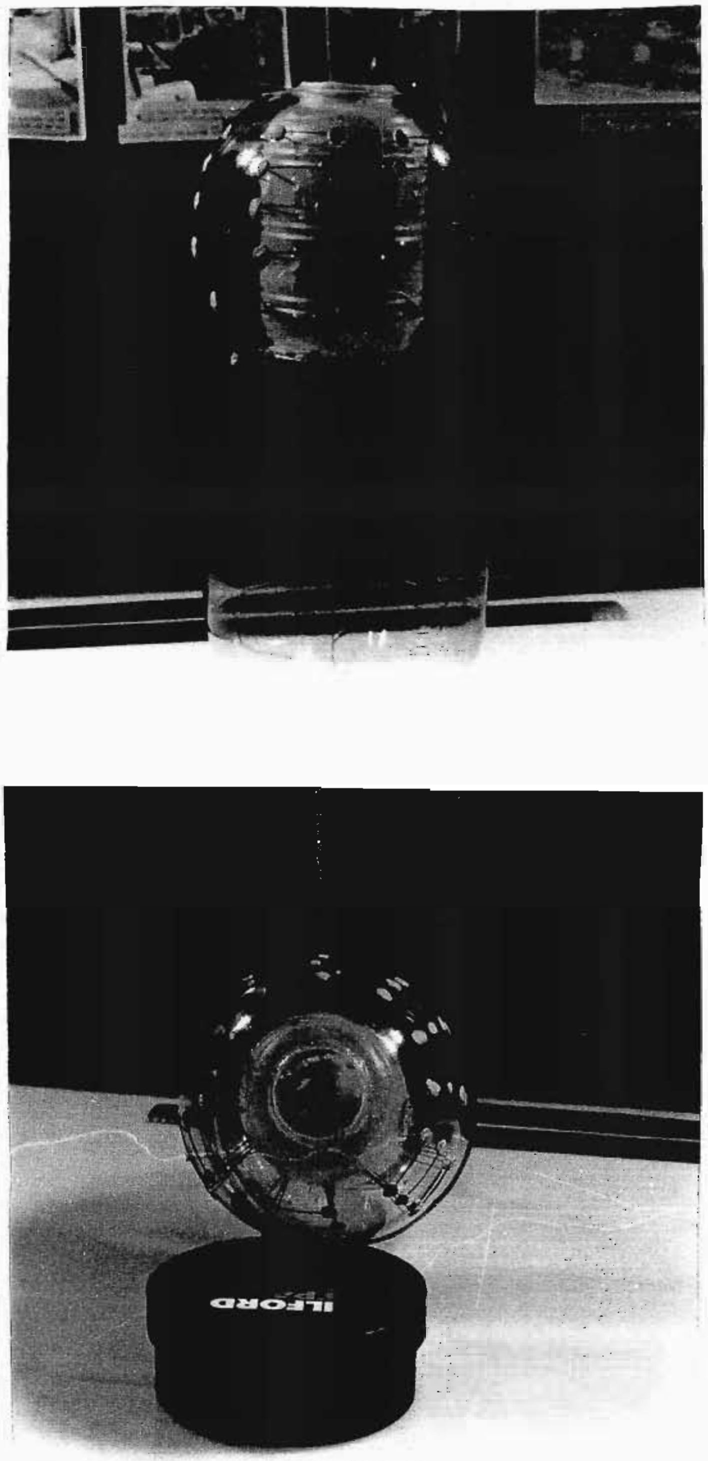

Figure 69: Didactic double-walled vessel. The outer chamber is made from a clear plastic, connected to the inside plastic bottle by cotton.

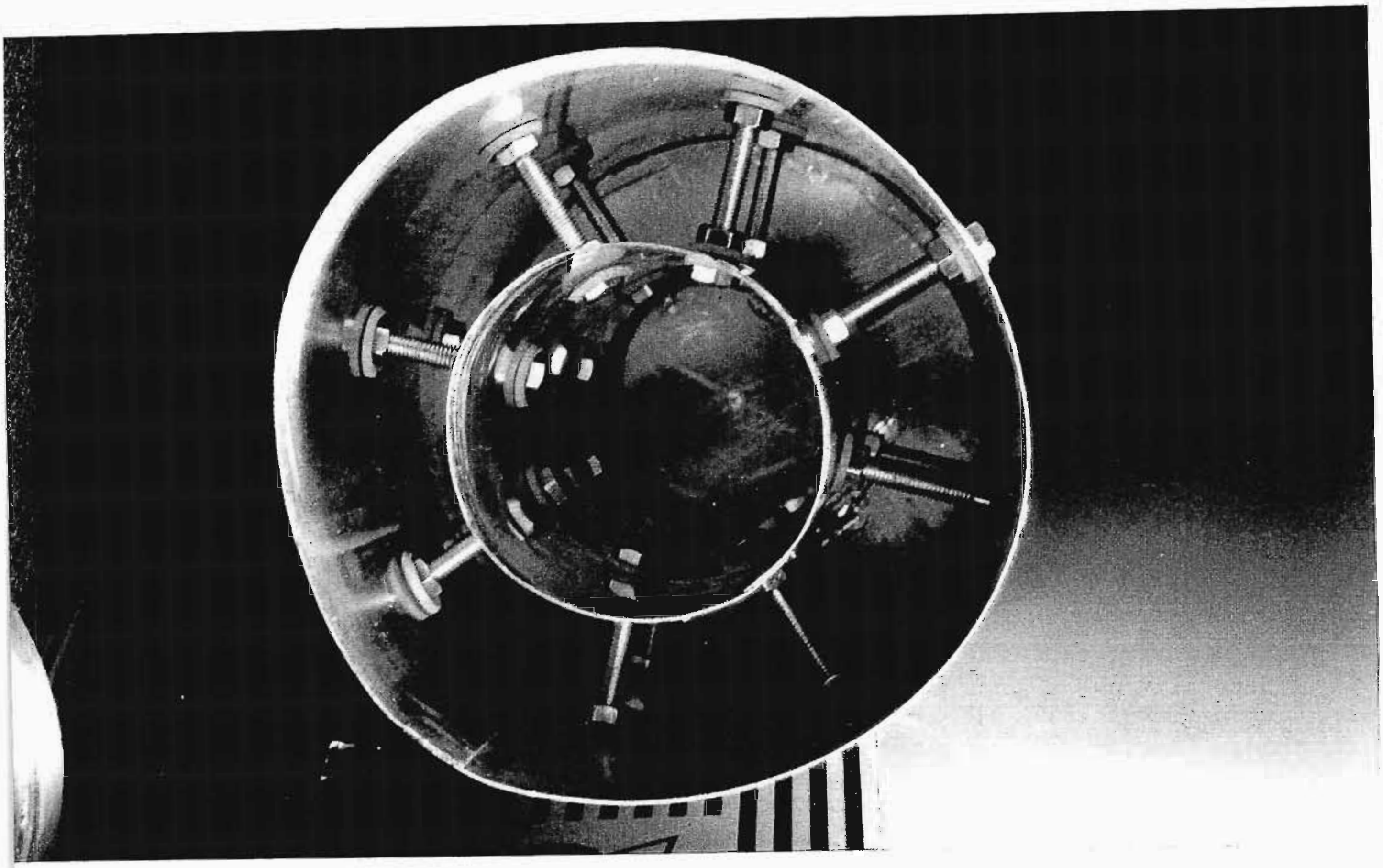

Figure 70: Cylindrical TVV made from 0.2mm brass sheet, which was capped at both ends by aluminium plates.

Experiments on a more 'useful' TVV were performed, using two concentric cylinders made of 0.2mm brass sheet (see Figure 70). The two 17cm long cylinders with $R_o = 2R_i = 6$cm were linked by sixteen 3mm diameter struts soldered at each end. In our first chamber these struts were bolted to the two surfaces, but this method caused leakage. The cylinders were capped and glued at both ends with 1cm thick aluminium plates, one of which had two ports for the pressure hose and the 4mm vacuum pipe. At an intermediate pressure of 2 bar, a partial vacuum of around 1mbar was achieved. These chambers were not meant to be high vacuum devices, and the operating pressure of 1mbar was typical for all TVV experiments. A few interesting results came from these experiments. Firstly, we found that the inner surface was more likely to rupture than the outer surface. This could be due to the fact that the inner surface supports the larger pressure difference. Secondly, we found in practice that the intermediate pressure needed to be slightly greater then the value predicted in § 6.2. The reason for this is discussed in § 6.5.

Several chambers using the SVV design were built and tested. For all of the experiments, standard cola cans were used as the unit cylinders, having radius $R_c = 3$cm and length $l = 11.5$cm . In order to facilitate the comparison of various SVVs later in this chapter, we shall use the abbreviation SVV-n to refer to an n-layer symmetry VV.

The first chamber consisted of six cans arranged symmetrically (see Figure 71) about the centre of a circle and closed at both ends with 1cm thick aluminium plates. Prestik was used to seal any leaks. This vessel was a successful low vacuum chamber. To increase the pressure on the outside surfaces, the experiment was modified to allow the SVV-6 to be submerged in water and lowered to increasing

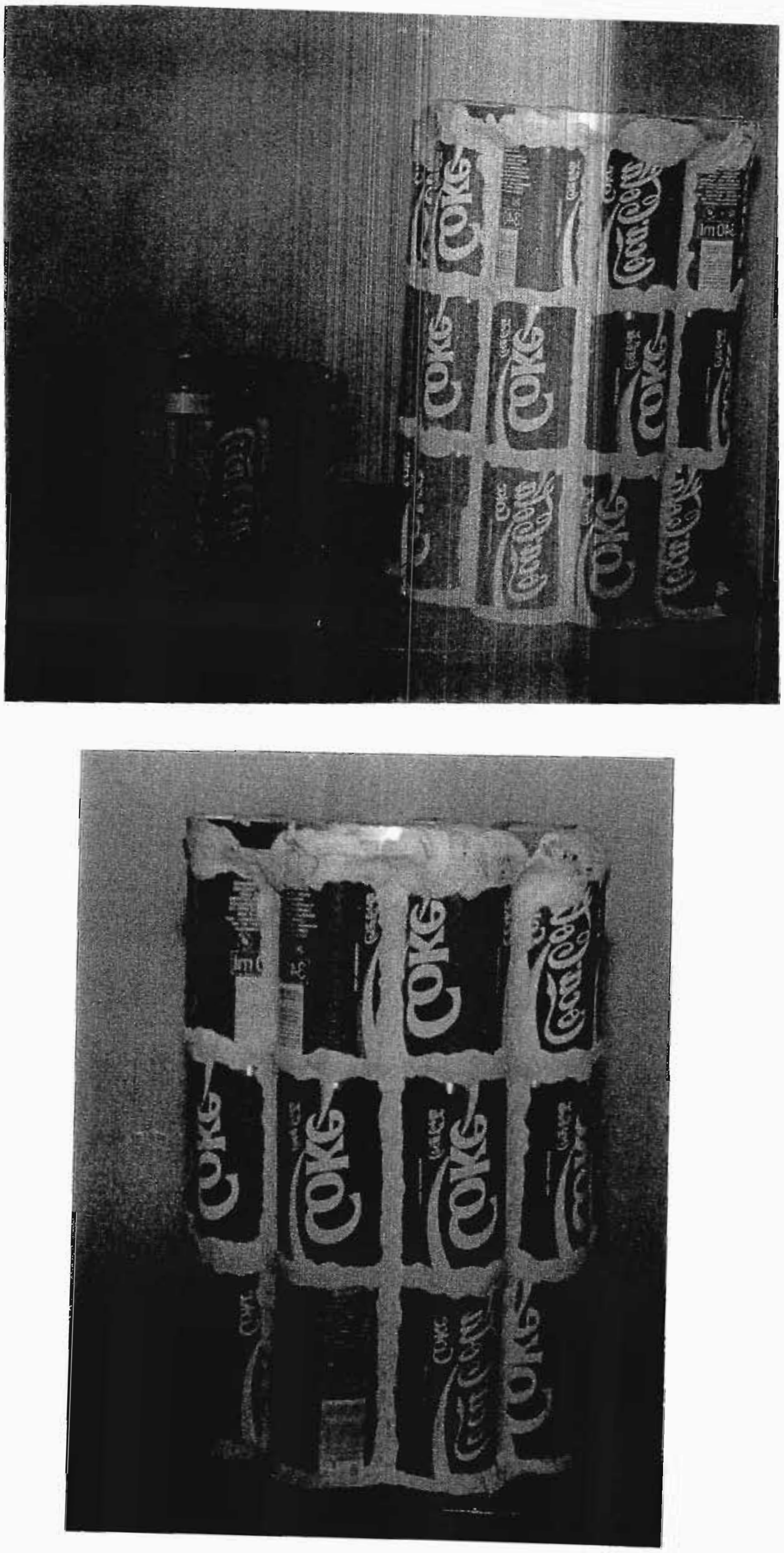

Figure 71: Coca Cola can SVV design: SVV-6 and SVV-10. The cans are arranged in layers and the resulting chamber is sealed with prestik.

depths. The vessel remained stable and held the low vacuum, although it should be said that we were limited to depths of between 2 and 3 meters (due to the pool depth and the limited vacuum piping).

In order to establish whether a chamber could be made that would have a useful working volume, a *two* layer SVV-10 was made which was later converted into a *three* layer SVV-10 (see Figure 71). Both chambers were successful and had interior volumes of around 3l and 4.5l respectively. This is comparable to small vacuum chambers used in industry. With the three layer chamber one could observe the slight inward movement as the cans took shape. An interesting result was the inward curvature of the three layer vertical column. This suggests that, as m is increased (by adding more layers), the vessel will be more unstable. The reason is that, although in principle there should be no limit, in practice the cans are never perfectly arranged with their longitudinal axis parallel; hence, the chamber could become unstable for large m simply because the small deviations are exaggerated as m increases. In particular, if the number of cans is large, even a small misalignment becomes serious: for if ϕ is small, the misalignment $\delta\phi/\phi$ can be large; and since $F_i = F_a/\phi$ is much larger than F_a, the resulting imbalance $2F_c\delta\phi$ can be of the same order as F_a itself. This may result in any initial geometric error becoming accentuated as the chamber "breathes" each time it is let up to air or pumped down. If an increase in the volume is the only requirement, then longer unit cylinders would be a better option to allow $m \to 1$. As might be expected, when n was increased, the initial symmetry of the arrangement was critical. Any deviation resulted in the vessel imploding.

This experimental vacuum work was later continued by another member of the *UND Laser Group* without prior knowledge of the results contained in the previous section. With his permission I give a brief account of the experiments, but focus rather on an explanation of what was observed.

A SVV-30 was built using the same cola cans as described above, with $m = 1, 2, 3, \ldots 8$ respectively. For all the vessels, support was needed on the interior of the vessel to avoid implosion. For the single layer SVV-30 a sand bowl of radius approximately equal to R_i was used. It was thought that the bowl would only help maintain symmetry and not supply any support. However, while the vessel held 94% vacuum with the bowl, the vessel collapsed when the bowl was removed. The experiment was repeated with the bowl replaced by a thin aluminium ring of radius again $\approx R_i$, but again the chamber imploded. For later versions of the SVV-30 $(m > 2)$, steel bicycle rims were modified to support each layer.

We suggest here that the reason for the stability of the SVV-6 and SVV-10 is that, in these cases, $n < 16$ while the unstable nature of the SVV-30 is due to the fact that $n \gg 16$. This implies that the bowl and bicycle rims act as supports and are the only reason for the chamber not imploding. Because $n > n_{max}$, the frictional force becomes too small and there is a net inward force on each can. This is balanced by the supports. The reason, then, that the SVV-30 with $m = 1$ imploded with the aluminium ring in place could be that the ring was very thin and did not provide enough support. Further support of this theory is lent by the fact that some of the cans in the experiment did eventually rupture. Since the ruptures were located at the contact points of the bicycle rim and the cans, it implies that the rims had a part to play in preventing the inward motion of the cans. To fully test this theory, vessels should be made with $n = n_{max} \pm \varepsilon$ and their relative stability compared.

The final point made here concerned the rupture of the cans. This rupturing of the cans in the TVV experiments brings home the limitations of the materials used. We give these considerations more attention in the next section.

6.5 Material Science Limitations

In this chapter, two vacuum designs have been presented. We now consider the limitations placed on these vessels by virtue of the materials used, and look at various safety aspects.

We consider first the TVV design. Clearly, the inner and outer walls require greater curvature than that of the chamber if the walls are not to be too thick. The need for a small radius of curvature R_c has to be balanced by the designer's desire to reduce the number of links and also by the need to avoid stress induced cracks at the link-wall attachment points (this is not the same R_c as in the SVV case, although there is an obvious analogy between the two terms). A little consideration of the geometry of Figure 65(b) will show that, for a thin double-walled chamber with $p \gg p_o$, R_c could be of the order of $2\Delta R$. Thus, for a 2m diameter cylindrical chamber pressurised to 10 bar, R_c is of the order of 20cm. This requires a tension T in the material such that

$$\Delta p = \frac{2T}{R_c}, \tag{6.24}$$

or

$$T = \frac{\Delta p R_c}{2} = 10^5 N m^{-1}. \tag{6.25}$$

Now, the ultimate strength of modern lightweight high-tensile materials varies up to a maximum of $p_m = 500$ MPa for SiC/SiC composite materials [*Schultz*,1991]. If d is the thickness of the foil, then $p_m d = T$ or $d = T/p_m = 0.2$ mm.

This 'ball park' calculation shows that very thin foils, definitely less than half a millimetre thick, could be used. Thus, TVVs could be much lighter than conventional vacuum chambers.

An important aspect of the material limitations is safety. Even small containers, pressurised to several bar, represent a hazard. The calculations in this chapter show that, contrary to a conventional vacuum chamber, there is little danger of materials (or people) getting sucked in, since there is more gas in the intermediate volume than is missing from the evacuated space. Implosion may be unlikely, but explosion is not. Any TVV would need to be carefully shielded. Alternatively, the intermediate volume could be pressurised with foam or liquid rather than gas (as has effectively been the case in the SVV experiments), rendering rupture inoffensive. We mentioned in § 6.4 that experiments suggest that the intermediate pressure needs to be a little higher then the equilibrium pressure p_{eq}, given in § 6.2. This is to avoid excessive curvature and consequent rupture of the membranes. Clearly, the radius of curvature R_c increases with pressure. At high pressure, R_c is of the same order of magnitude as the chamber radius. As p approaches a value some 10 to 20% above p_{eq}, the chamber takes on its ideal (slightly bumpy) appearance. As $p \rightarrow p_{eq}$, R_c decreases catastrophically and the chamber implodes.

Next, we consider the SVV-n design. Since this chamber will always implode when it becomes unstable, the safety rules for conventional chambers apply. In all our experiments the unit cylinders were pressurised with liquid. As noted previously, the cans ruptured due to the force applied by the additional support. Therefore, in general, it is worth examining the strength of the units cylinders individually, since, as the saying goes, *a chain is only as strong as its weakest link.*

There are always at least two forces acting on the unit cylinders due to the pressure difference. The first of these,F_c, is due to the end plate, and the second is a force perpendicular to the cola can axis, F_a. The force on the cylinder surface (F_a) is always constant, regardless of the SVV-n size. The force acting parallel to the cylinder's longitudinal axis, F_c, changes as n changes. To see this, we note that $R_i \propto n$ and $F_{end} \propto R_i^2 \propto n^2$. Now, since $F_c = F_{end}/n$, we might expect $F_c \propto n$. This is indeed the case, and a little algebra gives (for $n \gg 3$)

$$F_c = R_c^2 p_o \left(\frac{n}{\pi} - 2\right). \tag{6.26}$$

This shows that an increase in n does not cause the longitudinal force to be distributed further, thereby decreasing the force on each can (F_c), because, as n increases F_{end} increases faster (as n^2). To summarise, we have Equation (6.26) which describes the longitudinal forces due to the pressure difference, as well as the identity $F_a = const$ for the radial inward force (given by Equation (6.16)). One would think then that these two forces place additional restraints on n and R_c. Experiments on the cola cans, carried out by the author, in the *Department of Mechanical Engineering, UND*, shows that rupture of the cans occurs at

(i) $(F_c)_{max} = 7680N$

(ii) $(F_a)_{max} = 3000N$

The above figures serve to illustrate the point of the strength of a pressurised unit cylinder versus thick metal in compression. Using the figures above, we can determine that a vessel of $n \approx 275$ cans would still be very stable in the sense that the cans would not rupture! As a further indication of the can strength, the radial force F_a for our experiments was only 23% of the maximum allowed value.

The only disadvantage of the SVV design, is that the arrangement of the cans is critically dependent on the initial symmetry, causing implosion to occur easily. Also, all chambers were built with the layers in the horizontal plane and stacked vertically. It seems reasonable to assume that, when the axis is rotated to lie in the horizontal plane, the force of gravity would cause large chambers to become even more unstable. Only the SVV-6 was tested at different angles and found to perform successfully.

6.6 Applications: Present and Future

The history of the development of a scientific or technical concept may excite added interest if the concept happens to be subject to patent legislation. Anyone intending to construct a TVV would probably like to know of the existence of three relevant patents which we refer to as the Rome, the Paris and the Milan. All three patents are especially concerned with submarine applications in which the hollow walls of the submarine system are pressurised as in a TVV. But all three patents also take care to avoid being specific about the marine aspect and would therefore apply to TVV's.

The "Rome patent" of Marcella de Cesaris and family (U.K. 1 031 415 June 1966) essentially describes "a structure comprising walls of rigid material having cavities" containing "a compressible fluid under high pressure" "to prestress the structure". The structure "behaves as far as its compressive strength is concerned, as if its walls were of solid construction" although the weight "is considerably less than that of a comparable structure possessing solid walls". The mechanical resistance sometimes "surpasses that of a comparable structure with solid walls". Pressurisation

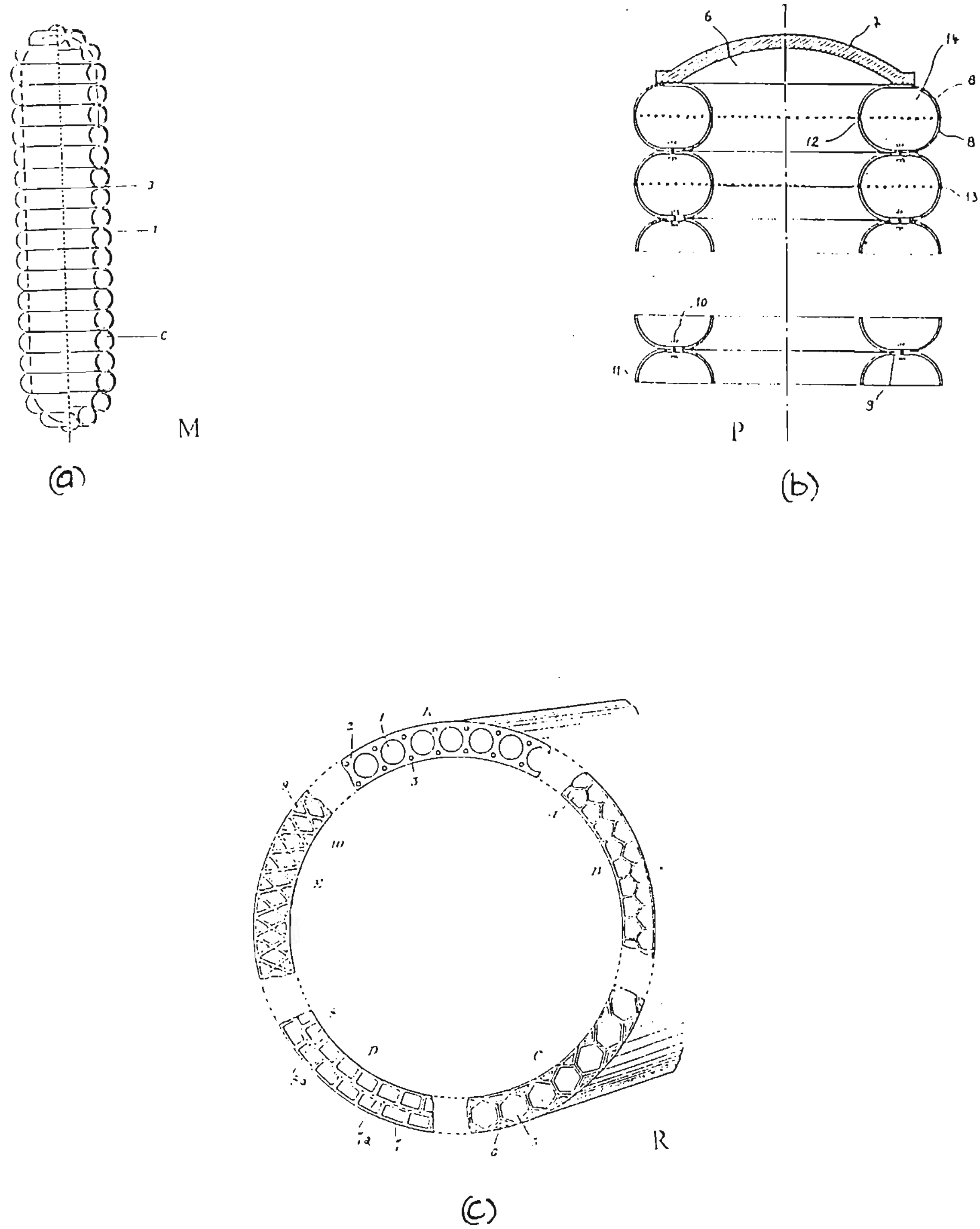

Figure 72: Three patents similar in concept to the TVV:(a) The 'Milan patent',1979, suggested for underwater hulls or tanks, (b) The 'Paris patent',1975, suggested for submarine work, (c) The 'Rome patent',1966, using pressured cavities for strength.

with "hydrogen to 200 atmospheres" may seem a little extreme. No specific mention of vacuum applications is made.

The "Paris patent" by Andre Grihangne and Guy Delamare (France 2 326 229 October 1975) is very similar to the "Rome patent" but much more elaborate. Amongst other ideas, the French imagine thin flexible walls, great economy of material and weight, walls purely in tension, walls that can be folded away, and non metallic walls made of woven coated fibre. Although the claims describe a reservoir or duct "under lower pressure than its surroundings", they do not appear to explicitly mention vacuum as an application. The main concerns of their work are submarine applications such as the suction of ocean floor metallic nodules and petrochemical ducting. The French patent also contains an elementary calculation of the intermediate pressure required to put the walls under tension for a specific pressure differential.

The "Milan patent" by Sub Sea Oil Services (U.K. 2 026 951 May 1979), also deals with underwater hulls or tanks with "toric components" pressurised with the aid of "compressed substances".

Any engineer wishing to design a TVV would find the drawings contained in these patent documents useful (see Figure 72). A tensional submarine vessel design could be almost instantaneously converted for vacuum work, simply by reducing the required strength and thickness of the walls.

Enquiries from various military and civilian bodies have failed so far to find any practical marine applications of this technology.

Because TVVs might well become cheaper to produce and much lighter than present day systems, they could find immediate use in laboratory experiments, electron beam welding and optical coating plants. Certainly the models made have a large enough volume to be deemed 'useful'.

TVVs could also find uses in the design of gas lasers and laser systems[*Michaelis, Forbes*, 1993]. Future laser systems involving testing chambers could have these chambers replaced by tensional vessels. As an example, the test chamber used for the spinning pipe gas lens could easily be replaced by a TVV. The metal end plates would be replaced with thick optical glass, and the struts could act as ducts for the electrical connections. Gas lasers work on the principle of having a gas at pressure p enclosed by a thin permeable material surface. This volume is placed in a vacuum to enable the high energy electrons to penetrate the surface (and hence the gas). Because of the necessity for a vacuum, most gas lasers are bulky and expensive. If a TVV was employed here, however, the outer wall would be replaced by two surfaces in tension and could easily be built around the electron guns without adversely affecting the structure of the vessel (the gun could even be incorporated as a strut).

In the near future, both laser and magnetic fusion look set to achieve breakeven. Both these experiments involve the use of very large and expensive vacuum chambers. In particular, the laser fusion experiments have the problem of containing the 400MJ yield of a successful inertial confinement implosion. Perhaps a flexible double- or multiple-walled chamber might reduce the cost of such a device : its flexibility and the thinness of the walls would reduce the diameter (see Figures 73(a) and (b)).

In a *New Scientist* article [*J Braun*, 1994], plans are presented to build a rail line 'under the Alps' to connect cities in Switzerland. Because of the prohibitive effect of air resistance at high speeds, the whole system, with the exception of the station platforms, will operate in a partial vacuum. For some parts of the network,

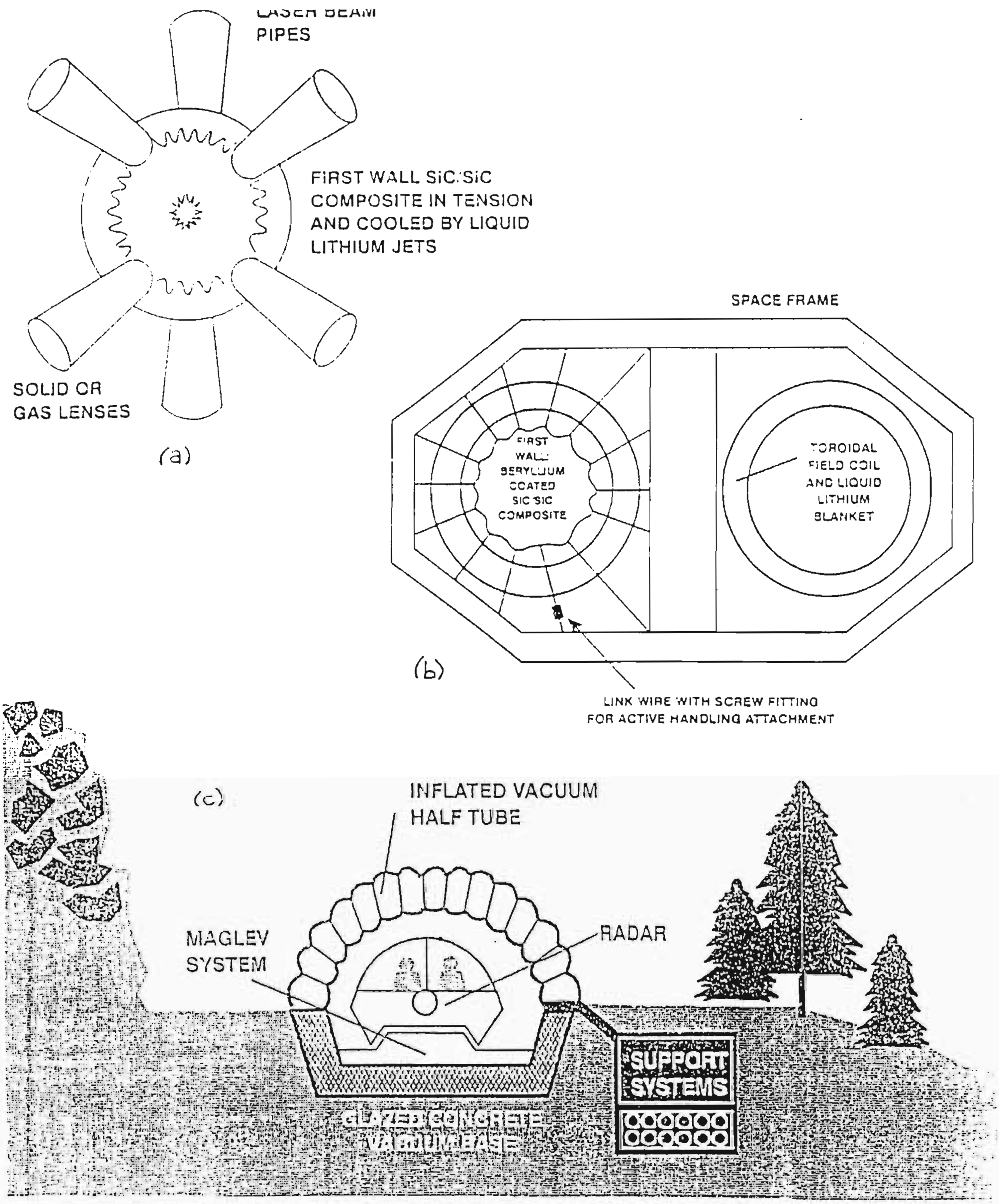

Figure 73: Present and future applications of TVVs:(a) Laser fusion chamber, (b) Magnetic fusion chamber and (c) "Vaclev" - a TVV used in proposed Maglev systems.

a TVV system could create the desired partial vacuum at a fraction of the cost. The upper half of the tube could be a TVV, while the lower part a vacuum glazed high-alumina cement or 'Hialvac'. Such a system would make other high speed proposals look uneconomical and anti-ecological (see Figure 73 (c)).

6.7 Conclusion

In principle, there are several good reasons for using TVVs and SVVs as opposed to compressional vacuum vessels. TVVs are cheaper, less bulky and much lighter, making them more portable than their compressional VV counterparts. TVVs are not high vacuum vessels but rather low vacuum vessels with both present and future applications. All of the principle experiments have been successful, for both the TVV and SVV. As far as we know, the principle is a novel one. Although, given its simplicity, it could be a very old concept. Nevertheless, in the context of modern high tensile materials and the ever expanding applications of vacuum vessels, we think the idea worth re-examining. We believe that these materials, together with the TVV principle, could lead to alternative vacuum chamber designs.

7 Future Research Topics

7.1 Introduction

This thesis has concerned itself with finding answers to questions, but equally important is knowing what questions to ask. And, as is probably the case in all other disciplines, the work done in this thesis has generated more questions than answers.

In this final chapter, future research topics are presented in the form of questions raised by the author, and possible starting points for solutions are suggested. The idea is to give anyone interested a place to start, and also to outline some of the extentions the author wishes to pursue.

7.2 Continuous Gas Lenses

It would be extremely useful to be able to build up index of refraction profiles for the various gas lenses. However, due to the non-linear nature of certain gas lenses, finding n profiles analytically is difficult. Fortunately, it is possible to adapt certain interferometers to act as refractometers, thereby allowing the refractive index to be determined experimentally.

The principle is very simple. If a substance of thickness t, having a refractive index n, is introduced into the path of one of the interfering beams in the interferometer, the optical path in this beam is increased because of the fact that light travels more slowly in the substance and consequently has a shorter wavelength. The optical path is now nt through the medium, and the increase in optical path due to the insertion of the substance is $(n-1)t$ (relative to air). This will introduce $(n-1)t/\lambda$ extra waves in the path of one beam; so if we call Δm the number of fringes by which the fringe system is displaced when the substance is placed in the beam, we have

$$(n-1)t = (\Delta m)\lambda$$

In principle, a measurement of Δm,t and λ thus gives a determination of n. For the application to gas lenses, the Jamin and Rayleigh refractometers would be ideally suited. (The Mach-Zehnder refractometer also exists). [*Jenkins, White*,1981]

The Jamin refractometer is shown schematically in Figure 74 (a). The two identical tubes T_1 and T_2 can now be used to measure the index of refraction of a certain gas at different temperatures and pressures. If the number of fringes Δm crossing the field is counted while the gas reaches the desired pressure and temperature, the value of n can be found.

The purpose of the compensating plates C_1 and C_2 in Figure 74 (a) and (c) is to speed up the measurement of refractive index. As the two plates, of equal thickness, are rotated together by the single knob attached to dial D, one light path is shortened and the other lengthened. The device can therefore compensate for the path difference in the two tubes. The dial, if previously calibrated by counting fringes, can be made to read the index of refraction directly (the sensitivity of the device depends on the fixed angle between C_1 and C_2).

The Rayleigh refractometer is based on a similar principle. The initial beam is split into two by a fairly wide double slit, and the two beams are brought to

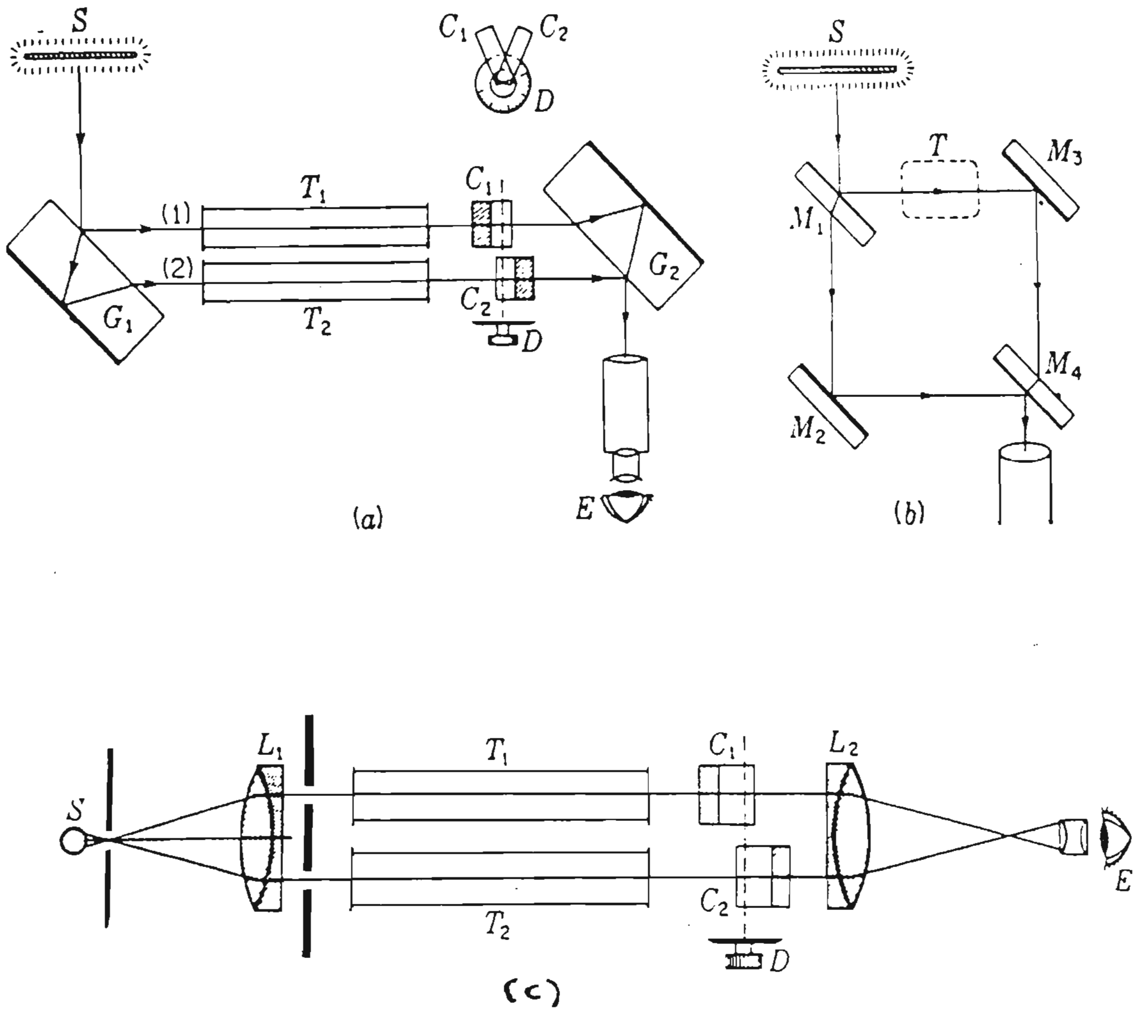

Figure 74: Diagrams of three refractometers. These could be adapted to measure the refractive index of the spinning pipe gas lens. The plates C_1 and C_2, together with the dial D can be used to calibrate the instrument to measure the RI value directly.[*Jenkins, White*,1981]

interfere by the lens L_2.

Using these types of refractometers, a few experiments could be done to yield insight into the behaviour of the refractive index of various gas lenses:

- **Pressure Effects.** By attaching pressure/vacuum ports to the pipe T_2, the effects of pressure on the refractive index can be checked experimentally.
- **Temperature Effects.** Pipe T_2 would now be heated. By having both pipes mounted on adjustable X-Y mounts, the radial refractive index profile can be ascertained.
- **Rotational Effects.** Finally, by rotating pipe T_2, the effect on n by rotating the pipe can be found experimentally. Furthermore, these effects can be observed for various T and P, and perhaps the conjecture of the RI profile for high P operation, discussed in § 1.5.2, could be accurately shown.

7.3 The Pulsed Gas Lens(PGL)

It has been pointed out by Buccellato and Michaelis [*Buccellato*, 1993], that a pulsed gas lens could replace solid-state optical components in future Inertial Confinement Fusion (ICF) reactors. A model of such a cylindrical PGL is shown in Figure 75(a). To test the operating principle, pulsed refraction experiments were conducted using a gas-dynamic beam deflection device (Figure 75(b)). The concept is simple enough: a rectangular slab of high-pressure, high density, high refractive index gas is contained inside a box with a long rectangular window on top and two optical slit apertures on either side. The long window is instantaneously opened allowing a plane rarefraction

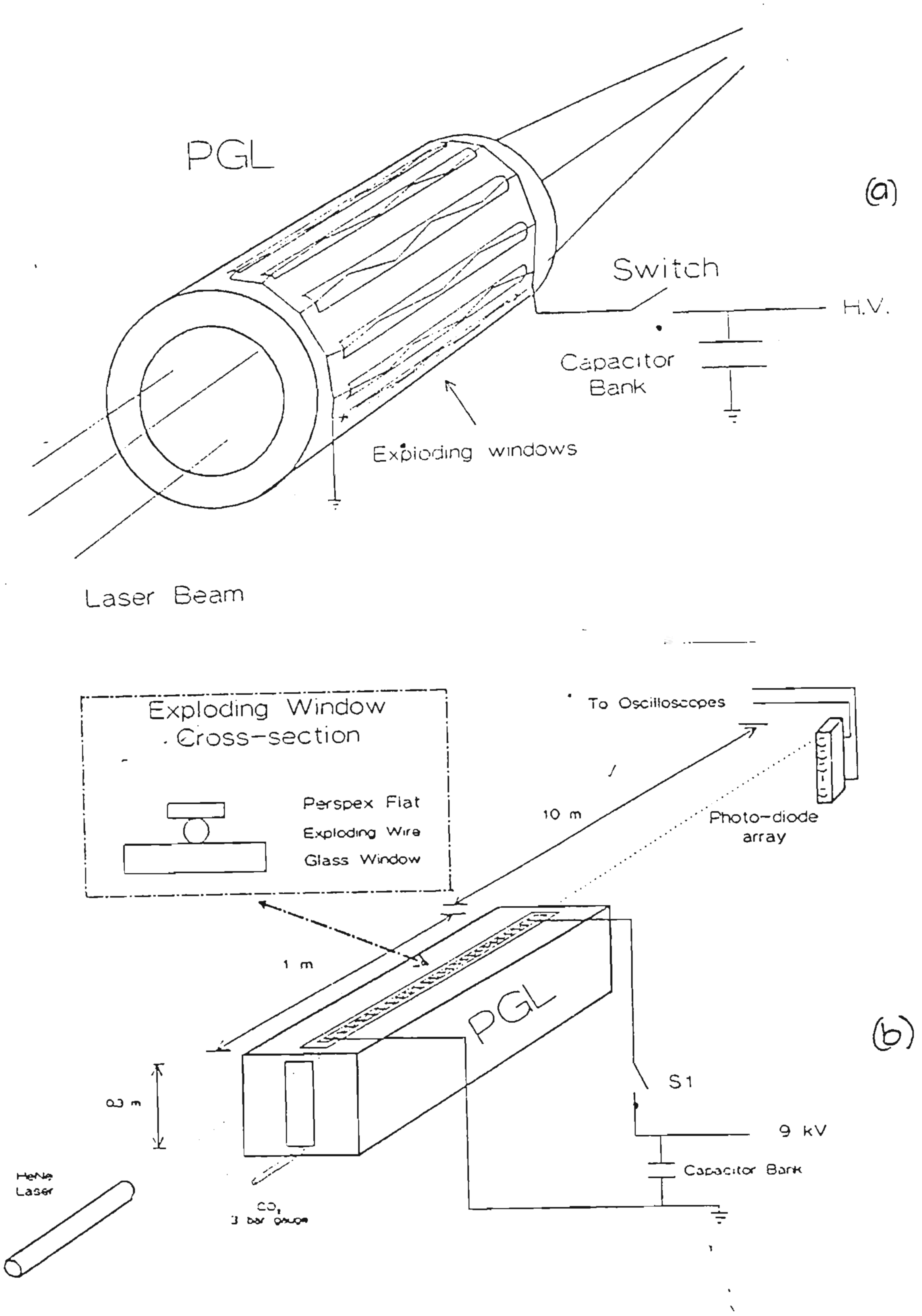

Figure 75: The PGL experimental design. In figure (a), the walls of the cylinder are instantaneously removed. If a laser beam passes through the cylinder at this moment, then the cylinder acts as a lens.(b) shows a simple test of this principle by using a rectangular box filled with gas, and a photo-diode array to detect the laser.

wave to propagate back towards the lower wall of the box. If a laser beam is passed through the box, the beam will be deflected downwards. It was hoped that this deflection would be detected by a series of photo-diodes, as illustrated in Figure 75(b).

However, due to the low intensity of the beam, and the short duration of the deflection, no conclusive results were obtained. In addition, only approximate calculations of the focal length of such a lens could be obtained, due to the non-linear behaviour of the gas flow. We now propose the following experiments:

7.3.1 Analysis of the PGL using a High Speed Camera

Much time has been spent by the author in assembling and operating a high speed camera (see Appendix A). Thus a more conclusive deflection experiment could be performed by replacing the photo-diode array with the high speed camera.

7.3.2 Analytical solutions for the gas dynamics in the PGL

Since no attempt was made to find analytical solutions for the gas flow, and since this would be useful in moving from the rectangular box simulation to the cylindrical model, an attempt is made here to start such mathematical modelling.

Assume that the density, pressure and velocity of the gas in the box are dependent only on the depth, x, and the time elapsed from opening, t. Then the equations that determine the state of the gas at any given time are the following:

$$\frac{\partial \rho}{\partial t} + \nabla.(\rho v) = 0 \tag{7.1}$$

$$\frac{\partial P}{\partial x} = \rho \frac{\partial v}{\partial t} \tag{7.2}$$

$$P = \rho RT \tag{7.3}$$

where $\rho = \rho(x,t)$, $P = P(x,t)$ and $v = v(x,t)$. These equations assume that the gas dynamics are determined by the continuity equation (Equation 7.1), Newton's second law as a pressure gradient (Equation 7.2), and the ideal gas law (Equation 7.3).

After much manipulation, these three equations combine to form the following partial differential equation:

$$RT\frac{\partial^2 v}{\partial x^2} + v\frac{\partial^2 v}{\partial x \partial t} + \frac{\partial^2 v}{\partial t^2} = 0 \tag{7.4}$$

This equation now needs to be solved analytically, if possible, with the boundary values, and the result compared to computational models investigated by Buccellato [*Buccellato*,1993].

7.3.3 Water Wave Simulations of the PGL

Following the success of the water simulations of the CSL (in Chapter 2), the author proposes the following simulation of the PGL (rectangular model): could it be that the effects on water levels at successive time intervals when breaking the wall of a dam (instantaneously) are related to the density and pressure profiles of the expanding gas in the PGL? Since the two situations have obvious similarities, and since $P \propto h$ and $\rho \propto h^2$, (h = water height), such a simulation could possibly yield useful insight into the gas dynamics of the PGL.

As a quick test, a computer simulation of the effects of removing a dam wall on the water, at successive time intervals is shown in Figure 76. This is an ideal case where the surface only "realises" the wall has been removed as the disturbance propagates into it. This is analogous to the gas at the bottom of the box only "real-

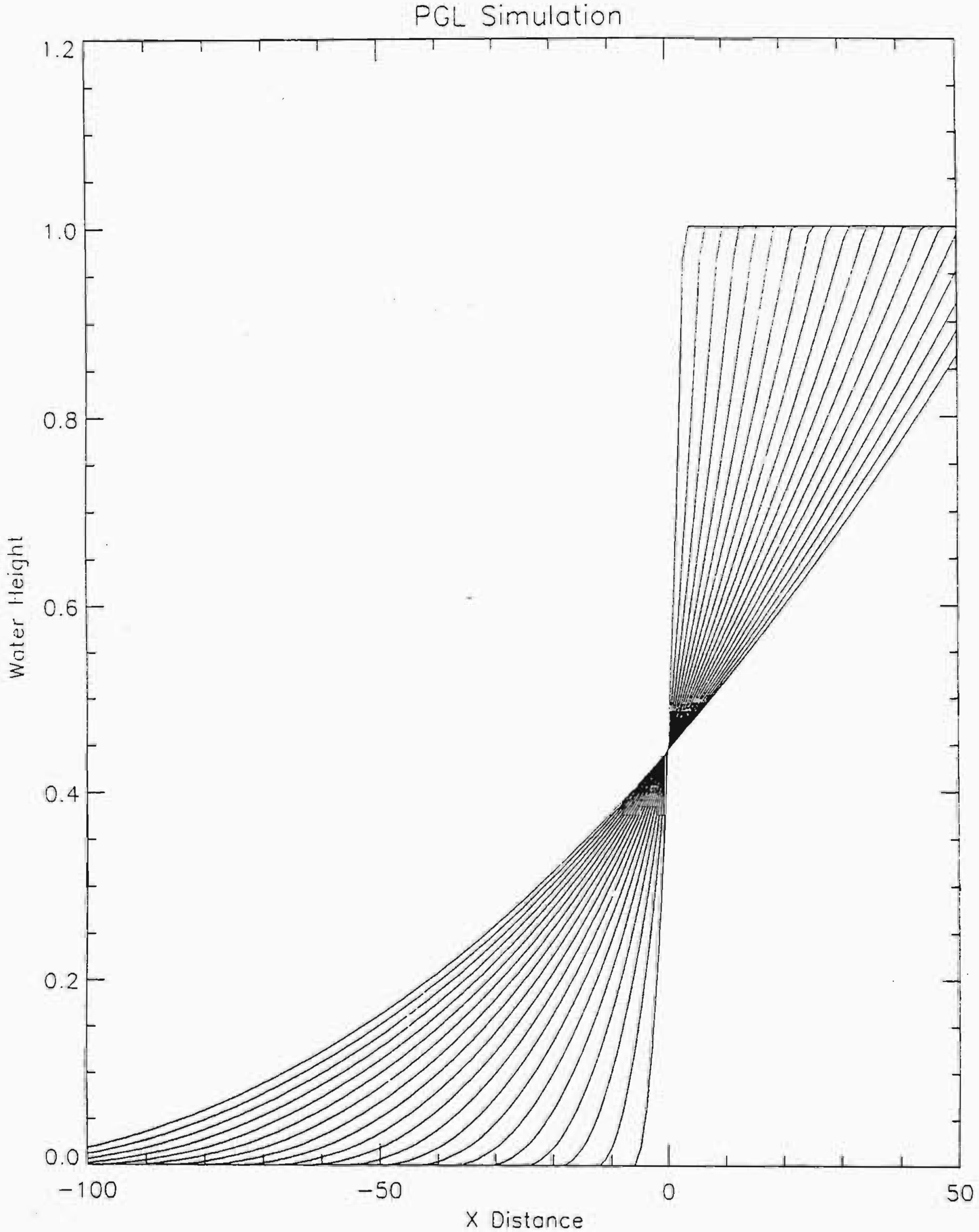

Figure 76: A computer simulation of the breaking dam problem. This is an ideal case, where the water level of the dam only changes as the disturbance propagates into the dam. This water simulation is an analogy to the PGL gas density and pressure as the gas is released.

ising" the PGL is opened when the rarefraction wave reaches it. Further simulations need to be conducted and these need to be compared to the experimental results and any analytical solution found for the gas dynamics of the PGL.

7.4 Convection Effects

Convection effects play a significant role in the focusing or de-focusing of gas lenses. Convection effects are also very difficult to model. However, it is necessary to understand the role convection plays in gas lenses. Some unanswered questions might read:

- How does convection influence the temperature gradients of a non-rotating pipe?
- What happens to these profiles when the pipe is rotated?
- Does convection have a significant de-stabilising effect on the symmetric temperature profile *thought* to be established by rotation?
- How do the convection effects change with pressure and pipe diameter?

Several images have been taken of the diffraction patterns during heating of the pipe, during the initial rotation, and as the pipe rotation is stopped. Analysis of these images might help answer some of the above questions.

7.5 Thermal Lensing

The analytical model for multiple pulses could be tested if a controlled experiment was performed with known optical absorptions. This is not a trivial matter, and is receiving attention presently. The model could also be improved by including lensing effects due to the optical coatings and the coating – surface interface. Modelling the coating in the same way as the substrate will not work because the thermal properties of thin films are very different to those of bulk material.

Models have already been completed[8] that look in great depth at the rotating window's temperature distribution and resultant phase distortions, but these results were not presented here.

However, the aerodynamic window has not been studied as yet, and it might be interesting to quantify the effect such an element has on the aberrations and therefore the resultant beam propagation.

Finally, a study has begun which looks at the effect of damaged optics on the total aberrations.

---

[8] By W. Groenewald: an internal report

8 References

1. Alda, J., Boreman, G.D., *Applied Optics*, **32** (13), pp 2431-2438 (1993)
2. Alda, J., et al, *SPIE Proceedings*, **2870**, pp 52-61 (1996)
3. Aoki, Y., and Suzuki, M., *IEE Transactions On Microwave Theory and Techniques*, **MTT-15** (1), pp 2-8 (1967)
4. Bacon, M., et al, *J. Appl. Phys.*, **66** (3), pp 1075-1079 (1989)
5. Bailey, R.T., et al, *J.C.S. Faraday II*, **76**, pp 633-647 (1980)
6. Baldock, G.R. and Bridgeman, T., *'The Mathematical Theory Of Wave Motion'*, Ellis Horwood Ltd, pp 198-210 (1981)
7. Barnes, K.R., *Monographs On Applied Optics, No. 3: The Optical Transfer Function*, Adam Hilger Ltd (1971)
8. Beck, A.C., *Trans. Microwave theory and tech*, **MTT-15** (7) (1967)
9. Benattar,R., et al, *Rev. Sci. Instrum.*, **50** (12), pp 1583-1585 (1979)
10. Bendow, B., Gianino, P.D., *Applied Optics*, **12** (4), pp 710-718 (1973)
11. Berreman,D.W., *The Bell Systems Technical Journal*,July 1964, pp 1469-1475

12. Bockasten, K., *Journal Of The Optical Society Of America*, **51** (9), pp 943-947 (1961)

13. Bogdanoff, D. W., et al, *Applied Optics*, **28** (18), pp 3960-3967 (1989)

14. Born, M. and Wolf, E., *'Principles Of Optics'*, 5th Ed., Pergamon Press (1975)

15. Braun, J., *New Scientist*, **142** (1925), pp12 (1994)

16. Buccellato, R., et al, *Laser and Particle Beams*, **10** (4) (1992)

17. Buccellato, R., et al, *Optics Communications*, **101**, pp 350-355 (1993a)

18. Buccellato, R., et al, *Optics and Laser Technology*, **4**, (25), pp 247-250 (1993b)

19. Cannon, J.N., and Kays, W.M., *Journal of Heat Transfer*, Feb. 1969, pp 135-139

20. Carslaw, H.S., Jaeger, J.C., *'Conduction of Heat in Solids'*, Clarendon (Oxford), pp 107-136, (1947)

21. Cazalet, R.S., et al, *Meas. Sci. Technol.*, **1**, pp 147-150 (1990)

22. Chenming, H., Whinnery, J.R., *Applied Optics*, **12** (1), pp 72-79, (1973)

23. Courant, R. and Friedrichs, K.O., *Supersonic Flow and Shock Waves*, Interscience Publishers (New York), pp 32-35, 335

24. Cunningham, P.F., et al, *J. Phys. E: Sci. Instrum.*, **19**, pp 957-960 (1986)

25. Cunningham, P.F., et al, *Meas. Sci. Technol.*, **2**, pp 217-225 (1991)

26. Cunningham, P.F., et al, *J. Phys. D: Appl. Phys.*, **24**, pp 1744-1747 (1991)

27. Dovichi, N.J., et al, *Anal. Chem.*, **56**, pp 1700-1704 (1984)

28. Dovichi, N.J., Harris, J.M., *SPIE Proceedings*, **288**, pp 3722-375 (1981)

29. Dubovik, A. (translated by Aksenov, A.), *'The Photographic Recording Of High Speed Processes'*, Wiley Interscience, pp 255-272 (1981)

30. Fang, H.L., Swofford, R.L., *J. Appl. Phys.*, **50** (11), pp 6609-6615 (1979)

31. Ferri, A., *'Elements Of Aerodynamics Of Supersonic Flows'*, MacMillan (1949)

32. Forbes, A., *Internal Report*, (1996)

33. Forbes, A., van Heerden, S.P., *SAIP conference*, July (1996)

34. Forbes, A., *Internal Report*, (1997)

35. Forbes, A., van Heerden, S.P., *SAIP conference*, July (1997)

36. Franko, M., Tran, C.D., *Rev. Sci. Instrum.*, **67** (1) pp 1-18 (1996)

37. Gleick, J., *Genius: R. Feynmann and modern physics*, Abacus (1993)

38. Gloge, D., *The Bell System Technical Journal*, Feb. 1967, pp 357-365

39. Gordon, J.P., et al, *J. Appl. Phys,*, **36** (1), pp 3-8 (1965)

40. Gori, F., Santarsiero, M., *Optics Communicationss*, **82** (3,4) pp 197-203 (1991)

41. Groenewald, W., *Internal Report*, (1996)

42. Harris, J.M., *'Analytical Applications of Lasers'*, Chapter 13, (John Wiley and Sons), ed. Piepmeier, E.H., (1986)

43. Hecht E., *'Optics'*, 2nd Ed., Addison-Wesley, (1989)

44. Herrit, G.L., Scatena, D.J., *Laser Focus World*, pp 107-118, July (1991)

45. Higgs, C., et al, *SPIE Proceedings*, **1625**, pp 365-369 (1992)

46. Hu, C., Whinnery, J.R., *Applied Optics*, **12** (1), pp 72 - 79 (1973)

47. Jenkins, F.A., White H.E., *'Fundamentals of Optics'*, 4th Ed., McGraw-Hill, (1981), pp 283-285

48. Johnston, T.F., *Laser Focus World* May, (1990)

49. Kaiser, P., *The Bell System Technical Journal*, Feb. 1968, pp 179-194

50. Kaiser, P., *The Bell System Technical Journal*, Jan. 1970, pp 137-153

51. Kitriotis, D., *Proceedings: Laser Induced Damage in Optical Materials*, pp 649-656 (1986)

52. Klein, C.A., *Optical Engineering*, **29** (4), pp 343-350 (1990)

53. Klopper, W., *Internal Report*, (1995)

54. Kreith, F., and Sonju, O.K., *J. Fluid Mech.*, **22** (2), pp 257-271 (1965)

55. Kulkarny, V.A., et al, *SPIE Proceedings*, **288**, pp 118-128 (1981)

56. Langhorn, C., Gruhlke, R., *Laser Focus World*, pp 89-93, Feb. (1993)

57. Lisi, N., et al, *The Colliding Shock Lens As An Intracavity Q-Switch Element* (1993)

58. Lisi, N., et al, *Optics and Laser Technology*, **26** (1), pp 25-27 (1994)

59. Mahajan, V.N., Opt. & Phot. News, **5**, 8, August, (1994a)

60. Mahajan, V.N., Opt. & Phot. News, **5**, 11, November, (1994b)

61. Mahajan, V.N., Opt. & Phot. News, **6**, 2, February, (1995a)

62. Mahajan, V.N., Opt. & Phot. News, **6**, 5, May, (1995b)

63. Marcuse, D., Miller, S.E. *The Bell System Technical Journal*, July 1964

64. Marcuse, D., *IEE Transactions On Microwave Theory and Techniques*, **MTT-13** (6), pp 734-739 (1965)

65. Marcuse, D., *'Light Transmission Optics'*, (Van Nostrand Reinhold, New York, 1982)

66. Martinez, C., Belanger, P.A., *SPIE*, **2870**, pp 62-71 (1996)

67. Martynenko, O.G., et al, *Izd. Nauka i Teknika*, Minsk (1972)

68. Martynenko, O.G., *Int. J. Heat Mass Transfer*, **18**, pp 793-796 (1975)

69. Masuda, W., Yuasa, M., *Journal De Physique* **41** (11), pp 423-429 (1980)

70. Matsuo, H., and Nakamura, Y., *J. Appl. Phys.*, **52** (7), pp 4503-4507 (1981)

71. Michaelis, M.M., and Willi, O., *Optics Communications*, **36** (2), pp 153-158 (1981)

72. Michaelis, M.M., et al, *Optics Communications*, **52** (6), pp 371-376 (1985)

73. Michaelis, M.M., et al, *Optics Communications*, **59** (5,6), pp 369-374 (1986)

74. Michaelis, M.M., and Bingham, R., *Laser and Particle Beams*, **6** (1), pp 83-91 (1988)

75. Michaelis, M.M., et al, *Laser and Particle Beams*, **9** (2), pp 641-651 (1991a)

76. Michaelis, M.M., et al, *Optics and Laser Technology*, **23** (5), pp 283-288 (1991b)

77. Michaelis, M.M., et al, *Nature*, **353** (1991c)

78. Michaelis, M.M., Forbes, A., *Proc 2nd Inter Workshop on Physics and Modern App. of Lasers*, pp 214-217, (Harare, Sep 1993)

79. Michaelis, M.M., Forbes, A., *Vacuum*, **45** (1), pp 57-60 (1994)

80. Michaelis, M.M., *American Journal of Physics*, **62**(8),pp 718-722 (1994)

81. Murison, M.A., *Harvard-Smithsonian Center for Astrophysics*, **TM95-04**, April (1995)

82. Neal, D.R., et al, *SPIE*, **2870**, pp 72-82 (1996)

83. Notcutt, M., et al, *Optics and Laser Technology*, **20** (5), pp 243-250 (1988)

84. Notcutt, M., et al, *Applied Optics*, **28** (13), pp 2464-2465 (1989)

85. O'Shea, D.C., *'Elements Of Modern Optical Design'*, Wiley Interscience, pp 360-364 (1985)

86. Ou, J-W., and Cheng, K.C., *Int. J. Heat Mass Transfer*, **20**, pp 953-960

87. Owens, J.C., *Applied Optics*, **6** (1), pp 51-59 (1967)

88. Pain, H.J., *The Physics of Vibrations and Waves*,3rd Ed., John Wiley and Sons (1988)

89. Phipps, C.R., and Michaelis, M.M., *Laser and Particle Beams*, **12** (1), pp 23-54 (1994)

90. Prinsloo, F.J., *Internal Report*, January (1995)

91. Reng, N., Eppich, B., *Optical and Quantum Electronics*, **24** pp S973 - S992, (1992)

92. Ronander, E., Rohwer E., *The TEA CO2 Laser in the Chemical Industry*,pp 151-155, Harare Proc., (1993)

93. Scatena, D.J., et al, *Rev. Sci. Instrum.*, **61** (9), pp 2412-2415 (1990)

94. Scatena, D.J., Herrit, G.L., *Laser Focus World*, December (1990)

95. Schmutz, L.E., Levine, B.M., *Laser Focus World*, April (1996)

96. Schultz, K.R., *J Fusion Energy*, **10** (57), (1991)

97. Schwendeman, D.W., and Whitham, G.B., *Proc. R. Soc. Lond.*, **A413**, pp 297-311 (1987)

98. Sheldon, S.J., et al, *Applied Optics*, **21** (9), pp 1663-1669 (1982)

99. Shen, P.W., et al, *Journal De Physique*, **C9**, pp 137-147 (1980)

100. Siegman, A.E., *SPIE Proceedings: Optical Resonators*, **1224**, pp 1-14 (1990)

101. Skiadaressis, D., and Spalding, D.B., *Imperial College Of Science and Technology Report*, London (1976)

102. Skienkiewicz, E., *Optica Applicata*, **XI** (2), pp 261-269 (1981)

103. Soloukhin, R.I., et al, *Int. J. Heat Mass Transfer*,**23** pp 1653-1661, (1980)

104. Sparks, M., *J. Appl. Phys.*, **42** (12), pp 5029-5046 (1971)

105. Special edition on Laser Beam Characterisation: *Optical and Quantum Electronics*, **24** (9), (1992)

106. Steier, W.H., *IEE Transactions On Microwave Theory and Techniques*, **MTT-13** (6), pp 740-748 (1965)

107. Stoker, J.J., *'Water Waves'*, Interscience Publishers, pp 3-27 (1957)

108. Swofford, R.L., Morrell, J.A., *J. Appl. Phys.*, **49** (7), pp 3667-3673 (1978)

109. Takahashi, H., et al, em Applied Optics, **28** (9), pp 1727-1730 (1989)

110. Twarowski, A.J., Kliger, D.S., *Chemical Physics*, **20**, pp 253-258 (1977)

111. van Heerden, S.P., et al, *SPIE Proceedings: Laser Beam Characterisation Conference*, Vol **2870**, pp 515-520, July (1996)

112. van Heerden, S.P., Forbes, A. *SAIP conference*, July (1997)

113. Waltham, J.A., et al., *Laser and Particle Beams*, **8** (1-2), pp 361-367 (1990)

114. Wang, J.Y., Silva, D.E., *Applied Optics*, **19** (9), pp 1510-1518 (1980)

115. WEB1: http://www.aoainc.com/AOS/AOtutorial.html

116. WEB2: http://op.ph.ic.ac.uk/ao/

117. Weber, H., *Optical and Quantum Electronics*, **24** pp S1027-S1049 (1992)

118. Weimer, W.A., Dovichi, N.J., *J. Appl. Phys.*. **59** (1), pp 225-230 (1986)

119. Weiss, J.D., *Applied Optics*, **21** (12), pp 2253-2261 (1982)

120. Whitham, G.B., *'Lectures On Wave Propagation'*, Springer-Verlag (1979)

121. Wilner, K., et al, *Applied Optics*, **21** (10), pp 11796-1800 (1982)

122. Xie, B.L., et al., *Chin Phys Lett*, **2** (11), pp 509-512 (1985)

A High Speed Camera

A.1 General Properties

It was the intention of the *laser group, UND* to perform experiments on pulsed gas lenses with the aid of a high speed motion analysis camera. For this purpose a second-hand Hitachi model 16HS high speed motion analysis camera (HIMAC) was purchased. There are several advantages to this type of camera. It makes use of a rotating 4-sided prism giving operating speeds varying from 500 pps (pictures per second) to a maximum of 5000 pps, where the latter can be doubled by using an 8-sided prism in place of the above mentioned 4-sided prism. The camera has small loss of incident light intensity due to the simple optical set-up: one rotating prism and one imaging lens. The greatest disadvantage of the camera is that, because of its age, it makes use of 16mm film as opposed to the standard 35mm film commonly used today. A major difficulty to be resolved was the problem of locating a company that could supply and develop 16mm film as well as produce the results in a reasonably short time. In the end, Eastman Color Negative EXR 500T film was used with a waiting time of around one week. Figures 77(a) and (b) show the workings of the camera.

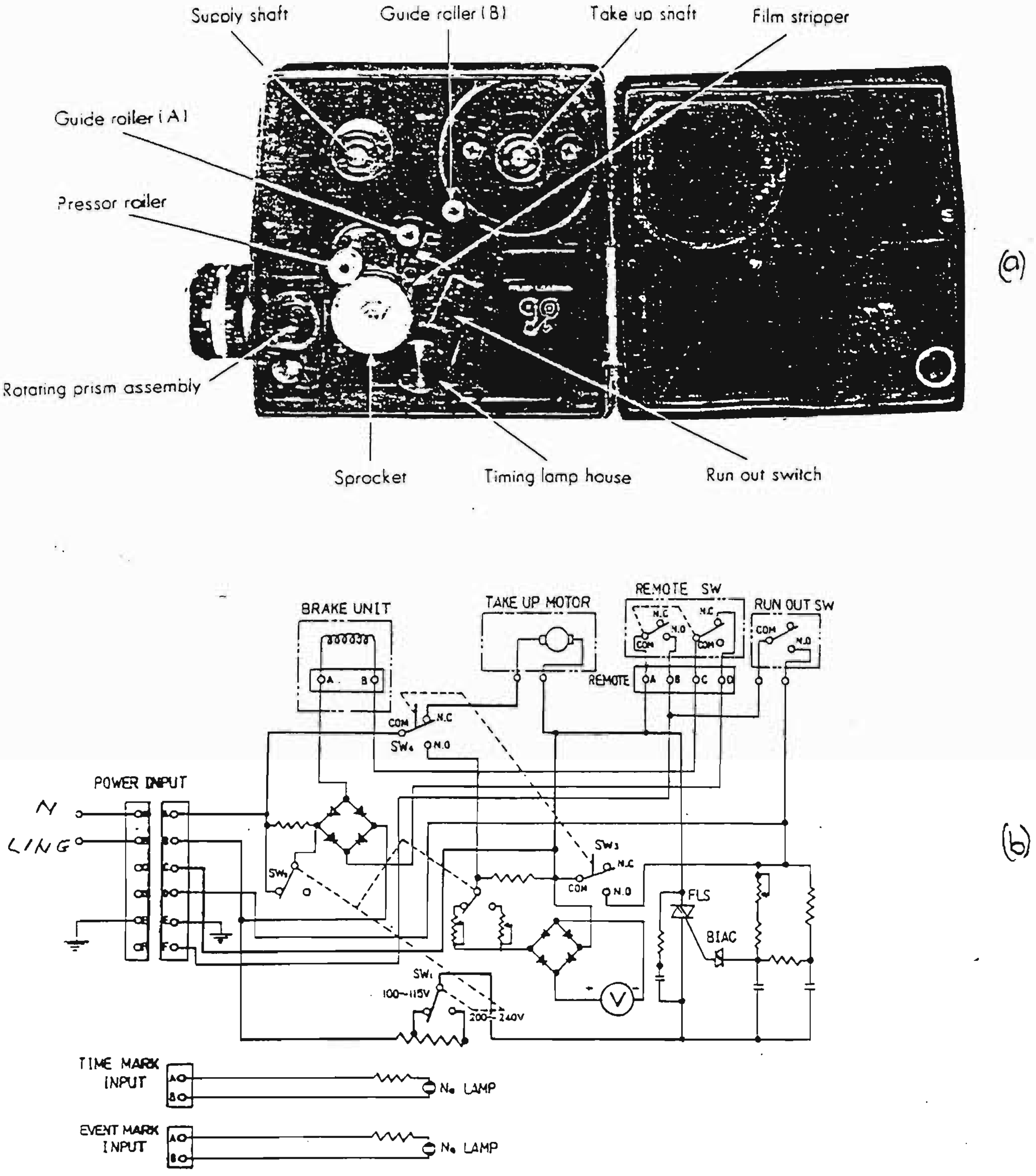

Figure 77: Diagrams of HIMAC: (a) Internal diagram, (b) circuit diagram.

A.2 Focusing

For focusing a Vivitar 35mm macro lens was used. To focus the camera the viewfinder must first be in focus. This is achieved by first focusing the finder so that the grain pattern of the focusing film can be seen (any used film will do), thereafter the lens is focused on the object to be filmed. We found it impossible to focus when new film had been loaded; thus, on all occasions, we focused the camera before loading the film, making sure that, during loading, the settings on the lens were not changed. The optical set-up for the camera is shown in Figure 78.

A.3 Photographing Speed

The camera speed can be set before use by using the speed control adjustment. If the camera speed is slower than optimal, blurring occurs due to large displacements of the object in any given frame. If it is too fast, no blurring occurs but film is wasted and sometimes photographic duration is reduced to the extent that it is difficult to film the entire event. To find the optimal speed, the following relation can be used:

$$R = \frac{mv\cos\theta}{Kd} \tag{A.1}$$

where

- R : photographing speed (pps)
- m : image magnification ($= b/B = h/H$)
- B : object field width (mm)

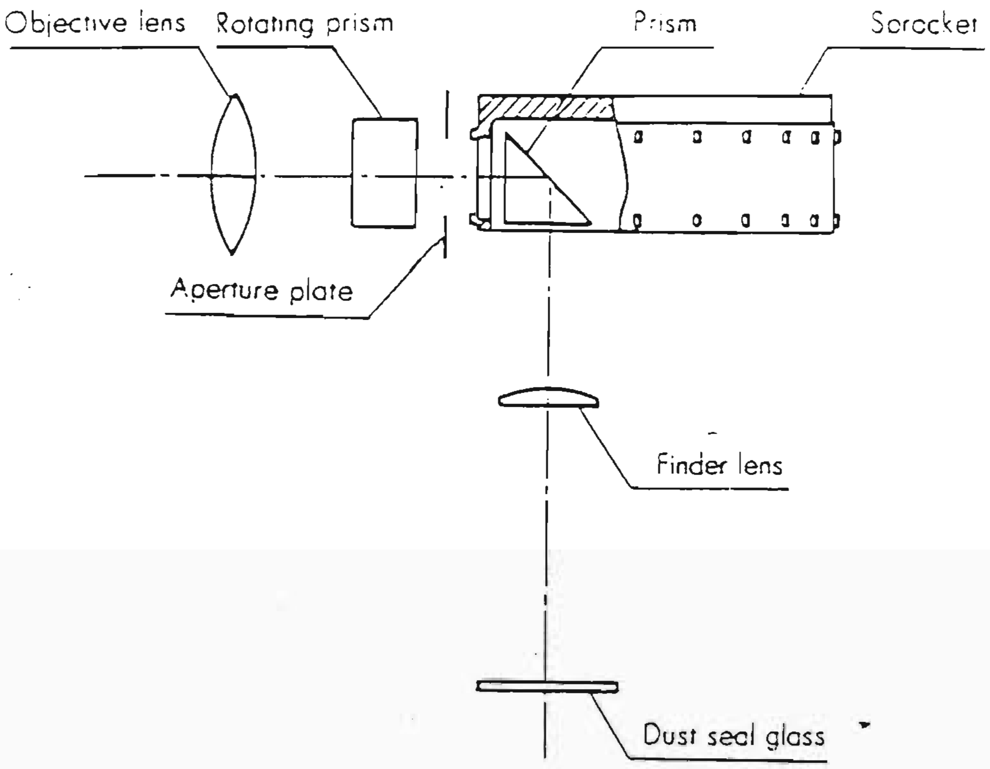

Figure 78: Optical arrangement for high speed camera.

- H : object field height (mm)
- b : picture width (mm) = 10.41
- h : picture height (mm) = 7.47
- v : object velocity (ms^{-1})
- θ : angle between object movement and film face
- K : camera shutter constant = 5
- d : tolerable image blurring on film face (mm) = 0.02 to 0.05

Apart from working at the correct speed, the camera should be synchronised with the event. Usually the camera is started first, with the event triggered after some delay. The reason for this is that the camera does not start at the desired speed but is accelerated at first from zero pps to the value set; thereafter, the speed remains constant. To facilitate camera-event synchronisation, the camera has an attachable mechanical synchroniser.

Sometimes the event duration is much shorter than the total time available from using all the film. In such cases one would like to suspend the operation of the camera when the camera is filming in order to save film. This is possible through the use of the brake unit. In theory this unit enables one to stop photographing at speeds of up to 2000 pps, but we found that, in practice, using the brake unit at speeds in excess of 1000 pps causes the film to snap.

A.4 Time Mark and Event Mark

As mentioned, the camera does not start at the desired speed but accelerates till it reaches this setting. Since the film speed is varying moment by moment, it is necessary to record the photographing speed at certain intervals. This is achieved by using a time mark. The camera has two neon tubes in the lamp house below the sprocket. One of these is triggered at a fixed frequency by an external generator called the *timing light pulse generator*, which can operate at frequencies of 10 Hz, 100 Hz and 1000 Hz. The emitted light is recorded on the side of the film as a time mark, from which the photographing speed can be deduced. The second neon light is used to mark the beginning and end of event filming, called the event mark, but was never used in our applications.

A.5 Comments

The camera is very useful but not easy to use. The manual, which is written in Japanese-English, does not help in this matter. Because the film is so sensitive, all loading and unloading has to be done in complete darkness. Because the HIMAC is a cine camera loading the film is a non trivial matter; but doing it in complete darkness is a test of ability! However, the advantages of the camera far outweigh its cumbersome nature, and I suspect that it will find many uses in the years to come. After all, *seeing is believing; maybe seeing faster is believing faster !*

B Calibration Techniques

B.1 Temperature Transducers

B.1.1 Introduction

There are several temperature transducers available; some of the most common include the thermocouple, RTD, thermistor, and the I.C. sensor. In our experiments, the thermocouple was used. Thermocouples have many advantages which made them suitable for our applications: they are self- powered, simple, rugged, inexpensive and operate over a wide temperature range. Of course, like other temperature transducers, they also have their limitations: they are non-linear, have a low output voltage, are the least stable and the least sensitive, and require a reference. However, because we required only an estimate of the temperature, and because we were operating the thermocouple over a small temperature range, the thermocouple was a suitable option.

B.1.2 Theory

In 1821, Seebeck reported the first of the thermoelectric effects to the Prussian Academy of Sciences. He had managed to produce potential differences by heating the junctions between dissimilar conductors. This potential difference, called the

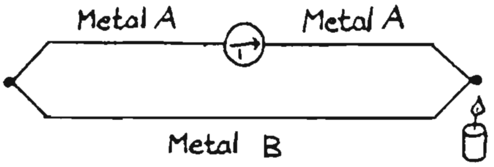

THE SEEBECK EFFECT.

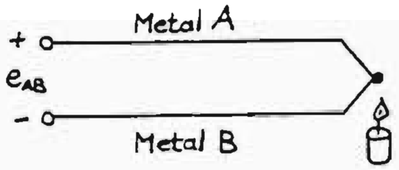

e_{AB} = SEEBECK VOLTAGE.

Figure 79: Thermoelectric circuit making use of the Seebeck effect.

Seebeck Voltage, is a function of the junction temperature T and the composition of the two metals. A simple thermoelectric circuit is shown in Figure 79. It was really only around 1910 that a satisfactory theory of thermoelectric effects was derived (by Altenkirch). He showed that the differential Seebeck coefficient α_{ab} is defined by:

$$\alpha_{ab} = \lim_{\Delta T \to 0} \frac{\Delta V}{\Delta T} = 0 \tag{B.1}$$

For small changes in temperature the Seebeck voltage is linearly proportional to temperature $V_{ab} = \alpha_{ab}T$.

There are a certain number of empirically derived 'laws' of thermocouples which are worth mentioning given their applicability to the understanding and diagnosing of thermocouple circuits.

Law of intermediate metals: (see Figure 80 (a)). Inserting a metal c between metals a and b will not change the output voltage V, regardless of the temperature of the metal c. The voltage V is that from the junction a-b at temperature T. This has the corollary that only the two outer metals contribute to the output voltage.

Law of interior temperatures: (see Figure 80 (b)). The output voltage V will be that of an a-b couple at temperature T, regardless of the external heat source applied to either measurement lead.

Law of inserted metals: (see Figure 80 (c)). The output voltage V will be that of an a-b thermocouple at temperature T, provided both ends of the c wire are at the same temperature. The reason for this is that the two junctions b-c and c-b act in opposition.

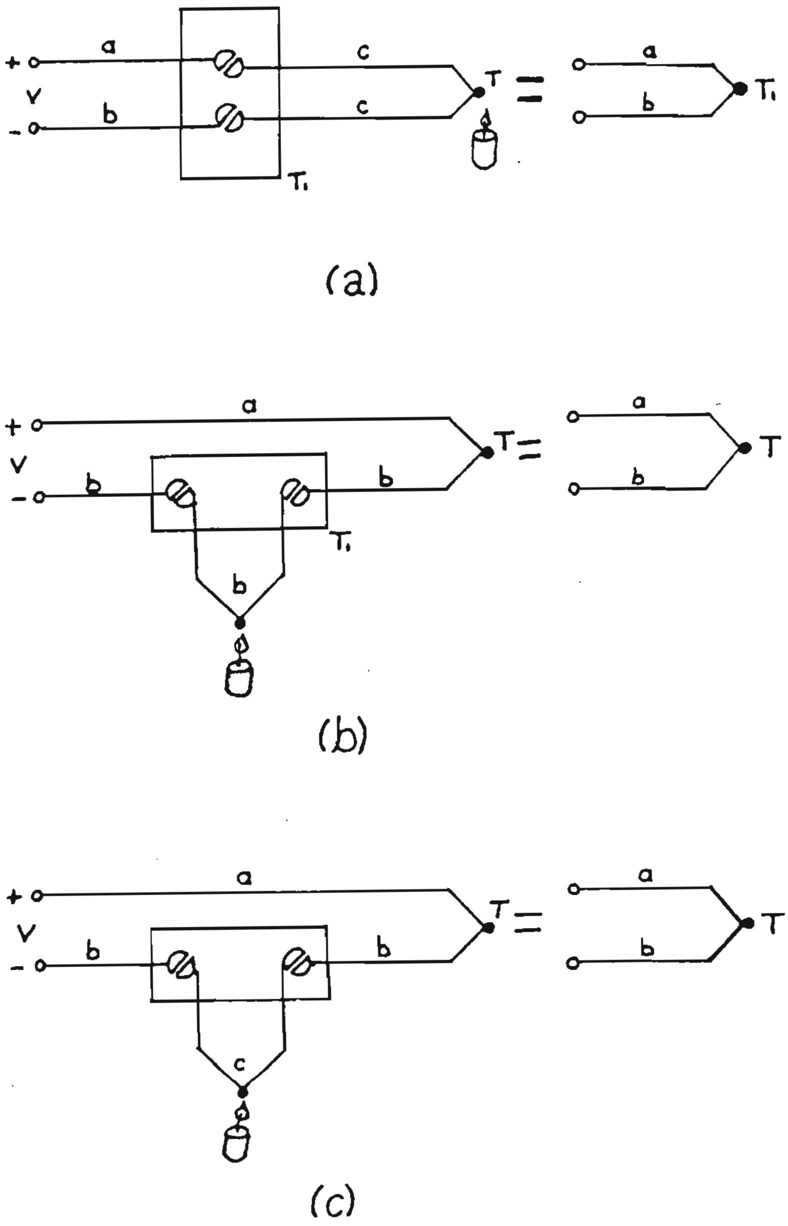

(a)

(b)

(c)

Figure 80: Thermoelectric Laws: (a) Intermediate metals, (b) Interior temperatures, (c) Inserted metals.

B.1.3 Calibration of Thermocouples

In our experiments, Ni–Eureka wires were used as the thermocouples. For temperatures above 50°C the induced emf increased linearly with an increase in temperature. To calibrate the thermocouple, the junction was immersed in a Pyrex beaker containing oil. The free ends of the wires were connected to a FLUKE 75 multimeter. As the oil was heated, the temperature was measured using a standard mercury thermometer and the corresponding increase in potential difference was noted. The temperature range tested was from room temperature to 180°C, and the procedure was repeated several times to check consistency. The results were plotted as voltage vs temperature and are shown in Figure 81. The thermoelectric circuit is shown and clearly there are three junctions involved, with junctions J_2 and J_3 at the same temperature T_{ref}. Using the laws of thermocouples, this gives the relationship between voltage, V, and temperature, T (of J_1) as

$$V = \alpha(T - T_{ref}) \tag{B.2}$$

where T_{ref} is room temperature, which was almost constant. Because we only required an estimate of the temperature value, constructing an elaborate reference was not necessary. From the graph, it was found that our Seebeck coefficient is $40\mu V°C^{-1}$. Generally the Seebeck coefficient is not constant but is a function of temperature. Our thermocouple is close to type K, and over the small range that we used it, type K thermocouples have constant Seebeck coefficients.

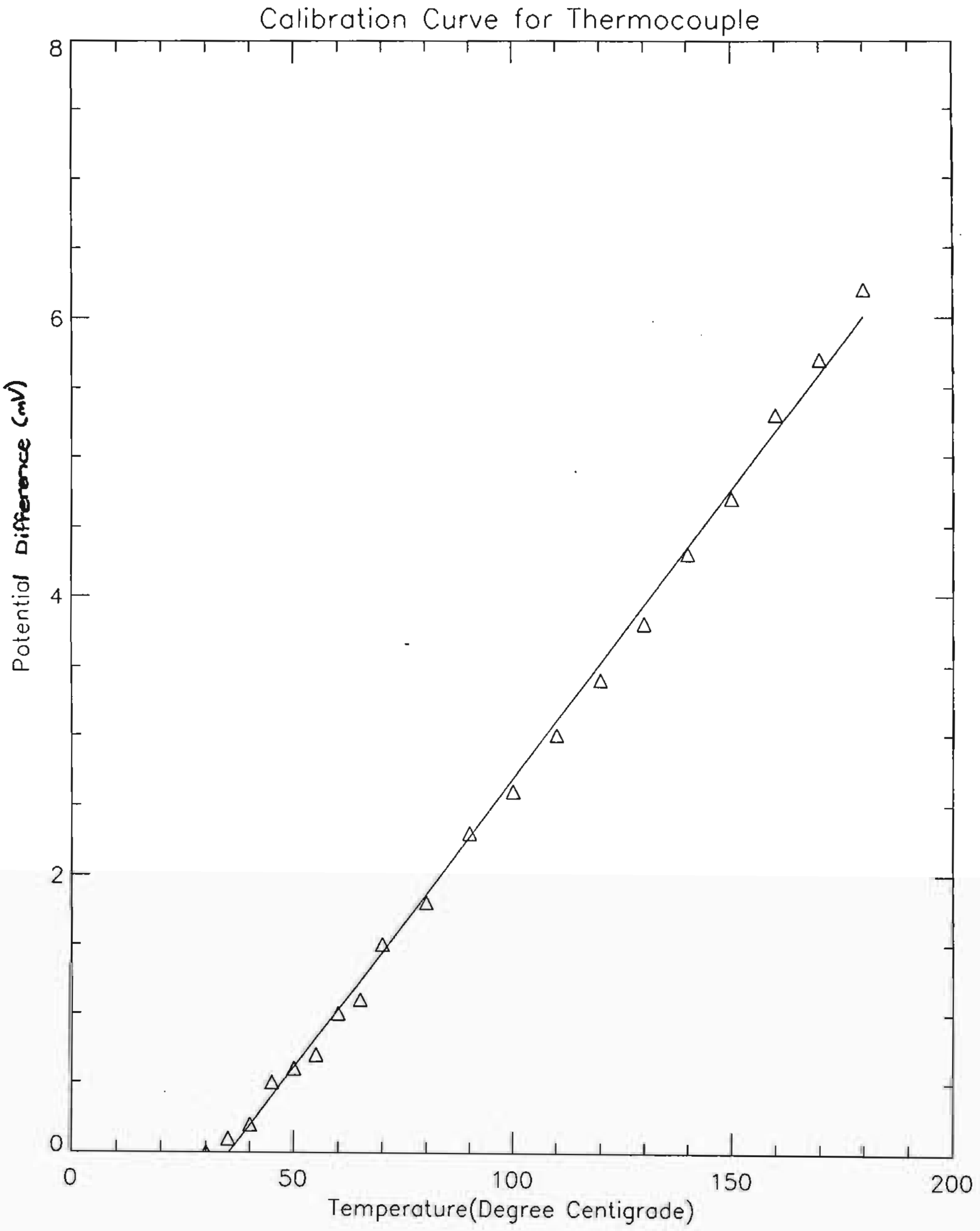

Figure 81: Calibration curve for thermocouples. The graph is almost linear in the range this thermocouple was used for.

B.1.4 Comments

In our experiments, we used a series of five thermocouples to measure the pipe temperature along its length. This method also enabled us to determine when any given thermocouple was not performing, by comparing the voltmeter readings for each junction. This was important because thermocouples can be very temperamental. Poor junction connections can lead to spurious results and one should avoid any steep temperature gradients, stress and vibrations. It is also suggested that some sheathing be used when the thermocouples are operated in a 'hostile' environment – we used a thermal insulator to protect the wires both thermally and electrically. With these few precautions, the thermocouples were found to be easy to use and reliable.

B.2 Pipe Calibration

B.2.1 Introduction

The spinning pipe gas lens experiments required that the pipe spin at a constant rate, or as close to it as possible. The spin about the pipe's longitudinal axis should also be variable. The pipe was friction-driven by means of brass rollers which were themselves driven by a motor. The motor was connected to the mains via a variac to allow the speed of rotation to be varied (by controlling the potential applied to the motor). Since the variac was the control device, the variac was first calibrated with output potential and then against pipe rotation speed in hertz.

B.2.2 Calibration Technique

The input of the variac was connected to the mains, and the output to the motor and a FLUKE 77 multimeter. The % setting on the variac was varied and the corresponding change in potential was noted. For the 45mm, pipe the motor only began spinning the pipe at 36% ($96V$.). A PHYWE STROBOSKOP (digital stroboscope) was used to determine the rotation speed of the pipe. The variac was set to a given value and the frequency of the pipe found by varying the strobe frequency to coincide with that of the pipe (i.e. until the pipe appeared stationary). There was some uncertainty in the values due to the rather unstable method of rotation, and repeated experiments gave an indication of this uncertainty. This procedure was used for both pipes used in the experiments and the results are shown in Figure 82. One of the biggest problems was with the design of the motor – pipe system. When the pipe *jumped* due to the method of rotation, the experiment had to be started again with the pipe recalibrated.

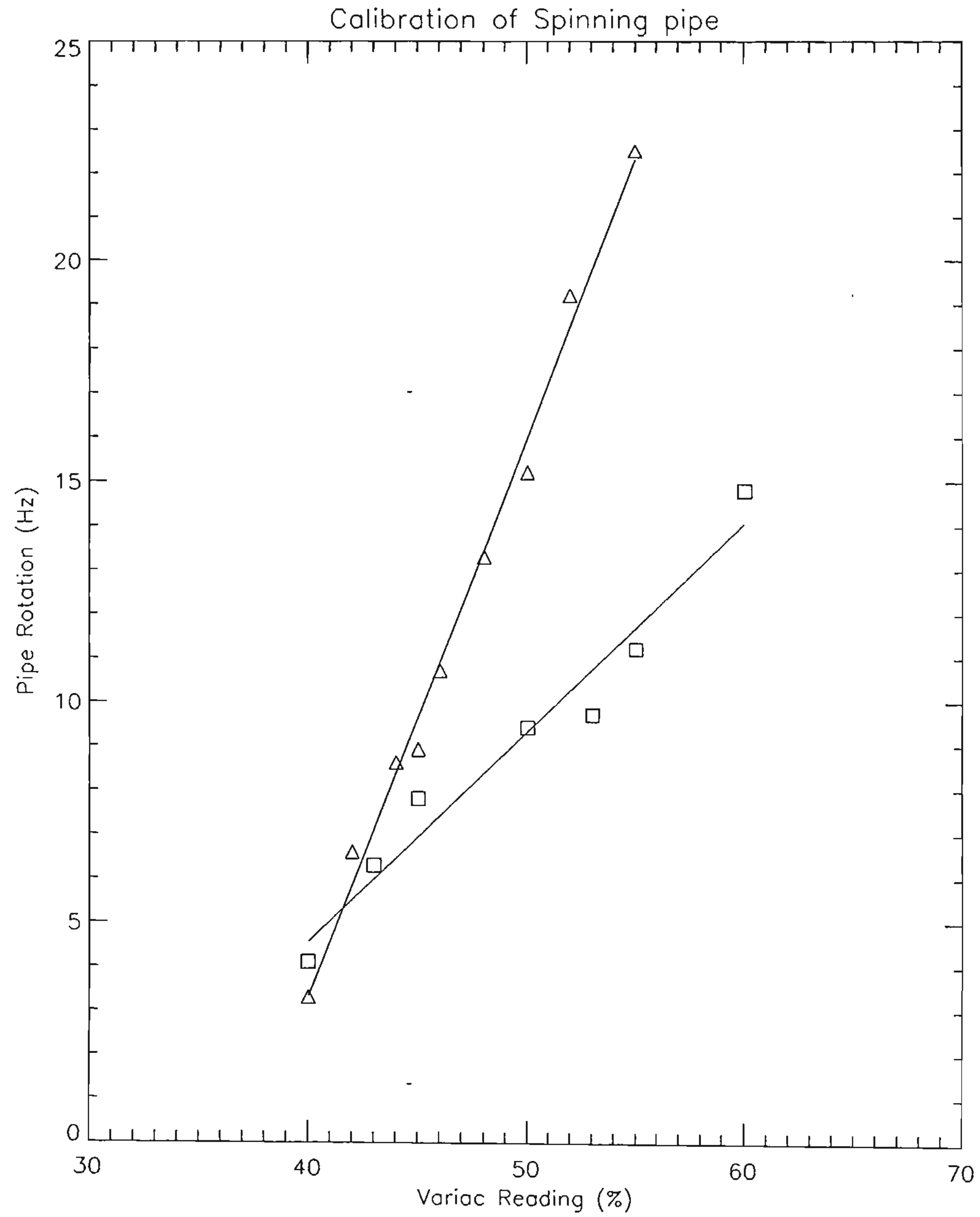

Figure 82: Calibration curve for spinning pipe. Every time the pipe displaced out of position it had to be recalibrated.

C Mathematical Results

C.1 Approximations

It can be verified that all the approximations made in deriving the shallow water theory applied to the sloping bottom surface are valid under the conditions that:

(i) $ak \ll 1$

(ii) $a \ll h$

The equations then that we need to consider are the following approximations:

$$| q.\nabla q | \ll | q_t | \tag{C.1}$$

$$| \nabla\eta | \ll 1 \tag{C.2}$$

$$\eta \ll \left| \frac{\phi_y}{\phi_{yy}} \right|_{y=0} \tag{C.3}$$

$$[\phi_{ty}]_{y=0} \ll g \tag{C.4}$$

Rather than prove each individually I will illustrate by means of example that the above approximations hold under conditions listed above. Consider equation (C.2) :

$$\nabla\eta = \frac{\partial\eta}{\partial x} = ak\cos(kx - \omega t)$$

The magnitude of this is of course $\mid ak \mid$ and hence

$$\mid \nabla\eta \mid \ll 1 \Leftrightarrow ak \ll 1$$

Similarly, if we were to consider equation (C.3) :

$$\eta = a\sin(kx - \omega t)$$

and

$$\left(\frac{\phi_y}{\phi_{yy}}\right)_{y=0} = \frac{1}{k}\tanh(kh) \approx h$$

Since η is at most equal to a, it follows that equation (C.3) is true *iff* $a \ll h$.

Finally, we note that the first equation, (C.1), is in fact a tensor equation and can be rewritten as

$$\mid q_i \nabla_i q_j \mid \ll \left|\frac{\partial q_i}{\partial t}\right|$$

where summation is implied over the dummy index i. Put another way, we have that the left hand side of the above equation is $q_i A_{ij}$ where A_{ij} is a 2×2 matrix.

C.2 Phase and Group Velocity

In chapter 3 the dispersion relation for shallow water waves was examined. As expected, the phase and group velocity of the ripples are equal and constant: typical behaviour for non-dispersive media. What is interesting though is to consider any general function $\omega = \omega(k)$ and consider the phase and group velocity.

We then ask the question: *is there a wavenumber (wavelength) for which the phase velocity (wave velocity) is a minimum?* Writing this mathematically we are asking:

$$\text{when is } \frac{dV_p}{dk} = 0 \tag{C.5}$$

Since $V_p \equiv \omega/k$ we have :

$$\begin{aligned} \frac{dV_p}{dk} &= \frac{d(\omega/k)}{dk} \\ &= \frac{1}{k}\frac{d\omega}{dk} - \frac{1}{k^2}\omega \\ &= \frac{1}{k}\left(\frac{d\omega}{dk} - \frac{\omega}{k}\right) \end{aligned} \tag{C.6}$$

Clearly (C.6) will be zero when the bracketed term is zero, which coincidentally happens to be when $V_p = V_g$! Two interesting results can be derived from this:

(i) The relation (C.5) can also imply that V_p is independent of k. This is true for non-dispersive media and under such conditions it is well known that $V_p = V_g \, \forall \, k$. Hence this treatment gives mathematical support to the relations found in chapter § 2.

(ii) Since in general $V_P \rightarrow V_p(k)$ we have the unusual result that the phase velocity, or wave velocity, is a minimum with respect to k when $V_p = V_g$, which happens to be the same condition for a nondispersive media. Thus it seems that in any dispersive medium, the minimum phase velocity is that value that V_p would take when placed in a non-dispersive medium, ie $V_p = V_g$.

I do not have a clearer explanation of the above result, coming upon it purely by accident. It is however an interesting result obtained from a very simple analysis, and on that basis alone warrants mention.

C.3 Useful integrals

The following integrals have useful properties which were used in finding the analytical solutions to the problems given in § 4:

When m and q are integers, we have ...

$$\int_0^{2\pi} \cos(m\theta)\, d\theta = \begin{cases} 2\pi, & m = 0 \\ 0, & m \neq 0 \end{cases} \tag{C.7}$$

$$\int_0^{2\pi} \sin(m\theta)\, d\theta = 0 \tag{C.8}$$

$$\int_0^{2\pi} \cos(m\theta)\cos(q\theta)\, d\theta = \begin{cases} 0, & m \neq q \\ \pi, & m = q \neq 0 \\ 2\pi, & m = q = 0 \end{cases} \tag{C.9}$$

$$\int_0^{2\pi} \sin(m\theta)\sin(q\theta)\, d\theta = \begin{cases} 0, & m \neq q \\ \pi, & m = q \neq 0 \\ 0, & m = q = 0 \end{cases} \tag{C.10}$$

$$\int_0^{2\pi} \cos(m\theta)\sin(q\theta)\, d\theta = 0 \tag{C.11}$$

C.4 Radial Polynomials

The list to follow gives the radial polynomials $R_n^m(r)$ for values of $m, n < 10$. When $n - m =$ odd, the radial polynomial is 0.

```
n m      Radial Polynomials
0 0      1
1 0      0
                 2
2 0      -1 + 2 r
3 0      0
                2      4
4 0      1 - 6 r  + 6 r
5 0      0
                  2       4       6
6 0      -1 + 12 r  - 30 r  + 20 r
7 0      0
                 2       4        6       8
8 0      1 - 20 r  + 90 r  - 140 r  + 70 r
9 0      0
                   2        4        6        8
10 0      -1 + 30 r  - 210 r  + 560 r  - 630 r  +

       10
  252 r
0 1      0
1 1      r
2 1      0
                   3
3 1      -2 r + 3 r
4 1      0
                   3       5
5 1      3 r - 12 r  + 10 r
6 1      0
                    3       5       7
7 1      -4 r + 30 r  - 60 r  + 35 r
8 1      0
                   3        5        7        9
9 1      5 r - 60 r  + 210 r  - 280 r  + 126 r
10 1      0
0 2      0
1 2      0
          2
2 2      r
3 2      0
             2      4
4 2      -3 r  + 4 r
5 2      0
            2       4       6
6 2      6 r  - 20 r  + 15 r
7 2      0
              2       4        6       8
8 2      -10 r  + 60 r  - 105 r  + 56 r
9 2      0
              2        4        6        8        10
10 2      15 r  - 140 r  + 420 r  - 504 r  + 210 r
0 3      0
1 3      0
2 3      0
          3
3 3      r
4 3      0
             3      5
5 3      -4 r  + 5 r
6 3      0
             3       5       7
7 3      10 r  - 30 r  + 21 r
8 3      0
              3        5        7       9
9 3      -20 r  + 105 r  - 168 r  + 84 r
10 3      0
0 4      0
1 4      0
2 4      0
```

```
3 4      0
          4
4 4      r
5 4      0
             4      6
6 4      -5 r  + 6 r
7 4      0
             4       6       8
8 4      15 r  - 42 r  + 28 r
9 4      0
               4        6        8        10
10 4      -35 r  + 168 r  - 252 r  + 120 r
0 5      0
1 5      0
2 5      0
3 5      0
4 5      0
          5
5 5      r
6 5      0
             5      7
7 5      -6 r  + 7 r
8 5      0
             5       7       9
9 5      21 r  - 56 r  + 36 r
10 5      0
0 6      0
1 6      0
2 6      0
3 6      0
4 6      0
5 6      0
          6
6 6      r
7 6      0
             6      8
8 6      -7 r  + 8 r
9 6      0
              6       8       10
10 6      28 r  - 72 r  + 45 r
0 7      0
1 7      0
2 7      0
3 7      0
4 7      0
5 7      0
6 7      0
          7
7 7      r
8 7      0
             7      9
9 7      -8 r  + 9 r
10 7      0
0 8      0
1 8      0
2 8      0
3 8      0
4 8      0
5 8      0
6 8      0
7 8      0
          8
8 8      r
9 8      0
              8       10
10 8      -9 r  + 10 r
0 9      0
1 9      0
2 9      0
```

```
3 9      0
4 9      0
5 9      0
6 9      0
7 9      0
8 9      0
          9
9 9      r
10 9      0
0 10      0
1 10      0
2 10      0
3 10      0
4 10      0
5 10      0
6 10      0
7 10      0
8 10      0
9 10      0
            10
10 10      r
```

Vacuum/volume 45/number 1/pages 57 to 60/1994
Printed in Great Britain

0042-207X/94$6.00+.00

Vacuum vessels in tension

M M Michaelis and A Forbes*, *Laser Applications Research Institute, and *Plasma Physics Research Institute, University of Natal, Durban 4001, South Africa*

received 24 August 1992 and in revised form 10 November 1992

The principle of tensional as opposed to compressional vacuum vessels is reviewed. Proof of principle experiments is performed. Conceptual extensions of the idea, the inflatable vacuum chamber, the lightweight or even weightless chamber, are proposed. Present and future engineering applications are briefly surveyed.

1. Principle of tensional vacuum vessels

Most vacuum vessels (VV) seem to have been constructed with walls in compression rather than in tension. This obvious (even subconscious) method of design fails to employ one of the best properties of metal: high tensile strength. It invites one of its worst structural properties: its propensity to buckle in compression. Nor does the compressional method allow for the use of novel high tensile materials.

The principle of the tensional vacuum vessel (TVV) is simple: two linked shells in tension rather than one in compression, the tension being provided by pressurising the intermediate space. Figures 1(a) and (b) illustrate the conceptual differences between a standard compressional VV and a TVV.

The force on each wall is given by the pressure difference times the area. If the smaller pressure difference times the larger area of the outer wall equals or exceeds the larger pressure difference times the smaller area of the inner, the system is stable.

Conceptually the simplest TVV would consist of two linked concentric spheres [see Figure 1(c)]. For equilibrium one writes

$$\sum F_{out} = \sum F_{in}$$

or

$$4\pi(p-p_0)R_o^2 = 4\pi p R_i^2, \tag{1}$$

where R_o and R_i are the outer and inner radii, respectively, and where p_o is the atmospheric pressure. So

$$R_o = R_i\sqrt{\left(\frac{p}{p-p_0}\right)}. \tag{2}$$

If we write $\Delta R = R_o - R_i$ for the thickness of the intermediate pace and if $p \gg p_0$ then

$$R_o = R_i\left(1+\frac{p_0}{2p}\right) \tag{3}$$

nd

$$\Delta R = R_i\frac{p_0}{2p}. \tag{4}$$

A more useful form is a double shell cylindrical TVV [see Figure 1(d)] with two coaxial shells of length l in equilibrium:

$$(p-p_0)2\pi R_o l = 2\pi p R_i l, \tag{5}$$

where

$$R_o = R_i\left(\frac{p}{p-p_0}\right).$$

Two important cases: for $p \gg p_0$ we get $R_o = R_i(1+p_0/p)$ and $\Delta R = R_i p_0/p$. A value of $p = 2$ bar yields $R_o = 2R_i$.

At one extreme one sees that, if the pressure is high, the double shell structure can be quite thin (typically if $p \approx 10$ bar, $\Delta R \approx R/10$). The other extreme indicates a simple route to the experimental proof of principle, described in the next section.

If the cylindrical shells are terminated with two flat end plates there will be a net outward force of approximately

$$F_{end} = \pi R_o^2(1-p_0/p)10^5\ \text{N}. \tag{6}$$

No claims are being made here about the novelty of this principle. It is extremely likely to be a very old concept. But in the context of modern high tensile materials and ever expanding applications of vacuum vessels, we think the idea worth re-examining.

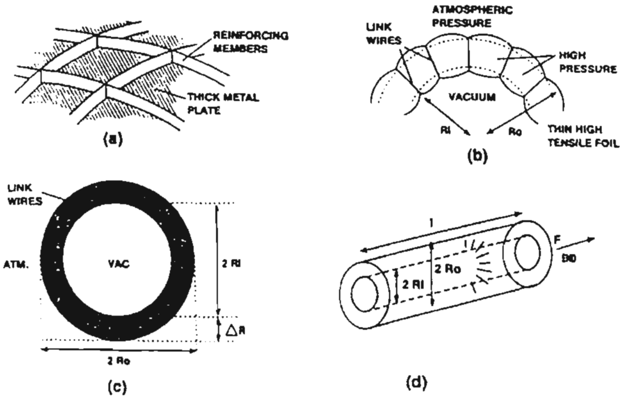

Figure 1. Vacuum vessel geometries. (a) Compressional. (b) Tensional. (c) Spherical. (d) Cylindrical.

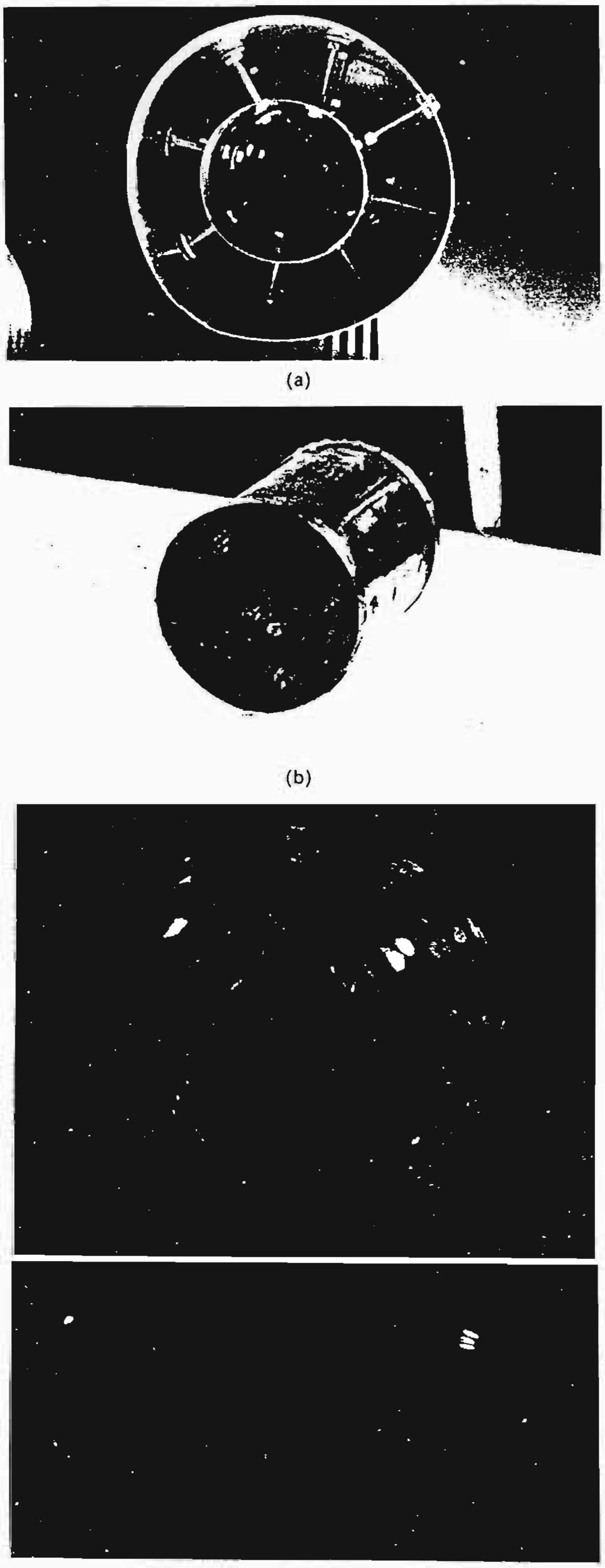

(a)

(b)

(c)

Figure 2. Cylindrical tension vacuum vessels. (a) Inside view of struts linking the two walls. (b) Chamber with ends glued on. (c) Didactic experiment with plastic bottles (front and side view).

2. Experimental chambers

Two types of experiments are conducted, the first to demonstrate the principle to doubting colleagues and engineers, the second to gain practical experience. In both types of experiment we used $R_o = 2R_i$.

The didactic experiments are carried out with flexible transparent plastic bottles linked with nylon wire and two domestic vacuum cleaners, one in the blowing, the other in the sucking mode [see Figure 2(c)]. The virtue of this type of experiment is that one can see and even feel the forces at work: switch off the 'blower' briefly and the chambers immediately start to implode. Switch it back on and one observes the tensional dimples forming in the outer shell as it takes the strain. Gentle finger pressure exerted on the outer shell causes the inner shell to buckle inwards.

More serious experiments are performed with two concentric cylinders made out of 0.2 mm brass sheet [see Figures 2(a) and (b)]. The two 17 cm long cylinders with $R_o = 2R_i = 6$ cm are linked by sixteen 3 mm diameter studs soldered at each end. The cylinders are capped and glued at both ends with 1 cm thick aluminium plates, one of which has two ports for the pressure hose and the 4 mm vacuum pipe.

This vacuum chamber is not intended to be a high vacuum device. The operation pressure is of the order of one mbar. But it serves to gain some technical 'know how'. An earlier version imploded catastrophically because we failed to appreciate that the intermediate pressure must in practice be higher than that predicted by the above simple theory. The reason for this 'overpressure' will become clearer in Section 4.

3. Two possibly novel concepts

Vacuum chambers can be bulky, expensive and space consuming devices. (One of the reasons that experiments involving vacuum are seldom demonstrated in the lecture theatre is that they require a lot of devoted manhandling.)

We suggest here that it might be possible to build a large cheap 'pop up' inflatable vacuum chamber along the lines of the didactic experiment described in the previous section: for low vacuum demonstrations this could be of the thin transparent plastic double wall type. For more serious industrial applications it might consist of three shells: the standard tensional shells and a loosely attached flexible inner guard shell [Figure 3(a)]. Both the low and high vacuum versions could be folded into small containers when not in use.

The second concept that we think could become of interest, if the double wall technology develops, is that of the lightweight vacuum chamber. In principle an evacuated chamber would be an ideal 'lifting body'. In practice the weight of the chamber is much greater than the buoyancy force: vacuum chambers require sturdy supports.

Could a tensional vacuum vessel become buoyant? A short and very rough calculation shows that a TVV fails to become lighter than air when evacuated, even if one neglects the weight of its components.

Consider a spherical double walled chamber according to equation (2). The intermediate volume of gas is

$$V = \tfrac{4}{3}\pi(R_o^3 - R_i^3). \tag{7}$$

thus

$$pV \approx 4\left[\left(\frac{p}{p-p_0}\right)^{3/2} - 1\right]R_i^3 p \tag{8}$$

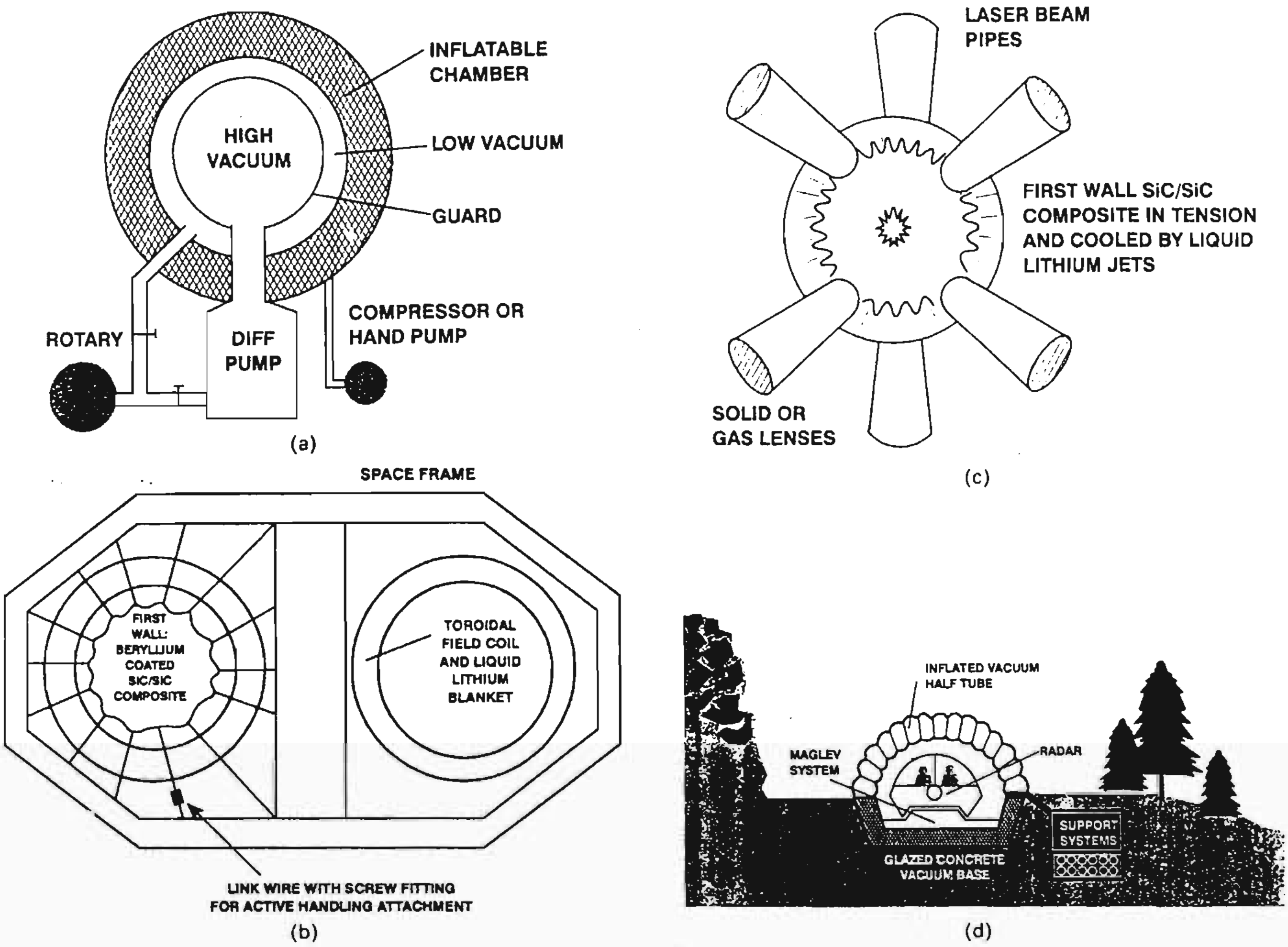

Figure 3. Applications of tensional vacuum vessels. (a) Pop-up system. (b) Tokamak first wall in tension. (c) Laser-fusion tensional VV. (d) Evacuated 'Maglev' concept. The upper half tube is a tensional VV. The lower could be vacuum glazed, high-alumina cement or 'Hialvac' (ref 4).

is very approximately the mass of the air in kilograms if p is now expressed in bars. The weight is approximately pVg and the effective weight of the gas in the system is

$$W'_g = g(pV - V_0), \tag{9}$$

where $V_0 g = \frac{4}{3}\pi R_0^3 g$ is the weight of the gas in both chambers prior to pumping.

A little algebra gives

$$W'_g \approx 4R_i^3 g\left[\frac{p^{3/2}}{(p-p_0)^{1/2}} - p\right] > 0. \tag{10}$$

For a thin-walled spherical double shell with $p \gg p_0$ we get $W'_{\text{eff}} = V_i g/2$, where V_i is the evacuated volume. That is to say there is 1.5 times more gas in the evacuated and pressurised system than there was in the now evacuated space.

A similar calculation for a cylindrical system gives $W'_{\text{eff}} = V_i g$. There is twice as much gas.

At first glance therefore nothing seems to be gained from a weight point of view by using a TVV. However, the high tensile materials can be very much lighter than the thick metal sheet used in standard compressional designs. Also the picture changes if the gas used to pressurise the intermediate space is 'lighter than air'. In the next section we show that it is even possible to design a chamber that is itself 'lighter than air', though such a chamber would be very large.

4. Material science limitations

Clearly the inner and outer walls require greater curvature than that of the chamber if the walls are not to be too thick. The need for a small radius of curvature R_c has to be balanced by the designer's desire to reduce the number of links and also by the need to avoid stress induced cracks at the link-wall attachment points. A little consideration of the geometry of Figure 1(b) will show that for a thin double-walled chamber with $p \gg p_0$ bar, R_c could be of the order of $2\Delta R$. Thus, for a 2 m diameter cylindrical chamber pressurised to 10 bar, R_c is of the order of 20 cm. This requires a tension T in the material such that

$$\Delta p = \frac{2T}{R_c} \tag{11}$$

or

$$T = \Delta p R_c/2 = 10^5 \text{ N m}^{-1}. \tag{12}$$

Research into fusion reactor[1] and aerospace technology[2] is useful in this context. The ultimate strength of modern lightweight high-tensile materials varies up to a maximum of $p_m = 500$

MPa for Si.C Si.C composite materials[2]. If d is the thickness of the foil then

$$p_m d = T \quad \text{or} \quad D = T/p_m = 0.2\ \text{mm}. \tag{13}$$

This 'ball park' calculation shows that very thin foils, definitely less than half a millimetre thick, could be used.

We are presently designing a 1 m long, 1 m diameter cylindrical chamber to test these ideas in practice. The total weight of the cylindrical walls could be as little as 5 kg, representing a considerable saving over a conventional VV. (This design still incorporates massive end plates—but these too could eventually be designed away.)

Another very rough calculation for spherical shells shows that a double-walled TVV with $R \approx 12$ mm and pressurised with helium gas could become weightless after evacuation. For two walls, each 0.5 mm thick, the volume of material is $V_m = 4\pi R^2\ 1000\ \text{m}^3$ and the weight $W_m = \rho V_m g$.

The buoyancy force is approximately

$$\left(V_i - \frac{\rho_{He}}{\rho_{N_2}}\rho V\right)g \approx 10(4R^3 - R^3) \approx 30R^3 \tag{14}$$

where the radius of the intermediate chamber, pressurised at 10 bar, is $\Delta R = R/20 = 5$ cm and the intermediate volume amounts to $V = 4\pi R^2 \Delta R = (\pi/5)R^3$. Equilibrium occurs for $\rho V_m g \approx 30R^3$, if $\rho \approx 3000$ kg m^{-3} and $R \approx 12$ m. (The result is not very different for $R_o = 2R_i$.)

An important aspect of the material limitations is safety. Even small containers, pressurised to several bar, represent a hazard. The above calculations show that, contrary to a conventional vacuum chamber, there is little danger of things (or people) getting 'sucked in' since there is more gas in the intermediate volume than is missing from the evacuated space. Implosion may be unlikely, but explosion is not. Any TVV would need to be carefully shielded. Alternatively, the intermediate volume could be pressurised with foam or liquid rather than gas, rendering rupture inoffensive.

Our experiments indicate that the inner shell is more likely to rupture than the outer, since it supports a greater pressure difference. They also show, as mentioned above, that the intermediate pressure needs to be a little higher than the equilibrium pressure p_{eq}, given by the simple formulae derived in Section 1. This is to avoid excessive curvature and consequent rupture of the membranes. (Clearly the radius of curvature R_c increases with pressure. At high pressure, R_c is of the same order as the chamber radius. As p approaches a value some 10–20% above p_{eq}, the chamber takes on its ideal 'slightly bumpy' appearance. As p approaches p_{eq}, R_c decreases catastrophically and the chamber implodes.)

5. Applications, present, future and far future

Double-walled vacuum chambers might well become cheaper to produce and much lighter than present day systems. As such they could find immediate use for laboratory experiments, electron beam welding and optical coating plants. In the near future both magnetic and laser fusion look set to achieve breakeven (nuclear fusion energy out = electrical energy in).

Studies of magnetic fusion reactors all envisage compressional chambers. As pointed out in ref 2, induced radioactivity and transmutation of the first wall material will be one of the major technical problems encountered in designing a tokamak reactor. A thin foil (1 mm) first wall attached to the tokamak space frame by a large number of high tensile wires would be an elegant solution [see Figure 3(b)]. Such a thin wall could be routinely and robotically replaced and if made of the graphite composite described in ref 2, would not be too difficult to recycle or store as low level radioactive waste. (The wall would need to be beryllium coated on the inside and cooled by the lithium liquid blanket on the outside.)

In laser fusion the same aspects with the activated first wall are encountered as well as an even more serious problem: that of containing the 400 MJ yield of a successful inertial confinement implosion. The α-particles would give an impulse of several kg m s per shot to the wall. Designs for a 10 m diameter compressional vacuum chamber are therefore in hand[3]. We suggest here that a flexible double- or multiple-walled chamber might reduce the cost of such a device: its flexibility and the thinness of the walls would reduce the diameter [Figure 3(c)].

Finally, we suggest that a cheap lightweight vacuum half tube could remove aerodynamic drag in transportation systems of the future [see Figure 3(d)]. Already 'high temperature' superconductor parcel transportation systems are in factory operation. It requires but little imagination to see a 'high T Maglev' travelling down an evacuated tube [Figure 3(d)] at 'door to door' speeds that would make other high speed proposals (Hotol, Sanger, NASA-Orient Express) look uneconomic and anti-ecological.

6. Conclusion

Modern high tensile, lightweight foils together with the concept of a pressurised double-walled vacuum chamber* could lead to alternative vacuum chamber designs.

Acknowledgements

Useful discussions were held with T B Doyle. D Davies showed great patience in constructing chamber after chamber. We thank W de Beer for the general support of his workshop and the Plasma Physics and Laser Applications Research Institutes for financial assistance.

References

[1] R J Piellisch, *Aerospace America*, **7**, 18 (1991).
[2] K R Schultz, *J Fusion Energy*, **10**, 57 (1991).
[3] J Pitts, In The Cascade inertial confinement Fusion Power Plant. UCRL 92558 Report, LLNL, Livermore, USA (1985).
[4] K F Poole and M M Michaelis, *Vacuum*, **30**, 415 (1980).

---

*Patent pending.

The influence of finite absorption in transmission optics on the propagation of high average-power pulsed CO_2-laser beams

S.P. van Heerden, W. Klopper, F.J. Prinsloo and A. Forbes

Atomic Energy Corporation of South Africa (Pty) Ltd
P.O. Box 582, Pretoria 0001, SOUTH AFRICA

ABSTRACT

The development of a high repetition rate TEA-CO_2 laser chain has a number of difficulties that must be overcome. One of these difficulties is to predict the free space propagation of the beam. A low energy (~100mJ/pulse), high-quality, CO_2-beam is amplified in a number of CO_2 - amplifiers to more than 1J per pulse. On propagation through the amplifier chain the primary beam encounters several transmission optics. It was found that the beam parameters of the primary beam change dramatically for high repetition rate operation (>100Hz). The alteration in beam parameters is brought about by thermal expansion and refractive index variations known as thermal lensing. This phenomenon is caused by the thermal gradient introduced to an optic by absorption of a laser beam with a Gaussian profile. Thermal lensing caused by the aforementioned laser system in transmission optics was investigated. The influence of several types of transmission optics in the amplifier chain was studied and compared. It was found that the use of a specific substrate (KCl or ZnSe) is determined by the position in the chain. A marked increase in thermal lensing effects was observed with damaged or contaminated optics.

Keywords: beam propagation, thermal lensing, absorption, transmission optics, CO_2 lasers

1. INTRODUCTION

For the generation of high repetition rate CO_2 laser pulses a line tuneable TEA-CO_2 oscillator and several TEA-CO_2 amplifiers are used. An intra-cavity aperture is used as a spatial filter for generating a TEM_{00} spatial mode with an $M^2 \approx 1.3$. At high repetition rates the average power delivered by this chain ranges from 300W to more than 1kW. The master-oscillator-power-amplifier (MOPA) chain consists of a CW-CO_2 injection seeded oscillator and several TEA-CO_2 amplifiers (see Fig. 4). Typically, the output of the chain is more than 1J at repetition rates higher than 500Hz. The beam has to propagate over extensive distances (longer than 50m) through the amplifiers and a multiple pass Raman cell. For this reason it is important to know the beam parameters of the CO_2 beam throughout the whole beam path. Clearly these parameters must be measured as a function of repetition rate. With these parameters known, one can correct for the induced lensing, or implement alternative solutions for the lensing problem.

A number of possible problem areas were isolated that could have an influence on the CO_2 laser beam propagation through the chain. They are: lensing in the transmission optics and radius of curvature changes of reflective metal mirrors due to the absorption of CO_2 radiation by the window/mirror substrate, possible effects (blooming) due to absorption in air or stationary volumes within the lasers, and possible effects due to the discharge volumes in the amplifiers.

In this paper only the effects of the high average power propagation through transmission optics will be dealt with. These effects were observed at average powers higher than 100W. The heating of transmission optics leads to a refractive index gradient that acts as a lens. This results in changes in the beam spot size in a time period of two to five seconds. The magnitude and the sign of the change depends on the position in the laser chain. These changes in the beam propagation through the amplifiers lead to poor energy extraction from some amplifiers, severe clipping by the electrodes of others and catastrophic window damage where the energy/power density increased to undesirable levels.

The lensing problem in the chain can be divided into three areas of investigation. They are: (a) oscillator configuration (here the effect of intra-cavity transmission optics and reflective optics can have an effect on the output beam parameters), (b) the transmission optics (windows) of the TEA-CO_2 amplifiers, and (c) the use of special optical elements for example beam combiners, Fresnel prisms (¼-wave elements) etc.

It was found that serious lensing occurs as a result of the high average power transmitted through the optics of the chain. The main contribution to the lensing, discussed in this paper, is due to the amplifier windows and the effect on the propagation is therefore a cumulative effect of all the windows in the chain. A number of possible solutions were identified. They are: (a) a reduction in the number of transmission optics in the chain, (b) the use of gas dynamic windows (especially the final window of the chain), (c) efficient cooling of optics, and (d) increasing the spot size through the final optic and thereby reducing the power density on the optics.

2. THEORETICAL BACKGROUND

The thermal lens effect is a time dependent phenomena where the spatial intensity profile of a Gaussian (TEM_{00}) laser beam is transformed into a spatial temperature profile within the substrate. This local heating is a result of absorption of laser radiation. A radially dependent temperature distribution is created which in turn produces a refractive index change by a factor *dn/dT*. It is this refractive index change which results in the absorbing medium acting as a lens. A second weaker effect, that of expansion due to the absorbed power, can be neglected as it contributes little to the lensing phenomena[1].

The first models to describe thermal lensing were qualitative and assumed a parabolic refractive index distribution[2,3,4]. The first step in deriving a quantitative model is the solution of the appropriate non-steady state thermal diffusion equation[6],

$$\frac{\partial T(r,t)}{\partial t} - D\nabla^2 T(r,t) = \frac{1}{\rho C_p} Q(r,t) \tag{1}$$

where $T(r,t)$ is the temperature, $Q(r,t)$ the source term, D the thermal diffusivity, ρ the density and C_p is the heat capacity. In solving this equation the following assumptions are made, all of which can be justified[5,6,7]: the laser beam is turned on at $t=0$ and turned off at $t=t_0$ (both instantaneously), the beam power and radius are constant within the sample, since the sample dimensions are much larger than the beam diameter, we assume the sample acts as an infinite disc with no heat conduction through the ends, and D is temperature independent. As a result of the above, only a radial temperature gradient is induced.

The source term, during excitation, is given by

$$Q(r,t) = \frac{2\ln(10)\,\alpha\, E_0\, e^{-2r^2/a^2}}{\pi\, a^2\, t_0}, \tag{2}$$

where E_0 is the pulse energy, α the absorption per unit length, and a is the radius of the beam impinging on the optic. Substituting equation (2) in (1) and solving for T gives

$$T(r,t) = \frac{2\ln(10)\,\alpha\, E_0}{\pi\, t_0\, \rho\, C_p} \int_0^{t_0} \frac{e^{-2r^2/(8D(t-t')+a^2)}}{8D(t-t')+a^2}\, dt'. \tag{3}$$

Due to the radial temperature distribution, a time dependent refractive index gradient is formed inside the sample given by

$$n(r,t) = n_0 + \left(\frac{\partial n}{\partial T}\right)_{T_A} T(r,t), \tag{4}$$

where n_0 is the initial refractive index and T_A is the ambient temperature. The focal length of the resulting thermal lens is given by[5,7]

$$\frac{1}{f(t)} = -L\left(\frac{\partial n}{\partial T}\right)\left(\frac{\partial^2 T}{\partial r^2}\right) \tag{5}$$

for a sample of length L. By transforming using the ABCD law, and considering the lens signal in the far field, one obtains the following expression for the focal length:

$$\frac{1}{f(t)} = \frac{2\ln(10) A E_0}{\pi k a^2 t_c}\left(\frac{\partial n}{\partial T}\right)_{T_A} \frac{1}{(1+2t/t_c)^2} \tag{6}$$

which is consistent with that found by others[8]. Here, $A=\alpha L$, k is the thermal conductivity, and t_c is interpreted as the relaxation time of the lens, given by

$$t_c = \frac{a^2}{4D}. \tag{7}$$

It can also be shown that the radius of the induced lens is given by[7]

$$w_L = \frac{a}{\sqrt{2}}. \tag{8}$$

The effective focal length induced by a single pulse is given by equation (6). However, in the case of multiple pulses impinging on a window with a finite absorption α, a cumulative temperature is experienced by the optic. The temperature in the optic will reach an equilibrium, which will then result in a lens of finite focal length. The net change in temperature due to *m* pulses is given by [9]

$$\Delta T = \sum_{n=0}^{m} \frac{2\ln(10)\,\alpha\,E_0}{\pi\,\rho\,C_p\,a^2\,(1+2nt/t_c)}\exp\left(\frac{-r^2}{a^2}\,\frac{2}{(1+2nt/t_c)}\right). \tag{9}$$

From the equation above and using equation (5), the focal length as a result of *m* pulses is given by [10]

$$\frac{1}{f(t)} = \sum_{n=0}^{m} \frac{2\ln(10) A\,E_0}{\pi k a^2 t_c}\left(\frac{\partial n}{\partial T}\right)_{T_A} \frac{1}{(1+2nt/t_c)^2}. \tag{10}$$

This result is identical to that for the single pulse case (see equation (6)), but with $(1+2t/t_c)^{-2}$ replaced with $\sum_{n=0}^{m}(1+2nt/t_c)^{-2}$. Here *t=1/(repetition rate)* and *n* is the number of pulses.

From Fig. 1 it is clear that the induced focal length decreases rapidly during the first few seconds until equilibrium is reached, which depends on the repetition rate. At 10Hz there is almost no change, while at 300Hz the change is almost a factor of 80 larger (i.e. if initially the window acts as a lens of *f=80m*, after a few seconds it acts as a lens of *f=1m*!). By treating the window/optic as a thin lens, and transforming the beam using the ABCD law, one finds that the beam radius varies as a function of time with a trend which is analogous to that shown in Fig. 1.

3. MEASURING TECHNIQUE

For the measurement of shot-to-shot variations of the beam size a measuring device was developed [11]. The technique relies on the simultaneous measurement of the energy contained in three sections of the beam (see Fig. 2). The method, like most other techniques, assumes a near-Gaussian profile, and cannot analyse the actual intensity distribution of the beam.

The three-element detector operates on the principle that the beam is split into three sections. The individual detectors are calibrated against a commercial detector taking into account the reflectivity of the wedged mirrors. The middle section is a slit of know width *d*. It is possible to calculate the percentage of the pulse energy contained in the two sections on either side of the slit. Using the standard normal distribution one can determine how many standard deviations of a normal distribution is contained in the middle section and from this the beam waist and centroid.

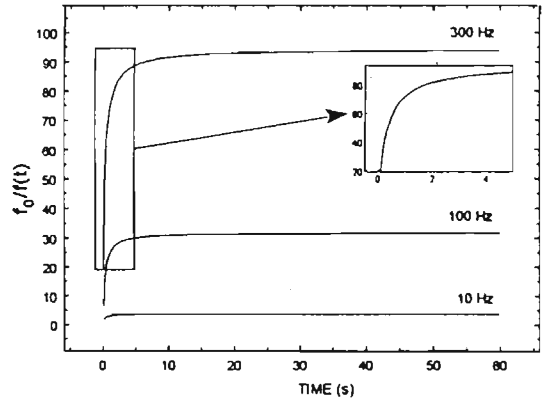

Fig. 1. Calculated focal length change as a function of time for three repetition rates.

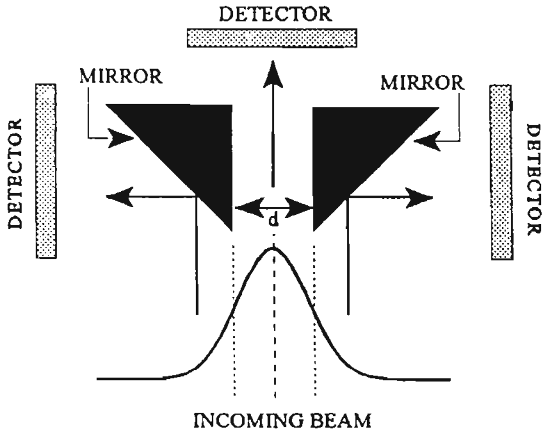

Fig. 2. Diagram illustrating the principle of the three-element detector.

4. EXPERIMENTAL RESULTS

4.1 Laser damage effects

An important feature of equation (10) is the dependence of the focal length on the absorption. As the absorption by the sample increases, so the focal length decreases, i.e. the window substrate acts as a stronger lens (see Fig. 3). This can have serious side-effects for the mode matching in the laser chain. For damaged optics the lensing is enhanced and it can have far reaching implications on the propagation of the high average power laser beam through the chain. Fig. 3 shows the lensing through the chain (see Fig. 4) with three amplifiers in operation. It is clear that with ideal (on specifications) ZnSe windows in the final amplifier, some lensing is observed (if compared with the "no windows" trace in this figure; note that whether the change in the beam radius is seen as an increase or decrease depends one where one measures). However, with damaged ZnSe windows and the beam radius measured in the same position, the lensing is far stronger and takes longer to stabilize. This is not surprising given that the focal length is inversely proportional to the absorbance (see equation (10)). The coefficient of absorption α is related to the optical quality of the window. Damaged optics have higher absorbance[12] which results in the thermal lensing being more pronounced for damaged or inferior quality optics.

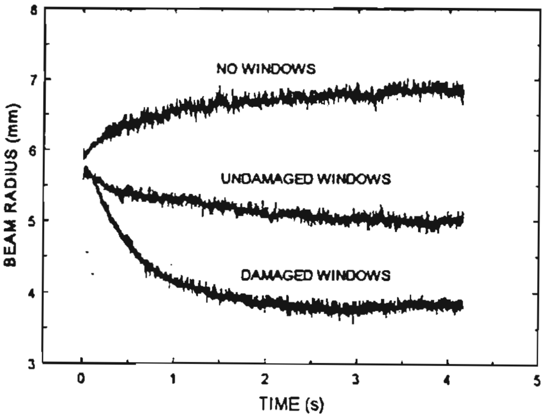

Fig. 3. Changes in the beam radius at a position at the end of the amplifier chain. Shown is the reference (i.e. no windows), minor change due to clean, undamaged windows and the emphasised change due to damaged windows.

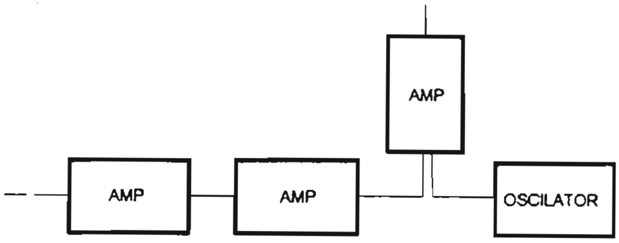

Fig. 4. Layout of the MOPA chain.

4.2 Rotating windows

As a means of reducing the induced temperature gradient (or average power density) the amplifier window was rotated with the beam passing off-axis through the window. When an undamaged ZnSe-window is rotated, the result is a decrease in the thermal lensing (see Fig. 5). However, with the same technique applied to a damaged window it shows very little improvement in the lensing, while the beam size and position became erratic (see Fig. 6). These changes in the size are probably due to an unsymmetrical thermal gradient induced by localized window damage. However, the wedge on the optic had an influence on the pointing stability of the beam.

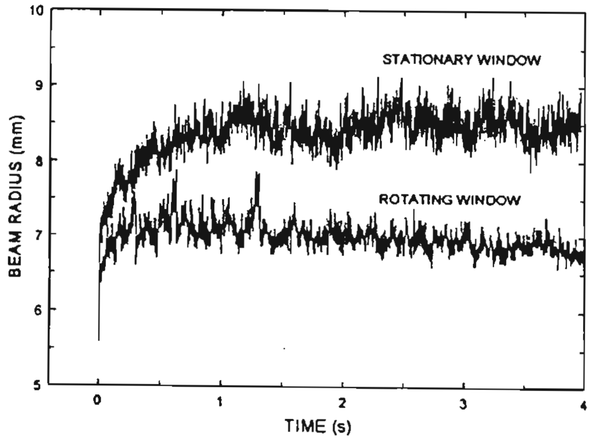

Fig. 5. Improvement in lensing due to rotation of the final exit window of the CO_2-amplifier chain.

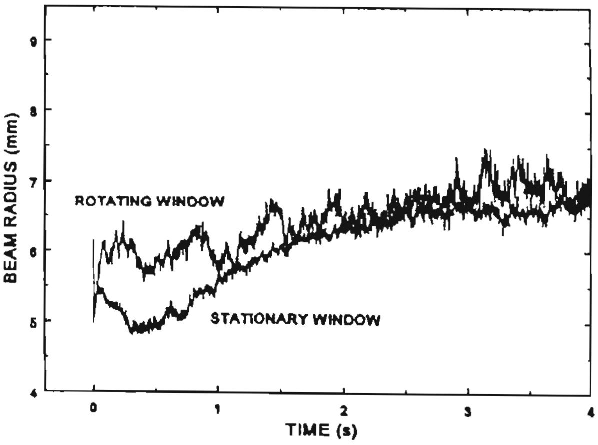

Fig. 6. No apparent improvement in lensing behaviour for damaged rotating window.

When a KCl window is rotated, a similar result as the damaged ZnSe window (periodic beam radius structure) was observed. Clearly an optic with a wedge will introduce a periodic structure on the position of the beam, and will have a serious effect on the pointing stability of the beam. It is apparent that there is no advantage to be gained by rotating a KCl window (see Fig. 7). This could be due to a combination of low conductivity and a very long relaxation time t_c. The temperature rise of a KCl optic is higher than that of a ZnSe optic, and there is a larger temperature difference between the centre and the edge of the KCl optic, both due to the smaller thermal conductivity of KCl. Because of this, and the long relaxation time t_c, rotating the window has little effect on the lensing. The major disadvantage of the rotating window option is the specification on the allowed wedge angle.

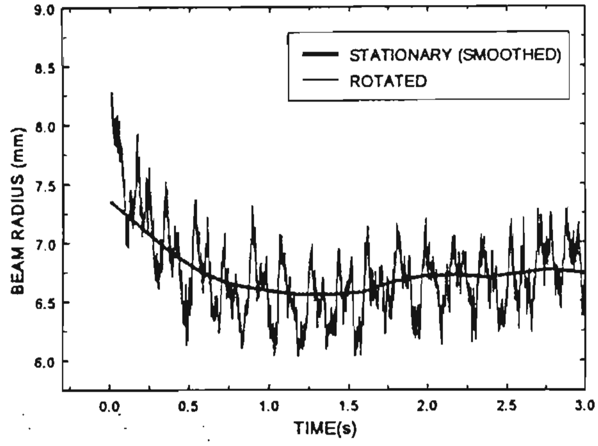

Fig. 7. Periodic beam radius structure due to the rotation of a KCl window.

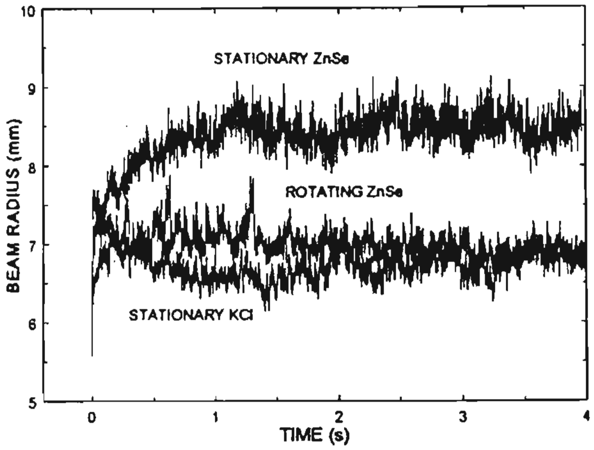

Fig. 8. Comparison of window material with regard to lensing behaviour.

4.3 Comparison of KCl and ZnSe

As mentioned above, the temperature gradient induced in KCl is much larger than that of ZnSe. However, the lensing effect generated by the KCl optic is significantly less than that generated by the ZnSe optic. The reason lies in the refractive index variation lensing mechanism which is related to the structure of the substrates, i.e. ionic for KCl and covalent for ZnSe. As a result of these structural differences KCl has a negative *dn/dT*, which generates a diverging lens, while ZnSe has a positive *dn/dT*, which generates a converging lens. The negative lens effect of the KCl is however reduced by the converging lens effect induced by the thermal expansion of KCl. This effect is five times larger for KCl than that of ZnSe. In the case of ZnSe the thermal expansion effect simply enhances the effect of the refractive index variation. As a result of this, the degree of lensing in ZnSe optics is more pronounced than that generated in KCl optics as shown in Fig. 8.

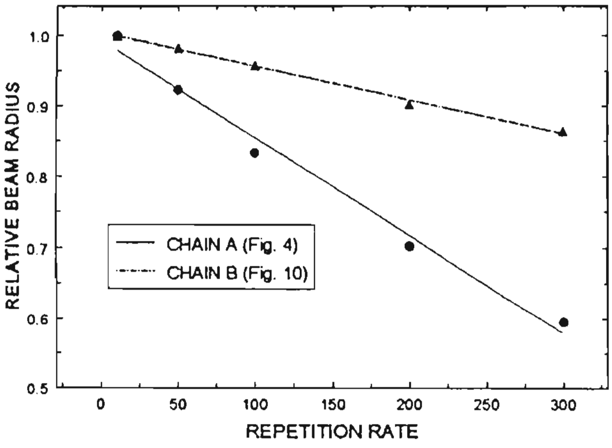

Fig. 9. Improvement in the lensing as a result of the reduction in the number of transmission optics in the amplifier chain.

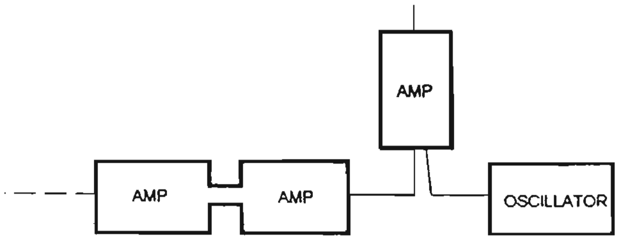

Fig. 10. Improved tandem layout for a reduction of the number of transmission optics.

4.4 Reduction in number of amplifier windows

Fig. 9 shows the result of reducing the number of transmission optics in the chain on the cumulative lensing in the chain. This reduction was achieved by placing the final four amplifiers in a tandem configuration. With this operation the number of transmission optics were reduced from 10 to 6. The important reduction was in the final amplifiers where the lensing effect is enhanced due to the high power loading on the optics (see Fig. 10 for the improved chain configuration).

5. CONCLUSIONS

Thermal lensing is clearly a problem that has to be solved in order to produce a high repetition rate CO_2 beam with predictable beam propagation parameters. Furthermore, a single solution will most probably not solve the problem and one will have to look for a combination of solutions, each with it's own contribution. At high repetition rates the effect of discharge instabilities can also contribute to uncertainty in describing the propagation of the laser beam.

6. ACKNOWLEDGEMENTS

The authors would like to thank A. Gildenhuys, R. van Heerden and M. Gouws for running all the various experiments.

7. REFERENCES

1. C. Langhorn, R. Gruhlke, "How to reduce thermal focusing in high-power laser optics", Laser Focus World, 89-93, Feb 1993.
2. J.P. Gordon , R.C.C. Leite, R.S. Moore, S.P.S. Porto, J.R. Whinnery , "Long-transient effects in lasers with inserted liquid samples", J. Appl. Phys. **36**(3), (1965).
3. C. Hu, J.R. Whinnery, "New thermo-optical measurement method and a comparison with other methods", Appl. Opt. **12**(1), January 1973.
4. J.R. Whinnery, Acc. Chem. Res. 7(225), (1974).
5. M. Franko, C.D. Tran, "Analytical thermal lens instrumentation", Rev. Sci. Instrum **67**(1),1-18, January 1996.
6. A.J. Twarowski, D.S. Kliger, "Multiphoton absorption spectra using thermal blooming", Chem. Phys. 20, 253-258, (1977).
7. D. Kitriotis, "A model for probing small absorption changes during multiple pulse laser-induced damage", Proc. Laser Induced Damage in Optical Materials, ed. H.E. Bennet et. al., pp. 649-656, (1986).
8. N.J. Dovichi, J.M. Harris, "Frequency response of the thermal lens", SPIE Vol 288, Los Alamos conference on Optics, pp. 372-375, (1981).
9. F.J. Prinsloo, Private communication, (1995).
10. A. Forbes, "Multiple pulse Laser induced focusing effects of transmission optics", To be published.
11. W. Klopper, "Establishing dimensions of laser beam", Patent 95/9674, 14 Nov 1995, South Africa.
12. D.J. Scatena, G.L. Herrit, "How to avoid contamination problems in CO_2 laser optics", Laser Focus World, Dec 1990.

Laser and Particle Beams (1996), *vol.* 14, *no.* 3, *pp.* 473–485
Printed in the United States of America

Progress with gas lenses

By M.M. MICHAELIS, M. KUPPEN, A. PRAUSE,
A. FORBES, N. VIRANNA, AND N. LISI
Plasma Physics Research Institute, University of Natal, Durban, South Africa

(Received 15 March 1995; revised 27 March 1996; accepted 31 March 1996)

Three gas lenses appear promising for fusion and other applications. We review progress of the understanding and scaling of two of these lenses and discuss their potential for industry, advanced research, and fusion.

---

1. Introduction

Not infrequently, a technological innovation appears before its time and is consequently more effectively buried than if it had never occurred at all. Such was the case of holography and such, on a much less important scale, is that of gas lenses. These lenses (Marcuse 1982) were invented at Bell Labs in the early 1960s with electrical power and information transmission in mind. In their manifold early forms, they were bulky devices with a narrow field of view.

Yet these lenses have one property that should interest all those concerned with high-power lasers: the absence of a damage threshold. Whereas the breakdown threshold for solids (typically a few GW/cm^2 for 10-ns pulses of visible light) is also the destruction threshold (Melles Griot 1994), the threshold for gases [TW/cm^2 (Gower 1981)] simply means that the lens ceases to work. Reduce the power and it works again, unlike any damaged solid-state optical device. Until now, however, gas lens apertures looked set to remain in the millimeter range. We have recently shown that at least two gas lenses can be scaled up to centimetric diameters: the spinning pipe gas lens and the colliding shock lens. In our opinion, these two lenses and the vortex, negative lens (figure 1) look set to become the workhorses of what has been termed the field of "aerothermooptics" (Martynenko 1975). (Strictly speaking, "aeroptics" might be a better term since many of these lenses are gas-dynamic rather than thermal.) Apart from the airbag lens (once suggested as a corrective optical device for the Hubble telescope's early troubles), all gas lenses are graded index lenses with radial gradients.

As such, predictions can be made about their applicability with a few useful "ball park" calculations. [For a more rigorous treatment of gas lenses, see Marcuse (1982).] For a thermal lens operating at atmospheric pressure, the ray deflection Θ is of the order of 5 mrad, and the refractive index n differs from unity by $\approx 3 \times 10^{-4}$. So the ray deflection equations (Born & Wolf 1980) simplify to

$$\Theta = l\,\frac{dn}{dr},$$

where l is the length of the GRIN lens of radius R and r is the radius at which the ray traverses it. The Gladstone Dale equation gives the refractive index in terms of air densities

$$n \approx 1 + 3 \times 10^{-4} \rho/\rho_0. \tag{1}$$

0263-0346/96 $11.00 + .10

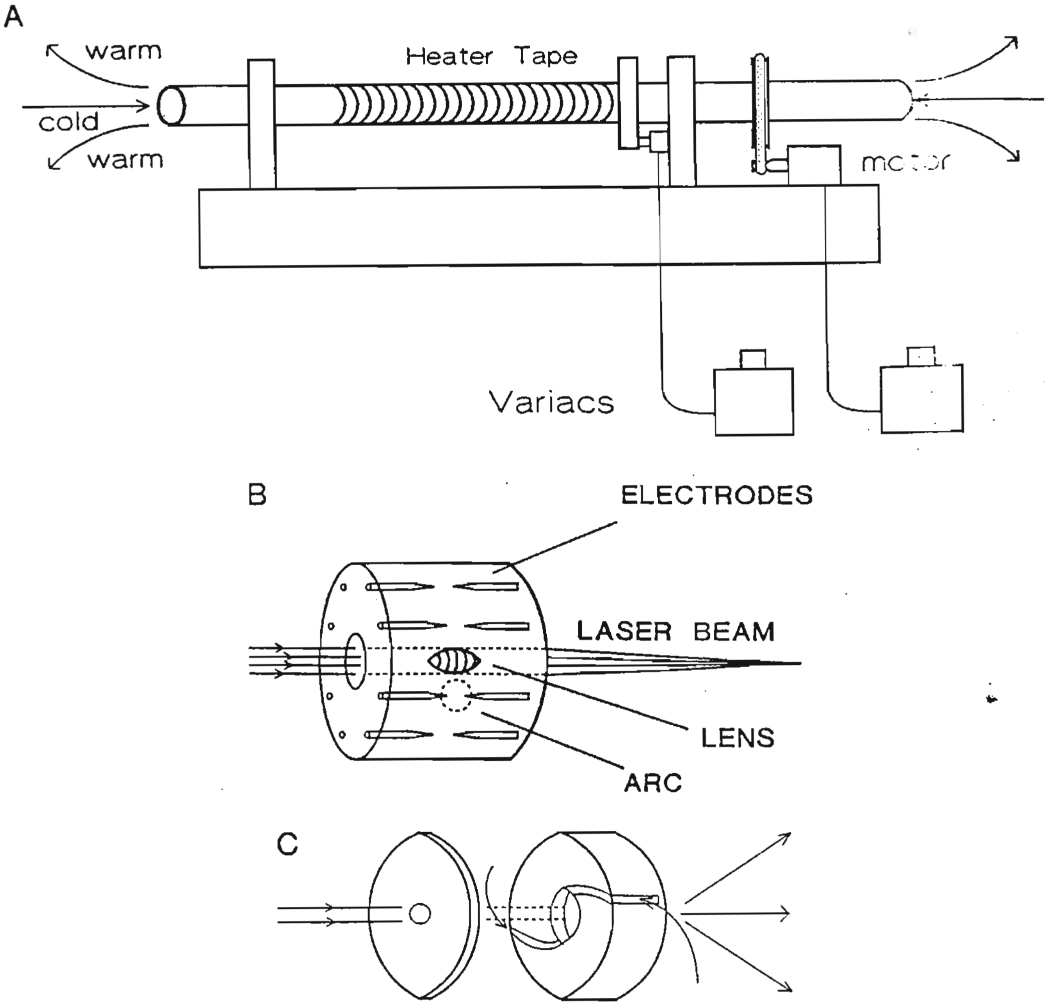

FIGURE 1. Three useful gas lenses: the spinning pipe gas lens (a), the colliding shock lens (b), and the vortex negative lens (c).

If one assumes the pressure within the lens to be atmospheric and the absolute temperature T to differ from the ambient by a small amount ΔT, application of the perfect gas law gives

$$\Theta \approx 10^{-6} l \frac{\Delta T}{\Delta r}. \tag{2}$$

If one assumes further that the temperature (and hence the density and refractive index) distributions are parabolic,

$$T = T_0 + \Delta T_{\max}(r/R)^2, \tag{3}$$

then

$$\Theta \approx 2 \times 10^{-6} l \Delta T_{\max}(r/R^2) \tag{4}$$

and the maximum deflection is

$$\Theta_{\max} \approx 2 \times 10^{-6} l \Delta T_{\max}/R. \tag{5}$$

For long focal length lenses with $f \gg l$, one may write $R \approx f\Theta_{\max}$ so

$$f = 10^6 R^2/(2l\Delta T_{\max}). \tag{6}$$

Some typical values are

$R = 5$ mm $\Delta T = 50°$C $l = 25$ cm $f = 100$ cm

$R = 2$ cm $\Delta T = 50°$C $l = 1$ m $f = 4$ m.

(These values agree very approximately with experiment. For example, a $R = 1.9$ cm lens with $T_{\text{wall}} = 60°$C and $l = 80$ cm gives a 3.5-m focal length.) A comfortable field of view in each case is about 10 mrad. These simple calculations show that thermal lenses are bulky devices with long focal lengths, large f#, and narrow fields of view.

Gas-dynamic lenses on the other hand demonstrated, over a decade ago, greater versatility. A simple calculation assuming a parabolic density profile

$$\rho = \rho_{\text{ATM}} + \Delta\rho_{\max}(r/R)^2 \tag{7}$$

yields

$$\Theta_{\max.\text{dyn}} = 3 \times 10^{-3} l/R \qquad (\Delta\rho_{\max} = 5\rho_{\text{ATM}}) \tag{8}$$

as opposed to

$$\Theta_{\max.\text{therm}} = 10^{-4} l/R \qquad (\Delta T = 50°\text{C}). \tag{9}$$

That is, a gas-dynamic lens with a maximum density of about 6× standard is 30 times more powerful, length for length.

2. Spinning pipe gas lens (SPGL)

This lens, invented at the Minsk Heat and Mass Transfer Institute (Martynenko 1975), overcomes one of the major difficulties associated with tubular laminar flow gas lenses: gravitational convection. This effect, Gloge (1967) calculated, limits the aperture of a tubular lens to about 8 mm. Above that aperture, the optical center of the lens is displaced below the tube boundary. Recently, one of us (Forbes 1996) operated a 5-cm-diameter, 1.5-m-long SPGL in a chamber that could be pressurized with various gases at several bar and also could be partially evacuated. An expanded HeNe laser beam is projected through the SPGL, which focuses it onto a white screen situated on a trolley some 5 to 15 m from the lens. The trolley also carries a TV camera connected to a frame grabber and digitizer. The exact details of this study, which is still continuing, will be published elsewhere when finalized, but they suffice at this point to elucidate the following behavior of the SPGL at high and low pressure. If the chamber pressure is high, quite close to the walls a strong temperature and optical path length (OPL) gradient is established (figure 2a). This region of high refractive index gradient produces an annular lens with a relatively short focal length (4 m at 2-bar gauge) and reasonable focus (figure 2c). Inside the annular region there coexists a long focal length ($f \geq 12$ m) GRIN cylindrical lens, the behavior of which is erratic. As the pressure of the chamber is reduced to about half a bar absolute, the two lenses merge into a better behaved, but long focal length lens ($f = 12$ m) (figure 2d). The focus of this low-pressure lens was at times about twice the diffraction limit. (Mechanical vibrations in the system at present are being eradicated to assess whether they are to blame for focal fluc-

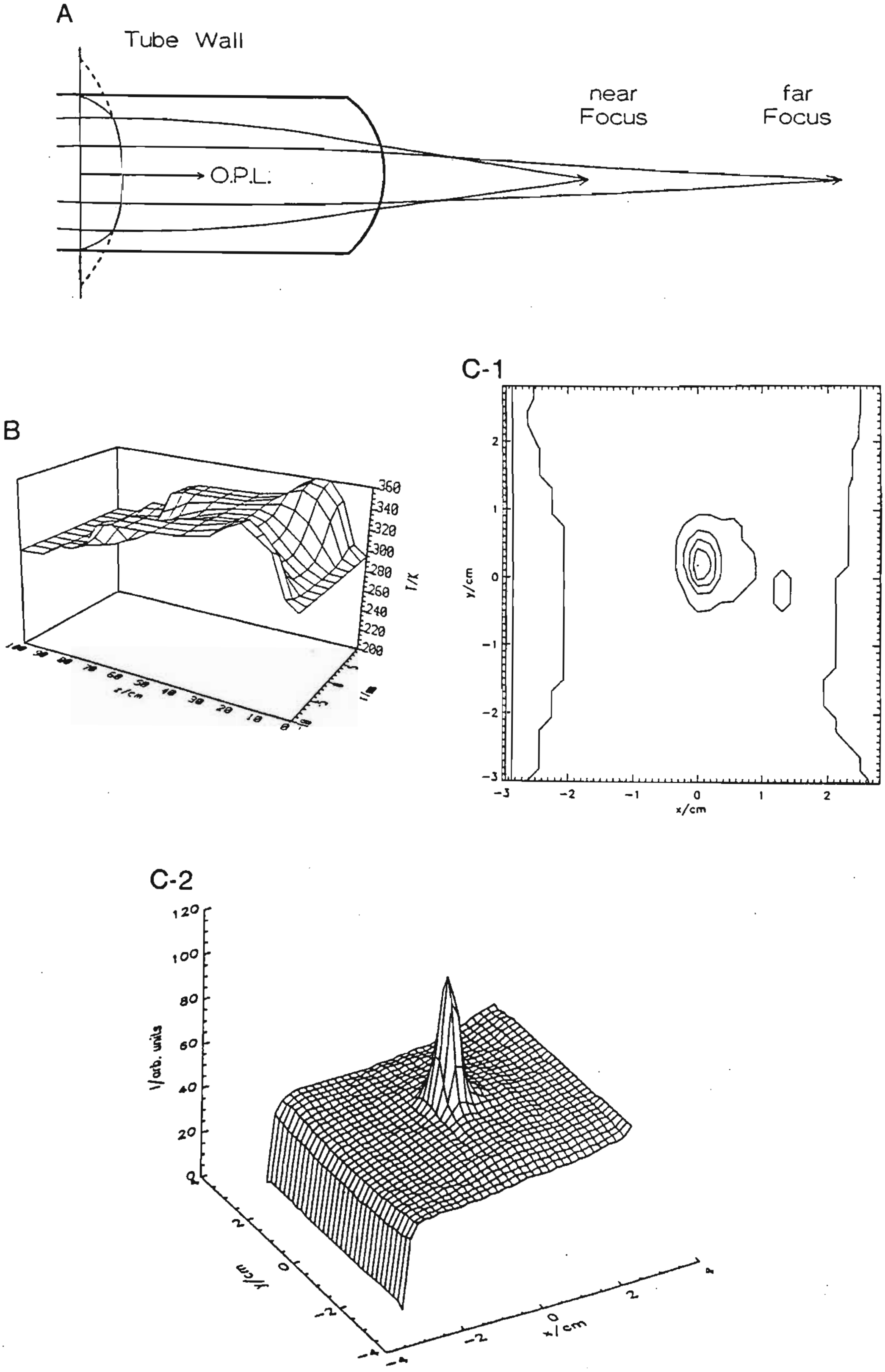
A
Tube Wall
O.P.L.
near Focus
far Focus
B
360
340
320
300
280
260
240
220
200
I/X
z/cm
100
90
80
70
60
50
40
30
20
10
0
C-1
y/cm
x/cm
-3
-2
-1
0
1
2
C-2
I/arb. units
120
100
80
60
40
20
0
y/cm
x/cm
-4
-2
0
2
4

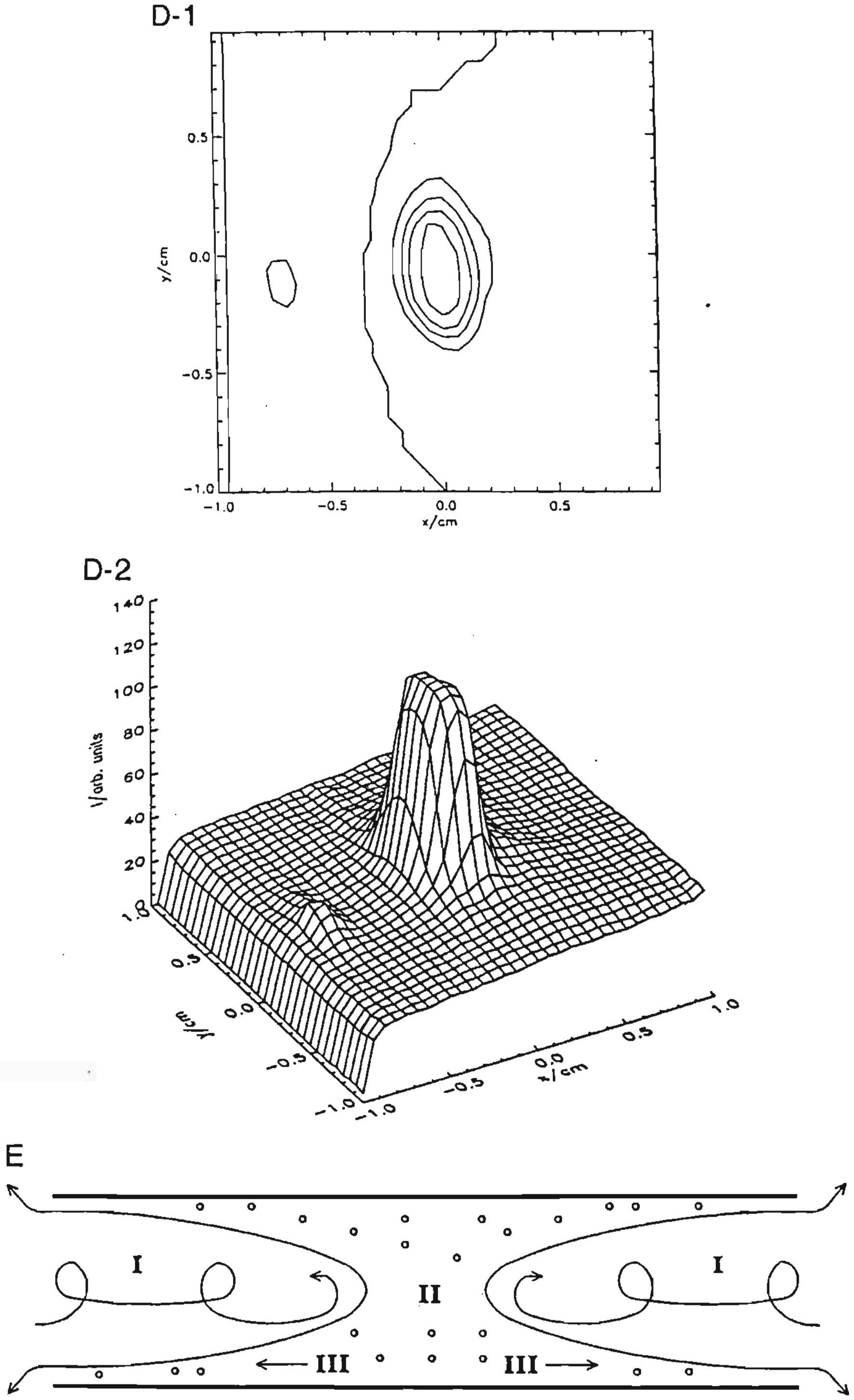

FIGURE 2. Large-diameter SPGL behavior. (a) Formation of two foci for high and for atmospheric pressures. The integrated path length (OPL) through the lens changes rapidly close to the wall and slowly in the central area. (b) Detail of the refractive index profile as measured by Lisi *et al.* (1994). (c) Densitometer traces of high-pressure, near focus. (d) Densitometer traces of low-pressure focus. (e) Visualization of flow with smoke streams.

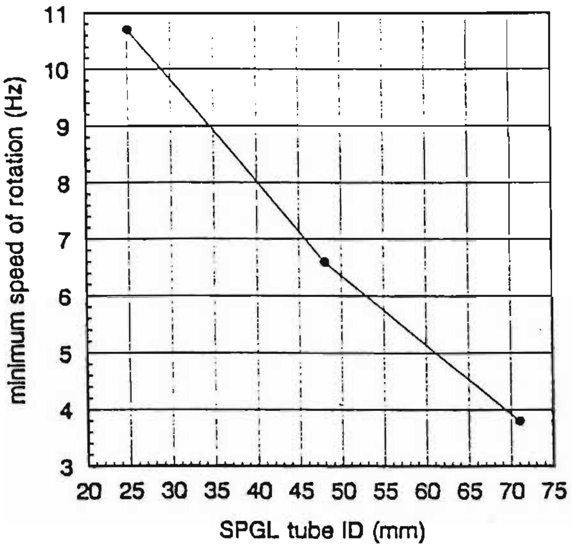

FIGURE 3. Plot of minimum SPGL rotation speed versus tube diameter.

tuations or whether these are fundamental to the SPGL.) One encouraging result is that the minimum SPGL rotation drops with tube diameter (figure 3).

This experiment was helpful in the context of scaling gas lenses in that it indicated two routes to obtaining more useful apertures in the 10-cm range: For long focal lengths, simply reduce the pressure to 1/2 or 1/4 bar. For short focal lengths, operate an annular lens at higher pressures and temperatures. Alas, the experiment also indicated that there will be no such thing as a short focal length, large circular aperture SPGL.

To help convince the high-power laser community that these CW lenses deserve serious attention, we publish here the first pictures of a partial eclipse of the sun, taken with our 2.5-cm aperture gas telescope (figure 4). The well-known ripples on the "surface of the moon" are of course not lunar mountains or craters, but rather the effect of refraction of the sharp edge due to atmospheric turbulence. The visibility of this effect indicates that the telescope is operating as expected from an SPGL, at three or four times the diffraction limit.

This astronomical application strengthens the case for research into the aerodynamics, aberrations, and scaleability of SPGLs. Three experimental papers have been published so far (Notcutt 1988; Michaelis 1991; Lisi 1994) showing that SPGLs behave very differently from ordinary lenses. The quality of the focus is good but fluctuates with time, and even at its optimum the focal region exhibits rotating "wings." Unfortunately, it will be very difficult to model an SPGL analytically or even computationally. The reasons for this will be clear to anyone who ever studied the once-popular Ranque-Hilsch vortex tube, used for gas refrigeration. In the vortex tube as in the SPGL, there are axially counterflowing but co-rotating gas streams, separated by a radially symmetric axial stagnation region. However, in the vortex tube the wall is stationary. In the later versions the two streams are well-defined cylinders coming from separate sources, the "hot" and the "inlet" nozzles. So in principle the vortex tube should be much easier to model than the SPGL. And yet it generated exciting aerodynamic controversy that lasted several decades (Young 1973).

The difficulty that will be encountered in trying to model the SPGL is emphasized further in the article by Cannon and Kays (1969). In this paper it was shown that tube rota-

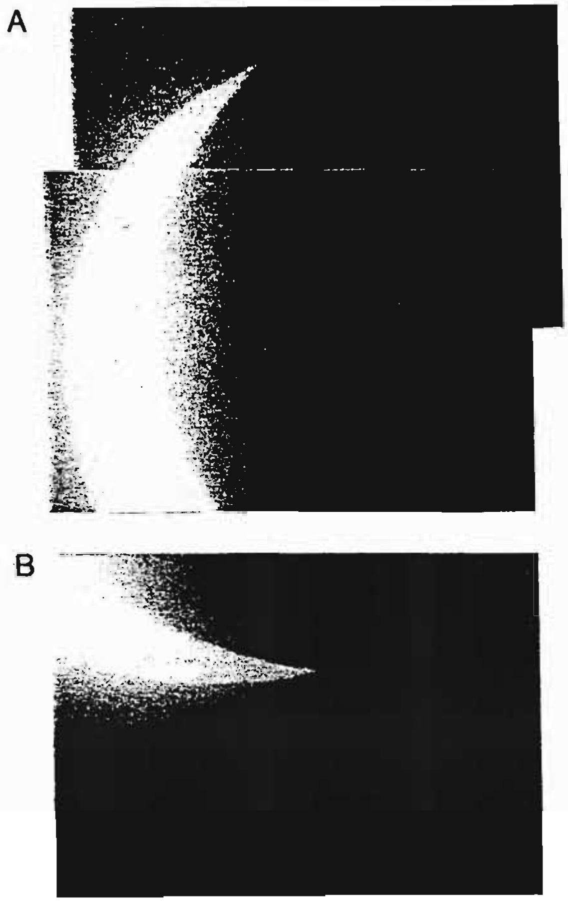

FIGURE 4. Gas telescope pictures of a partial eclipse as seen in South Africa in November 1994. (a) Mosaic of the upper limb. The focal length of the 5-m gas lens is such that each 35-mm negative covers about 1/3 of the sun's image. (b) Note that the lower edge is rippled.

tion stabilizes a "laminar rotating outer flow" which contains a "higher velocity core." "The inner core is non-rotating and if the entering pipe flow is turbulent, the core is noted to consist of decaying rather than active turbulence." To see how the flow patterns in the SPGL differ from the Ranque-Hilsch vortex tube and the Cannon and Kays experiment, we replaced the heated metal tube with a glass one and injected smoke streams close to one end. This experiment immediately illustrates the complexity of the SPGL flow. There are three distinct regions (figure 2e). Region I is similar to the Cannon and Kays "core" and to the "cold" vortex tube stream, and consists of two gently rotating plugs of gas moving slowly inward. Region II is an axially stationary but rapidly rotating region where the smoke trails instantly dissipate into a uniform cloud. The boundary between the plug I and regions II and III is very sharp. Region III resembles region II but carries air in the opposite axial direction to region I. Region III becomes very narrow close to each orifice.

Coupled to the vortex tube and the Cannon and Kays study, that of the smoke streams allowed us to understand qualitatively our own earlier measurements of the temperature and refractive index distribution in the SPGL (Lisi *et al.* 1994). For that paper we measured the distribution with a fine thermocouple and found it to have the shape shown in figure 2b: A flat edge close to the wall is followed by a steep radial drop and a low-temperature center with a parabolic distribution. This is explained as follows.

As the air of region I moves inward it is gently heated by thermal conduction, which explains the slow axial increase in refractive index toward the center of the tube. Region II forms a reservoir of warm gas that supplies region III with a steady stream of preheated gas, which explains the radially flat edge. The sudden cooling of the gas in region III near the ends probably is caused by turbulent mixing of the rapidly rotating sheath with gas from region I. The narrowness of the sheath is confirmed by the observation that the outgoing smoke appears to "peel off" the end of the rotating wall.

The difference in the optical behavior of the SPGL for high and low pressures now becomes clearer. At high pressure the temperature and refractive index profiles are similar to those measured by Lisi *et al.* (1994) (figure 2b). Rays entering the SPGL very close to the wall are virtually undeflected. Rays further in are strongly refracted by the steep refractive index gradient corresponding to the boundary between regions I and III, and are responsible for the near focus. Central rays traverse only regions I and II, which have a gentle parabolic or flat profile and create the far focus. At low pressure (longer mean free path) the I/III boundary becomes less sharp, and it is possible for the two foci to merge into one.

3. Colliding shock lens (CSL)

Another gas lens also indicates that it will scale up to centimetric, possibly even decimetric, apertures. This is the colliding shock lens recently invented by one of us (MM) and Buccellato (1993a). A number of electric arcs (eight or more) on the circumference of a circle generate shock waves in air that form a short-lived GRIN lens at the center (figure 1b). In a previous issue of this journal (Michaelis 1994), we discussed some applications that this lens would have if its aperture could be increased by increasing the diameter of the circle. We later showed that by scaling the electrical diameter from 1 cm to 8 cm, the optical aperture rose from 1 mm (*f* # 600) to 8 mm (*f* # 150), provided the number of arcs was doubled and the energy input increased by a factor of 25 (Kuppen 1995). With the present article in mind, we constructed a 26-cm-diameter lens that yielded a 1.5-cm aperture (*f* # 100) lens. We were able to use some very simple scaling theory from Kuppen (1995) to predict that a 1-m electric diameter lens will yield an 8- to 10-cm aperture lens with a focal length of some 5 to 10 m. A typical scaling argument for this lens runs as follows: Of the 50 kJ applied to the arcs, slightly less than 1% goes to forming the lens. This reduction factor accounts for the geometry of the intersecting shocks, which is represented by

$$G^2 = \frac{1}{20}\frac{r^3}{R^3}.$$

It also contains a second fitted parameter of order 1/2 for strong shocks, which takes into account the facts that not all of the electrical energy goes into the shock wave, and that not all of the shock wave energy is contained in the colliding supersonic shock fronts (Sedov 1959; Zel'dovich 1966; Bacon 1989). The GRIN lens then acquires a density that corresponds to the energy available to adiabatically compress the gas making up the "cigar"-shaped volume. The focal length in meters then is estimated from the density gradient with the approximate formula

$$f^2 = 1.4\frac{r^3}{(\rho^2 - 1)^2 R},$$

where r and R are the radii in millimeters of the GRIN lens and of the circle of arcs, respectively, and ρ is the density of the compressed air. The 1-m electrical diameter lens CSL is scheduled for testing in 1997.

4. Energy consumption of gas lenses

Unlike solid lenses, gas lenses require the input of electrical power, in the case of the SPGL, to keep the heater tape hot and the tube spinning and, in the case of the CSL, to power the arcs that drive the shocks. For the former lens, power consumption is modest: The pipe can be spun with a sewing machine motor and the heater consumes less than 100 W. For a 10-cm SPGL we anticipate power consumption of half a kilowatt. The larger CSLs however already are showing signs of being power-hungry. Whereas the 1-cm electric diameter lens requires only 0.7 J per shot, the 26-cm lens requires 36 J, and the 1-m device will need tens of kilojoules to generate a 10-cm GRIN lens. It should be pointed out however that 99% of the shock energy is at present wasted in 3D spherical expansion. We have already shown for our smallest lens that a factor ten can be gained by confining the shocks to two dimensions. It is conceivable that we may, after some research, be able to generate a 10-cm lens for as little as 1 kJ per shot.

These early arguments show that, although CSLs will scale to centimetric and possibly decimetric apertures, it will not be practical for energy reasons to run them at high repetition rates, except for subcentimetric apertures.

5. Application of gas lenses

Now that both pulsed and CW gas lenses have shown how they scale, we are able to look with greater confidence at short-, medium-, and long-term applications (figure 5). The obvious short-term applications are pulsed and CW CO_2 laser systems for industry: drilling, cutting, and welding (figures 5a and b). In our laboratory we are working on unusually robust systems involving a minimum of solid-state optical components. It is these delicate and expensive devices (ZnSe Brewster windows, anti-reflection–coated Ge output mirrors, lenses, polarizers, etc.) that have prevented the laser from fulfilling its industrial promise. These solid components are far from ideally suited to the "nonclean" room environment of industry. But gas lenses also have problems. That of the SPGL is its long focal length; that of the CSL is that, at high repetition rates, it may consume as many kilowatts as the laser itself. Nevertheless, we believe that the fact that they cannot be scratched makes them worth studying. Recently we showed that a mixture of solid-state and gas optics may be an answer. We demonstrated a novel all-gas Q-switch (Lisi 1995) that works with a combination of an SPGL and a CSL: only when the CSL has the right focal length is the laser cavity stable. The Q-switch was inserted in a ruby laser (figure 5c) and gave a 100-ns pulse. We are attempting to shorten this pulse by using pairs of CSLs. The aim of these experiments is to produce repetition rates that are not easily achievable with Pockels or Kerr cells. The CSL itself so far only has been run at 50 Hz, the limit of our power supply, but theoretical considerations based on our refractive fringe diagnostic of shocks indicate that the limit should be well beyond the 1-kHz rate.

Longer term applications of gas optics have been suggested by other workers. The free electron laser input and output regions require intensities too high for solid optics. Christiansen (1988) suggested using a vortex diverging lens to expand the narrow output beam so that it can be handled with conventional optical components (figure 5d). Similar difficulties with high average power beams have been encountered in laser isotope separation systems (figure 5e).

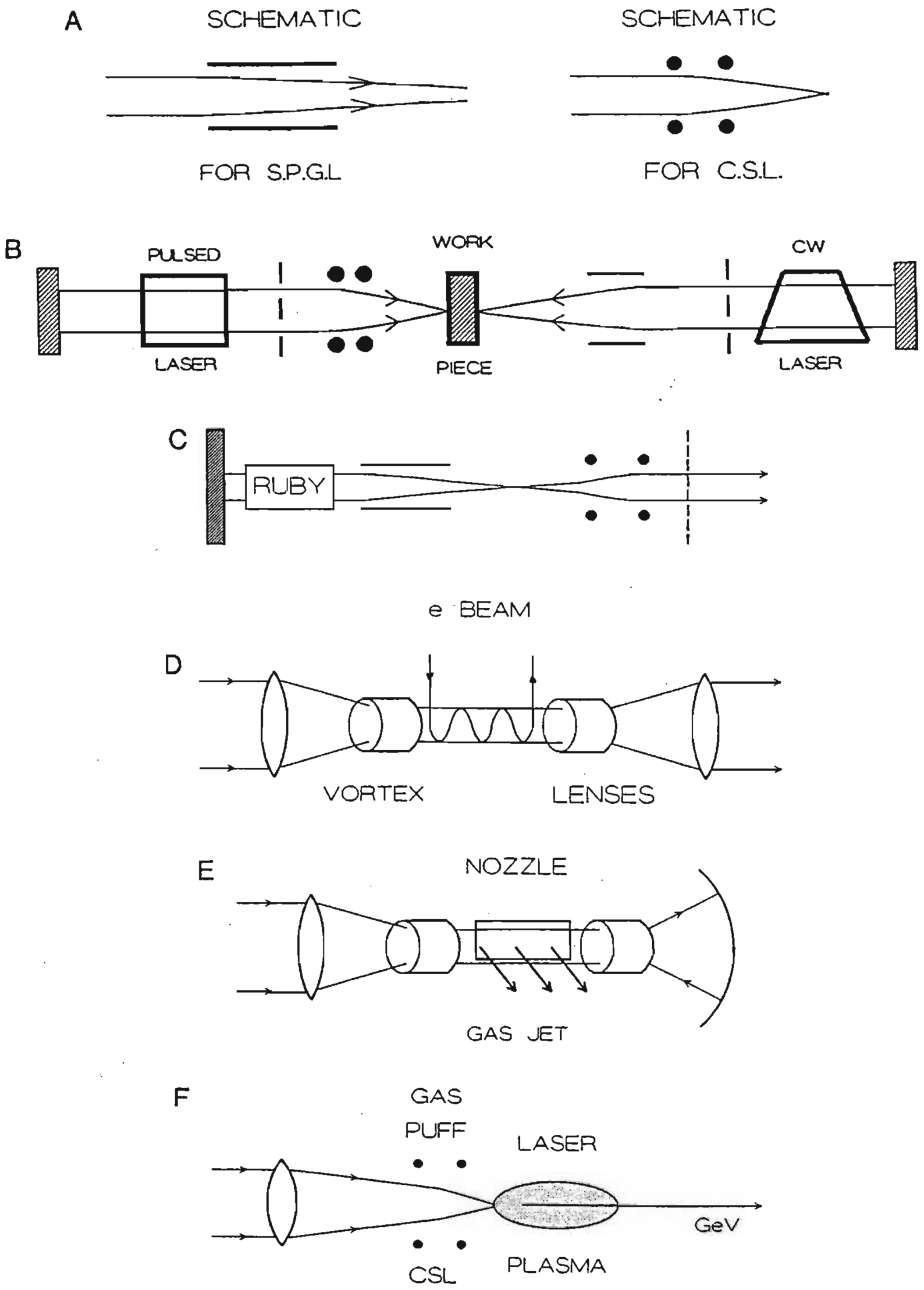

FIGURE 5. Configurations for various gas len applications: (a) drilling, cutting, and welding (pulsed); (b) idem (c.w.); (c) Q-switching; (d) FEL; (e) laser isotope separation; (f) laser plasma accelerator; (g) laser fusion. [In (d)–(g), the gas lens increases the achievable intensity.] (h) Decompression gas lens for long focal length applications such as satellite propulsion or space junk deceleration. (*Figure continues*).

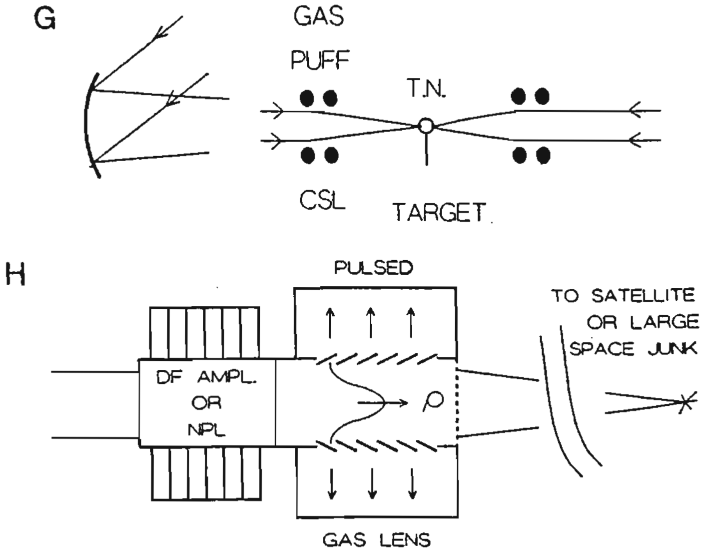

Figure 5 continued.

We also envisage analogous problems with rep-rated X-ray lasers of the future and have developed a cylindrical gas lens that could be employed to generate a line focus laser-produced plasma. This gas lens is produced by colliding some 40 shock waves, so that they form a 4-cm-long high gas density cylinder. This lens can function either as a cylindrical lens if irradiated through the lateral windows (figure 6) or as a strong axial CSL if irradiated through axial windows.

One area where gas lenses are playing a role, albeit an unwanted one, is that of nuclear pumped lasers (NPL). [For an overview of NPLs, see Miley *et al.* (1993).] The power of an NPL is limited by beam refraction resulting from pump power deposition and heating of the gas. Essentially, the heated gas moves to produce a time-variant gas lens. Torczynski and Neal (1993) describe experiments in which a probe laser beam is used to measure the changes in gas density as the nuclear pumping and heating progress. A density depression forms close to the walls in the region where energy deposition peaks. So there are two density maxima, one along the axis of the chamber and the other at the walls. The former is due to reduced energy deposition, the latter to cooling at the walls. The central maximum forms a strong time-varying lens that focuses most of the 1.50-m-diameter probe beam just outside the 60-cm-long chamber about 50 ms after pumping commences.

We suggest that it would not be difficult to design a pair of negative-pulsed gas lenses (PGL) that could be situated at either end of the nuclear pumped cavity to counteract the internal focusing. These PGLs would be of the type described in Buccellato (1993b). In that work, our group showed that short-pulse (1-ms) operation of a PGL is difficult. Longer pulses required for the NPL application would require easier and slower plenum opening times. The natural tendency for the power of a PGL to rise and fall could be tailored to counteract the same tendency of the positive NPL "lens." The "ball park" calculation, however, indicates that a PGL operating in air at 30 bar would need to be several meters long.

In the very long term, gas lenses could play a part in laser fusion reactors. All reactor designs forsee placing the final focusing optics tens of meters away from the target (Moses 1994). In the Russian "Tiger" design, for example, this distance is "from 30 to 50 m away

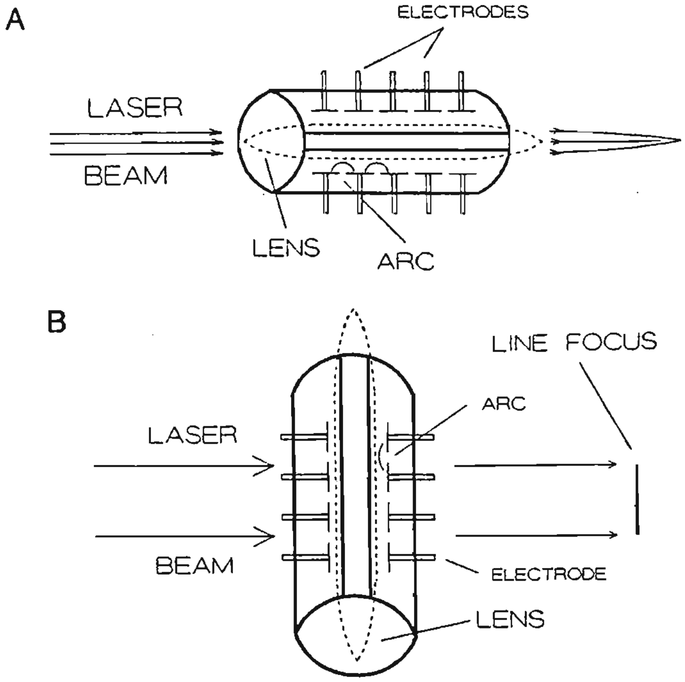

FIGURE 6. Cylindrical gas lens. Simultaneous arcs generate a cylinder of high-density air. The cylinder acts as a conventional GRIN lens for axial illumination (a) or as a line-focusing lens for transverse illumination (b).

from the target — the laser light being brought to the chamber via air tight metal pipes filled with inert gas at low pressure. The gas is necessary to protect the mirrors from ions, X-rays and the pressure is low to avoid gas break-down" (Basov 1996).

We suggest that the gas protection system could be configured to act as a pulsed lens similar to that described in the next paragraph. Alternatively (figure 5g), a CSL could be placed quite close to the target. The CSL would be operated in the gas puff mode so as to avoid gas contamination of the target. The CSL is the only lens capable of operating very close to the target under reactor conditions.

The final application we foresee in the very long term is that of laser impulse space propulsion (LISP). In this growing field (Kare 1987) there will be a gradual progression from relatively low-power applications such as de-orbiting space junk (Phipps 1996) to high power as applied to a variety of orbital manoeuvres, and finally to an actual laser launch. Lasers are the best option for de-orbiting the almost 1 million pieces of junk presently threatening long-term missions. The high specific impulse available from LISP makes it an exciting orbital alternative that is capable of prolonging the useful life of many satellites. An actual laser launch from the ground would require a very large laser indeed. This could be a DF laser (Phipps 1994) or an NPL. We believe that the only lens capable of focusing the beam from such a laser at distances varying continuously from 20 to 100 km and of transmitting average powers in the 100 MW–1 GW range for several minutes will be a gas lens. Buccellato *et al.* (1993b) suggested configuring the exhaust section of a DF laser as a rarefaction gas lens (figure 5h). This rarefaction gas lens is similar to the "pressure-gradient interface" for the 180-MJ DF laser designed by Phipps (1989) for fusion studies. Fast valves open in less than a millisecond, allowing the radially expanding gas from a central prepressurized tube to adopt a bell-shaped profile. (The same method also can be used to create a negative lens if the high-pressure region is on the outside of the tube.) So far this concept has only been tested with a 1D lens in our laboratory.

The quality of such a large gas lens and its long time scale (tens of ms) should allow the LISP active optics mirror (AOM) to be placed up-beam of the final amplifier. Considerable engineering and cost problems could develop otherwise in creating an AOM capable of handling hundreds of megawatts.

6. Conclusion

Decades may elapse before most of these applications occur. Yet the good optical quality of gas lenses, their power handling capabilities, and absence of damage threshold, as well as the fact that, unlike any other lens, their focal length can be adjusted electronically within microseconds, make them unlikely to remain an academic curiosity. Some scaled-up gas lenses should be ready for industrial use in the very near future. Others may reach maturity in step with the laser propulsion and laser fusion programs.

REFERENCES

BACON, M. *et al.* 1989 *J. Appl. Phys.* **66**, 1075.

BASOV, N.G. *et al.* (in press) *The Physics of Laser Fusion* (Editions Frontieres, Paris).

BORN, M. & WOLF, E. 1980 *Principles of Optics*, 6th ed. (Pergamon Press, Oxford).

BUCCELLATO, R. *et al.* 1993a *Opt. Comm.* **101**, 350

BUCCELLATO, R. *et al.* 1993b *Opt. Laser Technol.* **25**, 247.

CANNON, J.N. & KAYS, W.M. 1969 *J. Heat Transfer.* **Feb.**, 135.

CHRISTIANSEN, W.H. 1988 *SPIE* **1031**, 474.

FORBES, A. 1996 M.Sc Thesis, University of Natal.

GLOGE, D. 1967 *Bell Syst. Tech. J.* **Feb.**, 375.

GOWER, M.C. *et al.* 1981 *Opt. Comm.* **36**, 43.

KARE, J.T. 1990 *Proc. SDIO/DARPA Workshop on Laser Propulsion*, J.T. Kare, ed. (LLNL Conf. 8710452), Livermore, CA.

KUPPEN, M. *et al.* 1995 *Rev. Sci. Instr.* **66**, 5037.

LISI, N. *et al.* 1994 *Opt. & Laser Technol.* **26**, 25.

LISI, N. *et al.* 1995 *Appl. Optics* **34**, 942.

MARCUSE, D. 1982 *Light Transmission Optics.* (Van Nostrand and Reinhold, New York).

MARTYNENKO, O.G. 1975 *Int. J. Heat and Mass Transfer* **18**, 793.

MELLES GRIOT 1994 *Catalogue.*

MICHAELIS, M.M. *et al.* 1991 *Laser Part. Beams* **9**, 641.

MICHAELIS, M.M. *et al.* 1994 *Laser Part. Beams* **12**, 531.

MILEY, G.H. 1993 *Laser Part. Beams* **11**, 575.

MOSES, G.A. & PETERSON, R.R. 1994 *Laser Part. Beams* **12**, 125.

NOTCUTT, M. *et al.* 1988 *Opt. & Laser Technol.* **20**, 243.

PHIPPS, C.R. & MICHAELIS, M.M. 1994 *Laser Part. Beams* **12**, 23.

PHIPPS, C.R. 1989 *Laser Part. Beams* **7**, 835.

PHIPPS, C.R. *et al.* 1996 *Laser Part. Beams* **14**, 1.

SEDOV, L.I. 1959 *Methods of Similarity and Dimensional Analysis in Mechanics.* (Academic, New York).

TORCZYNSKI, J.R. & NEAL, D.R. 1993 *Nucl. Sci. and Eng.* **113**, 189.

YOUNG, J. & MCCUTCHEON, A.R.S. 1973 *Chem. Eng.* **279**, 522.

ZELDOVICH, YA.B. & RAIZER, YU.P. 1966 *Physics of Shock Waves and High Temperature Hydrodynamic Phenomena.* (Academic, New York).